

# UC San Diego

## UC San Diego Electronic Theses and Dissertations

### Title

High Energy Wide Area Blunt Impact Damage to Internal Structural Components of Composite Aircraft Fuselage Structures

### Permalink

<https://escholarship.org/uc/item/5cv3c44g>

### Author

Nam, Moonhee

### Publication Date

2021

Peer reviewed|Thesis/dissertation

UNIVERSITY OF CALIFORNIA SAN DIEGO

High Energy Wide Area Blunt Impact Damage to Internal Structural  
Components of Composite Aircraft Fuselage Structures

A dissertation submitted in partial satisfaction of the  
requirements for the degree Doctor of Philosophy

in

Structural Engineering

by

Moonhee Nam

Committee in charge:

Professor Hyonny Kim, Chair  
Professor Veronica Eliasson  
Professor Francesco Lanza Di Scalea  
Professor Vitali Nesterenko  
Professor Chia-Ming Uang

2021

Copyright

Moonhee Nam, 2021

All rights reserved.

The Dissertation of Moonhee Nam is approved, and it is acceptable in quality and form for publication on microfilm and electronically.

University of California San Diego

2021

## TABLE OF CONTENTS

Dissertation Approval Page .....	iii
Table of Contents .....	iv
List of Abbreviations .....	viii
List of Figures .....	x
List of Tables .....	xix
Acknowledgements .....	xx
Vita.....	xxii
Abstract of the Dissertation .....	xxiv
1 Introduction.....	1
1.1 Justification for Current Research .....	2
1.2 Overview and Past Research.....	4
1.3 Current Research Scope and Objectives .....	11
2 Literature Review.....	17
2.1 1st Generation HEWABI Research .....	17
2.2 CODAMEIN – Composite Damage Metrics and Inspection (high energy blunt impact threat) Research .....	29
2.3 Crashworthiness – Frame Failure .....	34
2.4 Literature Review Conclusion .....	38
3 Large Scale Experiments (2nd Generation Panels) .....	40
3.1 Benchmarking Existing Commercial Composite Fuselage .....	40
3.2 Specimen Description .....	41
3.3 Lay-up and Thickness of The Fuselage Components.....	46

3.4	Floor Beam and Joint Description .....	47
3.5	Composite Material Properties .....	49
3.6	Design Methodology with FEA Approach .....	50
	3.6.1 Finite Element Model Information .....	52
	3.6.2 Results of FE Model .....	57
3.7	Manufacturing.....	62
3.8	Experimental Setup.....	69
	3.8.1 Loading Cases.....	71
	3.8.2 Soft Contact Loading Head – Flat Rubber Bumper.....	72
	3.8.3 Upper and Lower Fixtures .....	74
	3.8.4 Strain Gauges on Floor I-Beam .....	77
	3.8.5 Terminology of Local Area .....	77
3.9	Specific Setup for Loc4 Tests.....	78
3.10	Experimental Results – Loc4.....	84
	3.10.1 Load-Skin Displacement Curve and Key Event Summary .....	91
	3.10.2 Cracking Initiation – Shear Tie Radius Delamination.....	93
	3.10.3 Crack Growth Along the Shear Tie Radius and Shear Tie Web-Stringer Hat Contact .....	97
	3.10.4 Stringer Hat Damage Initiation at Loc4 by Contact .....	105
	3.10.5 Catastrophic Failure on Shear Tie and C-Frame .....	108
	3.10.6 External Damage Detectability .....	119
	3.10.7 Experimental Conclusion – Loc4 .....	121
3.11	Specific Setup for Loc3 Tests.....	125
3.12	Experimental Results – Loc3.....	130

3.12.1	Loc3-1 Damage Sequence .....	134
3.12.2	Loc3-2 Damage Sequence .....	140
3.12.3	Experimental Conclusion – Loc3 .....	151
3.13	Experimental Conclusions .....	152
4	Experiment and FE Modeling of C-Frame Failure .....	156
4.1	Bending and Twisting Failure Observed in Frame03 Test .....	159
4.1.1	C-Frame Element-Level Tests.....	159
4.1.2	FE Model for C-Frame Bending and Twisting Test.....	166
4.1.3	Result Comparison (Test Versus FEA) and Conclusion .....	168
4.2	Direct Shear Failure Observed in Frame04-2 Test .....	174
4.2.1	C-Frame Failure Mechanism Observed in Frame04-2 Test .....	174
4.2.2	FE Model for C-Frame Failure in Frame04-2 Test .....	176
4.2.3	FEA Results Comparison to Tests and Discussion.....	178
4.3	Conclusion of Frame Failure Studies.....	182
5	Large Scale FE Model for Failure Prediction and Correlation with Large Scale Tests .....	185
5.1	FE Model Update – Bumper Size, Composite Material Property, Node-to-Node Tie Constraint .....	186
5.2	Predicted Events and Correlation with Test Results.....	190
5.3	Conclusion and Future Work.....	200
6	Conclusions.....	203
	References.....	206
	Appendices.....	209
A.	Mold Drawings .....	209

B.	Layup Instruction.....	216
C.	Specimen and Fixture Drawings.....	291



## LIST OF ABBREVIATIONS

UCSD	University of California, San Diego
HEWABI	High Energy Wide Area Blunt Impact
GSE	Ground Service Equipment
BVID	Barely Visible Impact Damage
FAA	Federal Aviation Administration
JAMS CoE	Joint Advanced Materials and Structures Center of Excellence
CODAMEIN	Composite Damage Metrics and Inspection
EASA	European Aviation Safety Agency
FOD	Foreign Object Damage
FE/FEA	Finite Element / Finite Element Analysis
CFRP	Carbon Fiber Reinforced Polymer
UD	Unidirectional
PW	Plain Weave
ASTM	American Society for Testing and Materials
SACMA	Suppliers of Advanced Composite Materials Assn
SBS	Short Beam Shear

DCB	Double Cantilever Beam
ENF	End Notched Flexure
SBR	Styrene Butadiene Rubber
AL	Aluminum
LP	Linear Potentiometer
LC	Load Cell
SG	Strain Gauge (Linear)
RS	Rosette Strain Gauge
CS	Contact Sensor
ST	Shear Tie
Str	Stringer
kN	Kilonewton
$\mu\text{m}/\text{m}$	Microstrain
kN	Kilonewton
NDT	Non-Destructive Testing
ILTS	Interlaminar Tension Strength

## LIST OF FIGURES

Figure 1.1: Composite usage in B787 (boeing.com/commercial/aero) [2], and B787 composite fuselage section (aviationpros.com) [4]. .....	2
Figure 1.2: Damage category defined by the FAA [7]. .....	3
Figure 1.3: GSE approaching to the aircraft fuselage; note rubber bumper at interface between GSE and aircraft [8].....	5
Figure 1.4: Severe internal damage by HEWABI (shear tie and C-frame fracture) [8]. ....	5
Figure 1.5: External skin after sustaining internal damage at levels shown in Figure 1.4 [11]......	6
Figure 1.6: Impact to aircraft fuselage; “Region 1” – acreage area for the 1 <sup>st</sup> generation HEWABI experiments. ....	7
Figure 1.7: 1 <sup>st</sup> generation HEWABI fuselage panel [8].....	7
Figure 1.8: Road map for approaching experiments and numerical simulation of High Energy Wide Area Blunt Impact [11]......	8
Figure 1.9: Experimental setup for structural-level Frame03 and 04 dynamic experiments [11]......	9
Figure 1.10: Analysis of the key failure modes in the fuselage panel through element-level experiments [11]......	10
Figure 1.11: Modeling definition for element-level studies exported into the large-scale FE model [11]. .....	11
Figure 1.12: Impact to aircraft fuselage; “Region 2” and frame to floor structure interaction. ....	12
Figure 1.13: Boeing 787 fuselage with the continuous shear tie and floor structure; Picture from Boeing Future of Flight Museum (Left) and The Birth of the 787 Dreamliner (Right) [19]. ....	13
Figure 1.14: 2 <sup>nd</sup> generation HEWABI panel test. ....	14
Figure 1.15: 2 <sup>nd</sup> generation HEWABI fuselage panel and its components.....	15
Figure 2.1: 1 <sup>st</sup> generation HEWABI fuselage panel [8, 11]......	19

Figure 2.2: Determination of the frame panel boundary conditions [8].	20
Figure 2.3: Impactor tip with the rubber bumper [8, 11].	21
Figure 2.4: Internal damages of Frame01 panel loaded onto shear ties [8, 11].	22
Figure 2.5: Internal damage sequence of Frame03 panel loaded onto shear ties [8, 11].	24
Figure 2.6: Direct shear failure of C-frames in Frame04-2 panel loaded onto strong shear ties [8, 11].	24
Figure 2.7: Shear tie element test for shear tie radial delam/crushing due to compression loading [11].	27
Figure 2.8: Shear tie element FE modeling methodology [11].	28
Figure 2.9: Shear tie element FE simulation correlated with the element test – Compression and Buckling [11].	28
Figure 2.10: CODAMEIN panel details: stringer, shear tie and frame [18].	30
Figure 2.11: CODAMEIN test setup details [17, 18].	31
Figure 2.12: Shear tie strain gauge data capturing local buckling [18].	32
Figure 2.13: Load-displacement curve [18].	32
Figure 2.14: FE modeling scheme for shear tie and fastener connection [18].	34
Figure 2.15: Fuselage section crash simulation model with critical area highlighted [21].	35
Figure 2.16: Aluminum load introduction devices (a) and 4 point bending test setup (b) [21].	36
Figure 2.17: 4 point bending test of composite frame and key failure modes [21].	36
Figure 2.18: Final FE model (Left) and predicted key modes observed in tests [21].	37
Figure 3.1: Boeing 787 Fuselage Configuration; Picture from Boeing Future of Flight Museum (Left) and from The Birth of the 787 Dreamliner by Edgar Turner (Right) [19].	41
Figure 3.2: 2 <sup>nd</sup> generation HEWABI specimen.	43
Figure 3.3: Panel comparison – stringer spacing [8, 11].	44

Figure 3.4: Panel comparison – stringer-skin section [8, 11]. .....	44
Figure 3.5: Panel comparison – shear tie [8, 11]. .....	45
Figure 3.6: Panel comparison – C-frame [8, 11]. .....	45
Figure 3.7: Passenger floor I-beam and floor joint assembly. ....	48
Figure 3.8: Full quarter barrel vs. truncated model. ....	52
Figure 3.9: Hashin-Rotem failure criterion – damage evolution bilinear law [8, 25]. ....	53
Figure 3.10: Bumper compression test and FE modeling [11]. ....	55
Figure 3.11: Conventional vs. continuum shell element defined in Abaqus 6-13 analysis user manual, section 29.6.1 [25]. ....	56
Figure 3.12: Mesh and effective fastener modeling.....	57
Figure 3.13: Comparison of full vs. truncated model for Loc3 loading on skin bay.....	58
Figure 3.14: Comparison of full vs. truncated model for Loc4 loading on stringer. ....	59
Figure 3.15: Maximum S11 comparison examples in the top layer at the load of 22.24 kN (5 kips). ....	60
Figure 3.16: Realistic boundary conditions in test environment – friction contact between the rubber bumper and the skin.....	62
Figure 3.17: Tools for specimen fabrication.....	63
Figure 3.18: Skin outer mold line tool [8]. ....	64
Figure 3.19: Assembled stringer tool and tool part removal after autoclave cure. ....	64
Figure 3.20: Ply cutting with cutting templates and hand layup.....	65
Figure 3.21: Vacuum bagging for all parts. ....	65
Figure 3.22: 1.8 m diameter autoclave in San Diego Composites (left) and autoclave cure cycle (right) [26]. ....	65
Figure 3.23: Trimming parts using diamond saws and machining shear ties by CNC.....	67
Figure 3.24: Stringer corner detail. ....	67

Figure 3.25: Match drilling using jigs and panel assembly using Hi-Lok fasteners .....	68
Figure 3.26: Test configuration.....	70
Figure 3.27: Numbering definition of the loading location. ....	71
Figure 3.28: Soft contact loading head. ....	73
Figure 3.29: Fixtures mounted for specimen testing. ....	75
Figure 3.30: Aluminum C-channel lower beam and its connection. ....	76
Figure 3.31: Strain gauges on I-beam. ....	77
Figure 3.32: Terminology of local areas. ....	78
Figure 3.33: Linear potentiometers (LPs) for the skin displacement (Left) and the external displacement (Right). ....	79
Figure 3.34: Contact sensor (CS) installed at Loc4. ....	79
Figure 3.35: C-frame strain gauges for Loc4 specimens. ....	81
Figure 3.36: Shear tie strain gauges for Loc4 specimens. ....	82
Figure 3.37: Stringer strain gauges for Loc4 specimens.....	83
Figure 3.38: Skin strain gauges for Loc4 specimens. ....	84
Figure 3.39: Loc4-1 (Left) and Loc4-2 (Right) test setup in South Powell Laboratory. ..	85
Figure 3.40: Discrepancy of west load cell value between Loc4-1 and Loc4-2 tests.....	88
Figure 3.41: Strain gauge data check on I-beam.....	89
Figure 3.42: Scale factor for west load cell value of Loc4-2_L6 test. ....	90
Figure 3.43: LP connection kinking of Loc4-2_L6 test at C-frame failure. ....	91
Figure 3.44: Load vs center skin displacement for all Loc4 tests.....	92
Figure 3.45: Paint chipping and delamination at shear tie radius region at upper (Left) and lower (Right) side of Loc4 mouse hole after Loc4-1_L1-4 with close-up view after Loc4-1_L4L5.....	94

Figure 3.46: Strain curves from SG12-13 back-to-back gauges near shear tie radius region at upper side of Loc4 mouse hole. ....	96
Figure 3.47: Strain curves from SG15-16 back-to-back gauges near shear tie radius region at lower side of Loc4 mouse hole. ....	97
Figure 3.48: Shear tie radius delamination and fiber crushing damage with crack growth after Loc4-1_L2L3 (Left) and L4L5 (Right) test.....	98
Figure 3.49: Shear tie radius delamination and fiber crushing damage with crack growth at maximum load of Loc4-1_L4L5 (Left) and after Loc4-2_L6 (Right) test. ....	99
Figure 3.50: Strain curves from SG12-13 back-to-back gauges near shear tie radius region at upper side of Loc4 mouse hole. ....	100
Figure 3.51: Strain curves from SG15-16 back-to-back gauges near shear tie radius region at lower side of Loc4 mouse hole. ....	101
Figure 3.52: Strain gauge location (SG06, SG07, SG08, and SG14) at Loc4. ....	102
Figure 3.53: Strain curves from SG06 installed on stringer upper side at Loc4.....	103
Figure 3.54: Strain curves from SG07 installed on stringer hat at Loc4. ....	104
Figure 3.55: Strain curves from SG14 installed on shear tie web near mouse hole section at Loc4. ....	105
Figure 3.56: Stringer cut by the shear tie web contact after Loc4-1_L4L5.....	106
Figure 3.57: Strain curves from SG07 installed on Str. hat at Loc4.....	107
Figure 3.58: Strain curves from SG08 installed on Str. lower side at Loc4. ....	108
Figure 3.59: Extensive shear tie, stringer, and C-frame damage after Loc4-2_L6 test. .	109
Figure 3.60: Extensive shear tie damage at maximum load in Loc4-1_L4L5 test (Left) and in Loc4-2L6 test (Right).....	110
Figure 3.61: Strain curves from SG10 near shear tie radius region at lower side of Loc2 mouse hole. ....	111
Figure 3.62: Strain curves from SG11 near shear tie radius region at lower side of Loc2 mouse hole. ....	112
Figure 3.63: Strain curves from SG14 installed on ST. web near mouse hole section at Loc4. ....	113

Figure 3.64: C-frame fracture at Loc4 and floor joint at maximum stroke in Loc4-2_L6. .....	114
Figure 3.65: C-frame damage initiation at the Hi-Lok fastener on the web at Loc4 right after shear tie web fracture in Loc4-1_L4L5. ....	115
Figure 3.66: Bending strain curves from SG-FN on inner surface of outer flange at Loc4. .....	116
Figure 3.67: Shear strain curves from RS01 and RS02 at Loc2 and Loc6 respectively.	117
Figure 3.68: Bending strain curves from SG19 and SG20 at Loc2. ....	118
Figure 3.69: Bending strain curves from SG21 and SG22 at Loc6. ....	119
Figure 3.70: No obvious external damage sign on skin (red hatched areas are pre-existing shim-to-skin disbanding from non-destructive testing). ....	120
Figure 3.71: Barely visible skin crack observed at Loc4 in the first panel.....	121
Figure 3.72: Stringer-shear tie contact, shear tie penetration, and locking C-frame. ....	122
Figure 3.73: Frame03 and Frame04-1 combined loading and energy per frame [8]. ....	123
Figure 3.74: Loc4-2 loading curve and energy.....	124
Figure 3.75: Linear potentiometers (LPs) for the external displacement. ....	126
Figure 3.76: C-frame strain gauges for Loc3 specimens. ....	127
Figure 3.77: Shear tie strain gauges for Loc3 specimens. ....	128
Figure 3.78: Stringer strain gauges for Loc3 specimens.....	129
Figure 3.79: Skin strain gauges for Loc3 specimens. ....	130
Figure 3.80: A-scan results after Loc3-2 test.....	131
Figure 3.81: Visible skin-stringer disbond after Loc3-2 test. ....	131
Figure 3.82: Force vs external displacement for Loc3-1 tests. ....	134
Figure 3.83: Paint chipping observed on Loc3 shear tie radius after Loc3-1_L1.....	135
Figure 3.84: No evidence of radius delamination in strain curves during Loc3-1_L1... ..	136



Figure 3.85: Shear tie crack observed in Loc3-1_L2.....	137
Figure 3.86: Shear tie strain vs load for Loc3-1_L2.....	138
Figure 3.87: The second crack on shear tie web after Loc3-1_L3.....	139
Figure 3.88: Stringer hat damage after Loc3-1_L3. ....	139
Figure 3.89: Shear tie radius damage at lower Loc1 and upper Loc5 after Loc3-1_L3. ....	140
Figure 3.90: Force vs external displacement for Loc3-2 test.....	141
Figure 3.91: Loc3-2_Preload damage – radius delamination detected.....	142
Figure 3.92: Complete fracture along the shear tie radius during Loc3-2_L4 test. ....	143
Figure 3.93: Back-to-back SG14-15 and SG16-17.....	144
Figure 3.94: Stringer hat cut at Loc4 by shear tie penetration.....	145
Figure 3.95: Strain curve from SG11 installed on Str. hat at Loc4. ....	146
Figure 3.96: Second fracture on shear tie web due to buckling by eccentric compressive load during Loc3-2_L4 test.....	147
Figure 3.97: Shear tie crack propagation and stringer cut at Loc4 mouse hole.....	148
Figure 3.98: C-frame crack at Loc4 under combined shear and bolt pulling state.....	149
Figure 3.99: Bending strain curves from linear gauges at Loc4 flanges. ....	150
Figure 3.100: Bending strain curves from linear gauges at Loc2 flanges. ....	150
Figure 3.101: Barely visible skin crack at skin bolt after Loc3-2 test. ....	151
Figure 3.102: Geometry interaction at mouse hole.....	154
Figure 4.1: C-frames failure development by the influence of three types of shear ties. ....	158
Figure 4.2: Combined bending-twisting failure in C-frames [8,11]. ....	159
Figure 4.3: C-frame bending and combined bending-twisting tests. ....	160
Figure 4.4: C-frame section information (Dimensions in mm). ....	161

Figure 4.5: Specimen preparation; wedge grip detail (Left) and specimen with end tabs bonded to outer flange (Right).....	162
Figure 4.6: Strain gauge location for bending test (Left) and for combined bending-twisting test (Right).....	162
Figure 4.7: Overall configuration and location of point load and string pot. ....	163
Figure 4.8: Loaded specimen view; bottom flange buckling prior to failure. ....	164
Figure 4.9: Compression flange fracture with fiber failure. ....	165
Figure 4.10: Challenges to controlling slip and adhesive detachment at joints.....	166
Figure 4.11: Meshed FE model.....	167
Figure 4.12: Applied BCs and tie-interaction at interfaces.....	167
Figure 4.13: Load-displacement curves for bending and combined bending-twisting case. ....	168
Figure 4.14: Buckling and stretching deformation shape in bending (Left) and combined bending-twisting (Right).....	169
Figure 4.15: Buckling in compression flange and stretching in tension flange of specimen A2.....	170
Figure 4.16: Buckling in compression flange and stretching in tension flange of specimen D1.....	170
Figure 4.17: Failure prediction in bending case.....	171
Figure 4.18: Failure prediction in combined bending-twisting case.....	172
Figure 4.19: Effect of boundary condition including slip phenomenon. ....	173
Figure 4.20: Direct shear failure in C-frames [8,11]. ....	174
Figure 4.21: C-frame failure mechanism in the 1 <sup>st</sup> generation Frame04-2 [8, 11]. ....	175
Figure 4.22: Effective fastener model reduced strength at outer plies [8].....	177
Figure 4.23: C-frame effective fastener modeling.....	177
Figure 4.24: Load-displacement curves of Frame04-2.....	179

Figure 4.25: Center C-frame behavior and fiber failure just before fracture. ....	179
Figure 4.26: Severed center C-frame and totally failed reduced strength plies. ....	180
Figure 4.27: Bolt failure test example under combined compression and local bending. .....	181
Figure 5.1: FE modeling definition update after Loc4 tests. ....	185
Figure 5.2: Compression coupon test (SACMA method) and test specimen (0° - 14 PW plies) after test. ....	188
Figure 5.3: Compression coupon test results. ....	189
Figure 5.4: Change of fastener modeling from strip surface tie to node-to-node tie between shear tie and C-frame. ....	190
Figure 5.5: Correlation with experimental results. ....	191
Figure 5.6: Interlaminar tension failure – curved beam tension specimen [29]. ....	192
Figure 5.7: Delamination initiation estimated by critical opening moment. ....	193
Figure 5.8: Shear tie radius damage initiation. ....	194
Figure 5.9: Shear tie-stringer contact. ....	195
Figure 5.10: Stringer hat damage initiation. ....	196
Figure 5.11: Entire radius fractured at Loc3 in FE simulation. ....	197
Figure 5.12: Shear tie fracture and component interaction. ....	198
Figure 5.13: C-frame damage initiation (numbered 6) and crack (numbered 7) at Loc4. .....	199

## LIST OF TABLES

Table 3.1: Component layups. ....	47
Table 3.2: Typical thickness values in areas outside doors. ....	47
Table 3.3: T800/3900-2 properties used in the design stage. ....	50
Table 3.4: Element type and mesh size used in FE model.....	54
Table 3.5: Maximum S11 comparison in outmost layers of shear tie and skin. ....	61
Table 3.6: Cured parts actual measured thickness compared to theoretical thickness. ....	66
Table 3.7: Coupon testing plan for T800/3900-2.....	69
Table 3.8: Loading protocol for Loc4 specimens. ....	86
Table 3.9: Loc4 key phenomena. ....	93
Table 3.10: Energy required at each key event.....	124
Table 3.11: Loading protocol for Loc3 specimens. ....	133
Table 5.1: Updated T800/3900-2 properties.....	187
Table 5.2: PW T800H/3900-2 compressive strength.....	189

## ACKNOWLEDGEMENTS

I would like to thank my advisor, Dr. Hyonny Kim for his end-less support and guidance throughout my PhD studies at UCSD. I am greatly indebted to my advisor. Without him this research would not have been possible. I also appreciate the contributions of my committee members, Dr. Chia-Ming Uang, Dr. Francesco Lanza Di Scalea, Dr. Veronica Eliasson, and Dr. Vitali Nesterenko for their invaluable advice.

Special thanks to all my colleagues including Chaiane Wiggers de Souza, Dr. Kostantinos Anagnostopoulos, and Dr. Andrew Ellison for their assistance during the experiments and finite element analysis. I also appreciate the invaluable former HEWABI research work from Dr. Gabriela DeFrancisci and Dr. Zhi Ming Chen. For manufacturing process, I appreciate the contribution of Chaiane Wiggers de Souza and the assistance of undergraduate and graduate students, Juan Guillen, Luis Alfonso, John Hamrang, Paul Lee, Yeon Jong Yoo, and Brian Perez. I also acknowledge Powell Laboratory engineers, Dr. Christopher Latham, Darren McKay, Noah Aldrich, Andrew Sander, Michael Sanders, and Abdullah Hamid for their technical support and guidance on large-scale experiments.

Many thanks to Dr. Larry Ilcewicz of the Federal Aviation Administration (FAA) and engineers of industry partners for their technical support and guidance. This work was sponsored by FAA with Cooperative Agreement Number 12-C-AM-UCSD.

Lastly, I would like to thank my parents, my wife, my son, my family, and my friends for endless help.

Chapter 3, in part is currently being prepared for submission for publication of the material. Nam, Moonhee; Wiggers de Souza, Chaiane and Kim, Hyonny. Nam, Moonhee was the primary investigator and author of this material.

Chapter 5 is coauthored with Wiggers de Souza, Chaiane. Nam, Moonhee was the primary author of this chapter.

## VITA

### Education

2006 Bachelor of Science, Myongji University, Yong-in, South Korea

2008 Master of Science, University of California Davis

2021 Doctor of Philosophy, University of California San Diego

### Experience

2009 Engineer, Department of Structural Engineering, Arcadis

2009-2012 Engineer, Department of Structural Engineering, Korea Engineering Consultants Corporation

2014-2020 Graduate Student Researcher, Department of Structural Engineering, University of California San Diego

2016-2020 Teaching Assistant, Department of Structural Engineering, University of California San Diego

## REGISTRATION

E.I.T. State of California, 2008

## TECHNICAL PAPER

Kim, H., Chen, Z.M., Anagnostopoulos, K., Nam, M., Luong, S., Impact Damage Formation on Composite Aircraft Structures, Project Description Paper Supporting Presentation Given at *Federal Aviation Administration Joint Advanced Materials and Structures (JAMS) 11th Annual Technical Review Meeting*, 31 March - 01 April 2015, Baltimore, MD.

## PUBLICATIONS

Wiggers de Souza, C., Nam, M., Kim, H., High Energy Wide Area Blunt Impact of Composite Aircraft Structures – Part A: Design and Analysis Methodology of Representative Substructure, *American Society for Composites 36th Annual Technical Conference*, 19-21 September 2021, College Station, TX.

Nam, M., Wiggers de Souza, C., Kim, H., High Energy Wide Area Blunt Impact of Composite Aircraft Structures – Part B: Testing and Internal Damage Modes, *American Society for Composites 36th Annual Technical Conference*, 19-21 September 2021, College Station, TX.



## ABSTRACT OF THE DISSERTATION

High Energy Wide Area Blunt Impact Damage to Internal Structural Components  
of Composite Aircraft Fuselage Structures

by

Moonhee Nam

Doctor of Philosophy in Structural Engineering

University of California San Diego, 2021

Professor Hyonny Kim, Chair

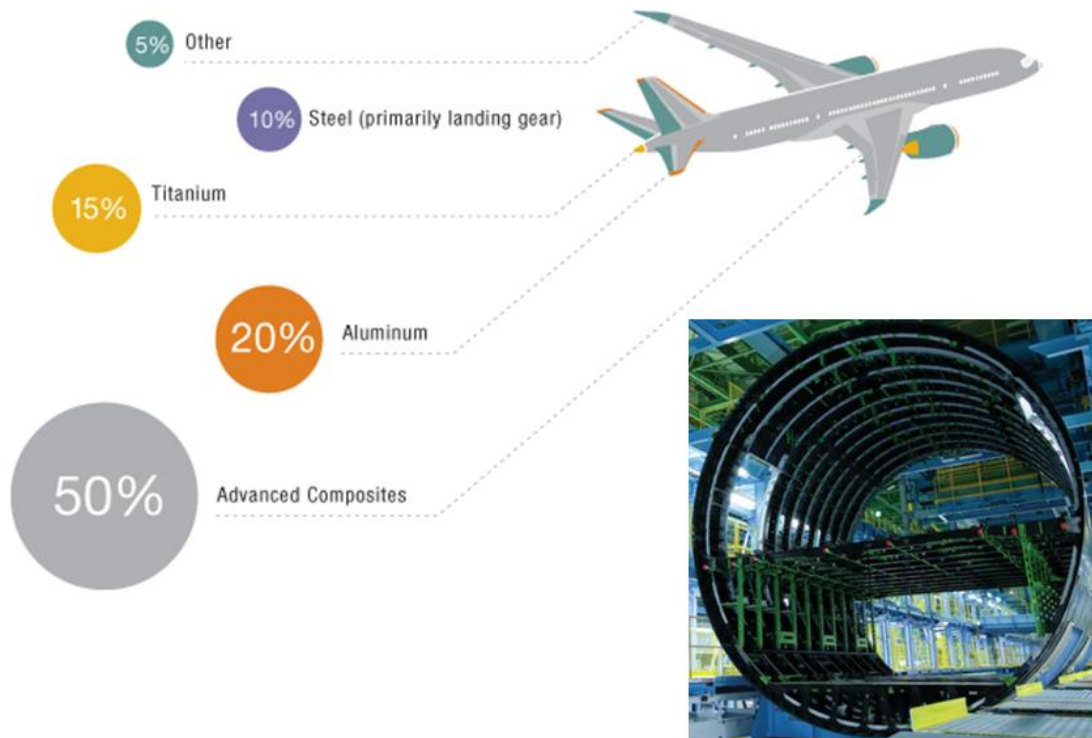
Since 2009, research focused on damage formation of composite aircraft fuselage by High Energy Wide Area Blunt Impact (HEWABI) has been conducted at UCSD. As a major damage source to composite aircraft fuselage structures, HEWABI, caused by accidental contact by heavy ground service equipment (GSE), potentially leaves significant internal damage in multiple structural components with barely visible damage signs on the outside skin surface. Accounting for key structural components existing in

real fuselage structures, specifically floor structures and continuous shear tie, a series of new 2<sup>nd</sup> generation large scale specimens were designed, fabricated, and tested. The objectives of the research described herein are to: (1) use of large-scale experiments to understand damage formation from HEWABI events near the floor structure location using the 2<sup>nd</sup> generation composite fuselage panel; of interest is examining how damage development is affected by the major changes from the 1<sup>st</sup> to 2<sup>nd</sup> generation panel design and boundary conditions, (2) investigation of C-frame failure both experimentally and analytically, and (3) evaluation of current FE modeling capability correlated with the 2<sup>nd</sup> generation HEWABI test results.

# 1 INTRODUCTION

---

Over several decades, composite material usage has been increased in modern commercial aircraft structures (wing, fuselage) because of high stiffness and strength to ratios, etc. Its application in the airframe and primary structures was 50% or more by weight e.g., the Boeing 787 Dreamliner and Airbus A350XWB as shown in Figure 1.1 [1-5]. However, there are lots of challenges in its application in terms of design, fabrication, and damage detection due to material complexity based on its heterogeneous nature. These include complicated fabrication process, different damage response from metals when barely visible damage is present, various complicated failure criteria needed for analysis, high cost, and weakness to transverse impact. Specifically focusing on transverse blunt impact, research to investigate the damage mechanisms in composite fuselage structures has been conducted at UCSD under funding from the Federal Aviation Administration (FAA) to provide guidance on topics related to airworthiness certification and damage tolerance [6-11].



**Figure 1.1: Composite usage in B787 (boeing.com/commercial/aero) [2], and B787 composite fuselage section (aviationpros.com) [4].**

## 1.1 JUSTIFICATION FOR CURRENT RESEARCH

The FAA defines damage categories corresponding to the subsequent residual load capability required of the damaged structure. Five categories of damage are defined in Figure 1.2 demonstrating the relationship between design load levels and damage severity [6-8]. For Category 1, the structure must sustain ultimate load capability for entire service life of the aircraft with barely visible impact damage (BVID), which is small manufacturing damage. For Category 2 and 3, the structure must sustain limit load capability for visible impact damage (VID) per normal inspection process and obvious damage detected within a few flights. GSE impact damage often leaves damage in

Category 2 and 3 [8, 11]. However, with severe internal damage, GSE impact damage is classified as Category 5. For safety and identifying the need to repair requirement, damage detectability is very important. However, HEWABI leaves low external damage sign on composite fuselage structures due to the broad area contact loading through the rubber (elastomer) bumpers (typical example in Figure 1.3). Thus, it is important to understand composite structure's response to HEWABI through the experiments, and predict failure initiation, propagation, and its extent by developing finite element (FE) modeling methodology validated by experiments to provide reliable recommendations for safety and inspection techniques [8, 16, 18].

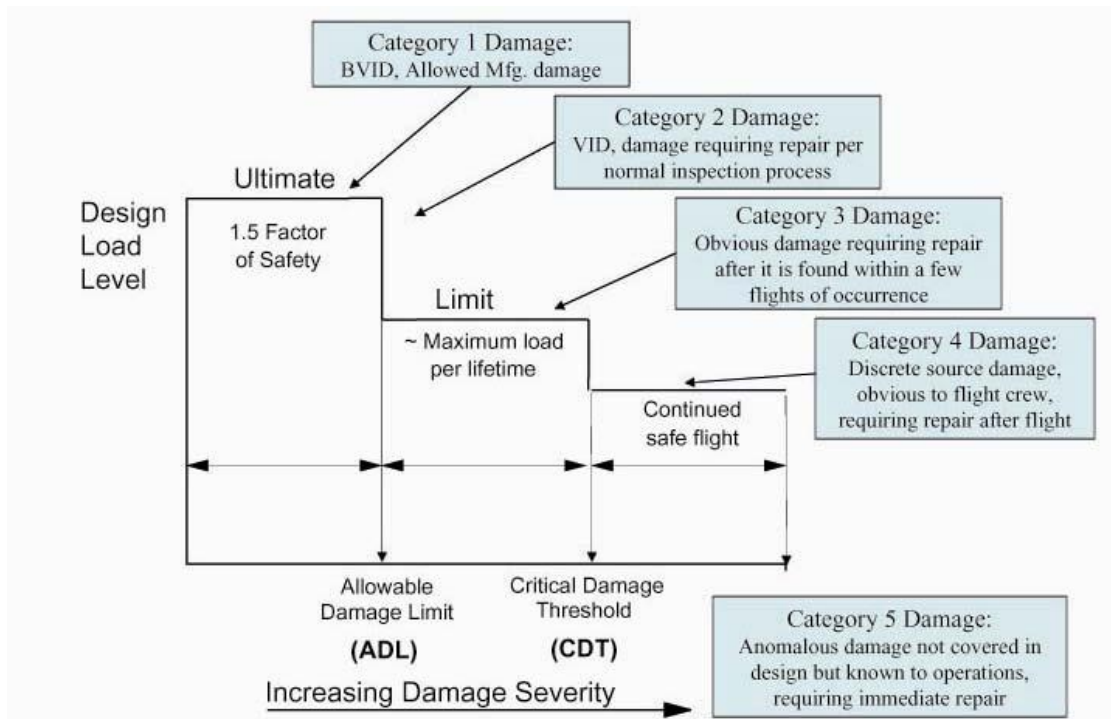


Figure 1.2: Damage category defined by the FAA [7].

## 1.2 OVERVIEW AND PAST RESEARCH

Since 2009, research about damage formation on composite aircraft fuselage by High Energy Wide Area Blunt Impact (HEWABI) has been conducted at UCSD in the joint programs, the Federal Aviation Administration Joint Advanced Materials and Structures Center of Excellence (FAA JAMS CoE).

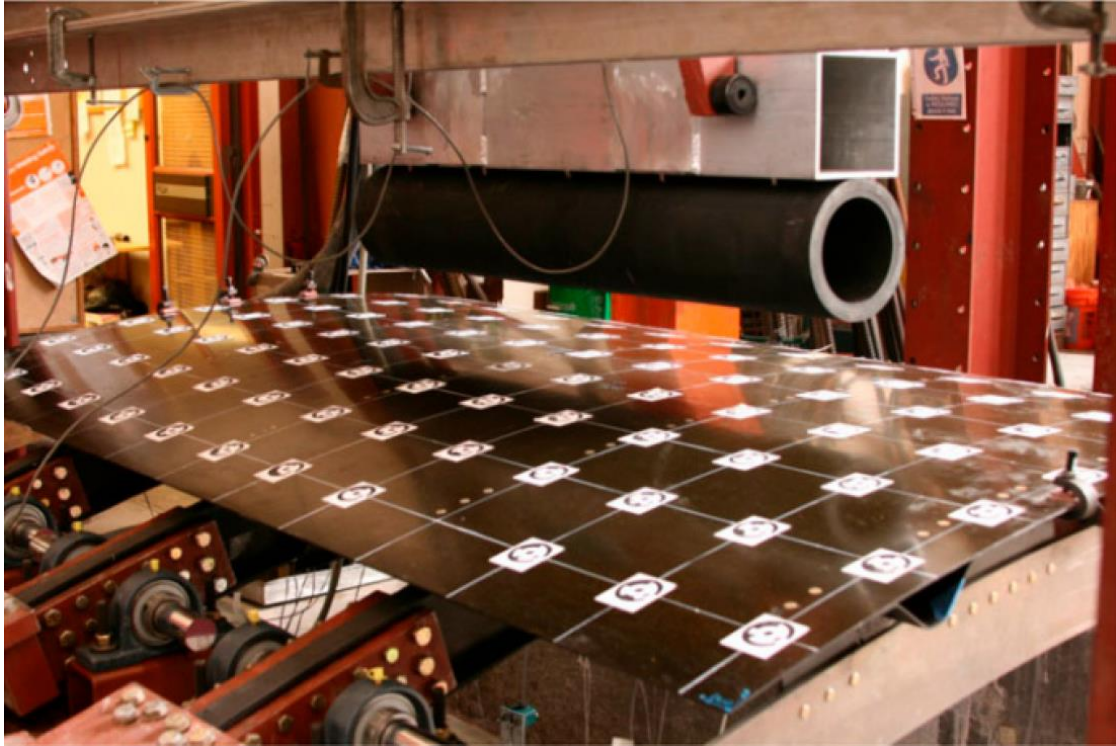
As a major damage source to composite aircraft fuselage structures, HEWABI, caused as a result of accidental contact by ground service equipment (GSE), potentially leaves significant internal damage with barely visible damage signs on the outside skin surface [8-11]. 50% of major damage was caused by contact with heavy GSE such as cargo loaders, catering trucks, other equipment that interface with the aircraft. GSE can have high mass up to 15000 kg with low operation velocity up to 1 m/s [10] resulting in very high impact energy levels to 7500 J. Furthermore, due to the soft rubber bumper typically placed where accidental contact could occur (see Figure 1.3), the local contact area develops over a wide area which can allow high forces to be developed, potentially causing damage of multiple internal structural components, but leaving little or no external damage to the high-strength composite outer skin as shown in Figure 1.4 and Figure 1.5 [8, 10, 11].



**Figure 1.3: GSE approaching to the aircraft fuselage; note rubber bumper at interface between GSE and aircraft [8].**



**Figure 1.4: Severe internal damage by HEWABI (shear tie and C-frame fracture) [8].**

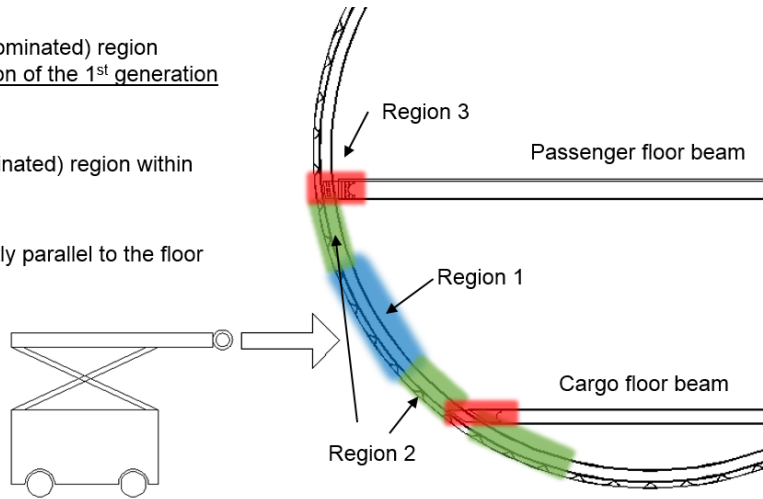


**Figure 1.5: External skin after sustaining internal damage at levels shown in Figure 1.4 [11].**

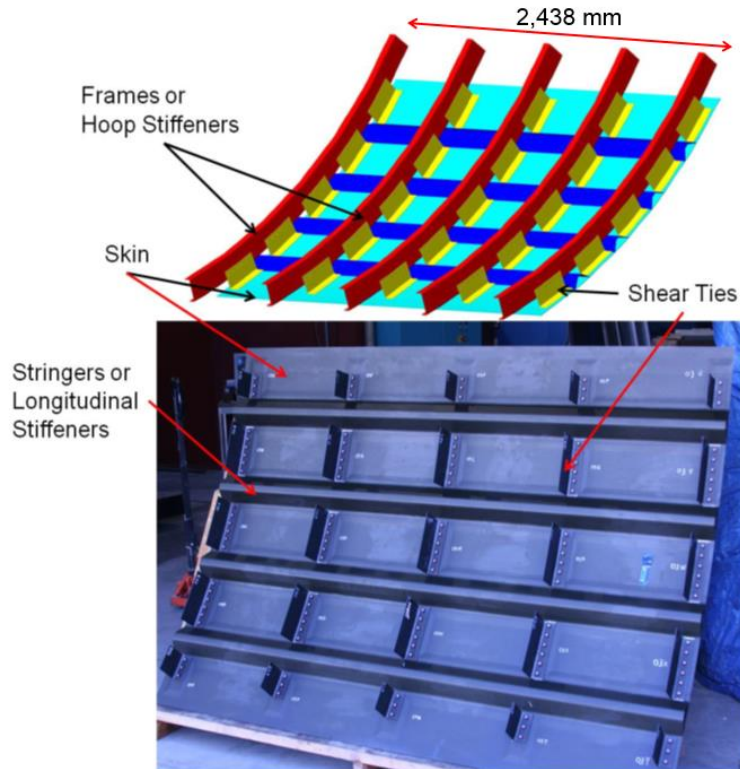
The previous HEWABI research at UCSD for the 1<sup>st</sup> generation fuselage panel was conducted by DeFrancisci [8] and Chen [11]. For the impact location at the acreage area which is the compliant (bending-dominated) region as shown in Figure 1.6. The 1<sup>st</sup> generation composite fuselage panel (overall size with 1,829 mm x 2,438 mm) was composed of the skin-stringer outer panel, discrete shear ties, and C-frames as shown in Figure 1.7.



- **Region 1** Compliant (bending dominated) region between floor joints; the condition of the 1<sup>st</sup> generation frame panel tests.
- **Region 2** More Stiff (shear dominated) region within proximity to the floor joint.
- **Region 3** Most stiff region directly parallel to the floor joint.

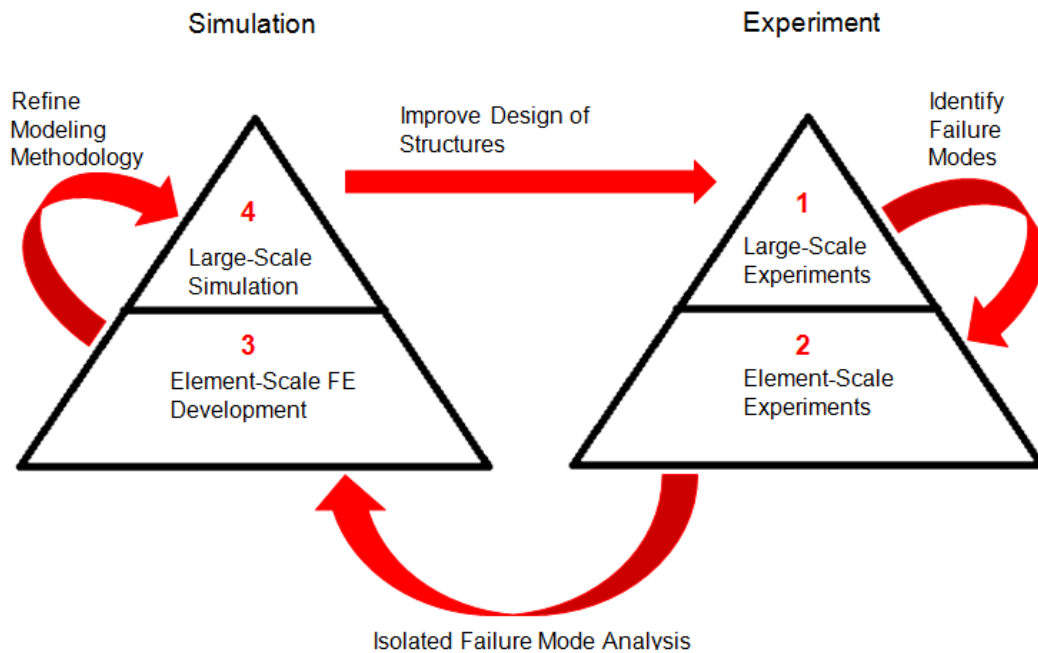


**Figure 1.6: Impact to aircraft fuselage; “Region 1” – acreage area for the 1<sup>st</sup> generation HEWABI experiments.**



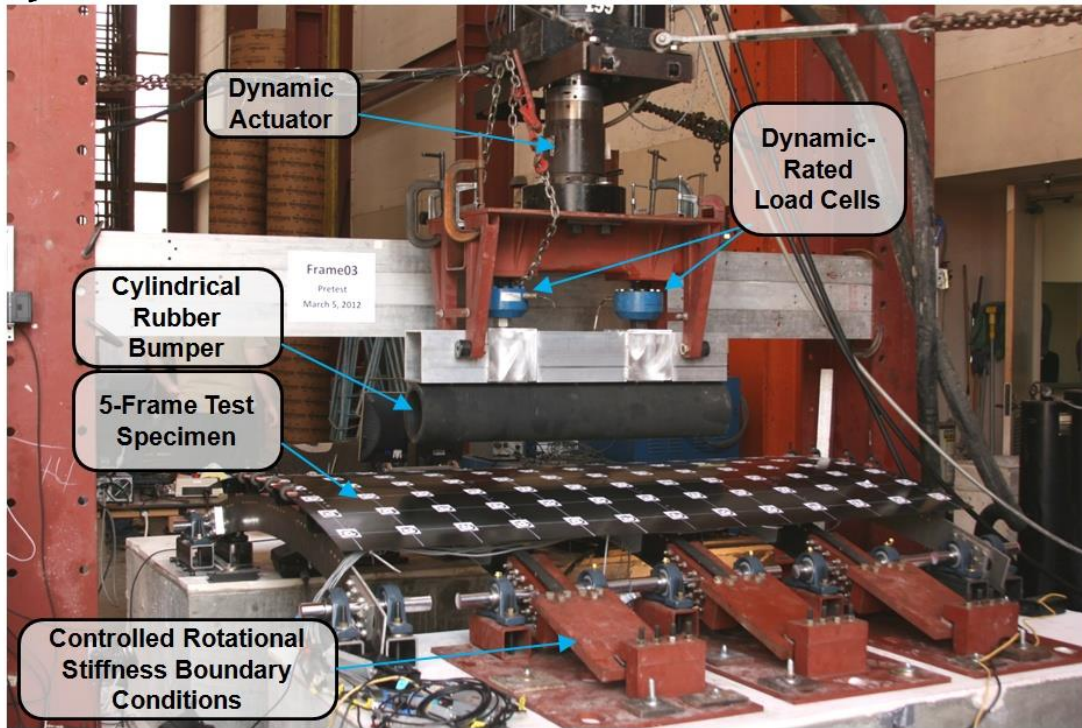
**Figure 1.7: 1<sup>st</sup> generation HEWABI fuselage panel [8].**

As named “inverted pyramid approach” by Chen [11], the research road map is shown in Figure 1.8. It was planned by transforming the “building block” approach often employed in aerospace industry for composite structure development. It has two separate pyramids: one for experiments and the other for FE simulation predicting damage phenomena observed in the large-scale experiments. For the experiment pyramid, through large-scale blunt impact experiments (an example is shown in Figure 1.9), the critical phenomena and damage mechanism was investigated. In particular, the structural response, key failure modes and their initiation, progression, and damage location and extent was examined. The example of key damage modes observed in the large-scale tests are shown in Figure 1.4 and Figure 1.10.



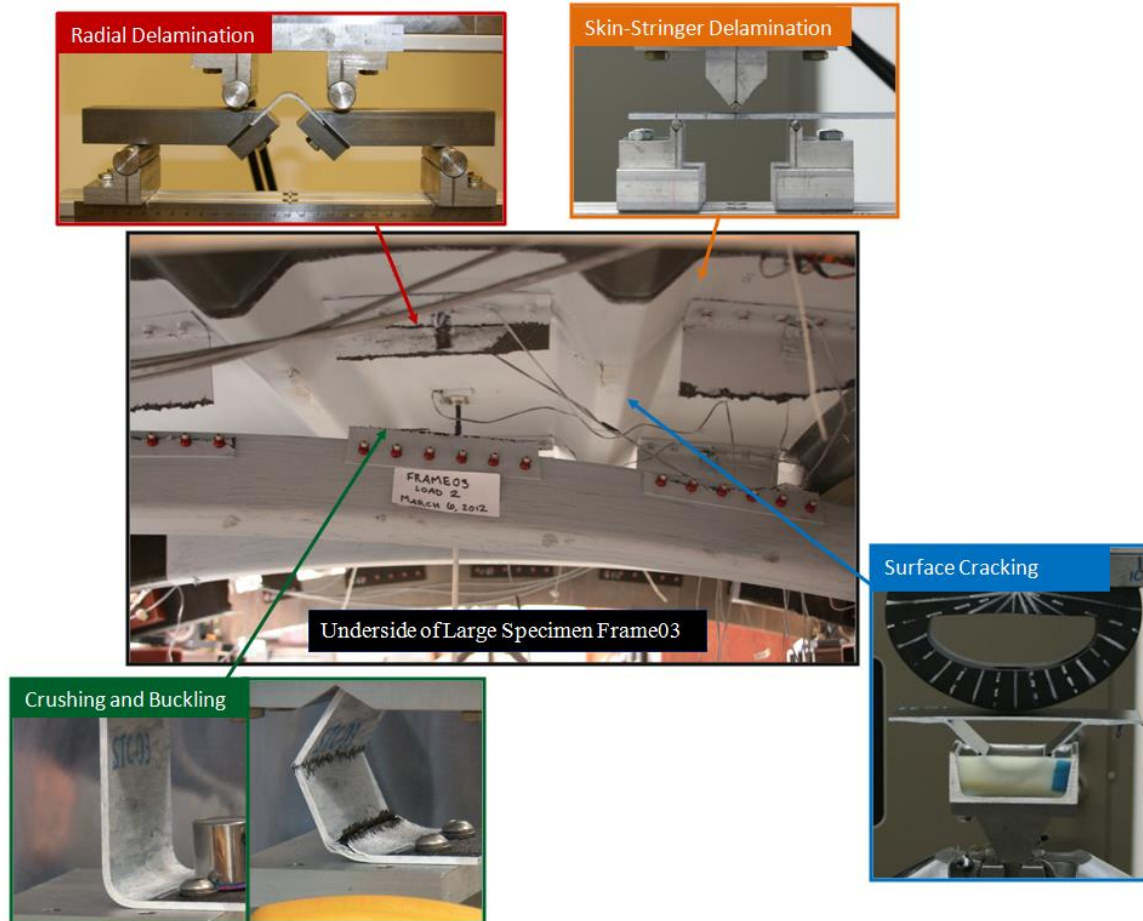
**Figure 1.8: Road map for approaching experiments and numerical simulation of High Energy Wide Area Blunt Impact [11].**

### Dynamic Test at 0.5 m/s



**Figure 1.9: Experimental setup for structural-level Frame03 and 04 dynamic experiments [11].**

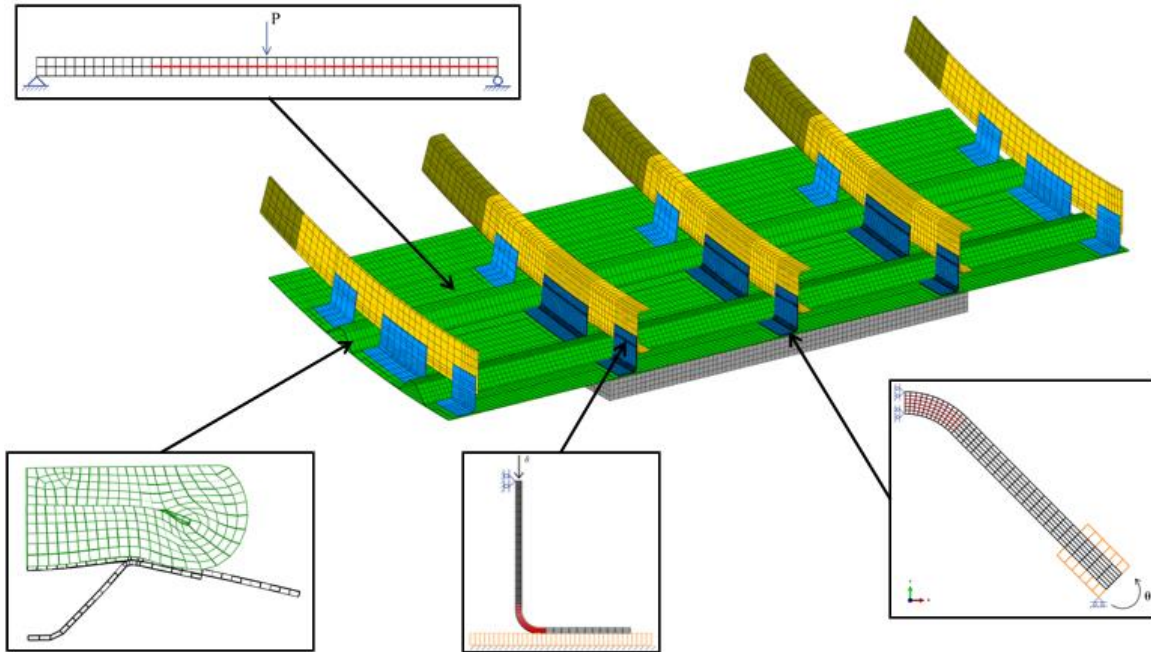
Per the experiment pyramid in Figure 1.8, follow-on successive experiments were element-scale, designed to induce the key failure modes, observed in large-scale experiments, to each relevant structural component. The examples of element-level tests are shown in Figure 1.10. Each relevant structural element specimen was designed to be more simple than the full-scale actual structure, while maintaining similar boundary and loading conditions. Thus, the small-scale experimental results were representative of the failure modes observed in the large fuselage panels. Through these failure-mode targeted element-level experiments, test data quantifying the specific failure phenomena were recorded and used for developing and refining finite element model definitions (FE simulation validation).



**Figure 1.10: Analysis of the key failure modes in the fuselage panel through element-level experiments [11].**

For the simulation pyramid in Figure 1.8 FE modeling methodology developed based on element-level test data and observations was developed first. Examples of sub-scale FE simulation are shown in Figure 1.11. A key step in the FE methodology is validation with the aforementioned element-level tests to establish confidence that a physics-based model has been established. Then, the modeling information developed in each small-scale FE model was transferred to the large-scale FE model to enable

prediction of damage beyond the damage initiation in the structure during the HEWABI event as shown in Figure 1.11.

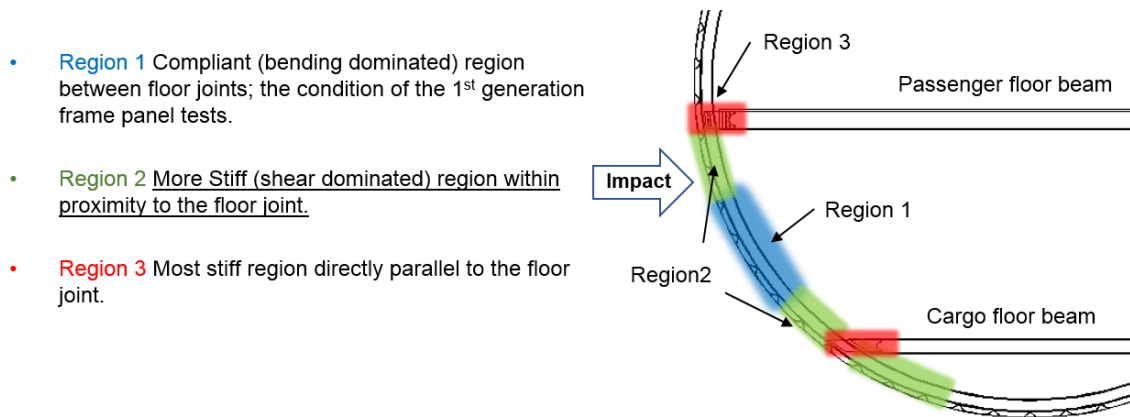


**Figure 1.11: Modeling definition for element-level studies exported into the large-scale FE model [11].**

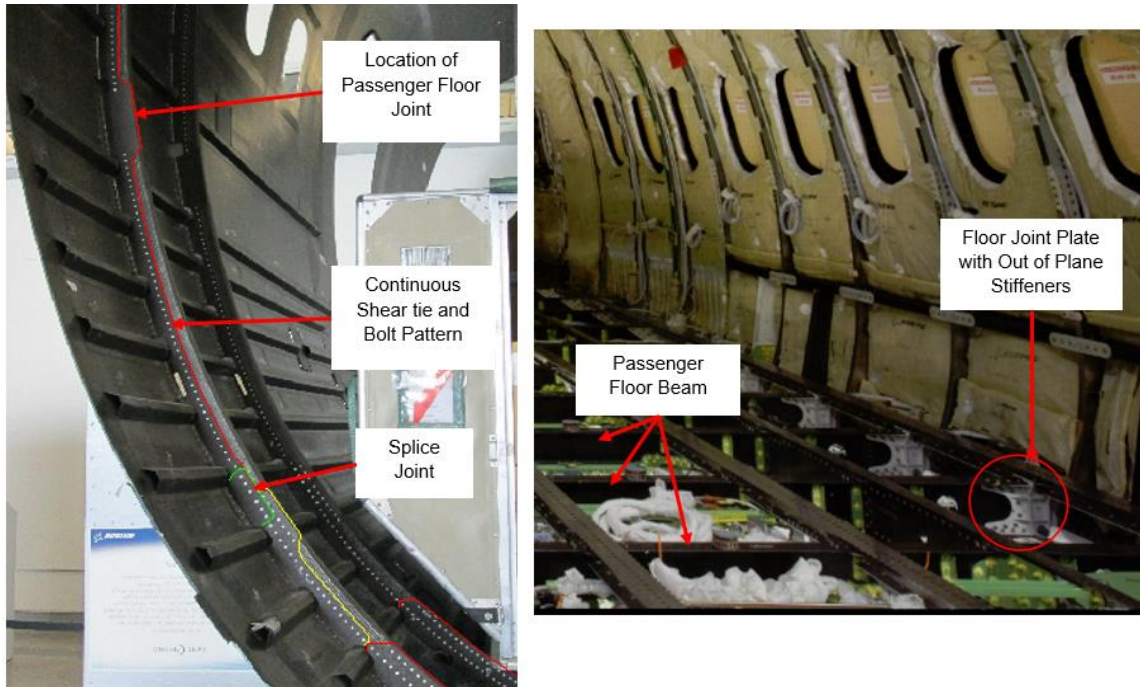
### 1.3 CURRENT RESEARCH SCOPE AND OBJECTIVES

After the previous HEWABI research for the 1<sup>st</sup> generation fuselage panel, more study was required to examine influence of the impact location near the floor structures. In Figure 1.12, the corresponding impact location of interest in this current phase of research is denoted as “Region 2”. It is more stiff and shear dominated relative the previous research investigation at "Region 1" due to frame to floor beam interaction. Different damage modes were anticipated than the observed damage modes in the 1<sup>st</sup>

generation panel tests. The two key structural components existing in real fuselage structures, shown in Figure 1.13, specifically floor structures and continuous shear tie (web connecting fuselage frames to outer skin), were reflected in the design of new fuselage specimen for impact location near the floor joint. These new specimens described in this current research are referred to as "2<sup>nd</sup> generation" specimens.

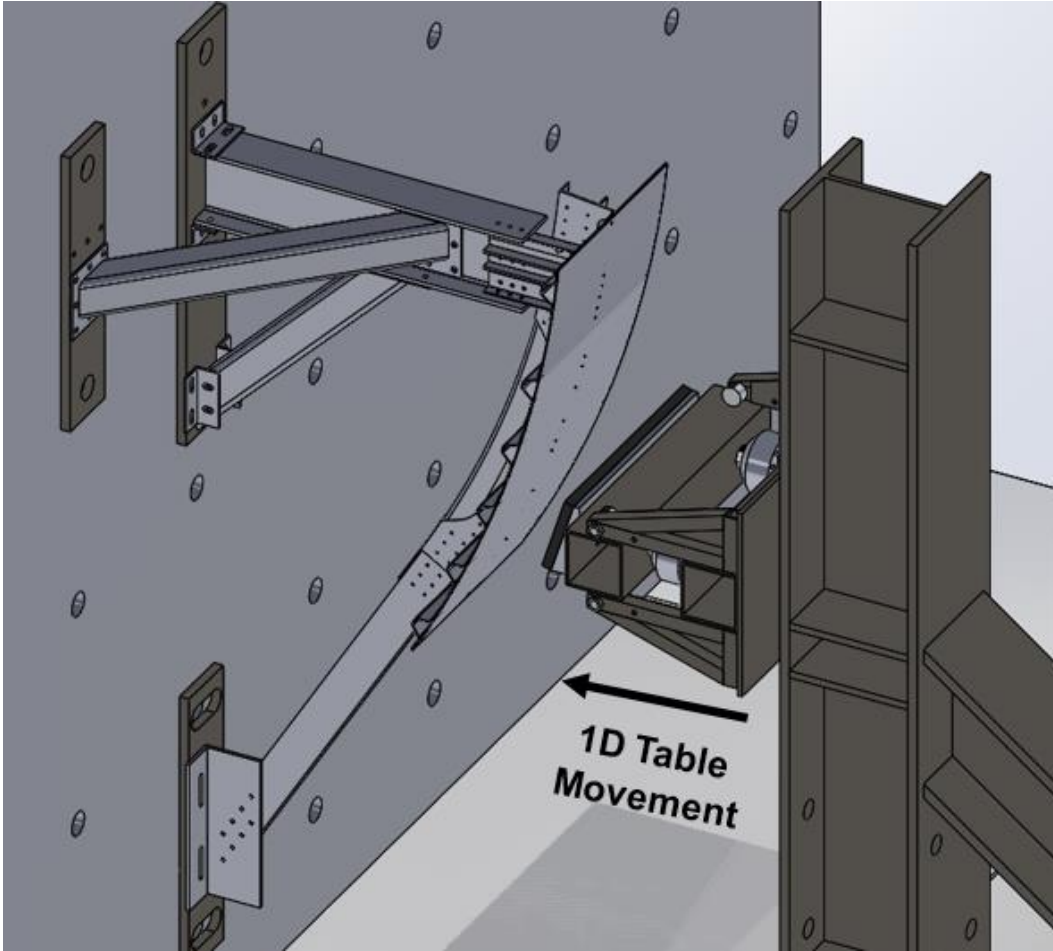


**Figure 1.12: Impact to aircraft fuselage; “Region 2” and frame to floor structure interaction.**



**Figure 1.13: Boeing 787 fuselage with the continuous shear tie and floor structure; Picture from Boeing Future of Flight Museum (Left) and The Birth of the 787 Dreamliner (Right) [19].**

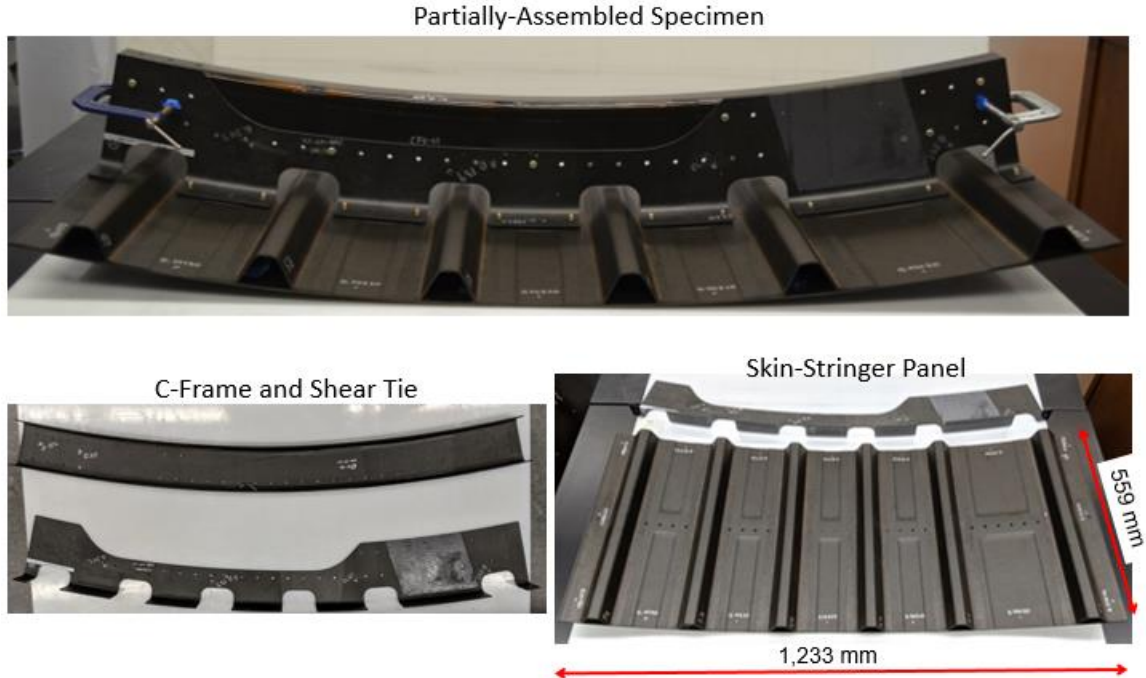
With the two major design changes representing more realistic design of current in-service composite fuselage structures, the 2<sup>nd</sup> generation HEWABI panels were fabricated, tested, and investigated at UCSD. The 2<sup>nd</sup> generation HEWABI panel test configuration is shown in Figure 1.14.



**Figure 1.14: 2<sup>nd</sup> generation HEWABI panel test.**

As shown in Figure 1.15, the 2<sup>nd</sup> generation fuselage panel is composed of the co-cured skin-stringer outer panel (overall size with 559 mm x 1,233 mm), one continuous shear tie, and one C-frame.





**Figure 1.15: 2<sup>nd</sup> generation HEWABI fuselage panel and its components.**

The first objective of this research is the use of large-scale experiments to understand the damage formation from HEWABI events near the floor structure location using the 2<sup>nd</sup> generation fuselage panel design. Of interest is examining how damage development is affected according to the major changes in the 2<sup>nd</sup> generation large-scale test specimen. Damage formation from HEWABI events near the floor structure location was evaluated. More specifically, damage initiation, location and key damage modes, sequence, extent, and external damage detectability were assessed with major outcomes being understanding damage mechanisms and creating datasets that can be used for subsequent modeling validation.

The second objective of this research is study for C-frame failure. As main load-bearing component to the transvers load from HEWABI, the C-frame resists transverse

load by reinforcing the skin-stringer outer panel. Its failure means overall fuselage structural failure as skin-stringer outer panel cannot resist the transverse load anymore. Thus, investigation of C-frame failure is important for aircraft safety. Using the 1<sup>st</sup> generation HEWABI research Phase 2 large panel test (Frame03 and Frame04-2) data, C-frame key failure modes were examined, C-frame element tests were conducted, and numerical investigation was followed. Lastly, C-frame modeling capability for failure prediction was evaluated.

The third objective of this research is evaluation as well as improvement plan of current FE model capability correlated with the 2<sup>nd</sup> generation Loc4 test results. From the preliminary FE modeling used during the specimen in design stage to refinements made after testing was completed, modeling definitions will be provided in detail. Prediction capability and limitation of current FE modeling technology will be discussed. The future work recommendations for improving FE capability will be stated.

About the 2<sup>nd</sup> generation HEWABI research, the following Chapter 3 and Chapter 5 include joint research work conducted with Chaiane Wiggers de Souza. Through the collaboration, the results of the 2<sup>nd</sup> generation HEWABI research have “equal attribution” to both Moonhee Nam and Chaiane Wiggers de Souza.

## 2 LITERATURE REVIEW

---

Experimental and numerical investigations on the large-scale impact behavior of composite aircraft fuselage structures are barely documented in the open literature [11, 18]. This chapter reviews the experimental investigation including test methodology used in large-scale impact experiments on complex fuselage structures composed of structural elements. Also of interest are subsequent element-level experiments designed to excite key failure mode observed in the large-scale impact experiments, as well as numerical investigation on defining accurate FE modeling methodology relevant to HEWABI of large-scale structures.

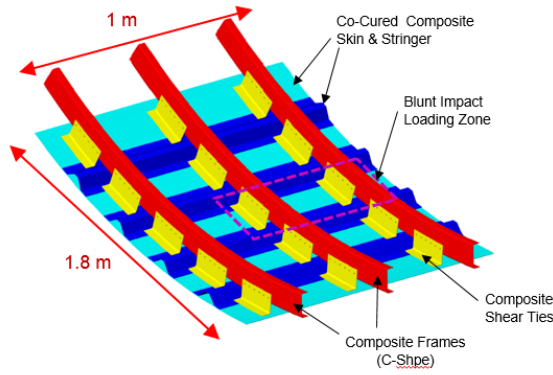
### 2.1 1ST GENERATION HEWABI RESEARCH

The 1<sup>st</sup> generation HEWABI research, conducted at UC San Diego by DeFrancisci and Chen [8, 11], is summarized here. The large-scale test definition of the 1<sup>st</sup> generation HEWABI research started by first identifying the Ground Service Equipment (GSE) collision threat and its characterization. Through meetings with industry partners (Boeing, Airbus, Bombardier, United Airlines, Delta Airlines, Cytec, EASA, and the FAA), GSE was identified as a key threat to aircraft safety. GSE activity was observed at LAX and photographic and video data acquired were used to quantify blunt impact events by GSE. Specifically, typical impact mass, velocity of GSE near aircraft and bluntness as well as likely impact locations upon the various aircraft size.

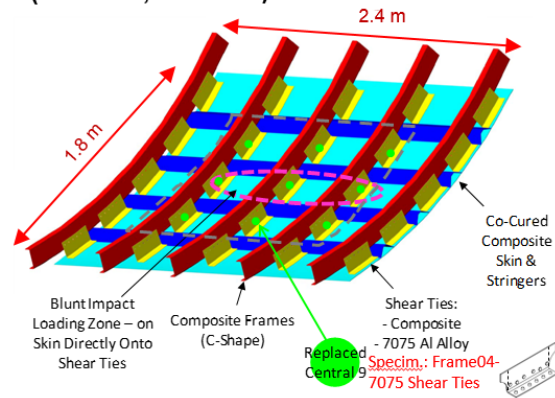
The typical mass of GSE ranges from 3000 kg to over 15000 kg, and its velocity ranges 0.5 m/s to 1 m/s [8, 11]. The high mass and low velocity combine to pose an impact threat having kinetic energy ranging from 375 J to over 7500 J. For example, a 15000 kg cargo loader traveling at 1 m/s has a kinetic energy of 7500 J. The generated energy level by GSE is significantly higher than the impact energy ranges from 10 J up to 100 J by typical pendulum impact and drop tests typically used in lab-scale experiments to evaluate Foreign Object Damage (FOD).

Based on the LAX observations and meetings with industry partners, excluding the specific reinforcement near the door, floor joint, and wing box, the general test panel geometry and layup were designed and reviewed. By focusing on impact to the acreage area, a general understanding of the damage formation and key failure mechanisms between the structural components would be achieved. The impact location and the stringer and frame stiffened panel design are shown in Figure 2.1 [8, 11]. Two phases of specimens were defined in these 1st generation tests, as shown in the figure.

**Phase 1 Frame Panel, Quasi-Static Tests  
(Frame01, Frame02)**



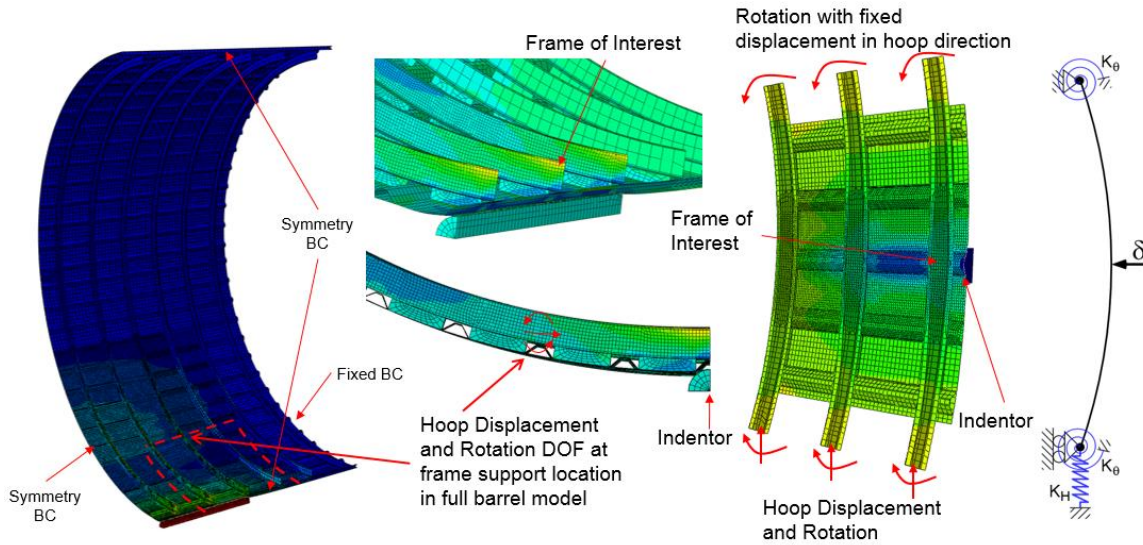
**Phase 2 Frame Panel, Dynamic Tests  
(Frame03, Frame04)**



**Figure 2.1: 1<sup>st</sup> generation HEWABI fuselage panel [8, 11].**

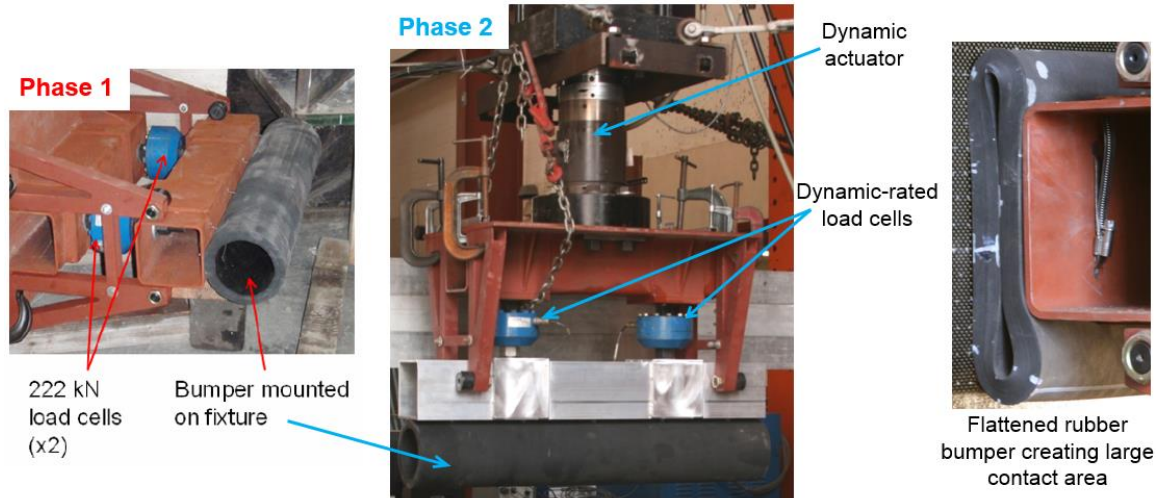
The low-velocity impacts caused by large masses can be treated as a quasi-static indentation problem [8, 13, 17]. That is because the impact duration is sufficiently longer than the time for the deformation wave to propagate from the impact site to the boundary conditions. Indeed, experimental results correlate well with this assumption for low and medium impact energies for lab-scale FOD tests [12]. As shown in Figure 2.1, displacement controlled quasi-static tests (at 3.0 mm/min) were conducted for careful investigation for the phase 1 panels and dynamic tests were conducted representing the actual impact rate (at 0.5 m/s) for the phase 2 panels [8, 11].

In the low-velocity impact event, the impacted structure boundary conditions as well as the mass, shape, and material properties of the impactor crucially affect the structural response because the deformation mode shape is governed by the first mode of vibration. Proper boundary fixtures were designed through iterative Finite Element Analyses to verify equivalent response between the full barrel model and sub-scale panel model shown in Figure 2.2 [8].



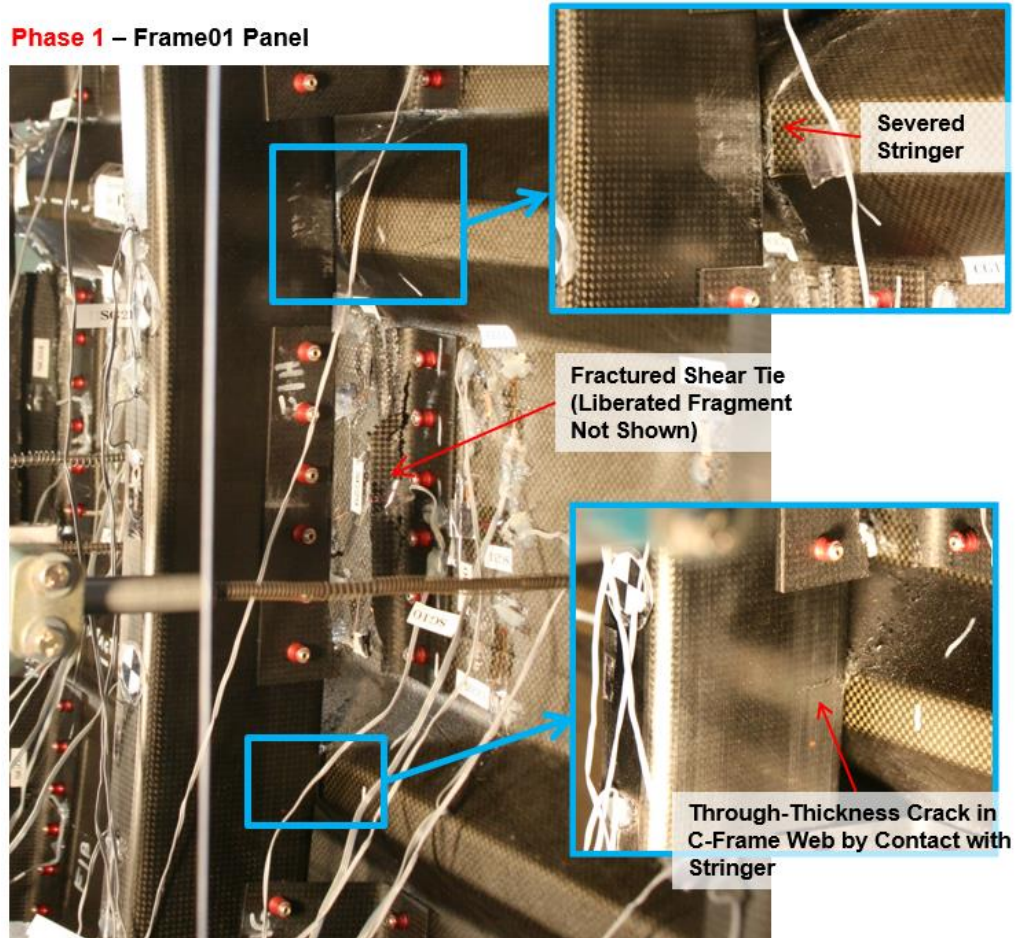
**Figure 2.2: Determination of the frame panel boundary conditions [8].**

The rubber bumper located between the GSE and aircraft generally creates a large contact area inducing more global response to the specimen, producing wide-spread damages but reducing damage detectability externally under impact events. For the C-frame stiffened panel tests, the long cylindrical bumper (outer diameter of 178 mm, wall thickness 25 mm, and overall length of 572 mm and 1.0 m for the phase 1 and phase 2 panel test respectively), as shown Figure 2.3, was installed on the impactor tip to produce wide area blunt impact. As shown the right photo in Figure 2.3, the hollow cylindrical bumper eventually flattens before significant loading develops, and can be represented by a flat rubber pad.



**Figure 2.3: Impactor tip with the rubber bumper [8, 11].**

Figure 2.4 shows internal damage after the Frame01 test which quasi-statically applied load directly onto two shear ties. The damage initiated at the shear tie curved corner, more specifically, shear tie corner delamination due to the composite material's low interlaminar tension strength (opening moment loading in curves sections induces radial tension stress). With more loading, the shear tie was fractured as shown in Figure 2.4 by the direct compressive load from the bumper. The following failure events were contact between the C-frame and the stringers, and local twisting of the C-frame due to absence of the stabilizing component (the fractured shear tie). The key failure last event was contact induced failures between C-frames and the stringers in the impact zone. As shown in Figure 2.4, the stringer was severed as the frame impinged into it. Through thickness frame cracks occurred. Delamination between the stringer flanges and the skin was also found due to the severed stringer crack reaching the stringer-to-skin interface.



**Figure 2.4: Internal damages of Frame01 panel loaded onto shear ties [8, 11].**

Figure 2.5 shows the internal damage sequence of the Frame03 panel during dynamic impact applied on the skin side at the location loading directly onto three shear ties. The damage initiated at the impacted shear tie curved corners, more specifically, delamination and fiber crushing damage. These failure modes are generated due to the local bending and shear stresses created by the direct compression from the bumper. With more loading, the three impact-loaded shear ties were completely fractured as shown in Figure 2.5. The following failure events were contact between the C-frame and stringers, as well as twisting of the C-frame due to of the stabilizing component (the now fractured



shear tie). Unlike in the quasi-static experiments, contact between C-frame and stringer did not prevent further C-frame twisting, thereby leading to wide-spread shear tie and C-frame failures away from the direct impact zone. The C-frame developed fracture near the boundary supports as shown in Figure 2.5.

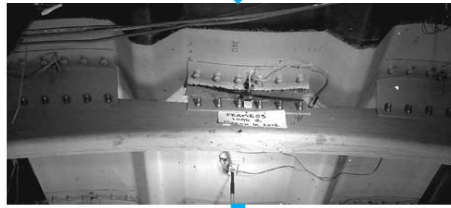
In the Frame03 test, initial failure occurred at the shear tie corners with delamination and crushing failure modes. Based in interaction with industry engineers, the composite shear ties were replaced with strong shear ties (aluminum 7075) in the Frame04-2 panel to investigate how shear tie strength affects resulting failure modes (see Figure 2.6). The strong shear ties did not fail (unlike the composite shear ties), leading to local direct shear fracture of all three C-frames at the impact location as shown in Figure 2.6.

Although severe and wide-spread internal damage modes were generated by HEWABI in the structural-level frame panel tests. There were no clear, externally visible indications of damage being present, despite the degree of major internal damage as shown in Figure 2.4 to Figure 2.6.

**Phase 2 – Frame03 Panel**



Compression Failure of the Loaded Shear Ties



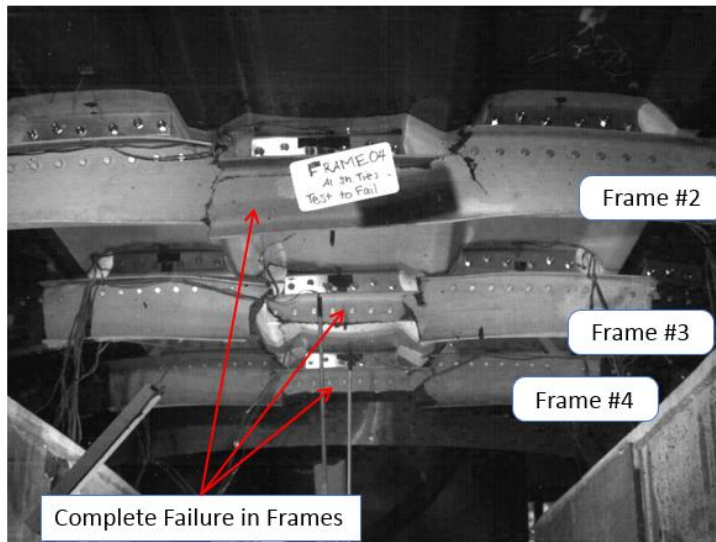
Rotation of C-Frame



C-Frame Failure near Boundary Supports in Bending and Twisting state

**Figure 2.5: Internal damage sequence of Frame03 panel loaded onto shear ties [8, 11].**

**Phase 2 – Frame04-2 Panel with Strong Shear Ties**



**Figure 2.6: Direct shear failure of C-frames in Frame04-2 panel loaded onto strong shear ties [8, 11].**

In Phase 1 (Frame01 and Frame02 tests) and Phase 2-Frame03 tests with composite shear ties, initial failure occurred in the shear ties. Specifically, shear tie curved corner radius delamination develops first, then fiber crushing and complete fracture due to direct compressive load from the bumper. The major difference in failure mechanisms is the C-frame's behavior after contact with the stringer. In the quasi-static tests, the C-frame was locked by the stringer (friction) contact after the shear tie fractured. This resulted in local crack formation in the C-frame by stringer-to-frame contact stress within the vicinity of impact zone. On the other hand, dynamic test results show the C-frame's large deformation after shear ties fractured under a combined bending-twisting state. This eventually led to fracture near the C-frames' boundary conditions which are away from the impact-contact zone. This suggests the loading rate (quasi-static loading vs. dynamic loading) can strongly affect the subsequent series of failure events and final failure mode(s). Stringer-frame contact played a key role in damage evolution affecting the subsequent failure modes.

When investigating Frame04-2 (strong shear ties) failure mechanism, Frame04-2's strong shear ties were not the first component to fail and were able to carry the impact load with minimal deformation of the shear ties. These directly transfer load to the C-frames, thereby resulting in localized shear fracture of the C-frames. Therefore, the shear ties played a key role in damage initiation and evolution affecting subsequent failure modes.

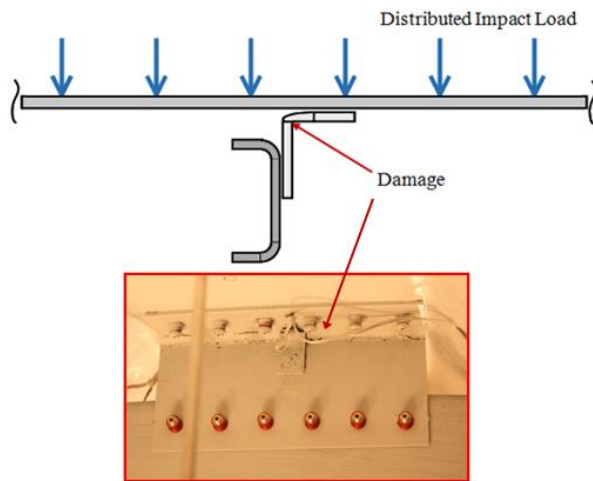
From the Phase 2 structural-level Frame03 experiment, key damage modes were identified. These are: delamination and crushing of the shear tie corner, skin-stringer

disbond, and skin cracking as shown in Figure 1.10. Each failure mode altered the local stiffness of the panel and re-directed the load path in the large-scale specimens.

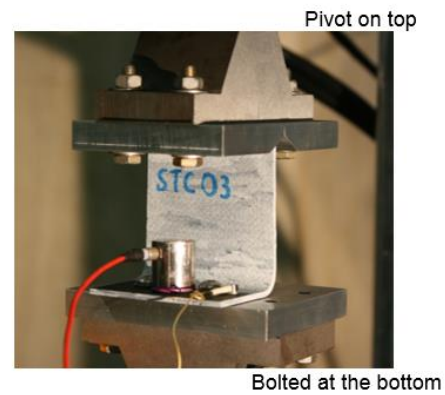
In order to better understand these key failure modes observed in the large-scale tests, the fuselage structure was broken down into smaller elements to examine the individual key failure mechanism as well as to refine finite element (FE) model definitions. Through focused element-level tests, less overall complexity allowed for development of accurate FE model that are validated by these tests. The modeling definitions were then transferred to the full-scale structural-level FE model as shown in Figure 1.11.

The shear tie coupon experiments and FE modeling methods are described briefly in this section. In the blunt impact testing early shear tie damage influenced the subsequent structural behavior, especially as the fractured shear tie could no longer stabilize the C-frame against rotation. In the large-scale Frame01 and Frame03 tests, the damage initiated at the shear tie curved corner, as shown in Figure 2.7. The successive shear tie element experiment was conducted to excite key damage modes at the shear tie curved corner: delamination, fiber crushing as well as buckling/fracturing due to compression loading.

Impacted Shear Ties – Delamination/Crush Observed in Large-Scale Tests

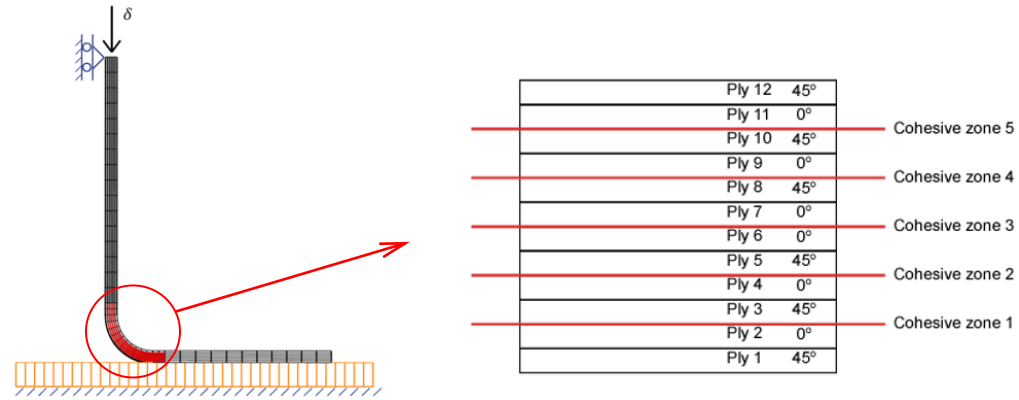


Shear Tie Element Compression Test



**Figure 2.7: Shear tie element test for shear tie radial delam/crushing due to compression loading [11].**

The shear tie compression test was simulated in Abaqus/Explicit correlated with the element test as shown in Figure 2.9. As described in Figure 2.8, to simulate inter-laminar failure (delamination) at the curved corner, cohesive surface interaction was used to connect surface pairs between sub-laminate (ply group) layers. Due to through-thickness laminar failure (crushing and fracture damage), 3D intra-laminar failure criterion (Hill-Tsai criterion) was used with 8-node solid elements (C3D8R) and enhanced hourglass and distortion controls to prevent spurious deformation modes and excessive element distortion.



- Fixed at aluminum plate, roller and applied displacement at flange
- Penalty contact constraint
- 1.27 mm mesh in curved corner, 3.3 mm elsewhere
- Solid (C3D8R) elements

- 12 element layers through the thickness
- Cohesive surface interaction at curved corner to simulate delamination
- Hill's 3D failure criteria for ply failure

Figure 2.8: Sher tie element FE modeling methodology [11].

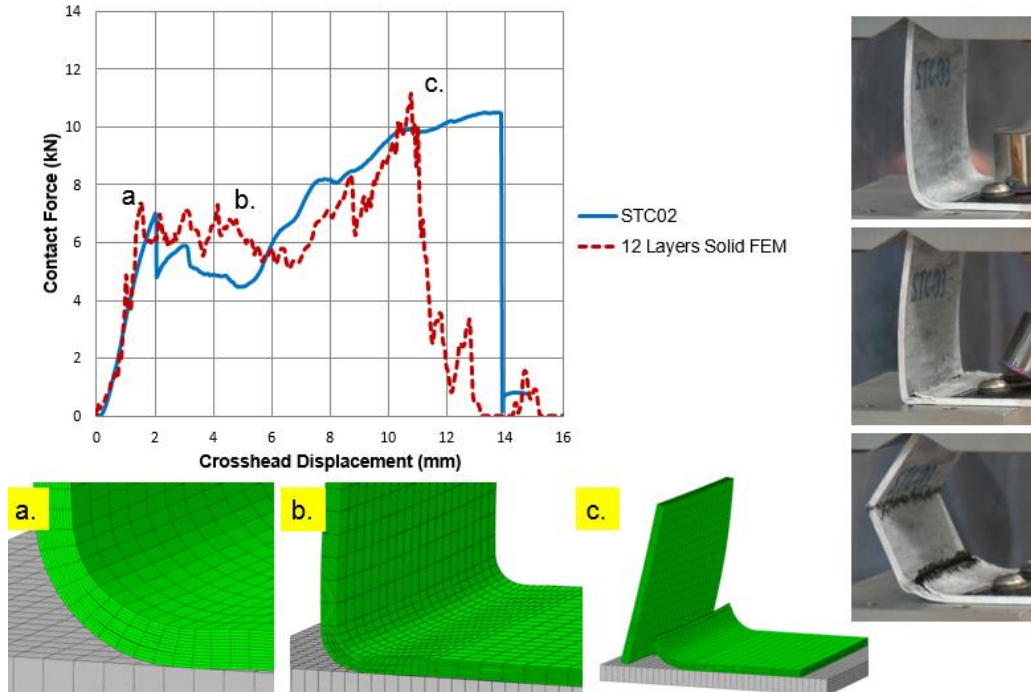


Figure 2.9: Shear tie element FE simulation correlated with the element test – Compression and Buckling [11].

In previous HEWABI research, the experimental and numerical investigations were performed by DeFrancisci and Chen [8, 11]. In the current research's 2<sup>nd</sup> generation panel testing and FE modeling, the methodology defined by these previous researchers was used as a basis for design, fabrication, testing, and analyzing the new composite test specimens.

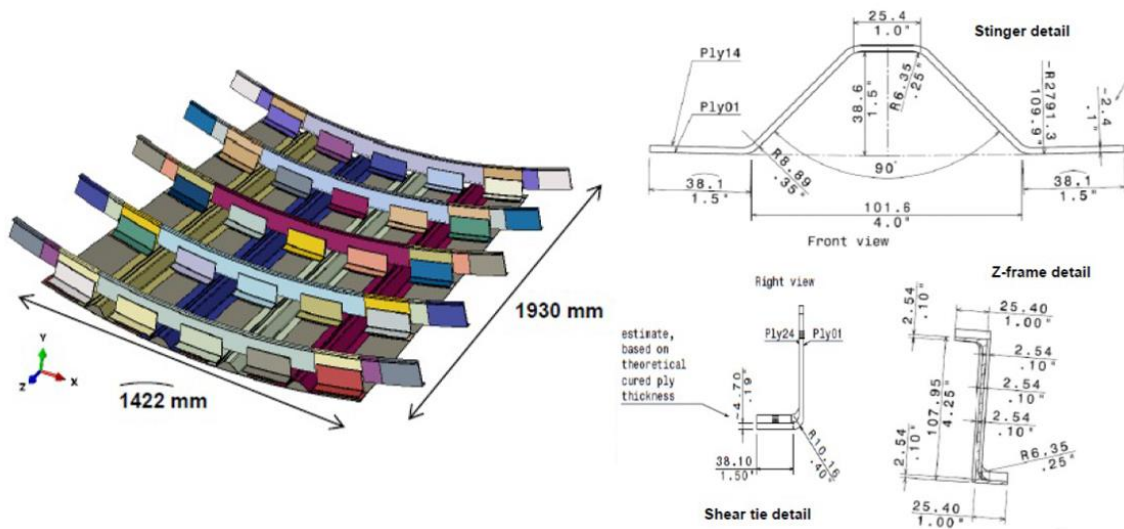
## 2.2 CODAMEIN – COMPOSITE DAMAGE METRICS AND INSPECTION (HIGH ENERGY BLUNT IMPACT THREAT) RESEARCH

A series of research named Composite Damage Metrics and Inspection (CODAMEIN - phase 1, 2, 3) was conducted in Europe sponsored by European Aviation Safety Agency (EASA) [14-18]. The experimental and numerical investigations were performed on hybrid composite-metallic aircraft structures representing CS-25 (large aircraft) fuselages by benchmarking UCSD HEWABI study. Based on the results of the research, recommendations for amending airworthiness certification specifications were made to EASA CS-25 [14]. This section summarizes the key features of that body of research, mainly focused on CODAMEIN III.

Through the review of actual in-service incident data and previous test results including input from UCSD, reasonable energy boundaries for a GSE blunt impact were estimated in a range between 1000 J to 3000 J [14].

The hybrid fuselage specimen (overall dimension with 1930 mm x 1830 mm) was composed of co-cured composite skin-stringer, discrete shear ties and aluminum Z-

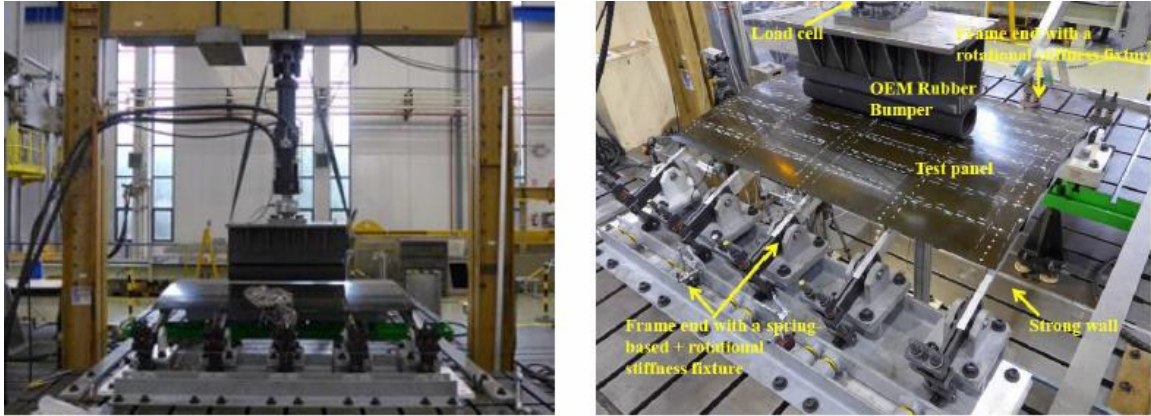
frames as shown in Figure 2.10. As a generic specimen design, it was based on the UCSD Phase 2 panels with similar material, layup sequence, component design and structural geometry except usage of metal circumferential Z-frame with its boundary condition. With permission from UCSD, new version of the UCSD panel were fabricated by a local San Diego company and sent to the CODAMEIN research team in Europe.



**Figure 2.10: CODAMEIN panel details: stinger, shear tie and frame [18].**

With the test setup shown in Figure 2.11, quasi-static loading tests were conducted. Damage formation, damage mechanisms, and major key internal damage modes were investigated [17, 18].





**Figure 2.11: CODAMEIN test setup details [17, 18].**

Initially, elastic buckling of the shear tie was detected from cracking noise and sudden reversed change of stiffness in strain gauge measurements (see Figure 2.12). Delamination in the shear tie radii was the first point of damage onset and center shear tie crack was observed clearly (see Figure 2.13). It was assumed that the shear tie radius crack led to contact between stringers and frames and it was decided to continue loading up to shear tie failure, accepting stringer-frame contact. After final loading with withdrawal of the impactor, the panel relaxed fully except for one small crack on outer skin surface, but internally, cracks along the radius of most of shear ties were observed to exist close to the impact area due to opening moment as well as plastic deformation of the aluminum Z-frame outer flange. This resulted in bending and shear load being transferred to the shear ties which caused tilting of the web.

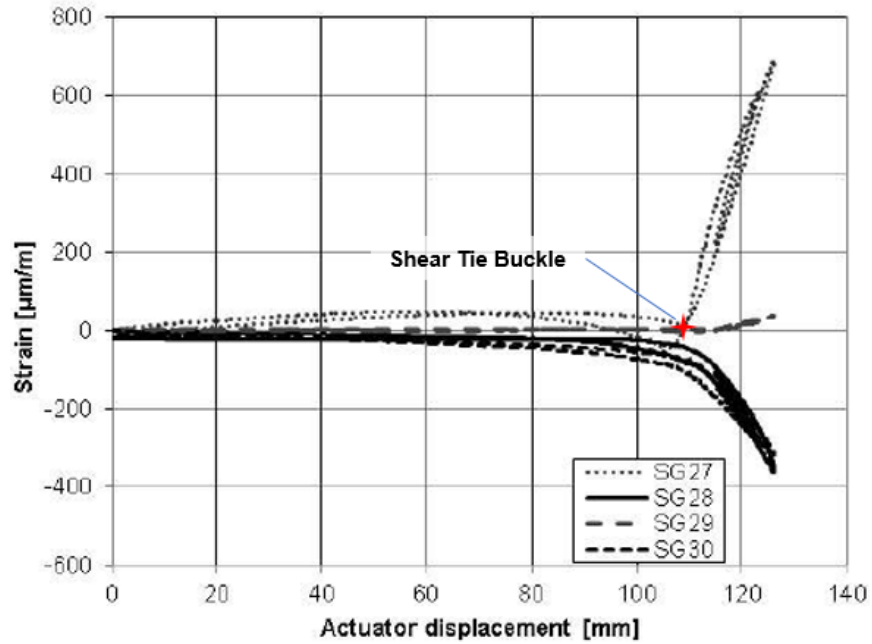


Figure 2.12: Shear tie strain gauge data capturing local buckling [18].

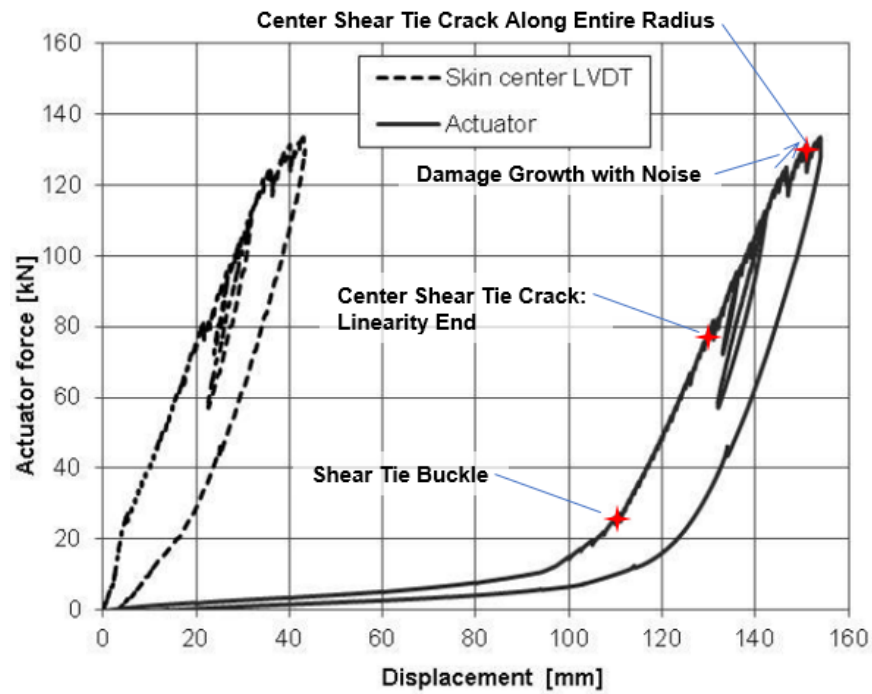
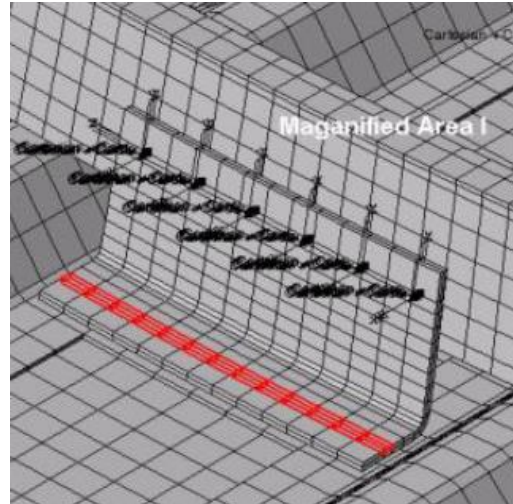


Figure 2.13: Load-displacement curve [18].

For FEA, the impactor loading rate was 1 m/s while the tests were performed under quasi-static loading conditions. Determination of the impact velocity was based on evaluation of dynamic effects and computational cost. The influence of low velocity impact loading was previously determined to be acceptably low [17]. Abaqus/Explicit solver was used with Hashin failure criterion to predict intra-laminar damage and failed material stiffness degradation. As the most critical structural component, the shear ties were modeled with a finer mesh (8 mm x 15 mm) especially at the radius corner as this is the key region of initial damage formation. Two layers of continuum shell elements with a cohesive zone interface between the sub-laminate layers was used to predict delamination damage. As shown in Figure 2.14, the fasteners attaching the shear tie to the skin were replaced by local tie constraints to reduce the tendency of elements within the shear tie feet to undergo hourglass modes that caused delamination. Weak layers were inserted in the shear tie feet to represent the weak fastener, while the fasteners that attached the shear ties to the frames were modeled using connector elements. For the representation of the fasteners, translational elasticity as well as axial and shear strengths were defined.



**Figure 2.14: FE modeling scheme for shear tie and fastener connection [18].**

The FEA predictions correlated well with the test results, especially the predicted shear tie failure initiation displacement within 6.8% discrepancy.

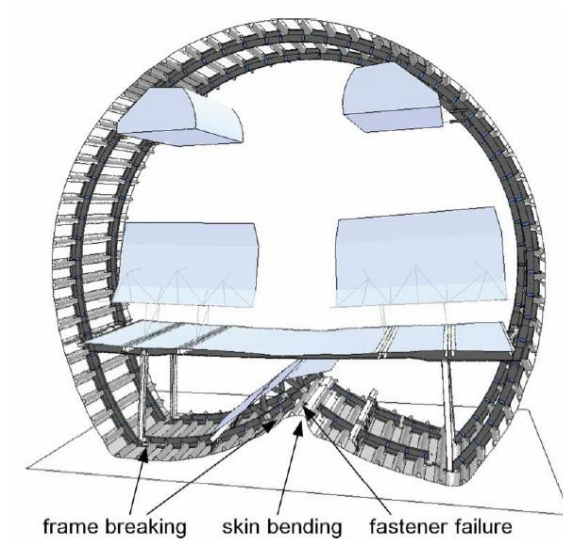
In CODAMEIN research, the experimental and numerical investigations were performed on the large-scale impact behaviors of composite aircraft fuselage panels [14-18]. For the future work of the 2<sup>nd</sup> generation HEWABI research, FE modeling methodology defining shear tie radius corner with sub-laminate layers and shear tie fastener connection to C-frame can be referenced.

### 2.3 CRASHWORTHINESS – FRAME FAILURE

In the past decade, crashworthiness research has been conducted for civil composite aircraft fuselage employing the building block approach through typical fuselage section drop tests and element-level tests as well as through large- and small-

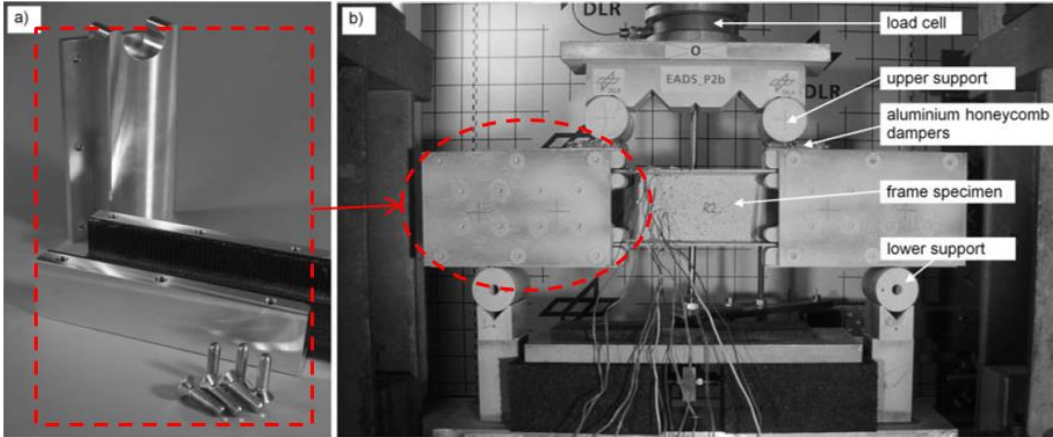
scale FE modeling/simulation [20-22]. The frame element is the major contributor to crash energy absorption. In this section, the element level frame failure tests and FE modeling methodologies, for structural level FE model validation, are introduced [21].

Fuselage crash simulation and critical failure modes are described in Figure 2.15. As shown, frame failure in a primarily bending state is the most dominant failure mode.



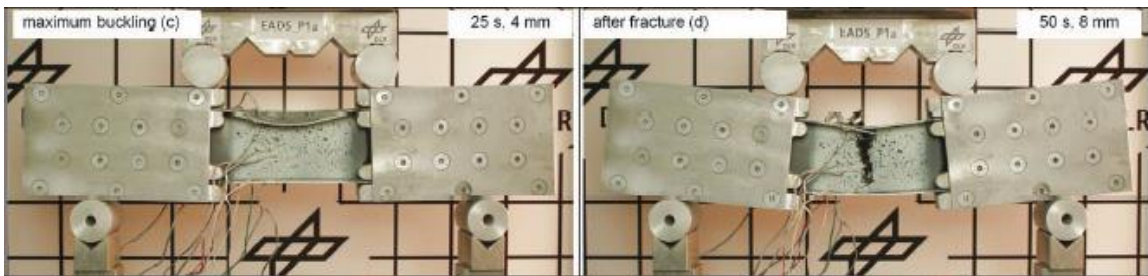
**Figure 2.15: Fuselage section crash simulation model with critical area highlighted [21].**

To excite key failure modes in a C-frame under pure bending state, 4 point bending test was prepared with load introduction devices which were attached by epoxy adhesive to C-frame then inserted into both end caps as shown in Figure 2.16.



**Figure 2.16: Aluminum load introduction devices (a) and 4 point bending test setup (b) [21].**

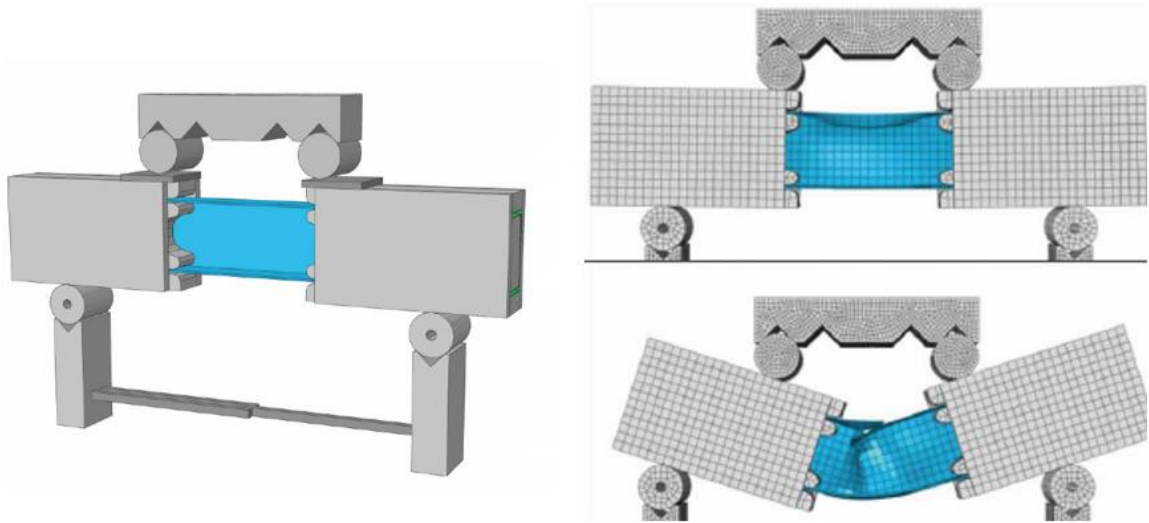
By approaching 4-point bending tests with straight C-frame, the key failure mode was identified which is compression flange buckling and fracturing as shown in Figure 2.17.



**Figure 2.17: 4 point bending test of composite frame and key failure modes [21].**

FE simulation of frame bending tests were aimed at validating the stiffness and strength as well as investigating the failure mechanism and energy absorption of the failing frame.

As shown in Figure 2.18, to allow for correct load introduction, the whole test setup was modeled. For the C-frame, conventional shell elements were applied with Hashin failure criterion. To bring the simulation load-displacement curve close to the experiment results, cured epoxy adhesive was modelled with solid elements to represent its compliance under load, and a contact formulation with friction coefficient of 0.5 was applied at the interface between the adhesive and the metal surface in the end caps. The FE simulation predicts the key mode observed in tests as shown.



**Figure 2.18: Final FE model (Left) and predicted key modes observed in tests [21].**

This paper was referenced for C-frame bending and bending-twisting tests inducing key failure mode observed in the 1<sup>st</sup> generation Phase 2 HEWABI Frame03 test especially for element level test methodology.

## 2.4 LITERATURE REVIEW CONCLUSION

Previous HEWABI, CODAMEIN, crashworthiness research is directly related to current HEWABI research. In large-scale and sub-scale impact testing as well as FE modeling, the methodology defined in the referenced research were used as a basis for design, fabrication, testing, and analyzing the new composite specimen tests.

In the previous HEWABI and CODAMEIN research, first, impact characteristics were investigated. As a major damage threat to composite aircraft fuselage, significant high impact energy is generated by GSE accidental contact. The bluntness of the typically used rubber bumper causes the wide internal damage extent and reduces external damage detectability. It was confirmed that a flattened hollow rubber bumper can be replaced with flat rubber pad in test and FE simulation as a cost reducing and computational stability improving measure. Second, due to equivalence between low-velocity impact event and quasi-static indentation, new HEWABI tests can be conducted quasi-statically allowing more detailed observation of damage evolution. However, from the different C-frame failure modes between the 1st generation Phase1 (quasi-static) and Phase2 (dynamic) tests, the loading rate effect needs be examined with actual impact velocity. Thirdly, the importance of boundary condition in low velocity impact experiments was confirmed. The methodology of choosing proper boundary fixture can be applicable to new HEWABI test design. Through iterative FEA approach, equivalent response between full- and sub-scale structures can be verified.

Previous HEWABI and CODAMEIN research focused on the impact location at the acreage area which is the most compliant (bending dominant) region. The current



(newly reported herein) 2<sup>nd</sup> generation HEWABI research focuses on examining influence of the impact location near the floor structures. With floor structure and thicker continuous shear tie, more realistic component design and more likely location of GSE impact are reflected. The influence of loading location in the shear dominant region, interaction between new components, and accompanied failure mode and sequence will be examined.

Investigation of C-frame failure is important for aircraft safety. In previous HEWABI and crashworthiness research, the methodology of element level test and FE modeling was introduced. It will be referenced in C-frame element test and FE modeling. Different C-frame failure modes between previous and current HEWABI tests will be investigated and compared. The main factor influencing the C-frame failure modes will be examined in detail.

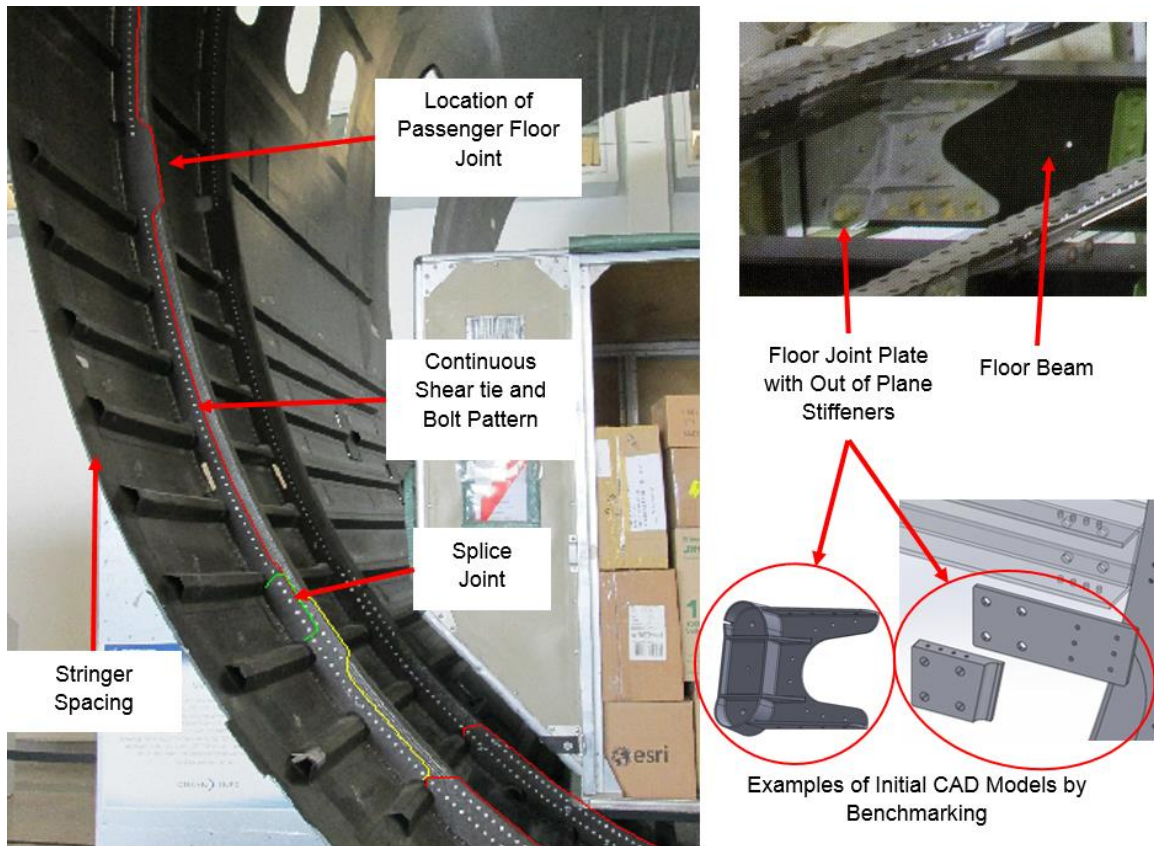
### 3 LARGE SCALE EXPERIMENTS (2ND GENERATION PANELS)

---

This chapter describes research investigations that required large, complex built-up composite structures to be designed, manufactured, and configured for testing. As each of these aspects are individually major undertakings for a single graduate student, the successful summed outcome reported herein required a close-working team effort. Thus, results reported here are equally attributed to myself and fellow graduate student Chaiane Wiggers de Souza. Specifically Sections 3.1 to 3.4, 3.6 to 3.9, and 3.11, are joint-effort products of this collaboration for which equal attribution is due. Sections 3.9 and 3.11 describe test setups for the two major loading configurations investigated, with my individual explanation and interpretation of these test results presented in Sections 3.10 and 3.12.

#### 3.1 BENCHMARKING EXISTING COMMERCIAL COMPOSITE FUSELAGE

As the second generation HEWABI specimen, the specimen configuration represents more realistic composite aircraft fuselage than the first generation HEWABI specimen [8] as some features i.e., continuous shear tie and floor structure are added. As shown in Figure 3.1, the Boeing 787 fuselage configuration was benchmarked in the design of the second generation HEWABI specimen. From these sources, information about dimensions and spacing of stringer stiffeners, configuration of shear ties, and their connection to the skins were used in the new specimen design layout.

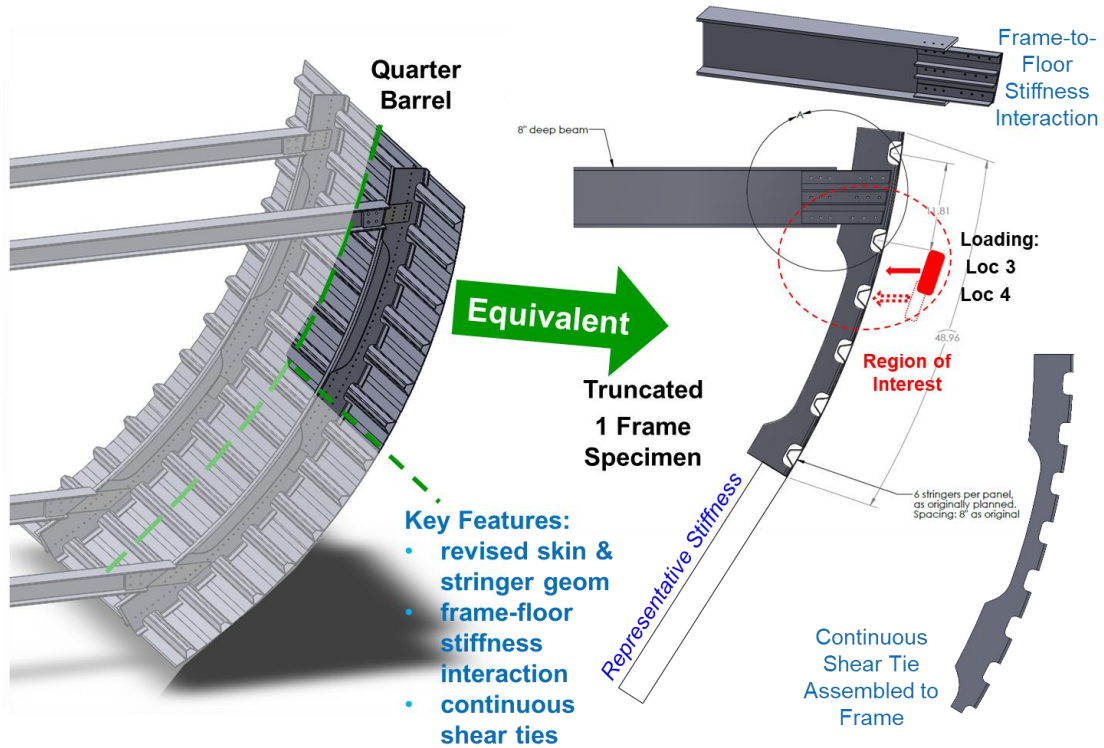


**Figure 3.1: Boeing 787 Fuselage Configuration; Picture from Boing Future of Flight Museum (Left) and from The Birth of the 787 Dreamliner by Edgar Turner (Right) [19].**

### 3.2 SPECIMEN DESCRIPTION

Through the discussion with the engineers of industry partners and FAA, the initial design of the second generation HEWABI specimen was revised and, via Finite Element Analysis (FEA) approach, the equivalency between the full quarter barrel and simplified truncated model, was verified as shown in Figure 3.2. This figure also shows the overall description of the 2<sup>nd</sup> generation HEWABI specimen composed of the co-cured skin-stringer outer panel (overall size with 559 mm x 1,233 mm), one continuous

shear tie, and one C-frame. As shown in Figure 3.2 to Figure 3.6, the key features, different from the first generation HEWABI specimen, are thicker and continuous shear tie (discrete shear ties were used in the first generation HEWABI specimen), closer spaced and smaller sized stringers, and the floor structure which creates increased stiffness at floor joint. In Figure 3.2, the loading locations were planned as Location 3 and 4 (Loc 3 and Loc 4) below but close to the floor structure which is expected to result in different damage mode and extent relative to the damage outcomes in the first generation HEWABI tests. Loc 1 and Loc 2 are the loading location at the centerline of the floor joint, and at the center of the first stringer below the floor joint, respectively (above Loc 3 and Loc 4 in Figure 3.2). Loc 1 and Loc 2 were not considered (per guidance of industry engineers) due to the lack of specific reinforcements at floor joint (Loc 1) in design of the second generation HEWABI specimen.



Partially-Assembled Specimen



C-Frame and Shear Tie



Skin-Stringer Panel



Figure 3.2: 2<sup>nd</sup> generation HEWABI specimen.

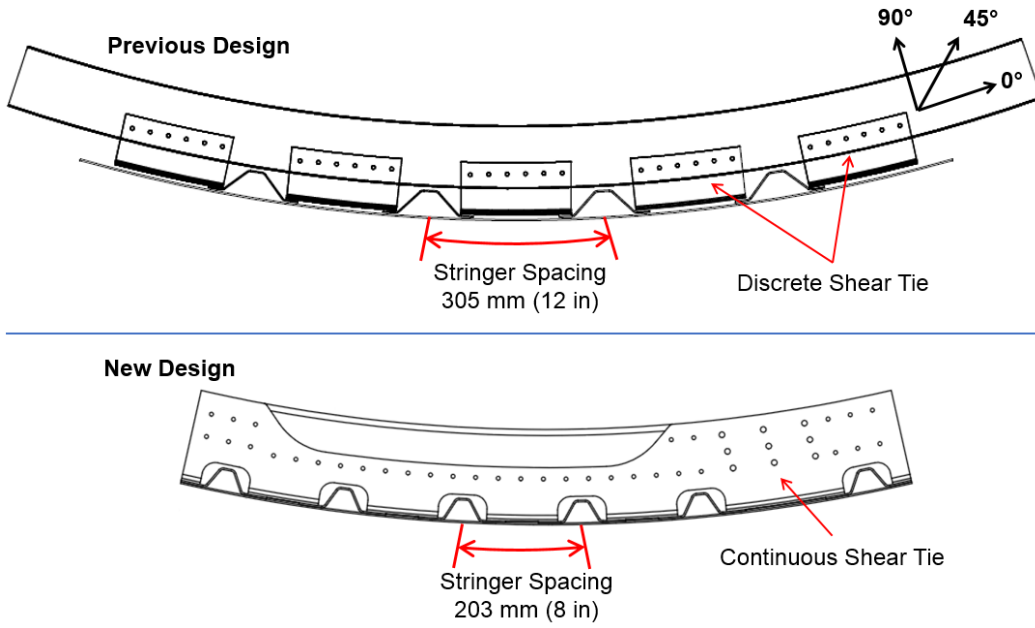


Figure 3.3: Panel comparison – stringer spacing [8, 11].

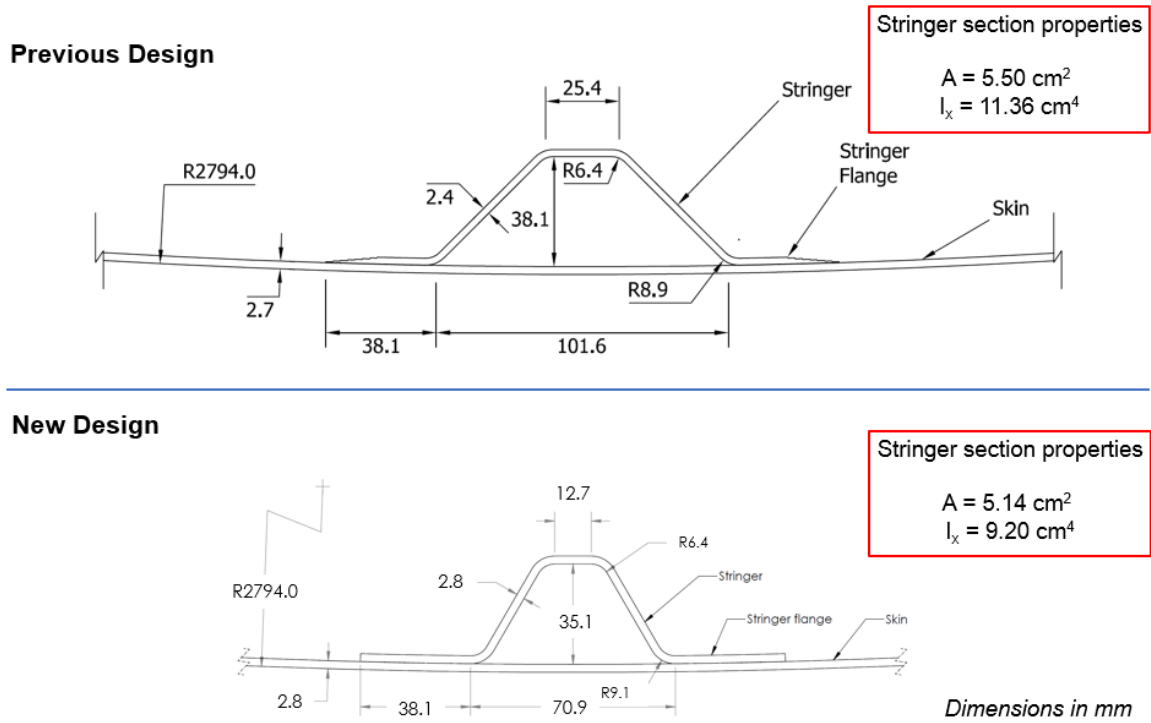
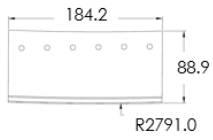


Figure 3.4: Panel comparison – stringer-skin section [8, 11].

Previous Design

THK = 2.5 mm



New Design

THK = 3.5 mm

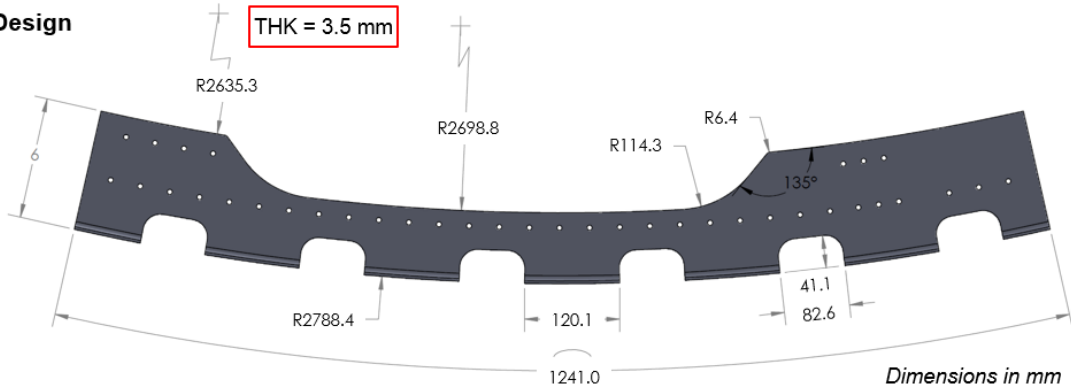
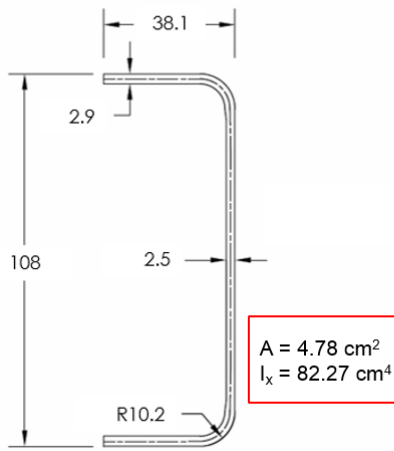


Figure 3.5: Panel comparison – shear tie [8, 11].

Previous Design



New Design

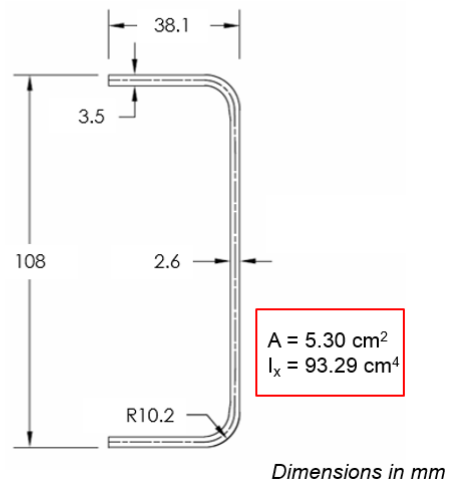


Figure 3.6: Panel comparison – C-frame [8, 11].

### 3.3 LAY-UP AND THICKNESS OF THE FUSELAGE COMPONENTS

The layup and thickness of each component is shown in Table 3.1. The layup design is closed to quasi-isotropic and aims to match the thickness of each component in real structures. The target thickness of each component referred to the typical thickness values in the area away from doors shown in Table 3.2 from the feedback of aircraft industry engineers. The specific reinforcements near the floor joint and around doors was not considered in the 2<sup>nd</sup> generation HEWABI specimen. That is because damage detectability was anticipated to be very low by the heavy reinforcement near the floor joint and doors. In Table 3.1, 0-degree direction of skin and stringer is along the axis of the stringers, and 0- degree of shear tie and C-frame is along the primary axis of the components (see Figure 3.3). The skin and stringers are mostly composed with unidirectional T800/3900-2 plies except outmost woven plies. The shear tie and C-frame are composed with all T800/3900-2 plain weave plies.



**Table 3.1: Component layups.**

<b>Part</b>	<b>Layup – T800/3900-2</b>	<b>Thickness</b>
Skin (Inner Plies Uni, Outer Plies Woven)	[0w/0/45/90/-45/0/90] <sub>s</sub> 0° dir. along stringer direction	2.79 mm (0.110 in)
Stringer (Inner Plies Uni, Outer Plies Woven)	[0w/0/45/90/-45/0/90] <sub>s</sub> 0° dir. along stringer primary axis	2.79 mm (0.110 in)
Shear Tie (All Woven)	[45/0/-45/0/45/0/-45/0] <sub>s</sub> 0° dir. along shear tie primary axis	3.53 mm (0.139 in)
C-Frame (All Woven)	[45/0/-45/45/0/-45] <sub>s</sub> (Web) [45/0/0/-45/45/0/0/-45] <sub>s</sub> (Flange) 0° dir. along frame primary axis	2.64 mm (0.104 in)  3.53 mm (0.139 in)

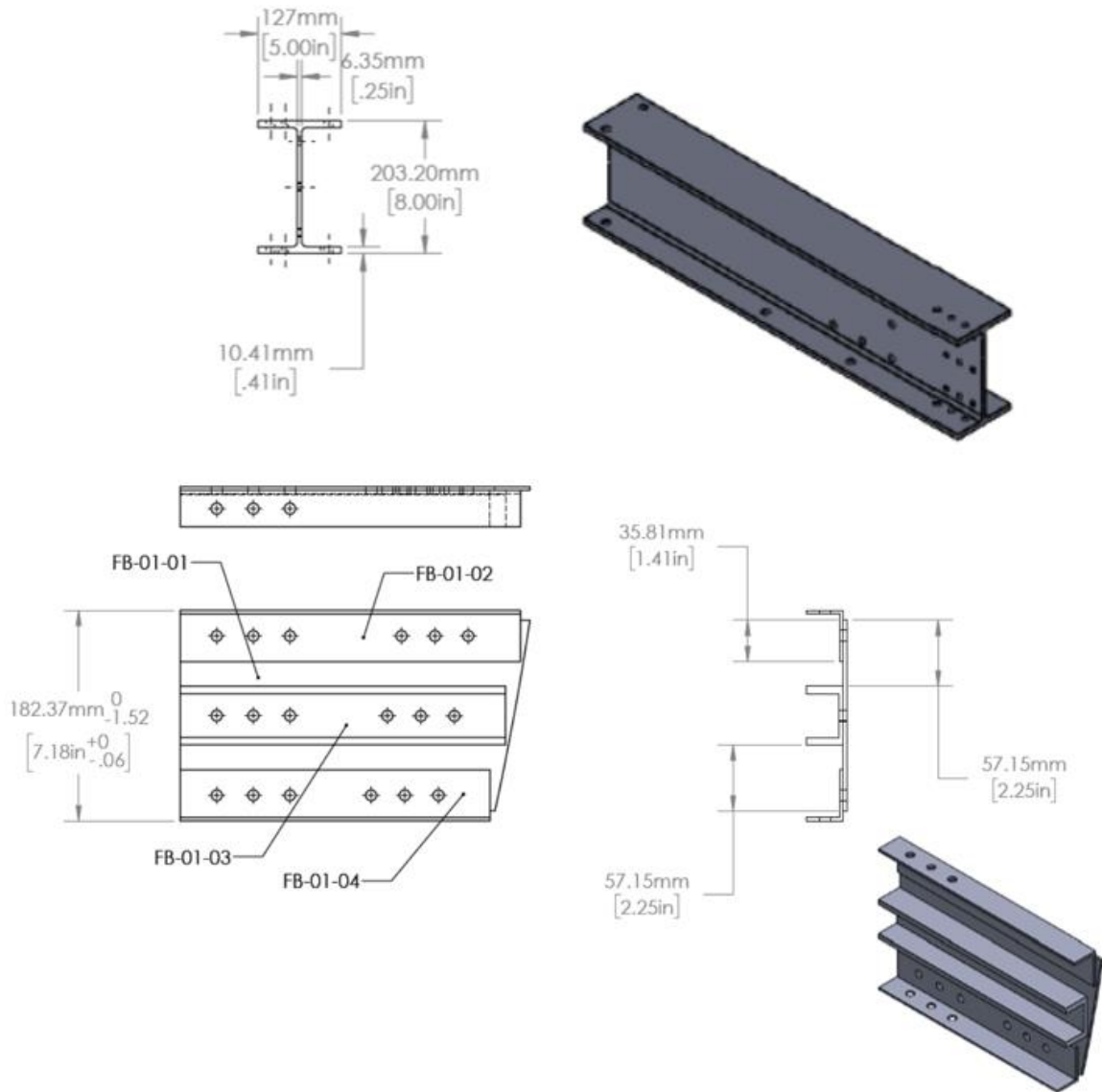
**Table 3.2: Typical thickness values in areas outside doors.**

<b>Part</b>	<b>Typical Thickness Values Outside Doors and Floor Location</b>
Skin	2.79 mm to 2.87 mm (0.110 in to 0.113 in)
Shear Tie	3.43mm to 3.53 mm (0.135 in to 0.139 in)
C-Frame	3.30 mm to 3.81 mm (0.130 in to 0.150 in)

### 3.4 FLOOR BEAM AND JOINT DESCRIPTION

With the design guidance from industry engineers, the initial floor I-beam depth was increased and out of plane stiffeners (L angles and C-channel) were added at the

floor joint shown in Figure 3.7. The material of floor structure components is aluminum 6061-T6. The design change is for very stiff in-plane and out-of-plane floor structures not allowing out-of-plane buckling at the joint.



**Figure 3.7: Passenger floor I-beam and floor joint assembly.**

### 3.5 COMPOSITE MATERIAL PROPERTIES

The composite materials used for the 2<sup>nd</sup> generation HEWABI specimen were UD T800S-24K/3900-2, and PW T800H-6K/3900-2. These are aerospace-grade carbon fiber pre-impregnated with epoxy materials used to make existing composite aircraft fuselage structures. In design stage, material properties are shown in Table 3.3. These material properties were from Toray (the material manufacturer) data sheet [26], existing literature by Tong (2003) [27], and property data in similar prepreg (Cytac X840/Z60) [11].

**Table 3.3: T800/3900-2 properties used in the design stage.**

	<b>Unidirectional</b>	<b>6K Plain Weave</b>
<b>Lamina Thickness and Density</b>		
Ply Thickness (mm)	0.195	0.220
Density, $\rho$ (g/cm <sup>3</sup> )	2.67	1.61
<b>Lamina Elastic Properties</b>		
Longitudinal Young's Modulus, $E_1$ (GPa)	159.96	80.00
Transverse Young's Modulus, $E_2$ (GPa)	8.96	80.00
In-Plane Poisson's Ration, $\nu_{12}$	0.28	0.06
In-Plane Shear Modulus, $G_{12}$ (GPa)	6.21	6.48
Transverse Shear Modulus, $G_{13}$ (GPa)	6.21	5.10
Transverse Shear Modulus, $G_{23}$ (GPa)	3.45	4.07
<b>Lamina In-Plane Strength</b>		
Longitudinal Tension Strength, $F_{1t}$ (MPa)	2799	993
Longitudinal Compression Strength, $F_{1c}$ (MPa)	1620	772
Transverse Tension Strength, $F_{2t}$ (MPa)	55.16	855
Transverse Compression Strength, $F_{2c}$ (MPa)	227.53	896
In-Plane Shear Strength, $F_{12}$ (MPa)	75.84	68.95
<b>Lamina In-Plane Fracture Energy</b>		
Longitudinal Tensile Fracture Energy, $G_{1t}$ (kJ/m <sup>2</sup> )	91.60	45.80
Longitudinal Compressive Fracture Energy, $G_{1c}$ (kJ/m <sup>2</sup> )	79.90	39.90
Transverse Tensile Fracture Energy, $G_{2t}$ (kJ/m <sup>2</sup> )	0.20	45.80
Transverse Compressive Fracture Energy, $G_{2c}$ (kJ/m <sup>2</sup> )	0.20	39.90

### 3.6 DESIGN METHODOLOGY WITH FEA APPROACH

Via Finite Element Analysis (FEA) approach, the single-frame test specimen was designed and evaluated such that it represented the response of a full quarter barrel

fuselage structure. In Figure 3.8, as the original fuselage structure, the left is full quarter barrel model having passenger and cargo floor beams and two C-frames by the symmetry boundary condition along the skin edge. The loading is applied uniformly across the specimen width. For the impact at loading location, Loc3 and Loc4, the full quarter barrel model showed localized damage around loading locations near the upper floor beam, and lower structure remained elastic. Thus, a simplified truncated model was built which showed equivalent response with the full quarter barrel model by applying proper boundary conditions. The extensive Finite Element Analysis was conducted to verify the equivalency between full model and truncated model. In Figure 3.8, the truncated model has key boundary conditions shown. The first one is the aluminum (6061-T6) C-channel lower beam having similar bending, torsional, shear stiffness with the lower structure of the full quarter barrel model. 914 mm (36 in) long C-channel was used with the section (stock) dimension, 101.6 mm x 57.15 mm x 4.83 mm (4 in x 2.25 in x 0.19 in). Another major boundary condition is zero z-displacement along the skin edge preventing lateral displacement with one C-frame. As the last major boundary condition, in design stage, the rectangular flat bumper size was 254 mm x 558.8 mm (10 in x 22 in) with 50.8 mm (2 in) thickness. The bumper width has same dimension with skin width, 558.8 mm (22 in). Later, the rubber bumper size changed during the test setup (Section 3.8.2). In the design approach using FEA, the pre-existing modeling definitions developed by DeFrancisci and Chen [8, 11] were employed.

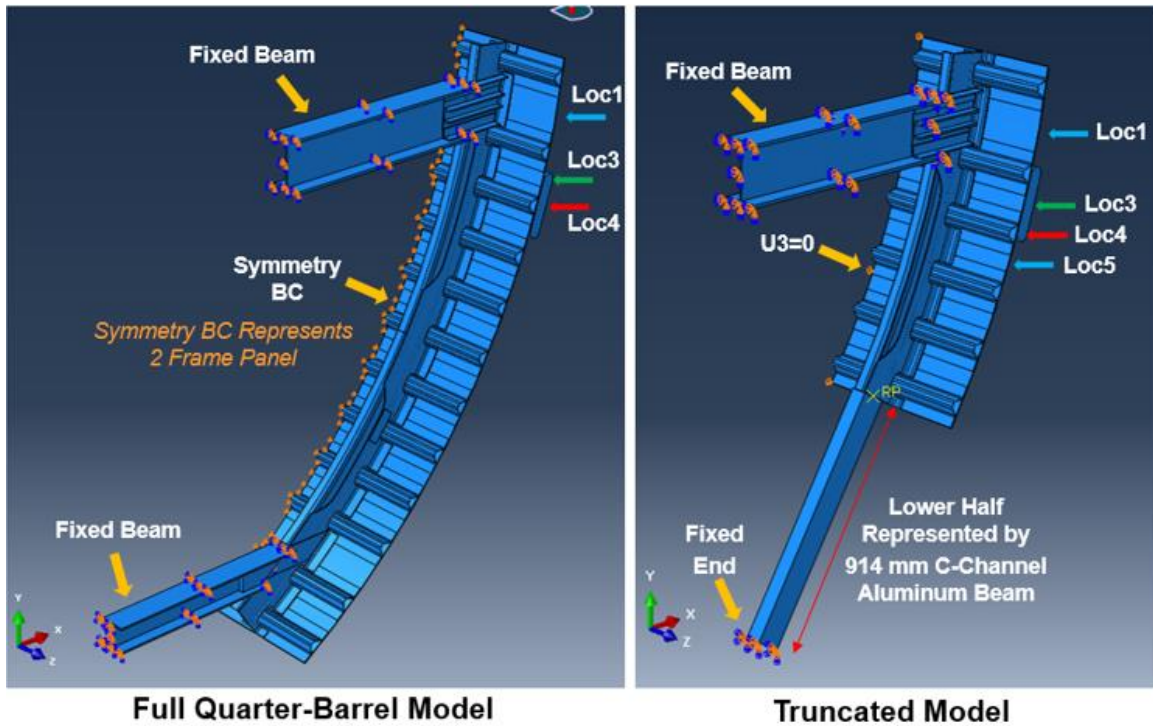


Figure 3.8: Full quarter barrel vs. truncated model.

### 3.6.1 FINITE ELEMENT MODEL INFORMATION

Abaqus/Explicit solver was used in FEA for the general elastic response as well as nonlinear behavior with the progressive failure analysis implementing the Hashin-Rotem failure criterion to all composite components. The Hashin-Rotem failure criterion is used to examine only in-plane ply failure modes (intra-laminar failure modes), but delamination failure mode (inter-laminar failure) is not represented. The Hashin-Rotem damage variables are fiber tension, fiber compression, matrix tension and matrix compression (four damage modes). Figure 3.9 shows the damage initiation criterion for fiber-reinforced composites and elastic-brittle bilinear damage evolution law. In Figure 3.9, from point “A”, failure initiates, and the stiffness degrades accordingly. More

detailed information of Hashin-Rotem failure criterion can be found in the journal paper of Hashin and Rotem [23, 24], Abaqus Analysis User’s Manual, Section 24.3 [25], and DeFrancisci’s Ph.D. thesis [8].

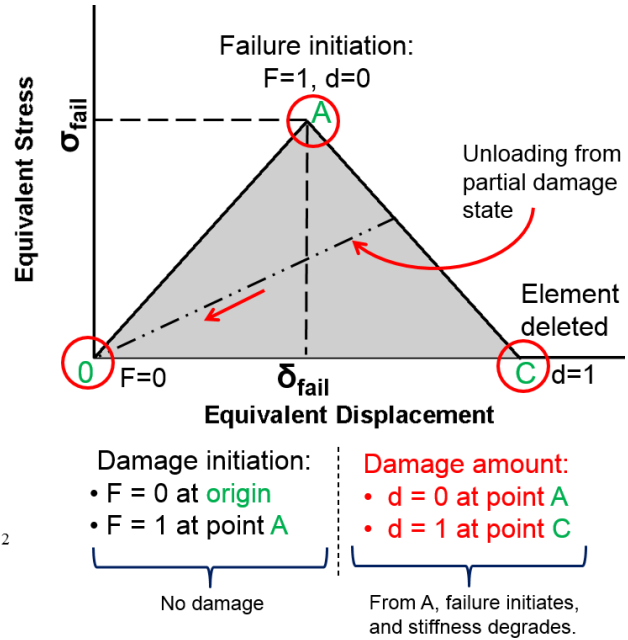
- **Hashin – Rotem failure**
  - » In-plane ply failure modes only; no 3D stress failure modes
  - » Four modes of elastic - brittle failure:
- **Fiber tension ( $\hat{\sigma}_{11} \geq 0$ ):**

$$F_f^t = \left( \frac{\hat{\sigma}_{11}}{X^T} \right)^2 + \alpha \left( \frac{\hat{\tau}_{12}}{S^L} \right)^2$$
- **Fiber compression ( $\hat{\sigma}_{11} < 0$ ):**

$$F_f^c = \left( \frac{\hat{\sigma}_{11}}{X^C} \right)^2$$
- **Matrix tension ( $\hat{\sigma}_{22} \geq 0$ ):**

$$F_m^t = \left( \frac{\hat{\sigma}_{22}}{Y^T} \right)^2 + \left( \frac{\hat{\tau}_{12}}{S^L} \right)^2$$
- **Matrix compression ( $\hat{\sigma}_{22} < 0$ ):**

$$F_m^c = \left( \frac{\hat{\sigma}_{22}}{2S^T} \right)^2 + \left[ \left( \frac{Y^C}{2S^T} \right)^2 - 1 \right] \left( \frac{\hat{\sigma}_{22}}{Y^C} \right) + \left( \frac{\hat{\tau}_{12}}{S^L} \right)^2$$



**Figure 3.9: Hashin-Rotem failure criterion – damage evolution bilinear law [8, 25].**

In Table 3.4, information of the element type and mesh seed size for each component is described. For the global mesh of 19 mm, the section of the mesh sensitivity study in DeFrancisci’s Ph.D. thesis [8] was referred to for guidance. For the locally refined mesh of 6 mm at critical locations where the load is highly concentrated, the section of the modeling of the Frame03 experiment in Chen’s Ph.D. thesis [11] was referred to for guidance.

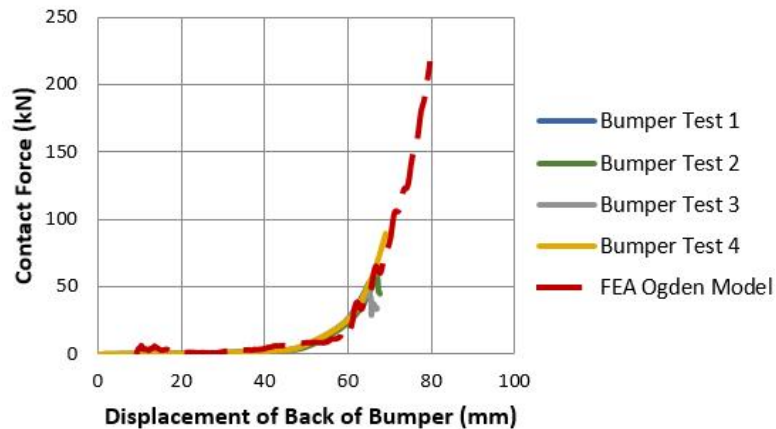
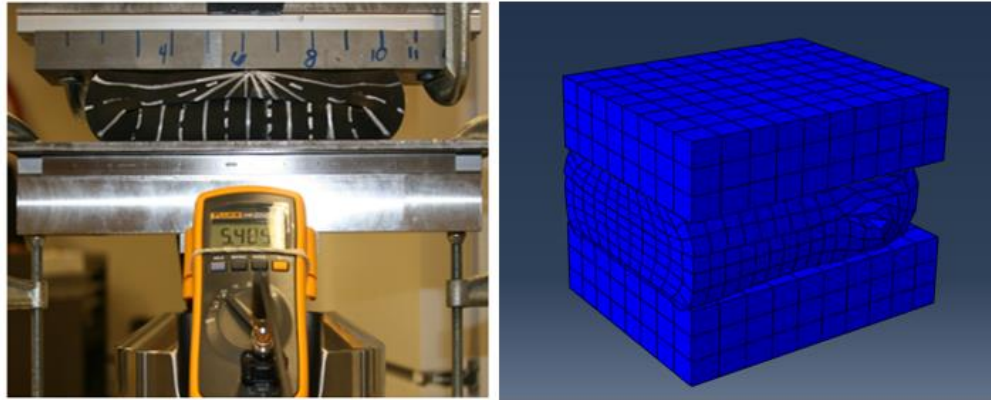
**Table 3.4: Element type and mesh size used in FE model.**

<b>Part</b>	<b>Element Type</b>	<b>Mesh Seed Size</b>
Floor Beam	Solid (C3D8R)	19.05 mm (0.75 in)
Rubber Bumper	Solid (C3D8I)	19.05 mm (0.75 in)
Composite Components	Continuum Shell (SC8R)	Shear tie: 6.35 mm (0.25 in) Other Components: 10.16 mm (0.4 in)
Floor Connection Plate and Stiffeners	Solid (C3D8R)	6.35 mm (0.25 in)
Lower Boundary Beam (for Truncated Model)	Conventional Shell (S4R)	6.35 mm (0.25 in)

8 node reduced integration solid (C3D8R) elements were applied to the metal floor beam and joint parts with enhanced hourglass and distortion control, which is to prevent spurious deformation modes and excessive element distortion under explicit FEA.

A flat rectangular soft rubber pad was modeled as a collapsed rubber bumper, which matches the deformed shape of the physical bumper. This is to decrease the settlement mainly caused when the cylindrical or D-shape bumper is fully compressed. 8 node solid (C3D8I) elements with incompatible modes were used to model the rubber bumper to accommodate the hyperelastic material model large-strain behavior. The enhanced distortion and hourglass control were applied as well. As shown in Figure 3.10, based on Chen's Ph.D. thesis [11], to present the rubber's compression response, the Ogden material model [11] was applied. These inputs enable modeling of the large deformation of the rubber pad without excessive element distortion.





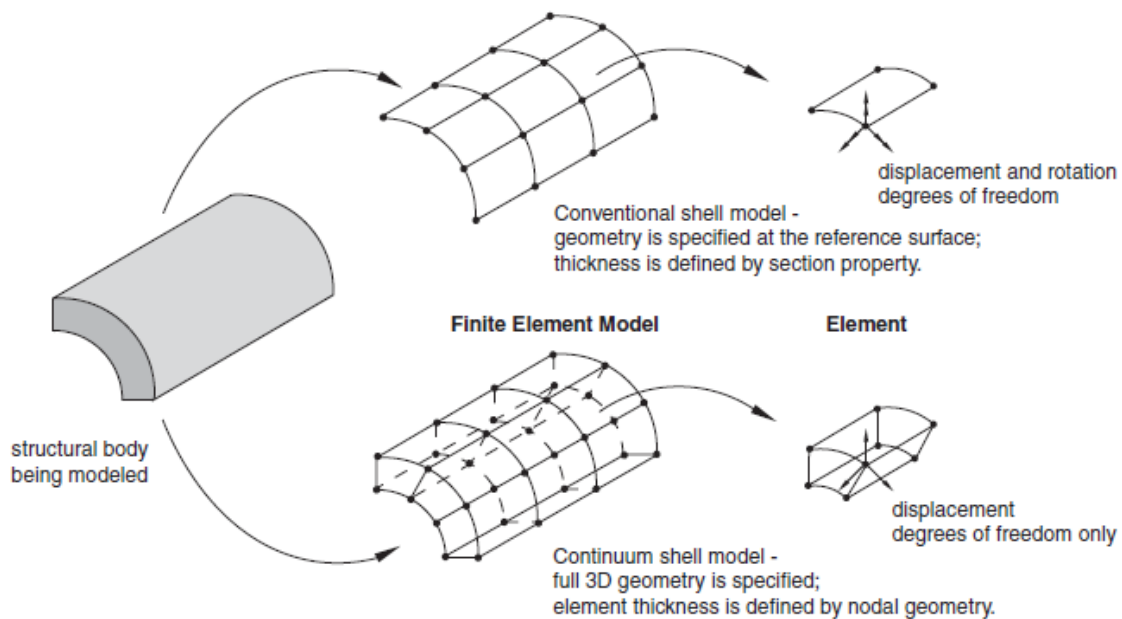
**Figure 3.10: Bumper compression test and FE modeling [11].**

The “hard” penalty contact interaction was applied to contact between the skin and the rubber bumper. Later, a friction coefficient of 0.3 was assigned to the contact.

For all composite components, 8 node reduced integration continuum shell elements (SC8R), with hourglass control, was applied. The composite layup was defined in the through-thickness direction in a single layer of continuum shell elements. As shown in Figure 3.11, a continuum shell element has 3-dimensional body with only displacement degrees of freedom. Continuum shell elements look like 3-dimensional continuum solid elements, but their kinematic and constitutive behavior is like

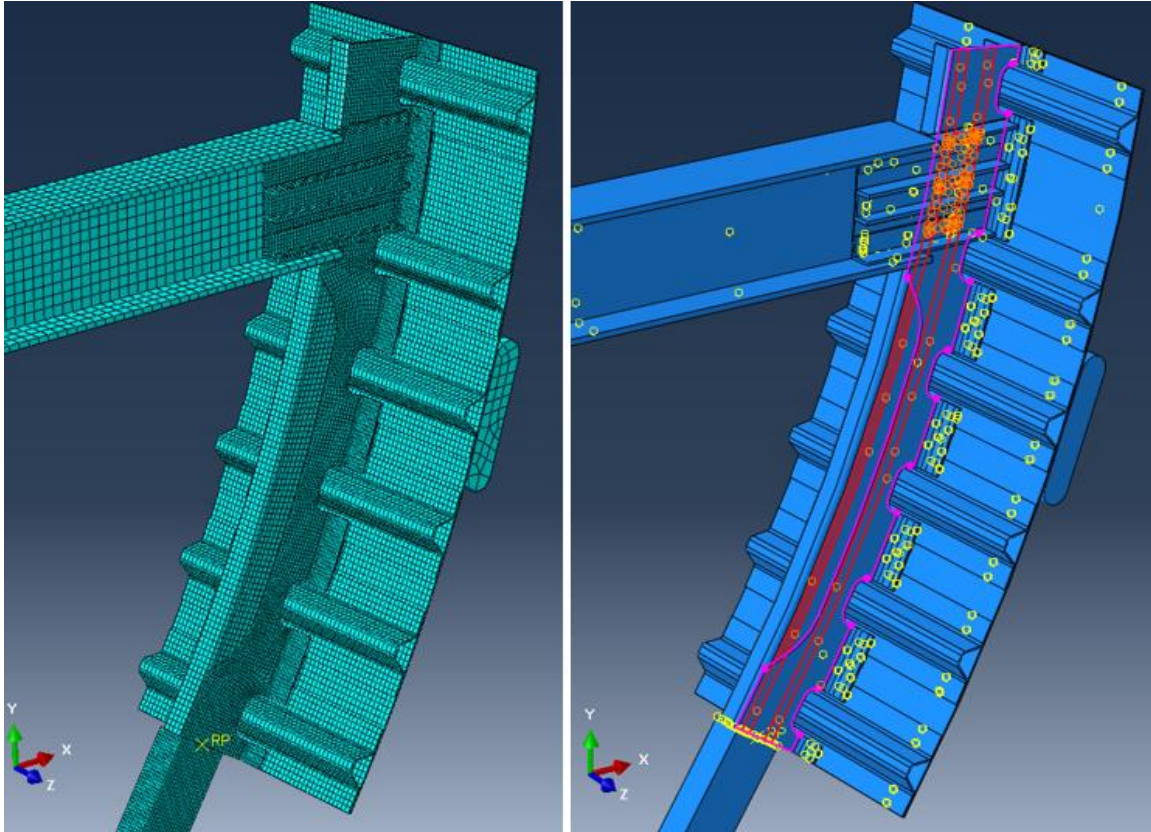
conventional shell elements. Continuum shell elements are more useful than conventional shell element when modeling complex multi-component assembled geometries due to its 3D body.

4 node reduced integration conventional shell (S4R) elements were used to model the metal lower boundary beam.



**Figure 3.11: Conventional vs. continuum shell element defined in Abaqus 6-13 analysis user manual, section 29.6.1 [25].**

In Figure 3.12, the left side shows the meshed truncated model. In the right side, the fasteners were modeled as strips with tie constraints to contacting surfaces between members connected each other instead of modeling each individual fastener in connection. The 17.78 mm (0.7 in) width of fastener line partition is based on the approach described in DeFrancisci's and Chen's Ph.D. theses [8, 11].



**Figure 3.12: Mesh and effective fastener modeling.**

### 3.6.2 RESULTS OF FE MODEL

The results of the FEA in design stage are shown in Figure 3.13 and Figure 3.14 for loading location, Loc3 and Loc4, respectively. The general elastic analysis as well as the progressive damage analysis implementing the Hashin-Rotem failure criterion were performed using Abaqus/Explicit solver. The response results show good agreement between the full model and the truncated model in both Figure 3.13 and Figure 3.14.

Furthermore, at the load of 22.24 kN (5 kips), in the outmost layer of the shear tie and the skin component, the maximum stress (S11, the stress in fiber direction) values

and its (critical) location were checked in the full model and the truncated model. These results also compare closely between the models as shown in Figure 3.15 and Table 3.5.

Thus, the two models are equivalent each other.

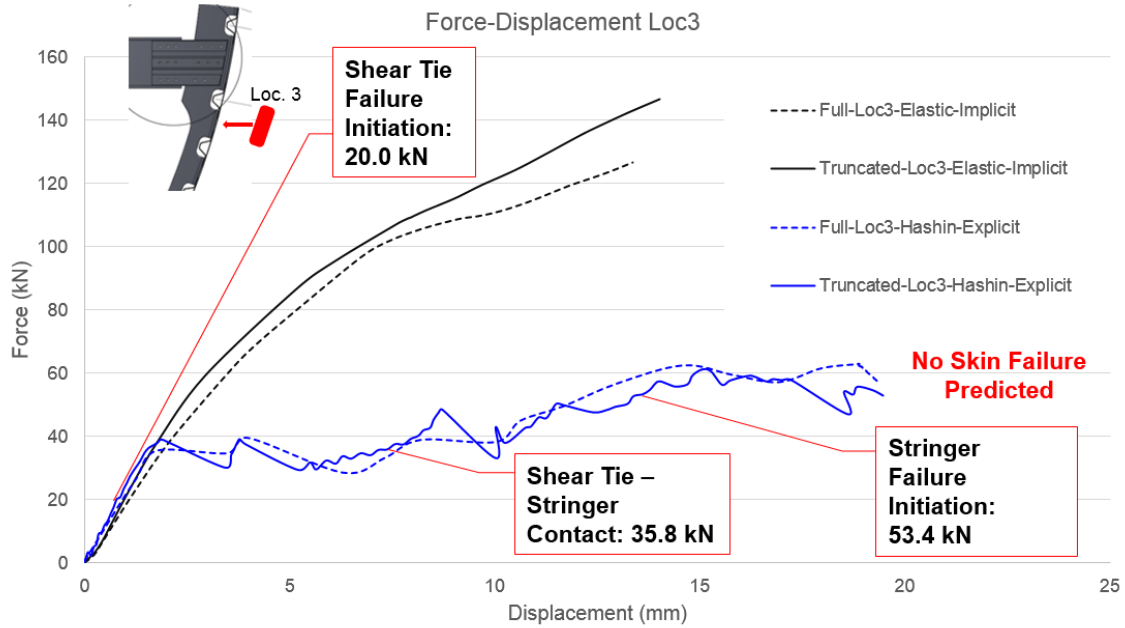
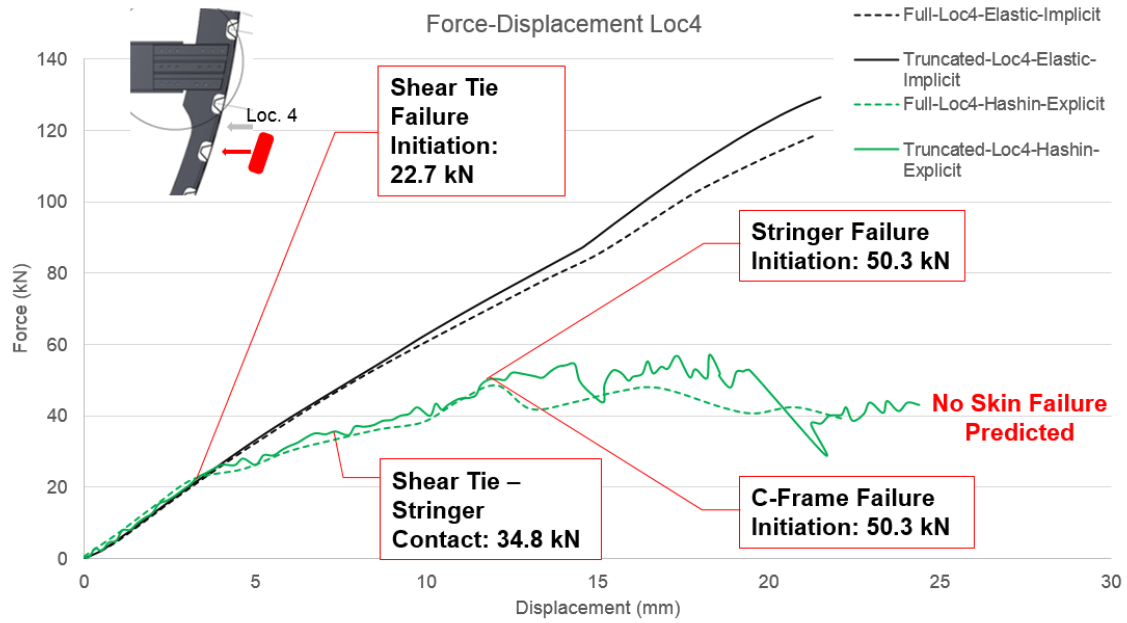
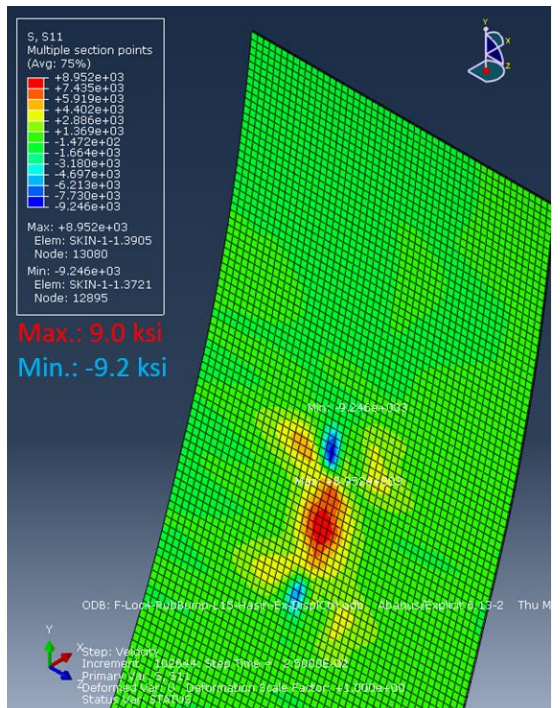
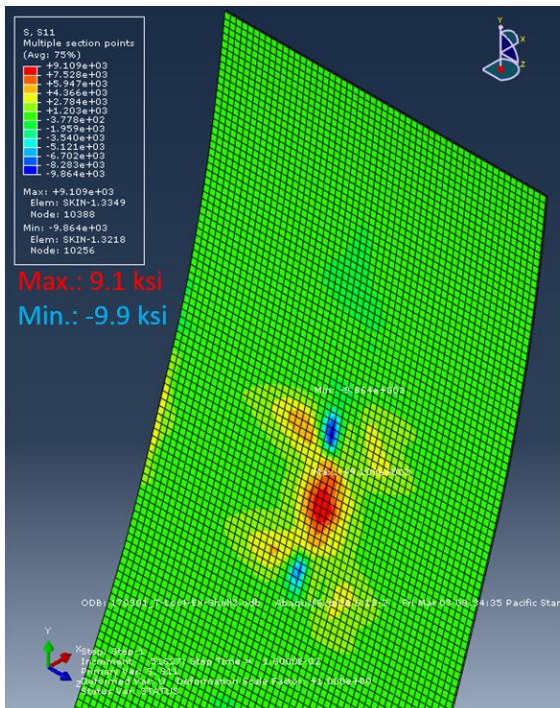
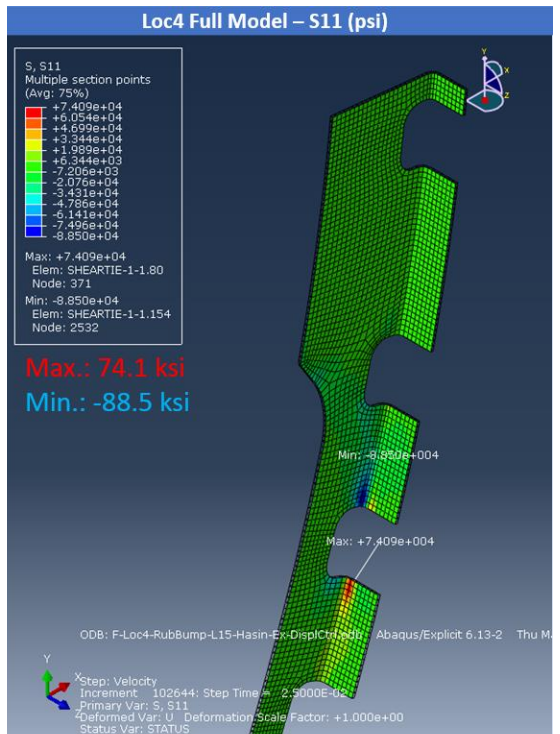
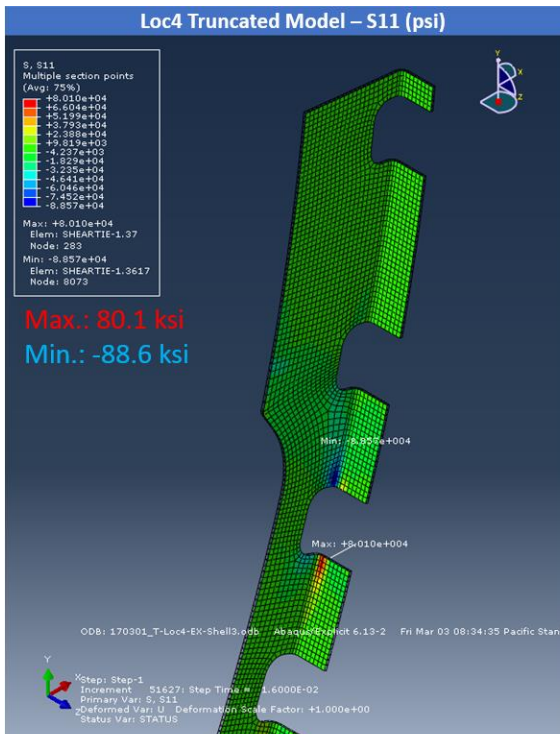


Figure 3.13: Comparison of full vs. truncated model for Loc3 loading on skin bay.



**Figure 3.14: Comparison of full vs. truncated model for Loc4 loading on stringer.**

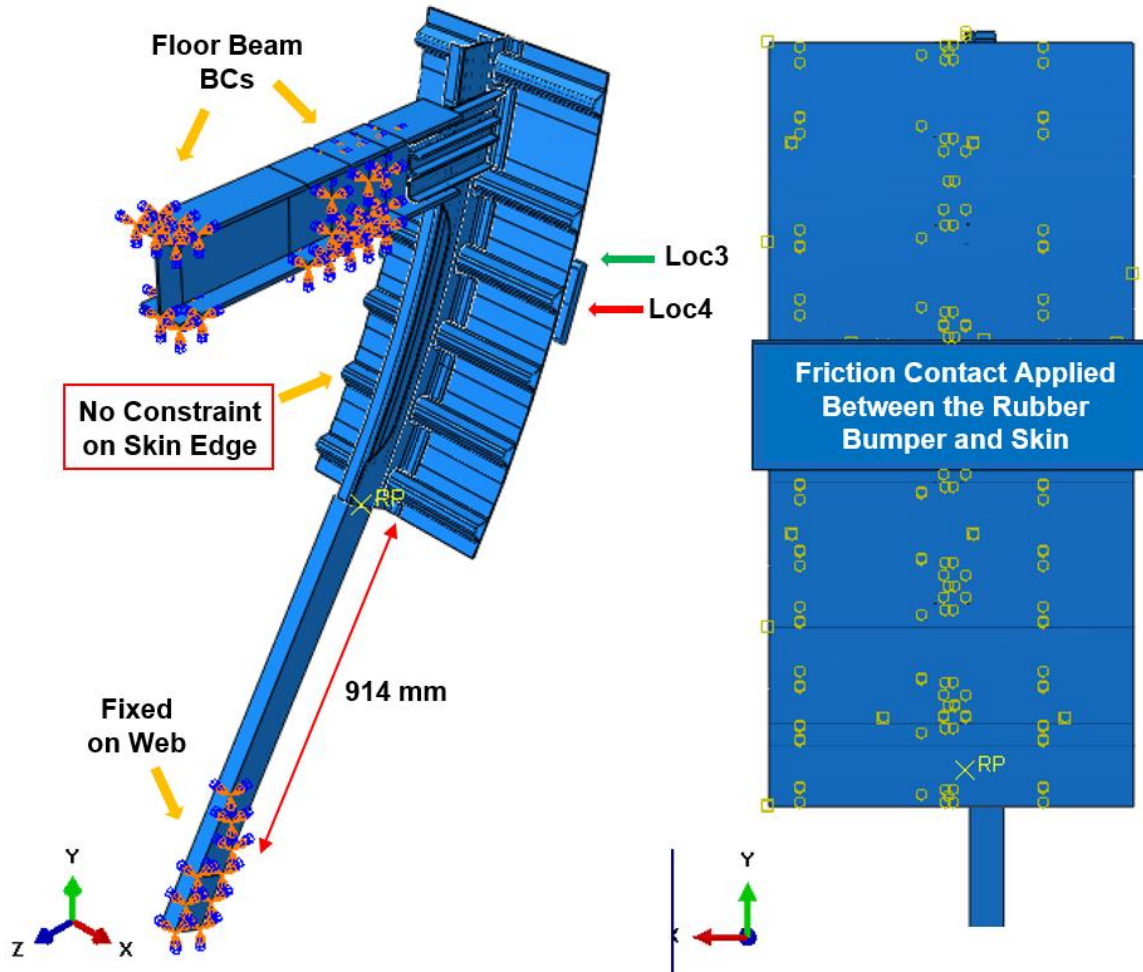


**Figure 3.15: Maximum S11 comparison examples in the top layer at the load of 22.24 kN (5 kips).**

**Table 3.5: Maximum S11 comparison in outmost layers of shear tie and skin.**

Part			Truncated –	Full –	Difference	Truncated –	Full –	Difference
			Loc3 (ksi)	Loc3 (ksi)	(%)	Loc4 (ksi)	Loc4 (ksi)	(%)
Shear Tie	T	Top	57.3	57.4	0	80.1	74.1	8
	C	Top	58.4	63.8	8	88.6	88.5	0
	T	Bottom	26.9	27.3	1	52.6	52.5	0
	C	Bottom	53.5	56.9	6	83.5	87.6	5
Skin	T	Top	12.4	11.3	10	9.1	9.0	1
	C	Top	20.6	19.4	6	9.9	9.2	8
	T	Bottom	43.7	43.5	0	37.1	37.4	1
	C	Bottom	6.7	6.2	8	6.4	4.6	39

Further study was performed about relaxing the zero x-direction ( $U1 = 0$ ) boundary condition along the skin side edge in the truncated model and applying friction as well as overhanging rubber pad along the stringer direction to prevent the specimen movement in the x-direction as shown in Figure 3.16. This is to reflect the realistic boundary conditions in the laboratory environment due to the difficulty to replicate the boundary conditions along the skin side edge. Thus, in FEA, the friction contact with a friction coefficient of 0.3 was assigned to the contact between the rubber bumper and the skin. With these changes, there was no effect on the FEA results. Therefore, the experimental boundary conditions were finalized. Test boundary conditions are described in detail including the bolted connection in Sections 3.8.2 to 3.8.3.



**Figure 3.16: Realistic boundary conditions in test environment – friction contact between the rubber bumper and the skin.**

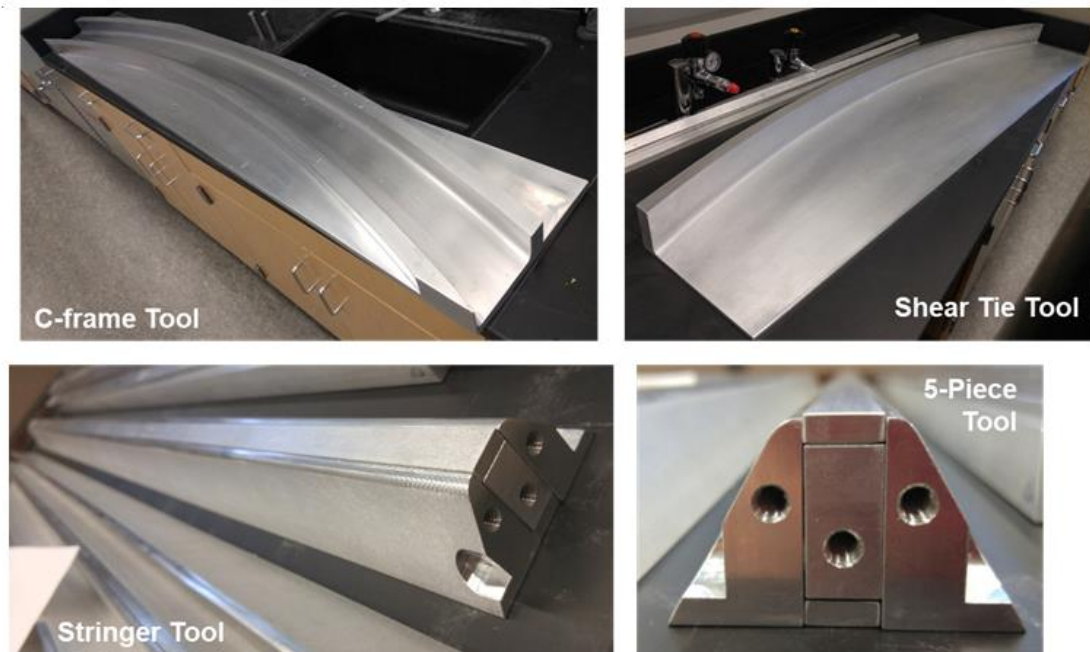
### 3.7 MANUFACTURING

The test panels were fabricated with T800/3900-2 aerospace-grade prepreg carbon/epoxy material from Toray. All manufacturing works were done at UCSD except the autoclave cure of all composite components which was done at San Diego Composites.

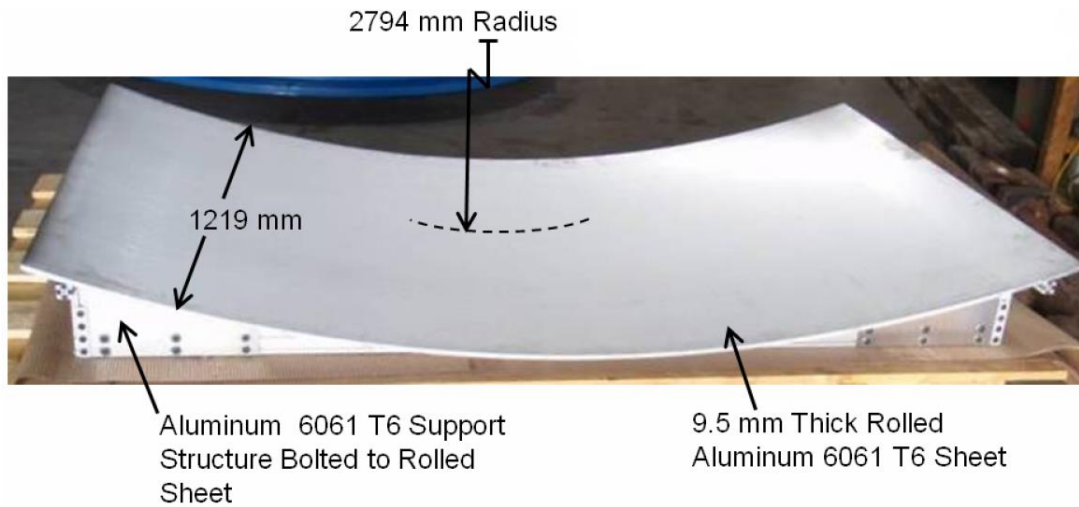


Based on the test plan with finalized geometry and layup design, the material quantity estimation and tooling design were conducted as well as the prepreg cutting plan, layup instruction, and layup check list were made. More detailed information of the mold dimension and layup instruction can be found in Appendix A and B – Mold Drawings and Layup Instruction.

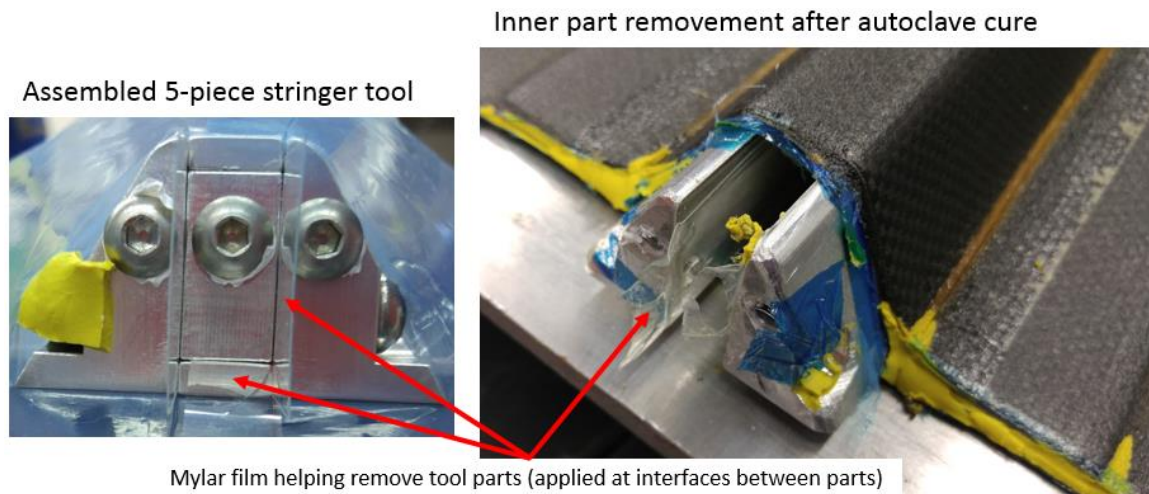
As shown in Figure 3.17, new tools were manufactured to fabricate each structural component. The stringers were co-cured with the skin. Thus, the layup for the stringers and the skin was conducted separately then assembled using the 5-piece stringer tools in Figure 3.17 and the curved skin tool shown in Figure 3.18. After the 350 degree F autoclave cure, the 5-piece stringer tool was removed (starting with the inner rectangular parts to the outer triangular parts) shown in Figure 3.19.



**Figure 3.17: Tools for specimen fabrication**

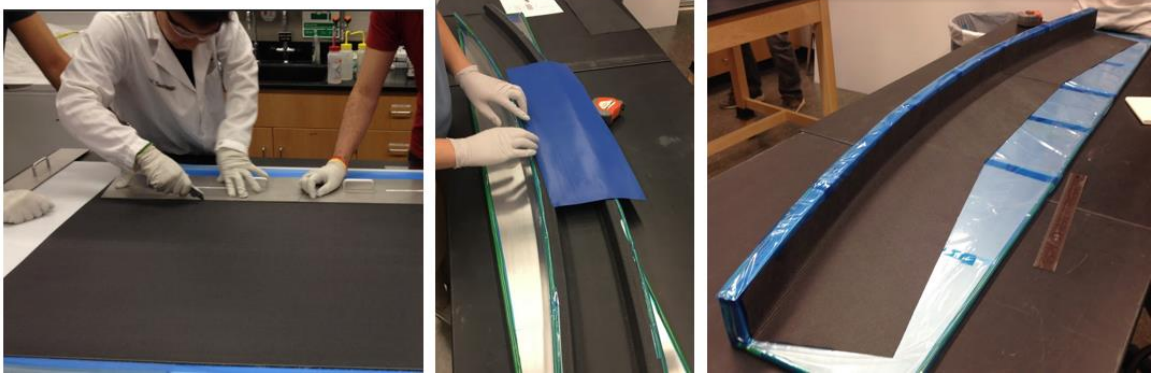


**Figure 3.18: Skin outer mold line tool [8].**



**Figure 3.19: Assembled stringer tool and tool part removal after autoclave cure.**

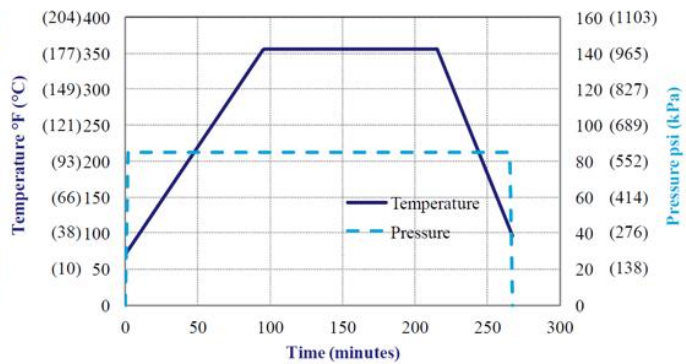
As shown in Figure 3.20 to Figure 3.22, ply cutting and layup for all parts was done by hand and then transported to San Diego Composites for autoclave cure at 350°F for 2 hour soak and under 90 psi pressure.



**Figure 3.20: Ply cutting with cutting templates and hand layup.**



**Figure 3.21: Vacuum bagging for all parts.**



**Figure 3.22: 1.8 m diameter autoclave in San Diego Composites (left) and autoclave cure cycle (right) [26].**

The final cured part thickness was measured and compared with anticipated theoretical thickness as a simple assessment of whether final resin-content was attained. Summarized in Table 3.6, the actual part thicknesses were within 6.2% of anticipated.

**Table 3.6: Cured parts actual measured thickness compared to theoretical thickness.**

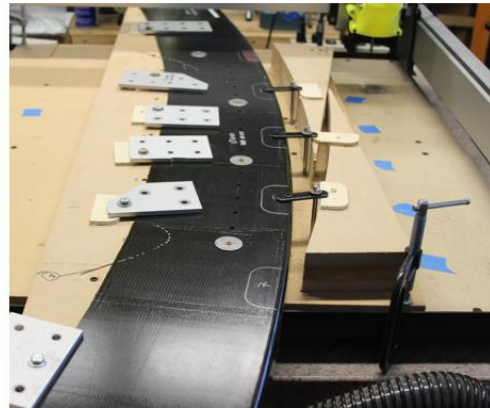
<b>Part</b>	<b>Measured Average Thk (mm)</b>	<b>Theoretical Thk (mm)</b>	<b>Difference (%)</b>
Skin	2.785	2.779	0.2
Skin + Stringer	5.398	5.568	-3.1
C-Frame Web	2.783	2.639	5.5
C-Frame Flange	3.619	3.519	2.8
Shear Tie Web	3.737	3.519	6.2
Shear Tie Flange	3.638	3.519	3.4

After autoclave cure, all parts were trimmed by diamond saws. Due to the complex geometry, continuous shear ties were machined (trimmed and drilled) using the carbide cutting tool on the CNC router machine as shown in Figure 3.23.

Trimming the co-cured skin-stringer part

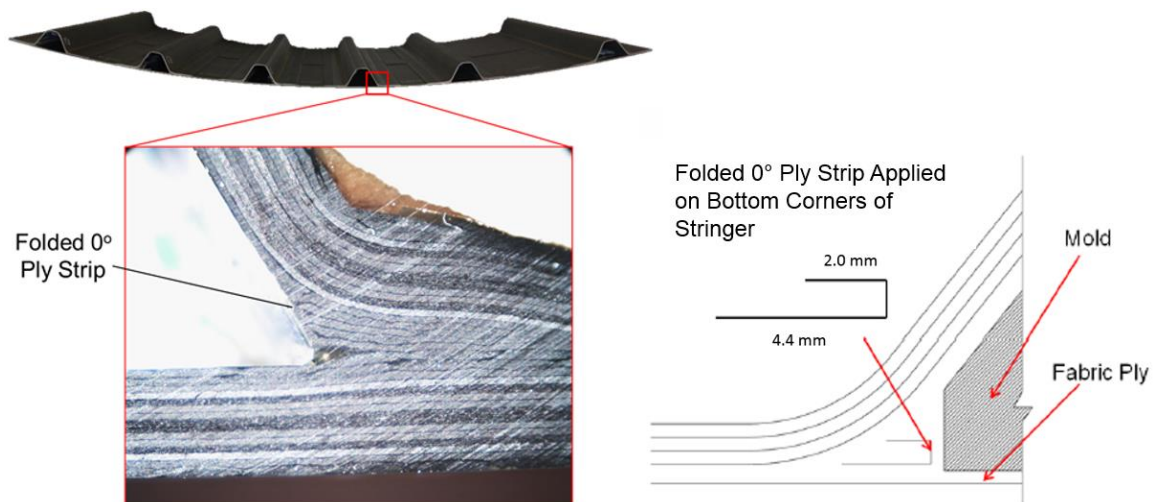


Machining the shear tie by CNC



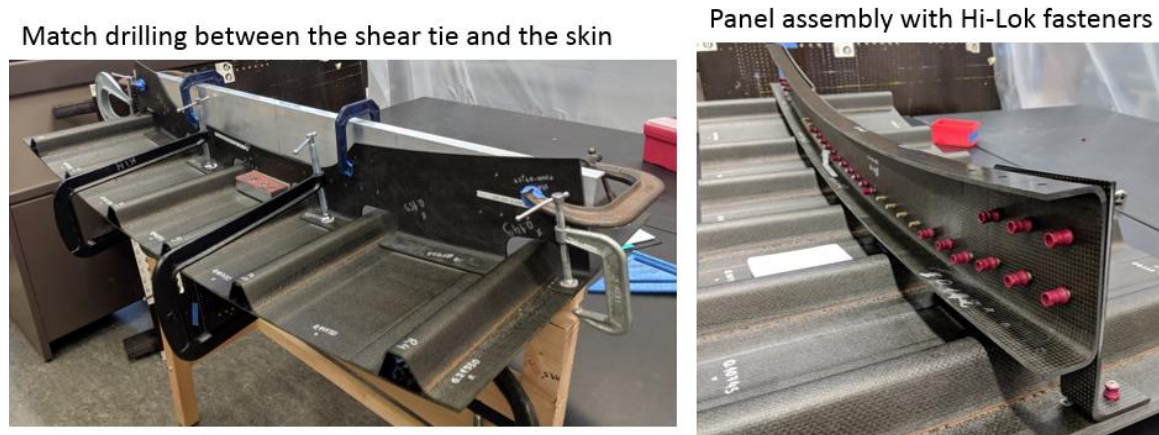
**Figure 3.23: Trimming parts using diamond saws and machining shear ties by CNC.**

The resulting stringer geometry produced consistent corner detail, as shown in Figure 3.24, where the stringer walls meet the skin and transition into flanges. This location is critical because delamination can be initiated here during the impact. To control this corner detail, a rolled strip of  $0^\circ$  unidirectional ply was inserted as shown, to achieve a more gradual radius geometry on stringer corners.



**Figure 3.24: Stringer corner detail.**

Parts were then assembled and aligned, and match-drilled to achieve final assembly with 6.35 mm (0.25 in.) Hi-Lok fasteners as shown in Figure 3.25. Hi-Lok HL19-PB-8-6 countersunk head fasteners and HL70-8 collars were used for the skin to shear tie connections, while Hi-Lok HL18-PB-8-5 protruding head fasteners and HL70-8 collars were used for the shear tie to frame assembly.



**Figure 3.25: Match drilling using jigs and panel assembly using Hi-Lok fasteners**

When conducting the layup and autoclave cure, some coupon plates were also fabricated to obtain T800/3900-2 material properties which were not available in the data sheets provided by Toray (the material manufacturer). The coupon tests were planned with the ASTM and SACMA standards as shown in Table 3.7. Firstly, the tensile, compression, and shear tests were planned to obtain the in-plane tensile, compressive, and shear strength. Secondly, the short beam shear (SBS) tests were planned to obtain the inter-laminar shear strength. Lastly, the double cantilever beam (DCB) and the end

notched flexure (ENF) tests were planned to obtain the mode 1 and mode 2 interlaminar fracture toughness.

**Table 3.7: Coupon testing plan for T800/3900-2.**

<b>Material</b>	<b>Test Type</b>	<b>Standard</b>	<b>Layup</b>
PW	DCB (Mode I Fracture)	ASTM D5528	[0] <sub>14</sub>
PW	ENF (Mode II Fracture)	ASTM D7905	[0] <sub>14</sub>
PW	SBS (Interlaminar Shear)	ASTM D2344	[0] <sub>28</sub> [45/0/-45/0] <sub>4s</sub>
PW	Tensile (1-Dir.)	ASTM D3039	[0] <sub>8</sub>
PW	Tensile (2-Dir.)	ASTM D3039	[90] <sub>8</sub>
PW	Compressive (1-Dir.)	SACMA SRM 1R-94	[0] <sub>14</sub>
PW	In-Plane Shear	ASTM D3518	[45/-45] <sub>2s</sub>
UD	DCB (Mode I Fracture)	ASTM D5528	[0] <sub>14</sub>
UD	ENF (Mode II Fracture)	ASTM D7905	[0] <sub>14</sub>
UD	Compressive (1-Dir.)	ASTM D3410	[0] <sub>8</sub>

### 3.8 EXPERIMENTAL SETUP

The 2<sup>nd</sup> generation HEWABI specimens were tested in the South Powell Laboratory at UCSD. The specimen was mounted to strong wall as shown in Figure 3.26 by boundary fixtures via bolted connections. The floor joint provides the most stiff load path zone by the interaction with the floor beam, and the aluminum lower beam provides

the representative torsional and bending stiffness. The specimens were quasi-statically and slow-dynamically loaded by the flat rubber bumper loading head, which is fixed on the vertical loading frame, under a displacement controlled shaking table stroke as illustrated in Figure 3.26. The reason of selecting the quasi-static and slow-dynamic loading test is that during the table system dynamic tests, the un-controllable dynamic overshoot and vibrations occurred at the hold period due to the high inertia of the vertical loading frame.

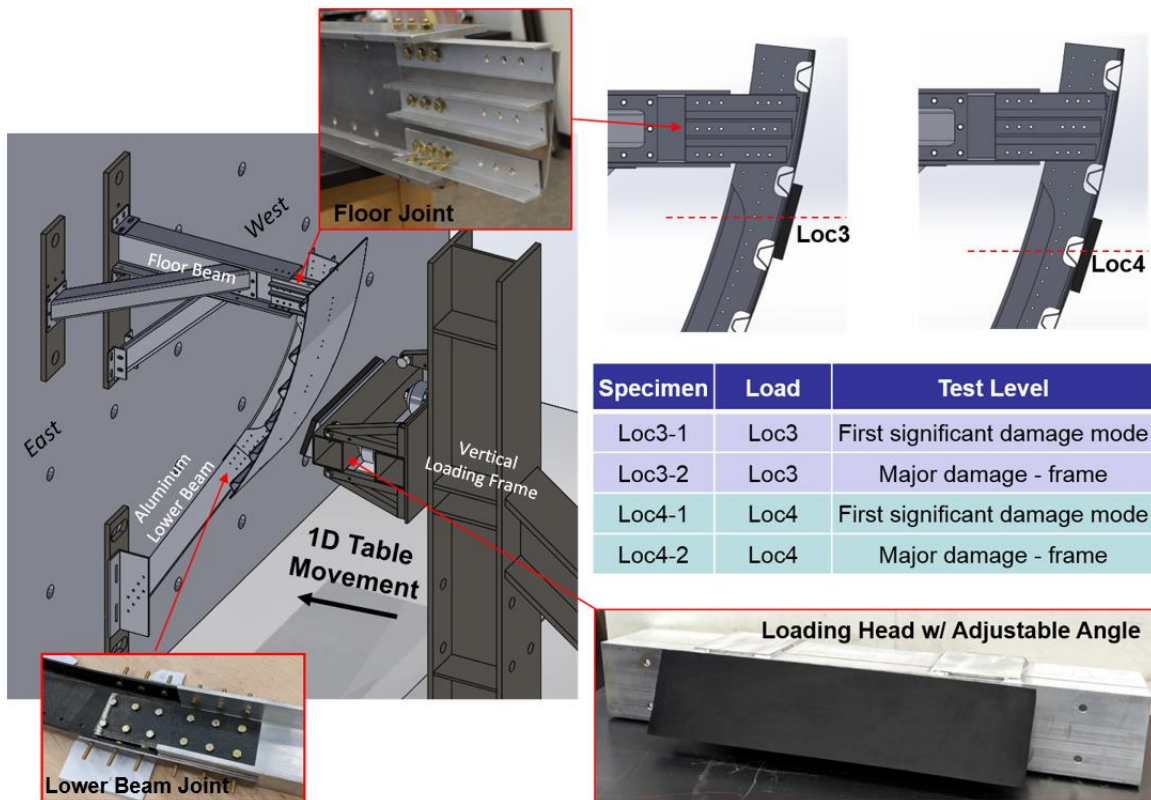
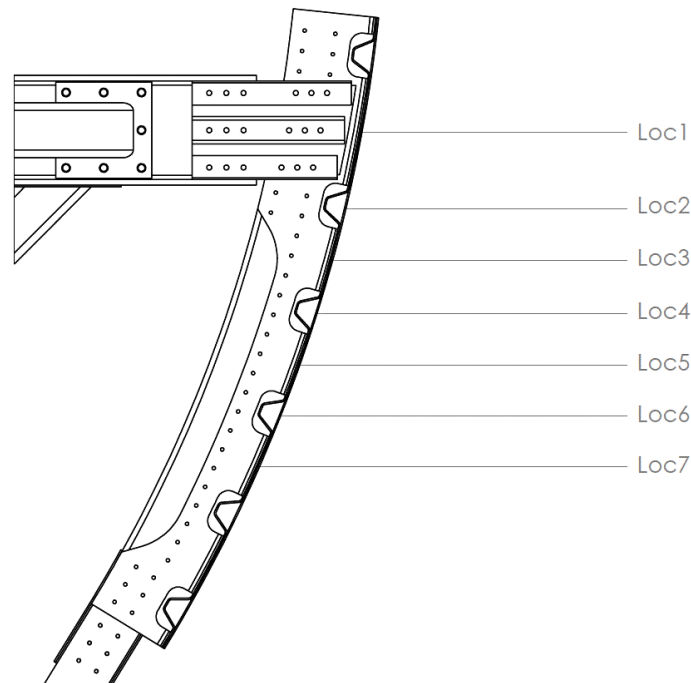


Figure 3.26: Test configuration.



The numbering definition for the loading location is related to geometric order of stringer, shear tie flange in the fuselage panel as illustrated in Figure 3.27; Loc1 is at the floor joint, Loc2 is at the stringer just below the floor joint, etc. At loading locations further down, away from the floor beam, more bending response is induced in the composite frame and shear tie. Only Loc3 and Loc4 were tested, per advice and guidance from aircraft industry research partners.



**Figure 3.27: Numbering definition of the loading location.**

### 3.8.1 LOADING CASES

Loading cases were defined to capture key phenomena and events predicted in the preliminary finite element analyses using Abaqus/explicit solver. For the first set of the

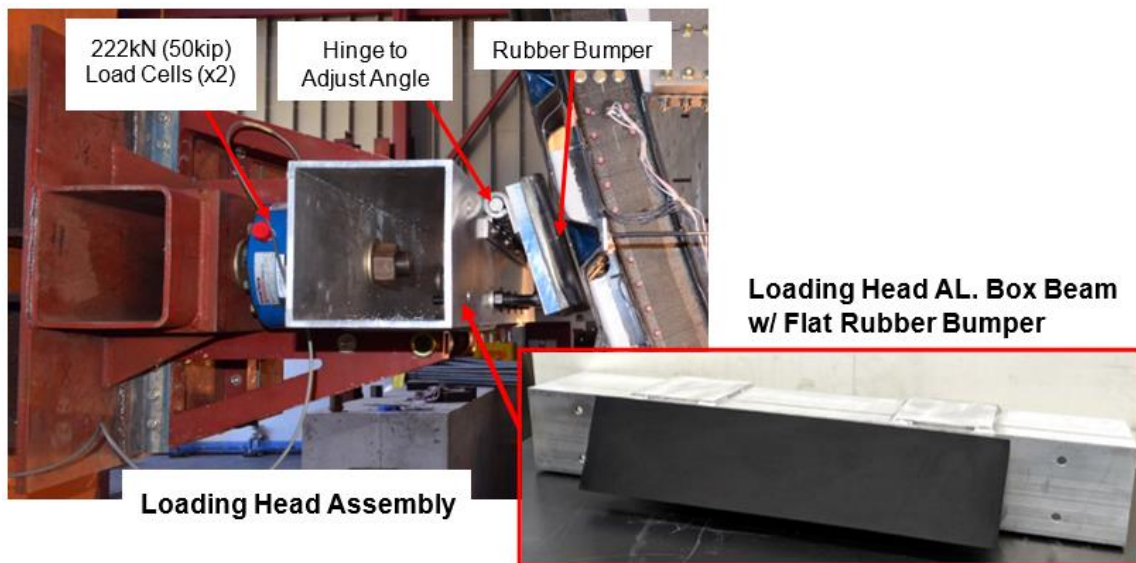
test panels, which are Loc4-1 and Loc3-1, the load level was limited to the development of first significant damage modes, mainly in the shear-tie and stringer, with a few load cycles. The loading rate was 3.0 mm/min (0.002 in/sec) representing quasi-static loading. For the second set of test panels, which are Loc4-2 and Loc3-2, the target end goal was to produce significant C-frame (and/or shear tie) damage during one load cycle. The loading rate was 61 mm/min (0.04 in/sec) and 30.5 mm/min (0.02 in/sec) for Loc4-2 and Loc3-2 respectively, representing the semi-dynamic or slow dynamic loading, and the data collecting frequency was 20Hz. The detailed loading protocol will be described in the experimental result section.

### 3.8.2 SOFT CONTACT LOADING HEAD – FLAT RUBBER BUMPER

The flat soft rubber bumper contact in the 2<sup>nd</sup> generation panel tests reflected the blunt impact against the fuselage portion which is close to the passenger floor beam and near-door of the aircraft fuselage. The flat soft rubber pad was used to decrease the uncertainties related to large deformation when using a hollow cylindrical or D-shape bumper as it is fully compressed. These issues were noted in the past 1<sup>st</sup> generation panel tests conducted by DeFrancisci and Chen [8, 11] and studies from those works have shown that the flattening of the hollow cylindrical rubber bumper does not contribute significantly to the specimen structural response. The flat rubber bumper section, representing the compressed cylindrical bumper, also has advantages in hyper-elastic FE simulation by avoiding convergence issues when fine mesh used [14].

During the specimen design stage, the initial size of rectangular flat bumper was modeled as 254 x 558.8 mm (10 x 22 in) with 50.8 mm (2.0 in) thickness. Later, to reflect the actual boundary conditions used in the laboratory tests, the bumper length was increased to have overhanging rubber pad sections along the stringer direction, which also served to prevent the specimen movement in the x-direction as shown in Figure 3.16.

During the test setup, to fit the rubber bumper to the existing loading head components, the bumper size was modified once more as shown in Figure 3.28. The 152.4 x 609.6 mm (6 x 24 in) and 25.4 mm (1.0 in) thickness Styrene Butadiene Rubber (SBR) sheet was bonded to the aluminum bumper plate, newly added to the loading head AL box beam, using the LORD 320/322 epoxy adhesive. The newly added bumper plate's angle is adjustable along the skin curvature by the hinge and heavy stop-screws as shown.



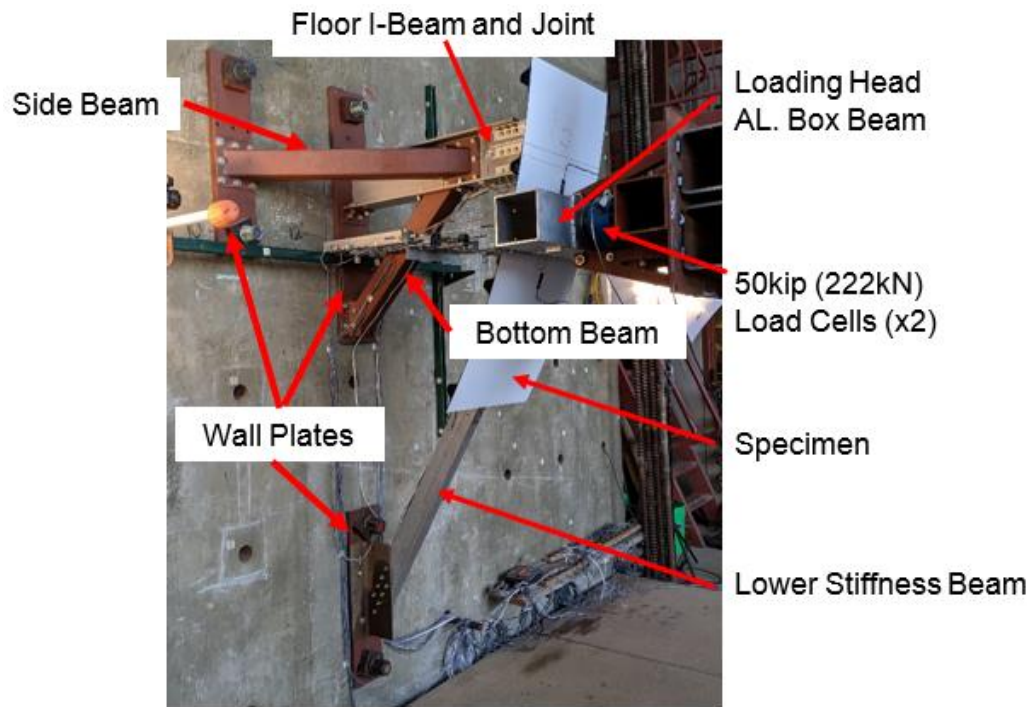
**Figure 3.28: Soft contact loading head.**

To prevent the skin-side displacement during the tests, the 50.8 mm (2 in) wider rubber bumper than the skin width was adopted to overhang the skin edges when the rubber pad is compressed. Also, to maximize friction between the contact surfaces (skin and rubber surfaces), the as-manufactured lubricant-like (mold release) coating layer of the rubber pad surface was removed by the acetone, and then, before the test, the rubber and skin surfaces were cleaned with the isopropyl alcohol. In the finite element analyses, the hyper-elastic properties verified by Chen [11] was implemented. For the improvement of rubber pad compression finite element model, additional rubber pad compression tests are needed to validate material properties updating the rubber pad modeling methodology. Also, for the friction contact definition in the finite element models, the actual friction coefficient value (0.3 was assumed in the FEA) needs to be studied further through rubber pad friction tests against the skin; The initial FEA results show good agreement between two key conditions: one model with the skin side displacement constraint and the other one with the friction contact definition.

### 3.8.3 UPPER AND LOWER FIXTURES

The mounted fixtures are shown in Figure 3.29. As described in Section 3.4, the floor beam should be very stiff and particularly not exhibit lateral or vertical deformations, thus the diagonal braces were applied, as shown. To represent target flexural stiffness interaction between the floor beam and specimen C-frame (acts as a torsional-rotational boundary condition for the C-frame), the connecting bracket plate was stiffened with L-angle and C-channel aluminum members as shown.

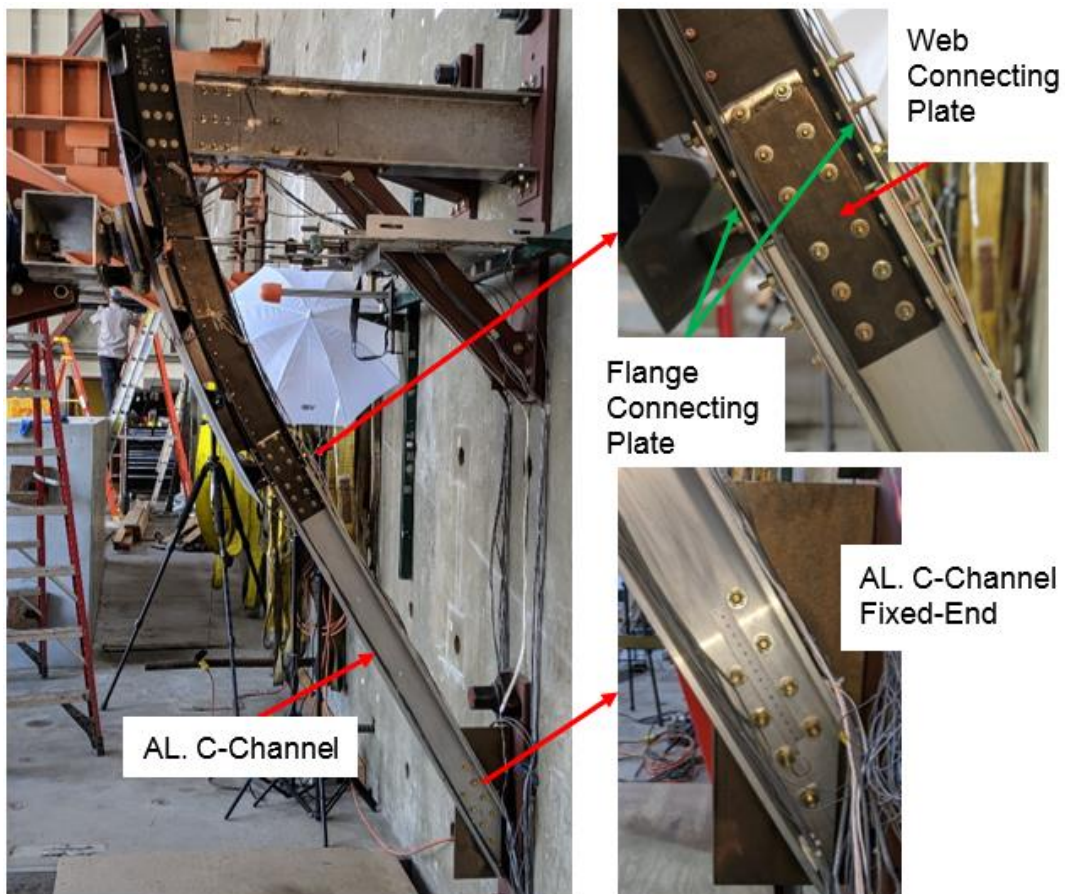
Avoidance of local failure at the bolted joints was ensured for the bearing and net-section failure by applying the maximum impact load (obtained via design-supporting FEA) directly at the floor joint. More detailed information of the floor structure and its connection can be found in Appendix C – Specimen and Fixture Drawings.



**Figure 3.29: Fixtures mounted for specimen testing.**

In Figure 3.30, the aluminum lower beam and its connections are illustrated. The AL 6061-T6 C-channel serving as the lower stiffness beam was connected by the bolted joint to provide the equivalent stiffness in the lower portion of the full barrel fuselage FE model. Bolted connections were designed based on the maximum section force from the FEA at the joint area. At the joint, the load carrying capacity of each connected member (the web and flange area of the composite C-frame and aluminum C-channel) was

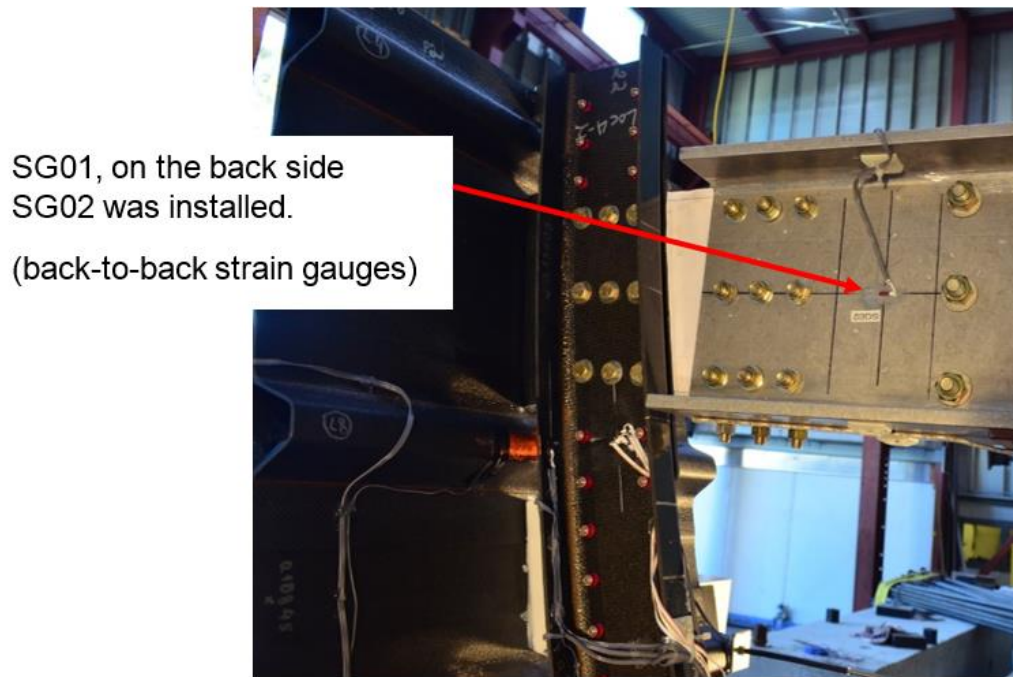
ensured for the bearing, shear-out, and net-section failure. The same design approach was applied for the fixed-end connection between the A36 steel L-angle and AL 6061-T6 C-channel. 114.30 cm (45 in) long AL C-channel was used with the section (stock) dimension, 101.6 x 57.2 mm with wall thickness 4.8 mm (4 x 2.25 in with wall thickness 0.19 in). 6.35 mm (0.25 in) diameter bolts were used to join the connecting plates.



**Figure 3.30: Aluminum C-channel lower beam and its connection.**

### 3.8.4 STRAIN GAUGES ON FLOOR I-BEAM

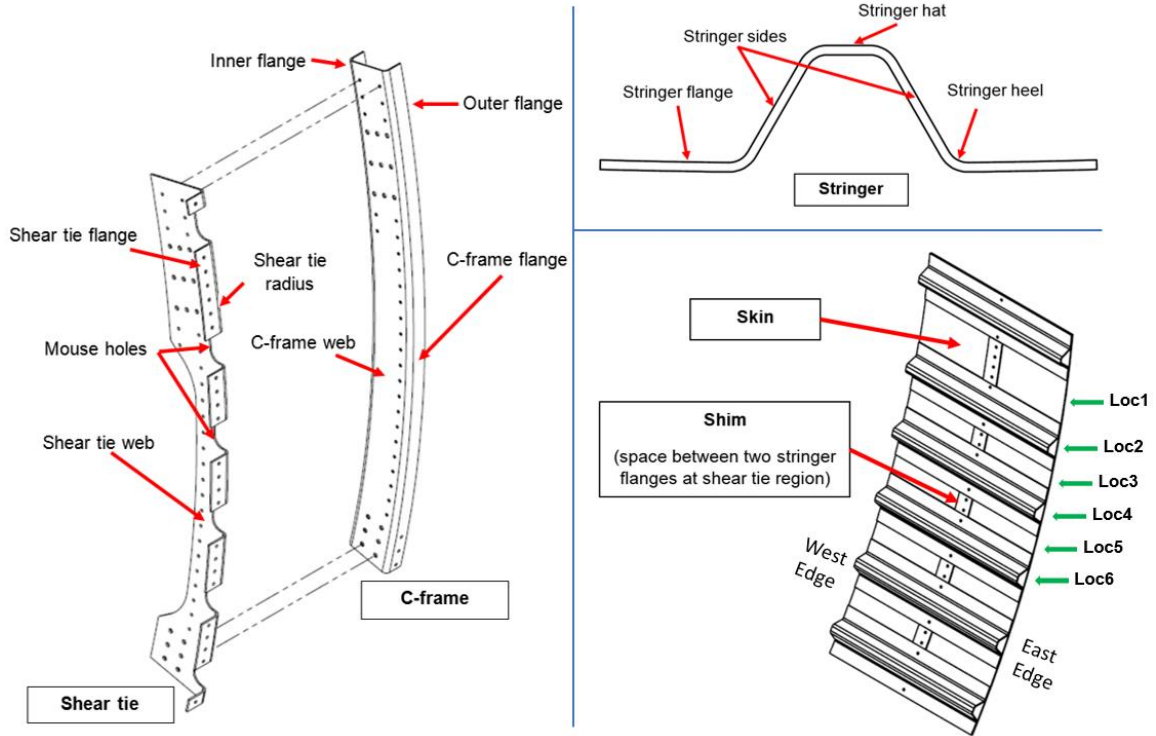
The I-beam was instrumented with back-to-back strain gauges on its web (Figure 3.31) to determine amount of load that follows the floor joint reaction load path.



**Figure 3.31: Strain gauges on I-beam.**

### 3.8.5 TERMINOLOGY OF LOCAL AREA

For the accurate description of the specific local region of each component as well as the component itself, the terminology of the local area is defined and illustrated in Figure 3.32. This terminology helps to describe the accurate critical location such as the name of strain gauge locations.



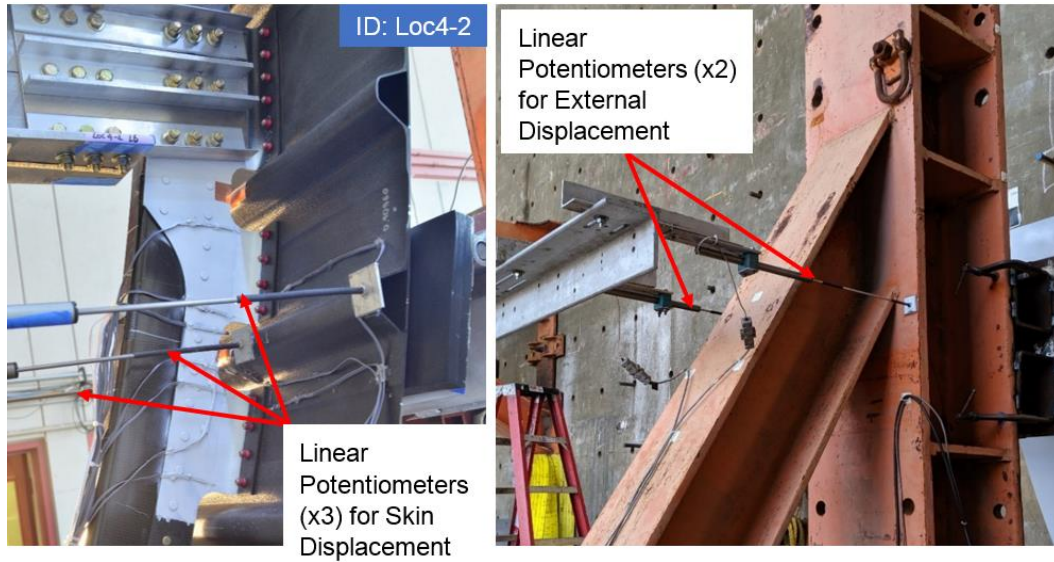
**Figure 3.32: Terminology of local areas.**

### 3.9 SPECIFIC SETUP FOR LOC4 TESTS

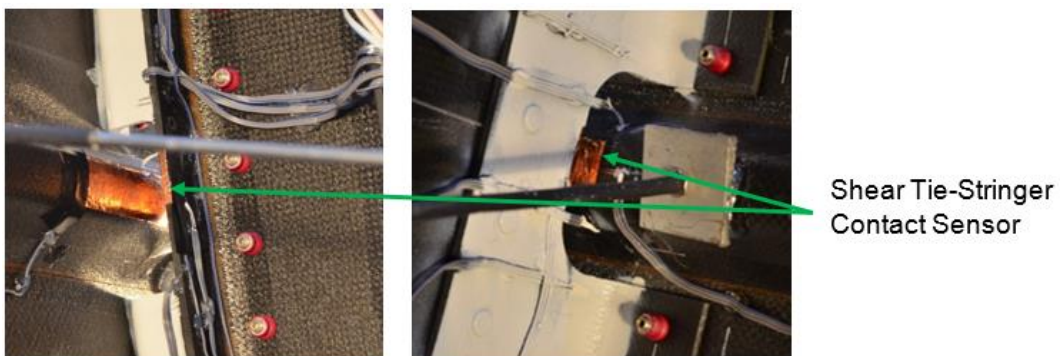
To measure the values of the displacement, load level, and strains as well as to monitor the shear tie-stringer contact occurrence, linear potentiometers (LPs), load cells (LCs), strain gauges (SGs), and contact sensors (CSs) were installed. The linear potentiometer installment example is illustrated in Figure 3.33. Three LPs, measuring the skin displacement, were attached on the stringer hat in the center, east and west edge of the specimen at Loc4. Two LPs, measuring the external displacement, were attached on the vertical loading frame at the loading position. Two load cells (called west and east LC) were assembled as part of the loading head block shown in Figure 3.28. The contact sensor was installed using thin copper tape positioned between shear tie and stringer as



shown in Figure 3.34 to indicate when the stringer makes physical contact with the shear tie during loading.



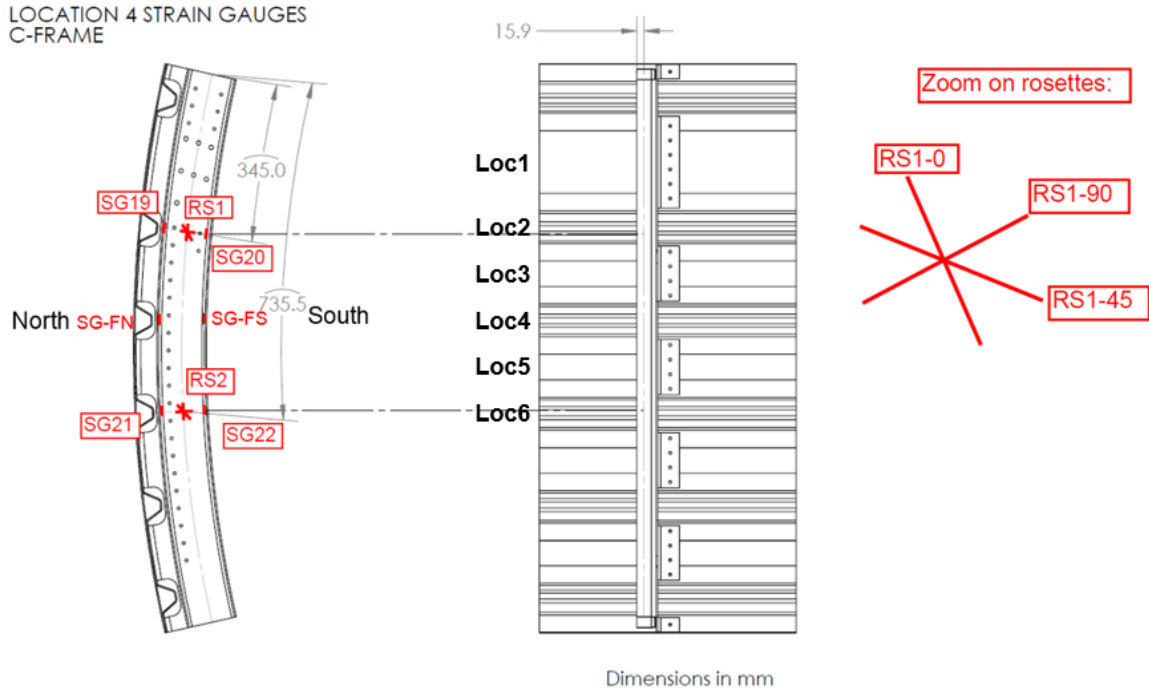
**Figure 3.33: Linear potentiometers (LPs) for the skin displacement (Left) and the external displacement (Right).**



**Figure 3.34: Contact sensor (CS) installed at Loc4.**

In Loc4 specimens, the strain was monitored by 22 strain gauges (SGs) – 20 linear strain gauges and 2 rosettes (0°, 45° and 90°). By the section force and stress analyses from the preliminary finite element models, strain gauge locations were determined based on the critical spots of high strain and to capture key events, such as shear tie radius delamination and web crack, stringer hat damage, and C-frame cracking. All SG locations are shown in Figure 3.35 to Figure 3.38.

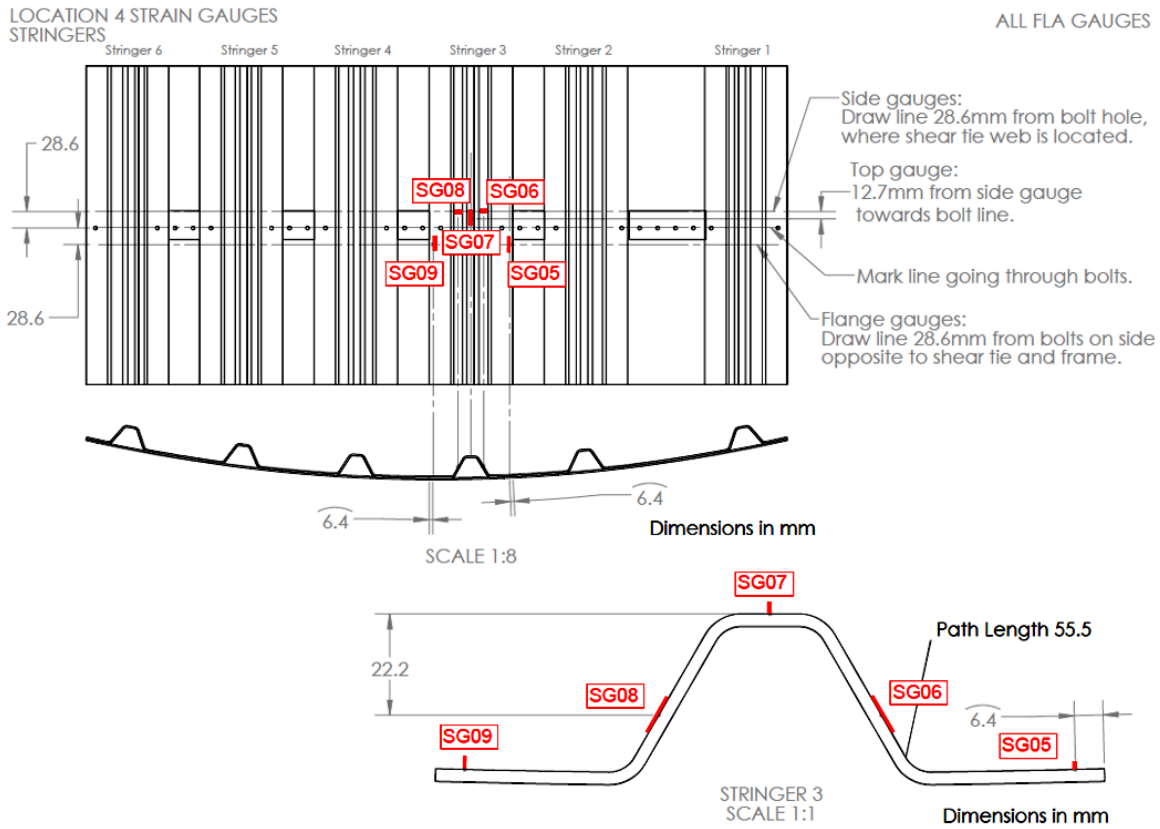
Based on the maximum section force locations in FEA and to measure the bending and shear stress level, the C-frame gauges were applied as shown in Figure 3.35. SG19-20, and SG21-22 were installed on the flange (only on the inner surface of the C-section) at Loc2 and Loc6, respectively. RS1 and RS2 were installed on the web at Loc2 and Loc6, respectively. SG-FN and SG-FS was additionally installed at Loc4 on the Loc4-2 test specimen.



**Figure 3.35: C-frame strain gauges for Loc4 specimens.**

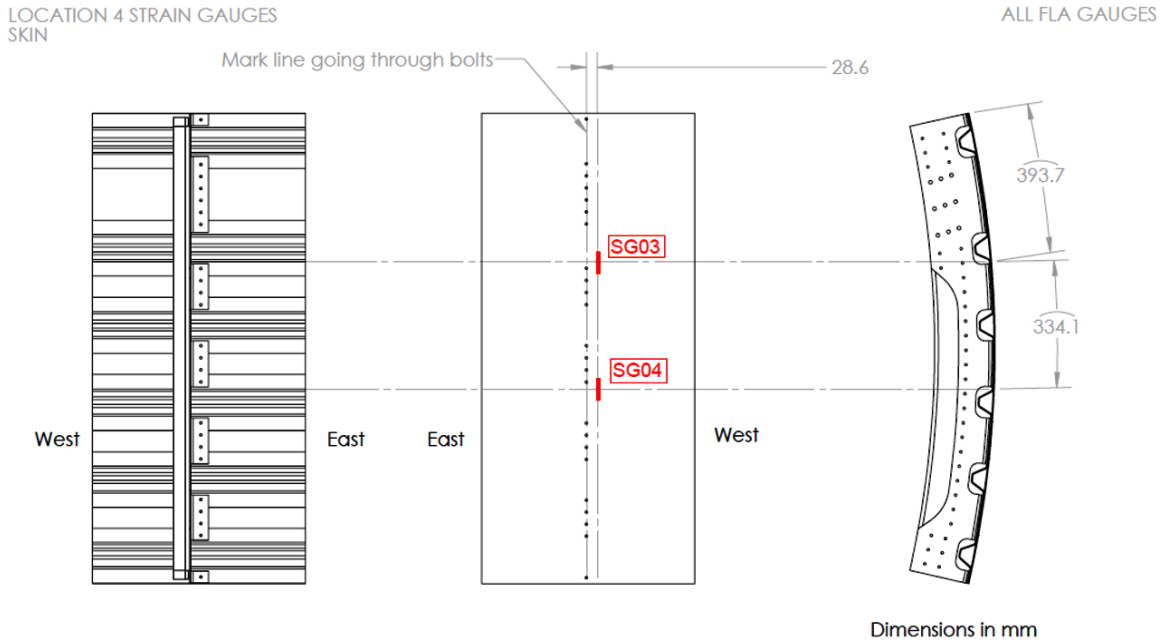
For the shear tie gauges in Figure 3.36, back-to-back gauges were installed near the shear tie radius region (SG10-11, SG12-13, SG15-16, and SG17-18) to investigate local bending behavior. Among the back-to-back gauges, SG12-13 and SG15-16 are in most critical radius region directly adjacent to the loading location. SG14 is for monitoring shear tie-stringer hat contact failure.





**Figure 3.37: Stringer strain gauges for Loc4 specimens.**

For the skin gauges in Figure 3.38, strain gauges are located at the maximum bending location of the skin.



**Figure 3.38: Skin strain gauges for Loc4 specimens.**

To record the structural behavior and internal damage initiation, and progression, four video cameras were used. Two cameras were located behind and on the east side of the specimens for the internal close-up view at Loc4, and the other two cameras were located at each side (the east side and west side) of the specimens for the overall side view.

### 3.10 EXPERIMENTAL RESULTS – LOC4

Figure 3.39 shows the east side pictures of Loc4-1 and Loc4-2 test setup in the South Powell Laboratory at UCSD. Based on the results from Loc4-1 test, in Loc4-2 test,

shear tie was painted more broadly to cover the failure area in the shear tie, thereby aiding observation of damage.



**Figure 3.39: Loc4-1 (Left) and Loc4-2 (Right) test setup in South Powell Laboratory.**

For Loc4 tests, the loading definition with six different loading levels is summarized in Table 3.8.

**Table 3.8: Loading protocol for Loc4 specimens.**

<b>Specimen ID</b>	<b>Load Level</b>	<b>Manual Load Stop Definition</b>
<b>Loc4-1</b>	Pre-test	1/4 load of expected shear tie radius delamination force by FEA
	L1	Shear tie radius delamination
	L2	Initial to moderate damage on shear tie radius region
	L3	Shear tie web - Stringer hat contact
	L4	Moderate damage on Stringer hat
	L5	Shear tie fracture
<b>Loc4-2</b>	Pre-test	1/4 load of shear tie radius delamination force in Loc4-1 tests
	L6	C-frame fracture

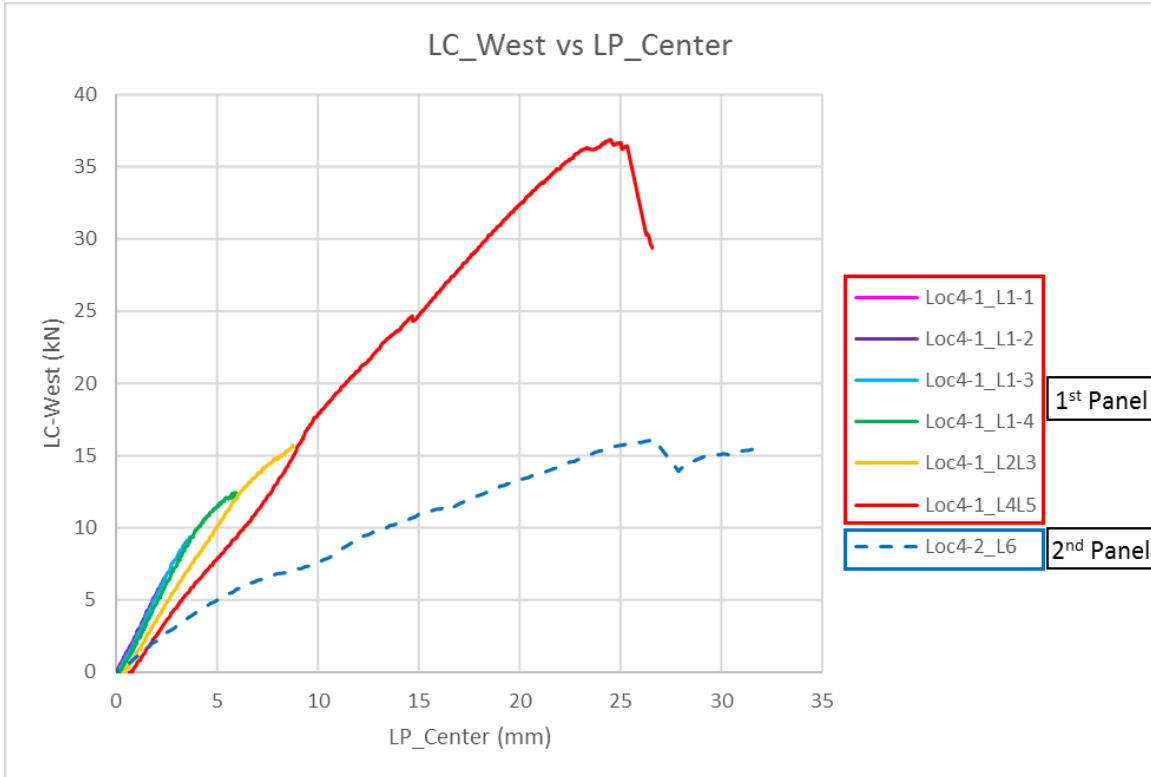
Before the main tests, the pre-test was conducted to check that all sensors were active, and data recorded correctly. For the first specimen Loc4-1, loading protocol was planned with a few load cycles, L1 to L5, correlated with the predicted key event sequence as described in Table 3.8. Loc4-1 specimen was quasi-statically loaded to observe the sequence of key event occurrence at each load level. For the second test specimen Loc4-2, the loading protocol was planned with semi-dynamic one load cycle, L6, to produce significant C-frame damage with fracture.

For each load cycle, the test was manually paused at the key events within the limit of pre-decided expected load-level and displacement. When the loading was paused, thorough visual inspection was conducted. After finishing all the tests, the major physical events are carefully assessed through the load-displacement curve, strain data, and video examination.



The original loading protocol for Loc4-1 specimen was revised in the Powell laboratory for the safety in observing internal damage events. L1 damage event is the first major cracking sound hypothetically indicating delamination initiation by the low interlaminar tensile strength of carbon/epoxy composite laminates. L1 test was stopped several times at each successive cracking sound for visual inspection at Loc4 radius section. Thus, a series of four L1 load cycles (L1-1 to L1-4) were applied. Later, major cracking sound initiation point was assessed through the visual inspection, correlated strain gauge data (strain softening) and video examination. L2 damage event is visually confirmed crack initiation and propagation at the shear tie radius region from the Loc4 mouse hole to Loc3 (upward) and Loc5 (downward) respectively. L2 event observation only relied on the video examination for safety, but L3 event is shear tie-stringer contact directly captured by the contact sensor. Thus, combined loading protocol that was actually applied is called L2L3. L4 damage event is moderate damage on the stringer hat at Loc4 which is assessed only by the correlated strain gauge data showing a large strain change. L5 damage is the visually confirmed significant shear tie damage with fracture. Thus, combined loading protocol that was applied is called L4L5.

In Loc4-2\_L6 test, the west load cell value showed the big discrepancy with the west load cell values in the previous Loc4-1 tests as shown in Figure 3.40. Since the East load cell was consistent with the prior Loc4-1 tests, an error in the West load cell was suspected.



**Figure 3.40: Discrepancy of west load cell value between Loc4-1 and Loc4-2 tests.**

In Figure 3.40, as the skin displacement, LP\_Center was measured by the linear potentiometer at the skin center shown in Figure 3.33. To verify the error in west load cell in Loc4-2\_L6 test, the strain data was checked in SG01 and SG02, which were the gages attached to the floor beam web as shown in Figure 3.31 and Figure 3.41. As shown in the plot in Figure 3.41, the average value of SG01 and SG02 between Loc4-1 and Loc4-2 tests shows very good agreement, further confirming the existence of error in the West load cell measurement. Thus, using the strain gauge data, the scale factor of the west load cell value in Loc4-2\_L6 test was estimated as described in Figure 3.42. As dividing the slope (0.148) of the linear fit of L1-1 strain-west load cell values by the slope (0.062) of the linear fit of L6 strain-west load cell values, the scale factor was

estimated as 2.408. This scale factor was applied to revise the load data in test Loc4-2\_L6.

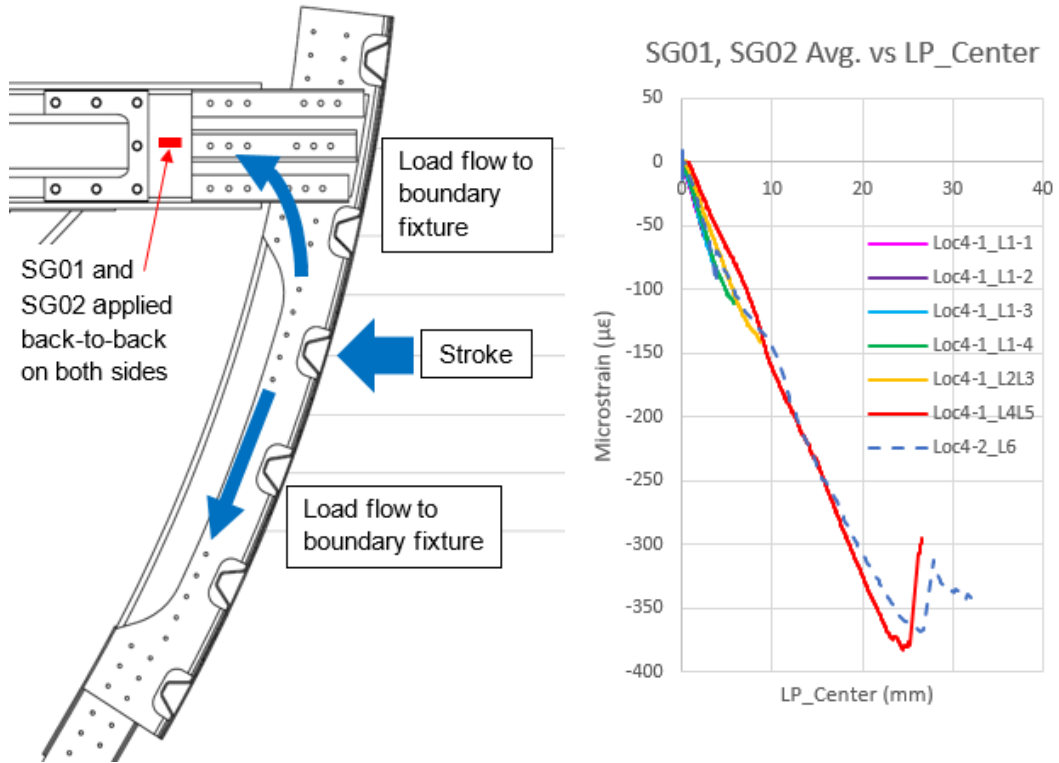
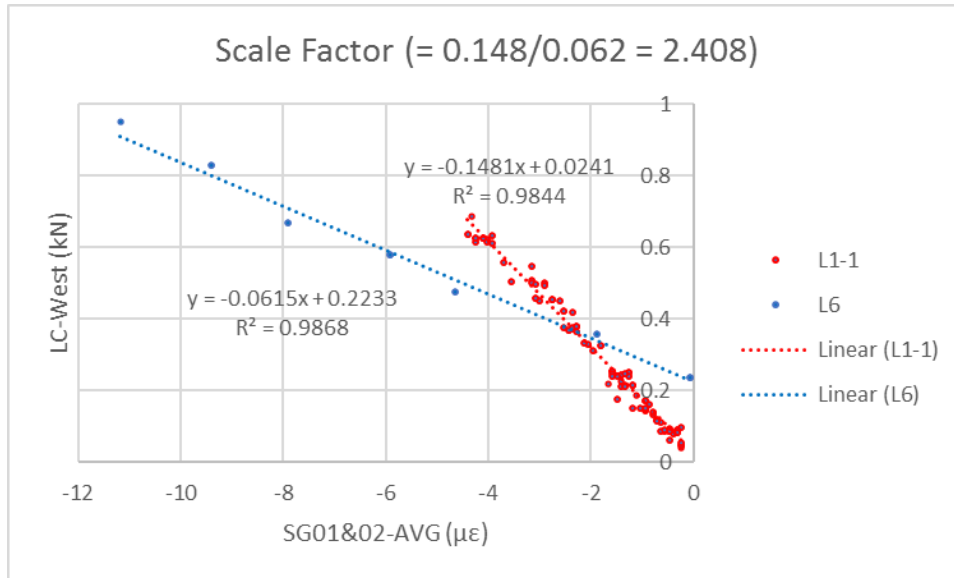
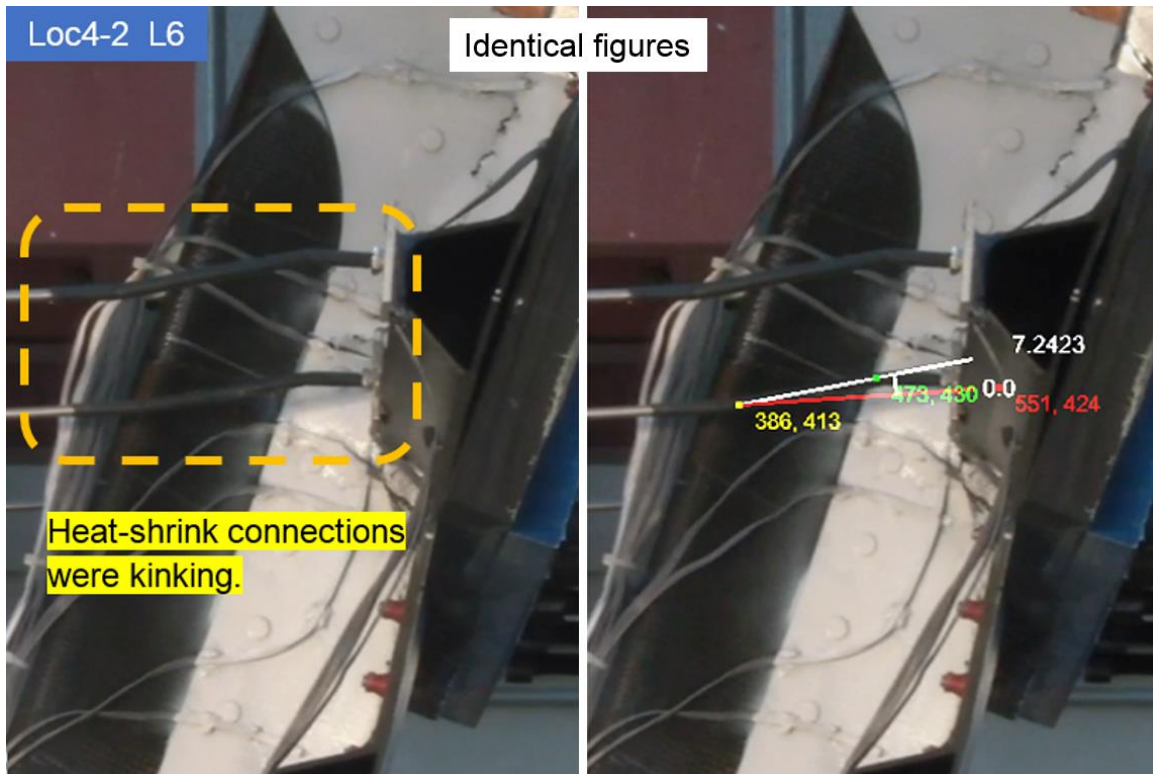


Figure 3.41: Strain gauge data check on I-beam.



**Figure 3.42: Scale factor for west load cell value of Loc4-2\_L6 test.**

During Loc4-2\_L6 test, the heat-shrink connection of the linear potentiometers (LPs) was kinking shown in Figure 3.43. In the right figure, as measuring the degree between the red line aligned with the LP rod and the white line aligned with the kink line by two yellow and green dots, the max kinking degree of LP\_Center is estimated as  $7.24^\circ$  at the C-frame failure event with maximum stroke. The value of cosine  $7.24^\circ$  is 0.992. Thus, the kinking phenomenon causes maximum 0.8% error in the displacement data which is small enough to be negligible.

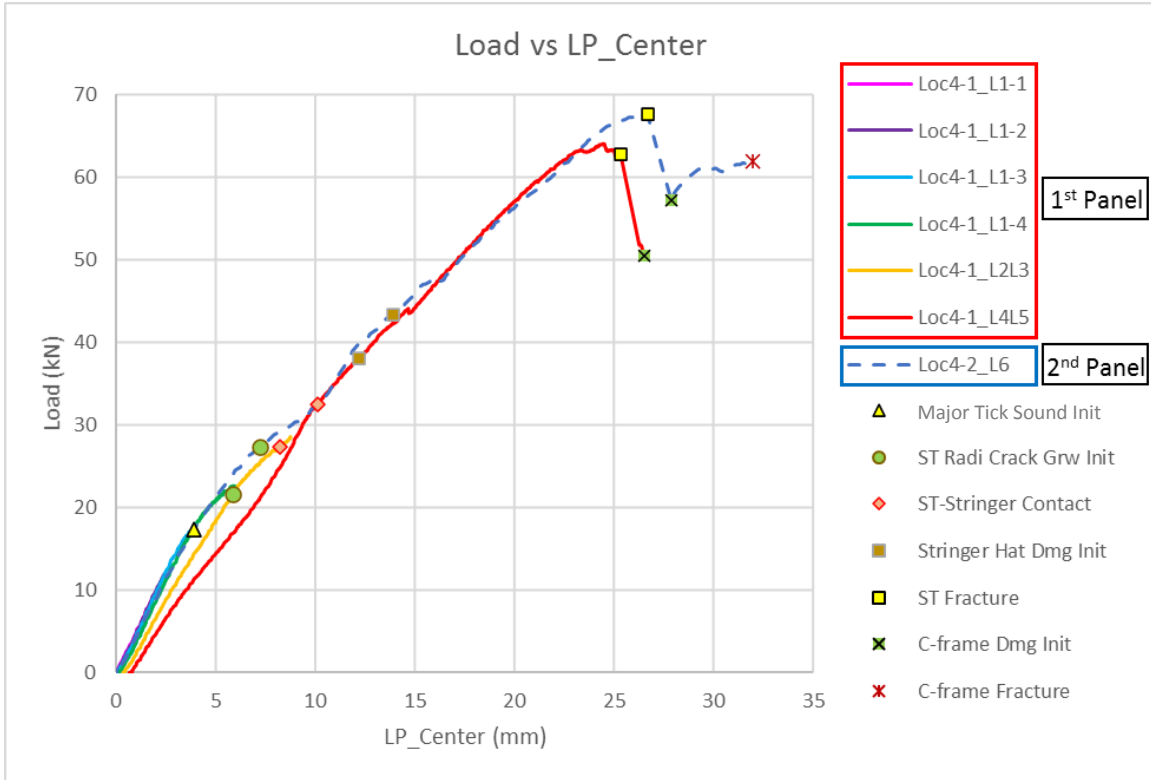


**Figure 3.43: LP connection kinking of Loc4-2\_L6 test at C-frame failure.**

### 3.10.1 LOAD-SKIN DISPLACEMENT CURVE AND KEY EVENT SUMMARY

The load-skin displacement curves for both Loc4-1 and 4-2 specimens are shown in Figure 3.44 with main events associated with key failure modes noted. For the 1<sup>st</sup> panel (Loc4-1), under successive increasing loading, the initial stiffness in each load cycle is observed to soften, as indicated by the decreasing initial slope. L6 loading was applied for the 2<sup>nd</sup> panel (Loc4-2) in one single load cycle up to the development of significant C-frame damage with fracture. The 2<sup>nd</sup> panel's key event sequence was assessed mainly by the video and strain data examination. In both tests, stiffness is observed to decrease at

each key damage event. Shear tie and C-frame fracture causes a big load drop and is the final failure mode.



**Figure 3.44: Load vs center skin displacement for all Loc4 tests.**

The key physical event information is summarized in Table 3.9. The identical key events and event sequence are observed in both Loc4-1 and Loc4-2 tests. Comparison of the load level at each key event, between Loc4-1 and Loc4-2 tests, shows 7% to 20 % difference. The maximum difference (16% to 20%) is shown between events in Loc4-1\_L2L3 and Loc4-2\_L6. Considering repeated loading and unloading from L1 to L5, especially of L1-4, in Loc4-1 tests inducing accumulated damages in Loc4-1 specimen,

the load level between Loc4-1 and Loc4-2 tests is quite close overall. Therefore, these tests are roughly equivalent to each other.

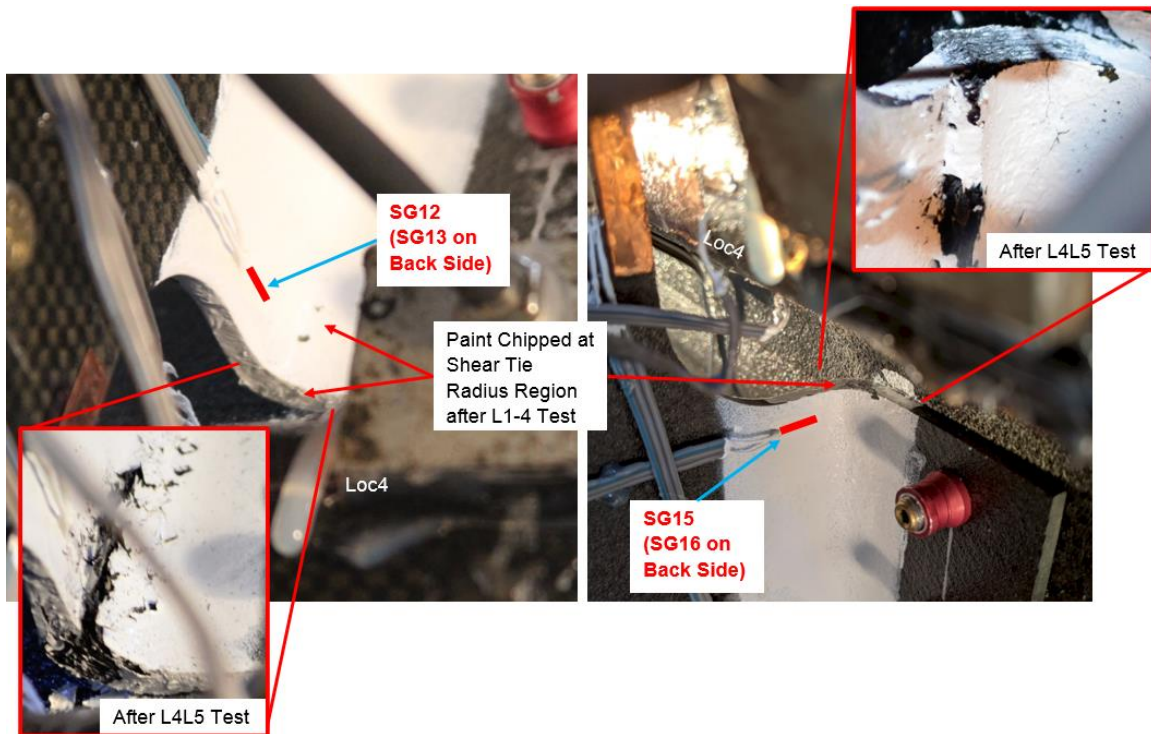
**Table 3.9: Loc4 key phenomena.**

Loc4-1			Loc4-2			Key Event
Load Cycle	LP_C (mm)	Load (kN)	Load Cycle	LP_C (mm)	Load (kN)	
L1-4	Not clearly captured		L6	3.92	17.36	Initial major cracking sound (Shear tie radius delamination)
L2L3	5.88	21.62		7.22	27.29	Crack growth init on shear tie radius region
	8.22	27.27		10.12	32.47	Shear tie web - Stringer hat contact
L4L5	12.17	38.10		13.91	43.38	Stringer hat damage initiation
	25.33	62.81		26.68	67.61	Shear tie web fracture
	26.52	50.47		27.89	57.14	C-frame damage initiation
-	-	-		31.99	61.97	C-frame fracture

### 3.10.2 CRACKING INITIATION – SHEAR TIE RADIUS DELAMINATION

The first major cracking sound was assumed delamination initiation due to the low interlaminar tensile strength of 42.29 MPa to 51.82 MPa for carbon/epoxy composite materials [11]. During the series of L1 loading, delamination of the shear tie radius region at the lower and upper side of Loc4 mouse hole was assessed by the combination of audible cracking sound, visual inspection, and strain data from back-to-back strain gauges (SG12-13 and SG15-16) near the radius region. The location of the gauges is shown in Figure 3.36 and Figure 3.45.

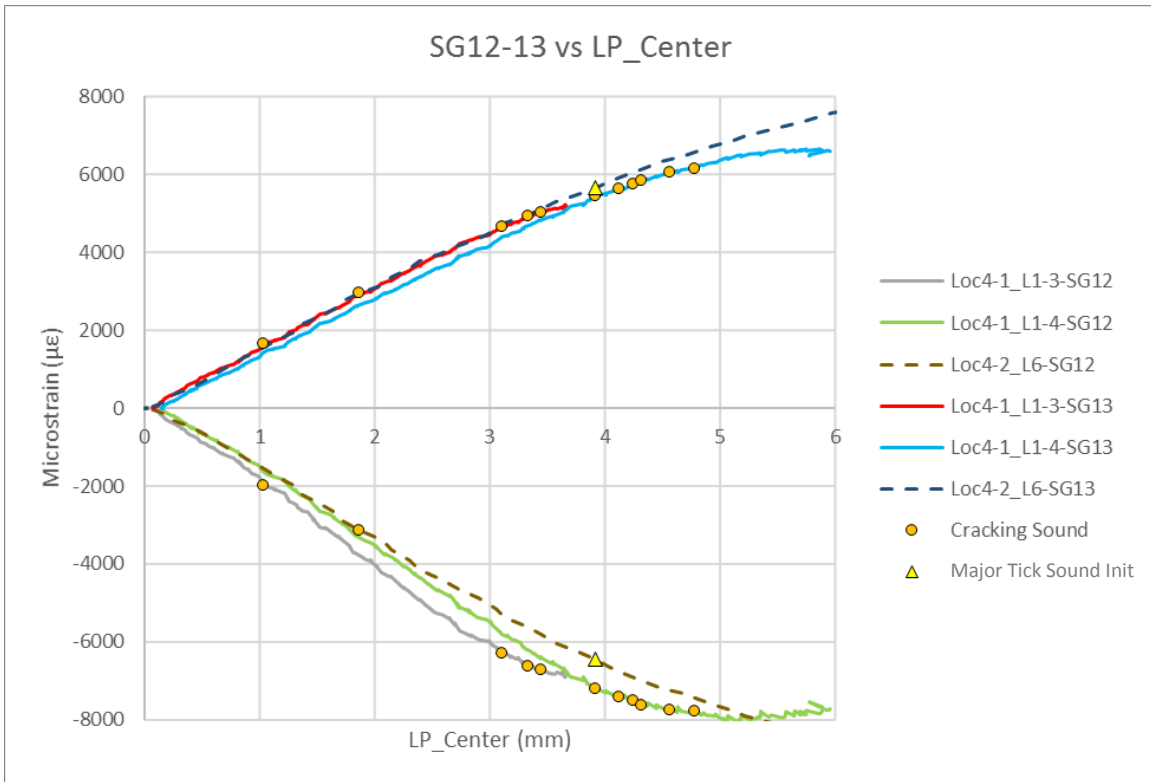
For Loc4-1 tests, the paint chipping point from the radius region was not clearly captured by the video record, but after Loc4-1\_L1-4 test, through the visual inspection, the paint chipping was observed at the radius region of the lower and upper side of Loc4 mouse hole as shown in Figure 3.45. For the Loc4-2\_L6 test, this initial damage mode was assessed with the video record, capturing the paint chipping at Loc4 upper mouse hole section. Figure 3.45 shows additional close-up view after Loc4-1\_L4L5 test capturing shear tie radius delamination and fiber crushing damage by the direct compressive load from the bumper.



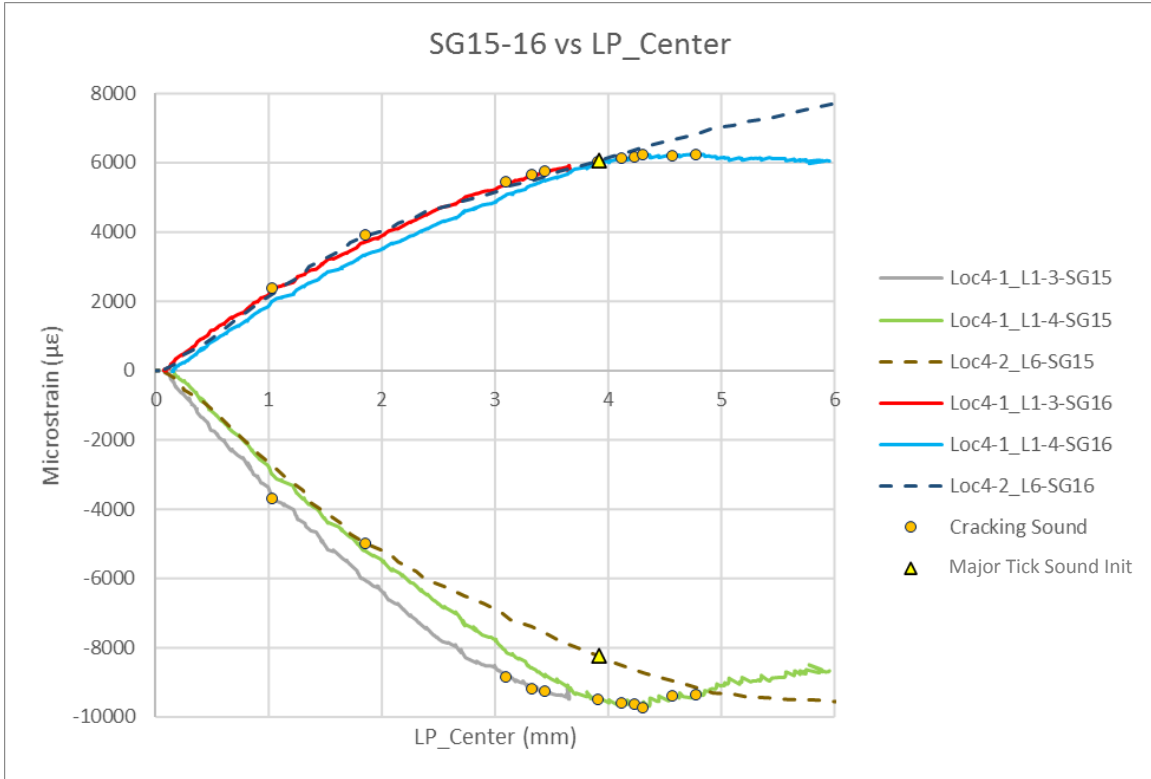
**Figure 3.45: Paint chipping and delamination at shear tie radius region at upper (Left) and lower (Right) side of Loc4 mouse hole after Loc4-1\_L1-4 with close-up view after Loc4-1\_L4L5.**



All strain data were examined in this stage. The strain data from the back-to-back strain gauges, SG12-13, and SG15-16, showed the highest strain level among all strain gauges. As shown in Figure 3.46 and Figure 3.47, the linear slope of strain curve starts to be softened with successive cracking sound events. The cracking sound events are highlighted with orange-colored circles in both Loc4-1 and Loc4-2 tests. For the Loc4-2\_L6 test, initial cracking sound events are highlighted with orange-colored circles, then the first major cracking sound is highlighted with a yellow triangle based on the video record examination. After the final mark of the cracking sound including the major tick sound marks in the plots, cracking sound keeps occurring up to the moment of final catastrophic damage. In the strain plots, the bending behavior of the region is also captured showing the negative strain from SG12, SG15 and the positive strain from SG13, SG16.



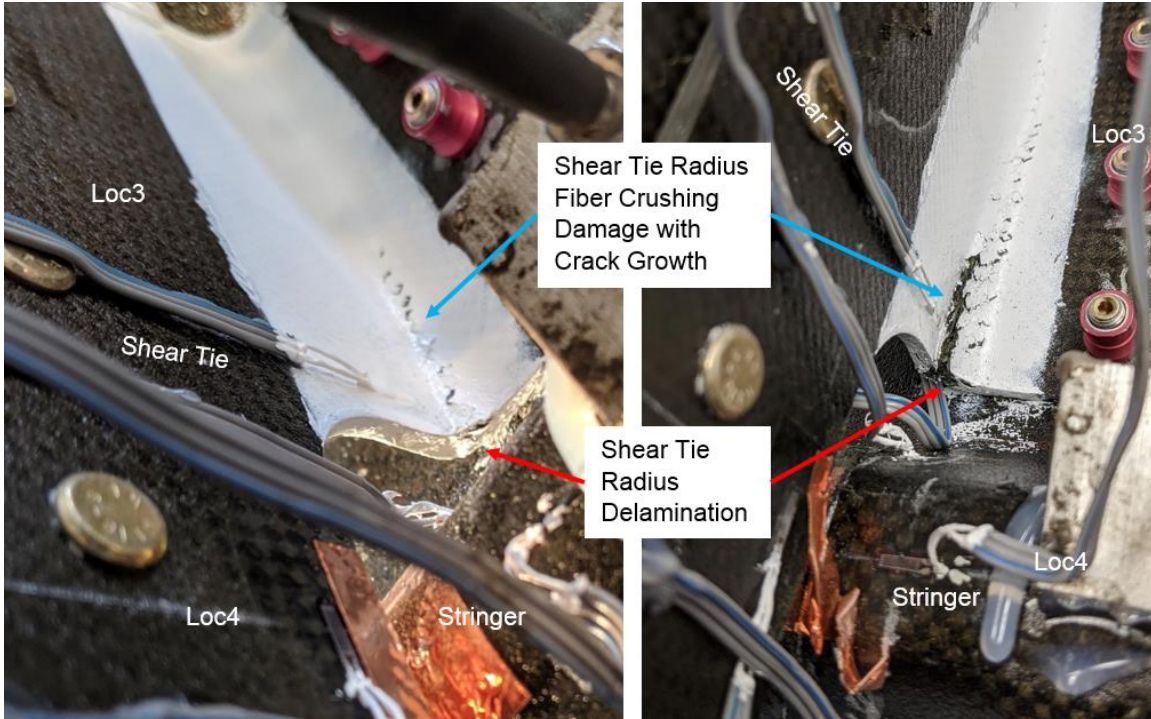
**Figure 3.46: Strain curves from SG12-13 back-to-back gauges near shear tie radius region at upper side of Loc4 mouse hole.**



**Figure 3.47: Strain curves from SG15-16 back-to-back gauges near shear tie radius region at lower side of Loc4 mouse hole.**

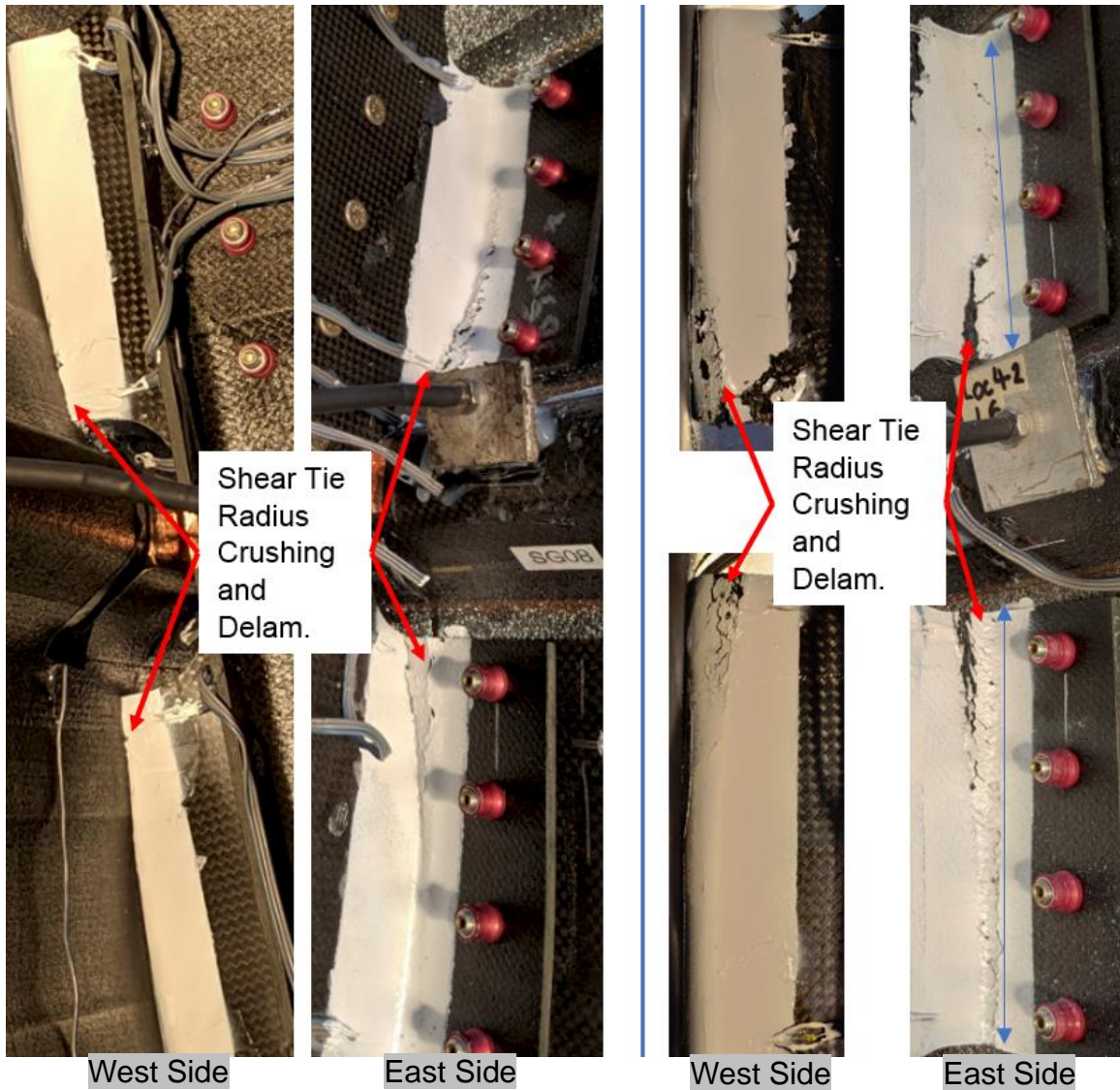
### 3.10.3 CRACK GROWTH ALONG THE SHEAR TIE RADIUS AND SHEAR TIE WEB-STRINGER HAT CONTACT

In Figure 3.48, after Loc4-1\_L2L3 and L4L5 tests, based on visual inspection, the shear tie radius delamination and fiber crushing damage are captured along the shear tie radius region showing crack growth due to the increasing direct compressive load from the bumper at Loc4.



**Figure 3.48: Shear tie radius delamination and fiber crushing damage with crack growth after Loc4-1\_L2L3 (Left) and L4L5 (Right) test.**

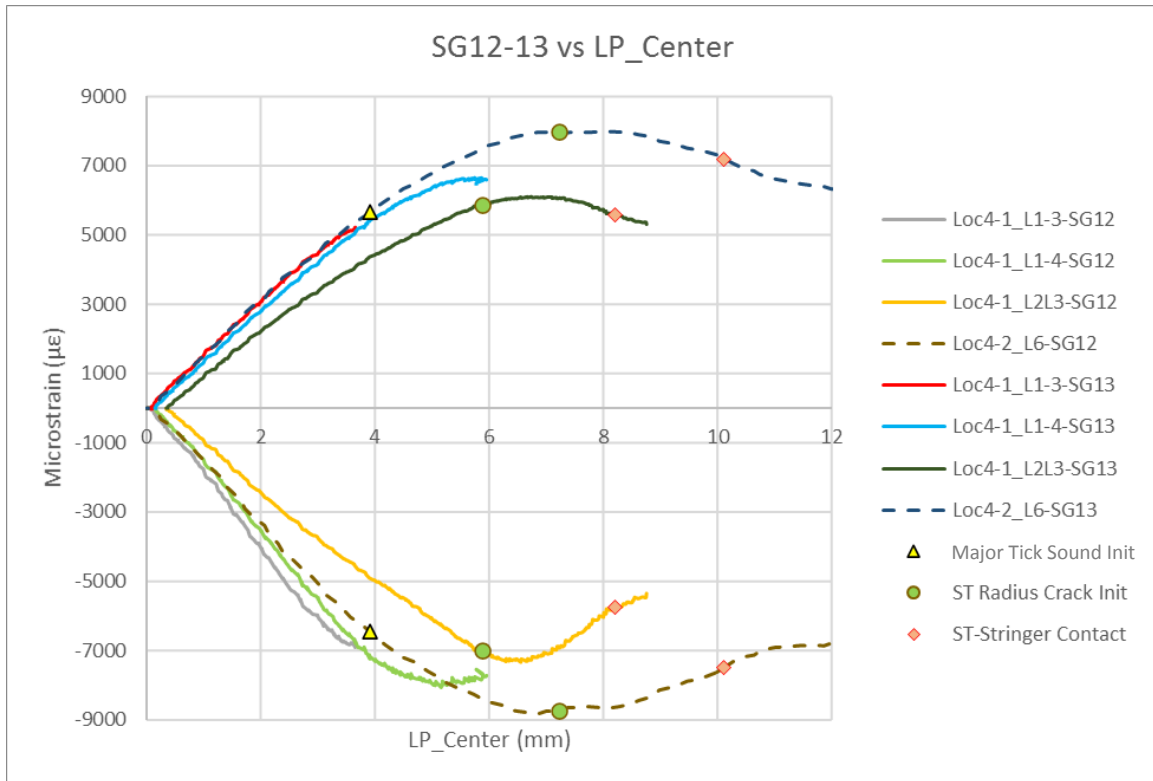
In Figure 3.49, the shear tie radius crushing was captured at the maximum load in Loc4-1\_L4L5, and after Loc4-2\_L6 test as well. During Loc4-1\_L2L3 and Loc4-2\_L6 loading, the crack growth initiated from Loc4 shear tie radius section and grew upward and downward along the shear tie radius region, as observed by the video examination.



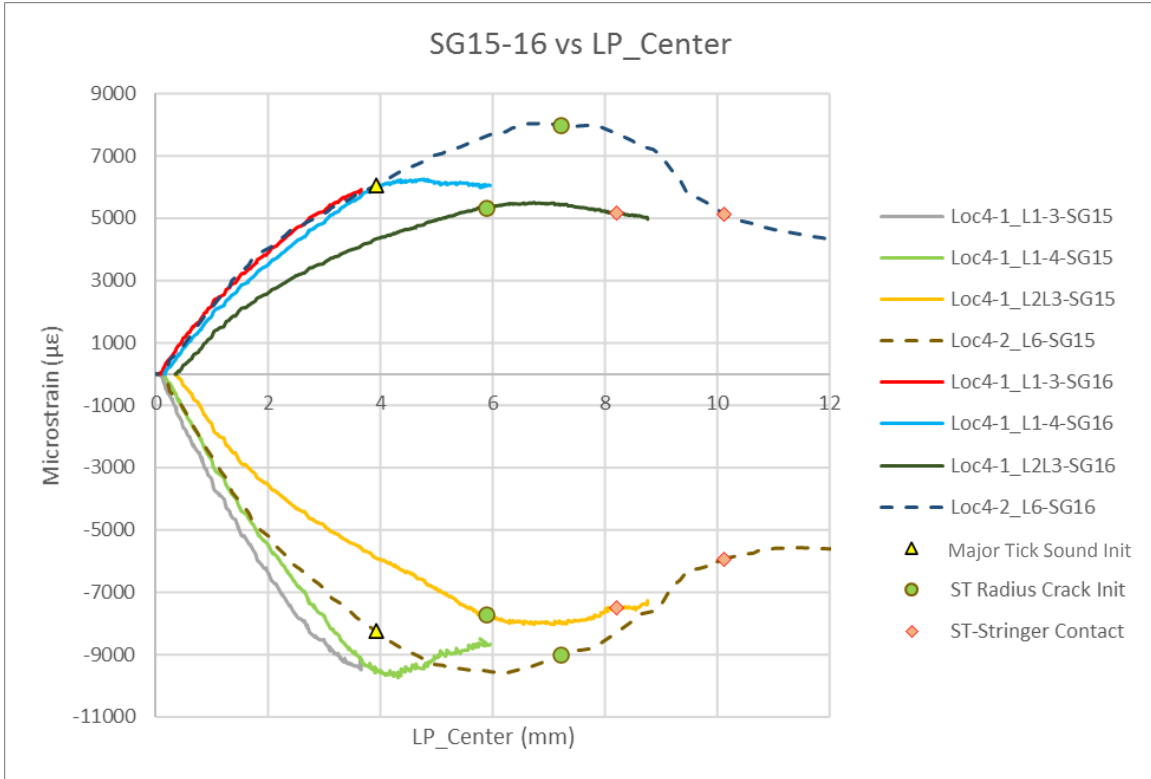
**Figure 3.49: Shear tie radius delamination and fiber crushing damage with crack growth at maximum load of Loc4-1\_L4L5 (Left) and after Loc4-2\_L6 (Right) test.**

All strain data out to the final failure event were examined in this stage. The strain data from the back-to-back strain gauges, SG12-13, and SG15-16, showed the highest strain level. The strain curves in Figure 3.50 and Figure 3.51, show the crack growth initiation point, marked with a green circle, which is near the maximum strain value in the curves. Also, the contact between shear tie web and stringer hat at Loc4 was detected

by the contact sensor in L2L3 and L6 loading notified with a red diamond in Figure 3.50 and Figure 3.51.

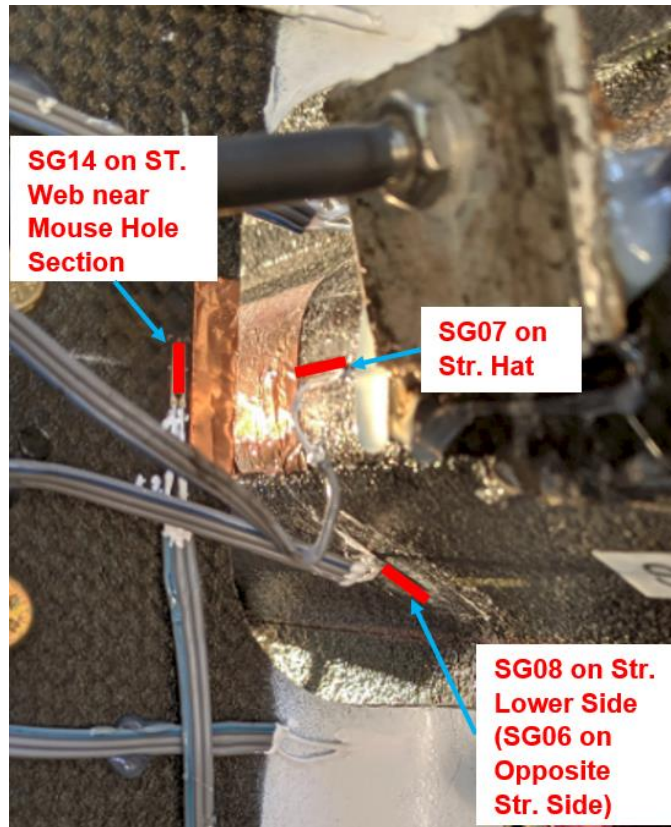


**Figure 3.50: Strain curves from SG12-13 back-to-back gauges near shear tie radius region at upper side of Loc4 mouse hole.**



**Figure 3.51: Strain curves from SG15-16 back-to-back gauges near shear tie radius region at lower side of Loc4 mouse hole.**

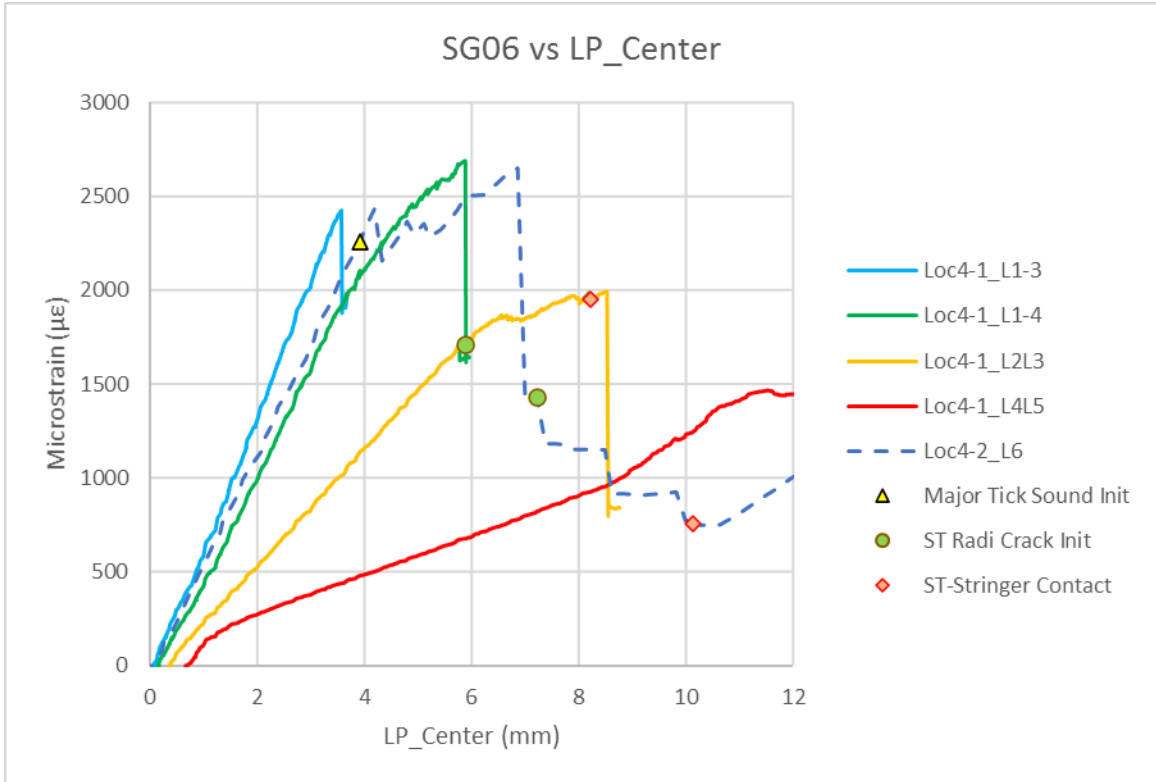
The locations of SG06, SG08, SG07, and SG14 are on the stringer upper and lower sides, stringer hat, and shear tie web near the mouse hole section, respectively, at Loc4 as shown in Figure 3.32, Figure 3.37, and Figure 3.52.



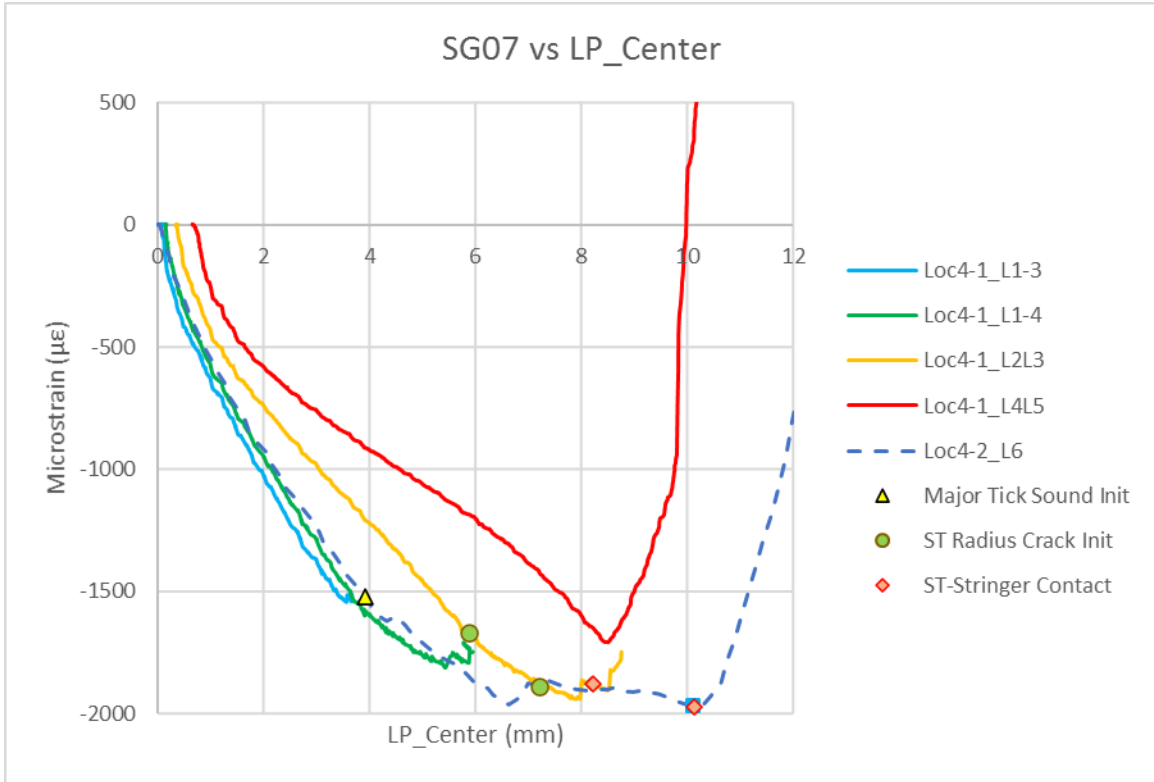
**Figure 3.52: Strain gauge location (SG06, SG07, SG08, and SG14) at Loc4.**

The shear tie radius crack growth occurred upward and downward from Loc4 is also captured in SG06 and SG07 data. In Figure 3.53 and Figure 3.54, at the shear tie radius crack initiation points, highlighted with a green circle. The large strain drop abruptly occurs as the stress was released at the locations on stringer while shear tie radius crack grows accompanying with the shear tie radius crushing damage.



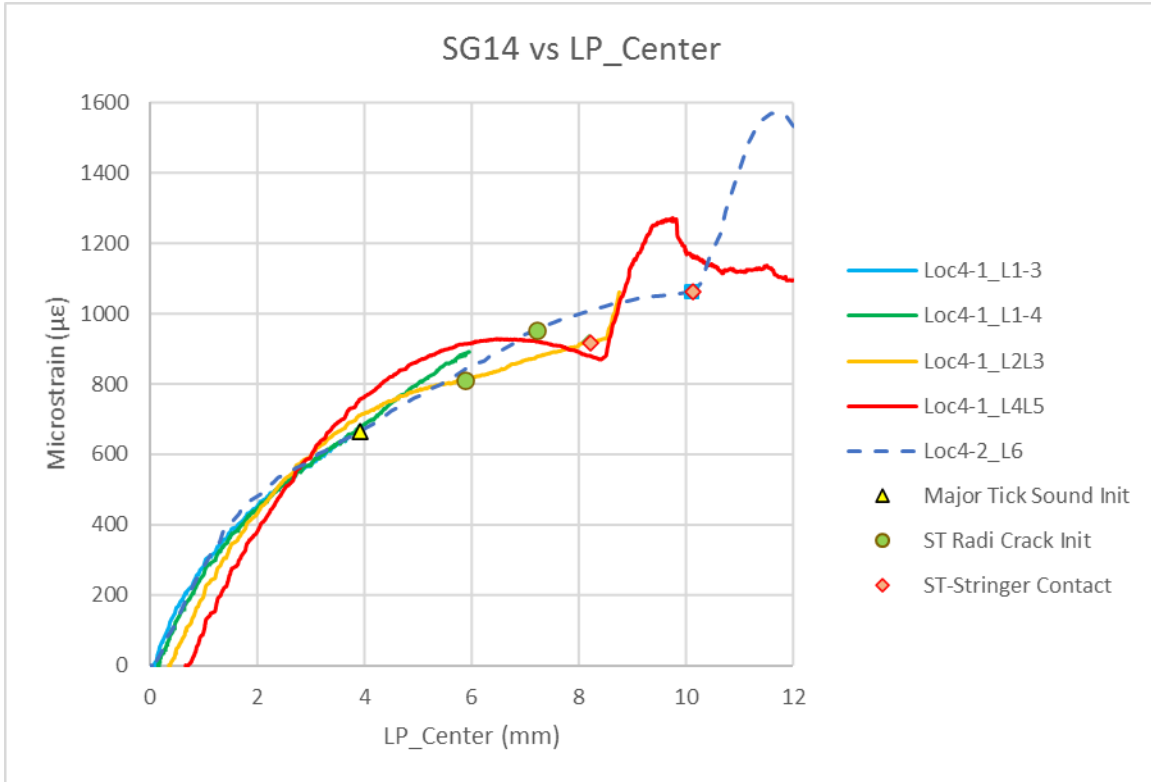


**Figure 3.53: Strain curves from SG06 installed on stringer upper side at Loc4.**



**Figure 3.54: Strain curves from SG07 installed on stringer hat at Loc4.**

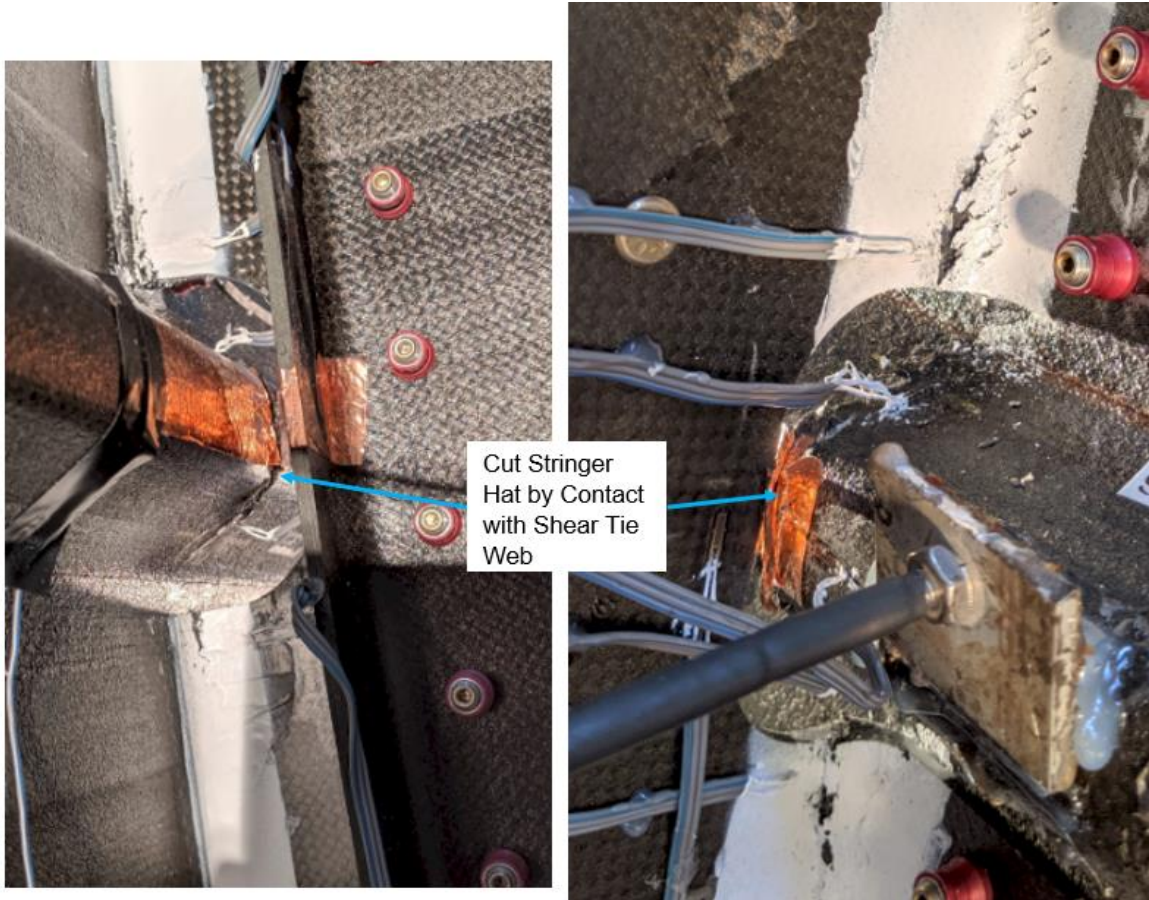
The nearest strain gauges from the contact sensor at Loc4 are SG07 and SG14. The locations of SG07, and SG14 are on the stringer hat, and shear tie web near the mouse hole section, respectively, at Loc4 as shown in Figure 3.52. The contact between shear tie web and stringer hat (indicated by contact sensor) is highlighted in the SG07 and SG14 strain curves. As shown in Figure 3.54 and Figure 3.55, from the contact point, marked with a red diamond, the strain starts to increase stiffly due to the local high contact stress.



**Figure 3.55: Strain curves from SG14 installed on shear tie web near mouse hole section at Loc4.**

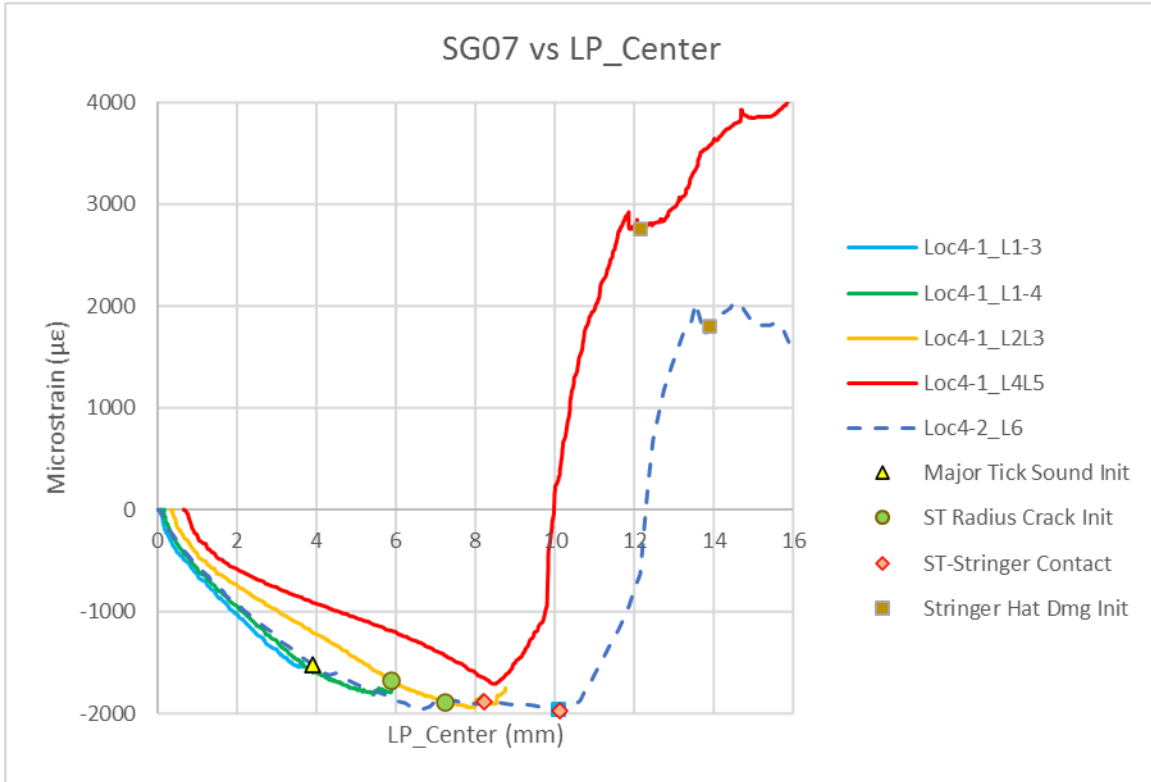
### 3.10.4 STRINGER HAT DAMAGE INITIATION AT LOC4 BY CONTACT

During L4L5 loading, due to the shear tie-stringer hat contact, stringer damage occurred with fiber failure. Figure 3.56 shows the cut stringer hat after Loc4-1\_L4L5 test. The stringer hat damage initiation was estimated in the strain data on stringer hat, and stringer side region (SG07, and SG06-08) shown in Figure 3.57 and Figure 3.58 marked with a brown square.



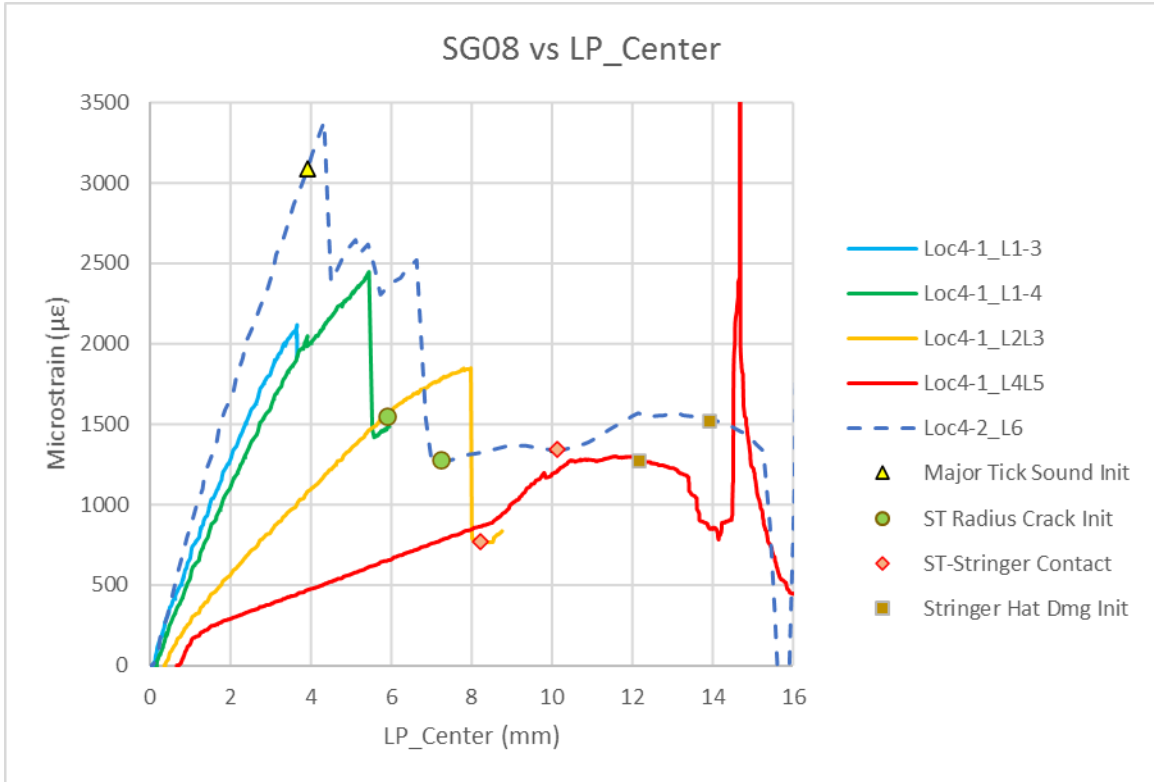
**Figure 3.56: Stringer cut by the shear tie web contact after Loc4-1\_L4L5.**

The locations of SG07, and SG08 are on the stringer hat and lower side, respectively, at Loc4 as shown in Figure 3.52. In Figure 3.57 (SG07 installed on Stringer hat at Loc4), the stringer hat damage initiation, marked with a brown square, shows a drop in strain as the local stress is released due to cutting of the stringer hat by shear tie web penetration.



**Figure 3.57: Strain curves from SG07 installed on Str. hat at Loc4.**

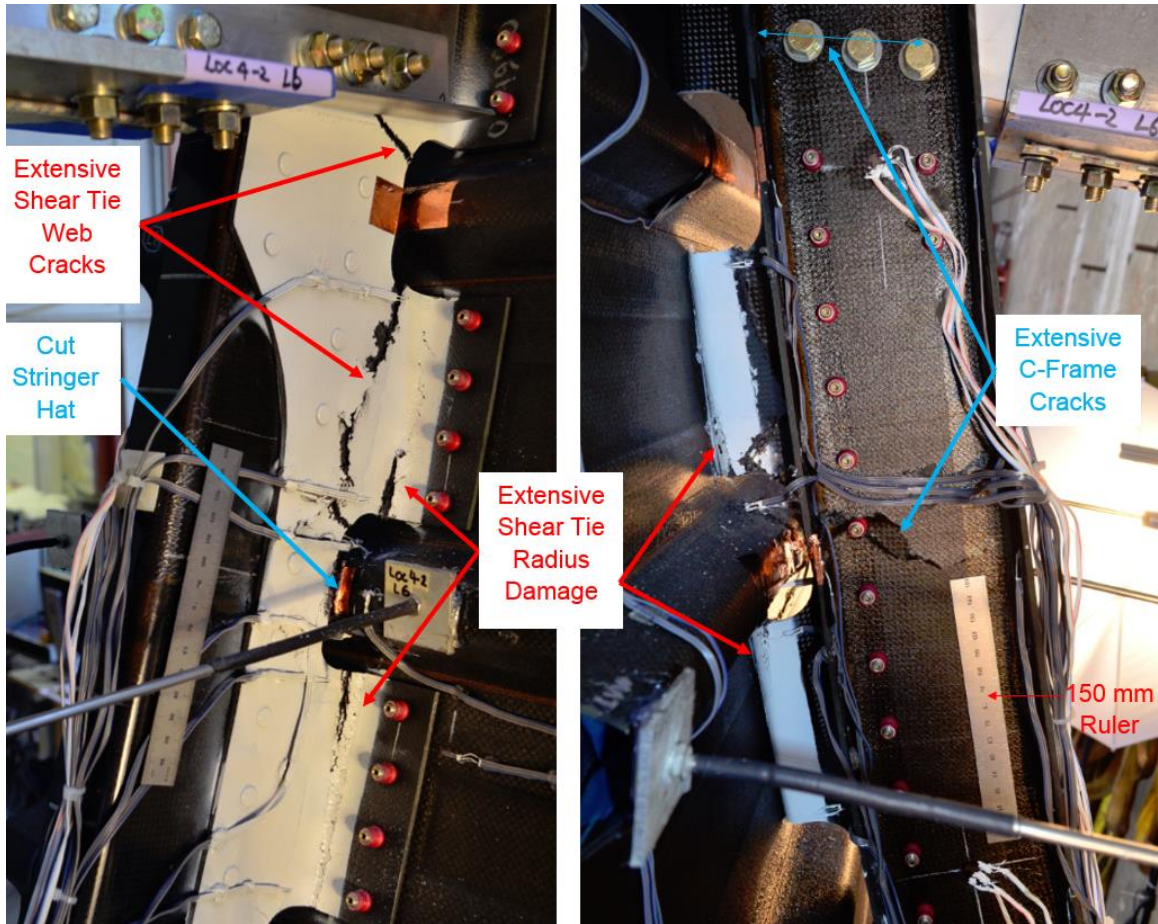
Figure 3.58 shows damage accumulation in Loc4-1 tests and subsequent L1 to L5 tests are passing through where last one left off. In Figure 3.58 (SG08 installed on Stringer lower side at Loc4), at the stringer hat damage initiation, marked with a brown square, the strain slope starts to be softened as the local stress is released due to cutting of the stringer hat by shear tie web penetration.



**Figure 3.58: Strain curves from SG08 installed on Str. lower side at Loc4.**

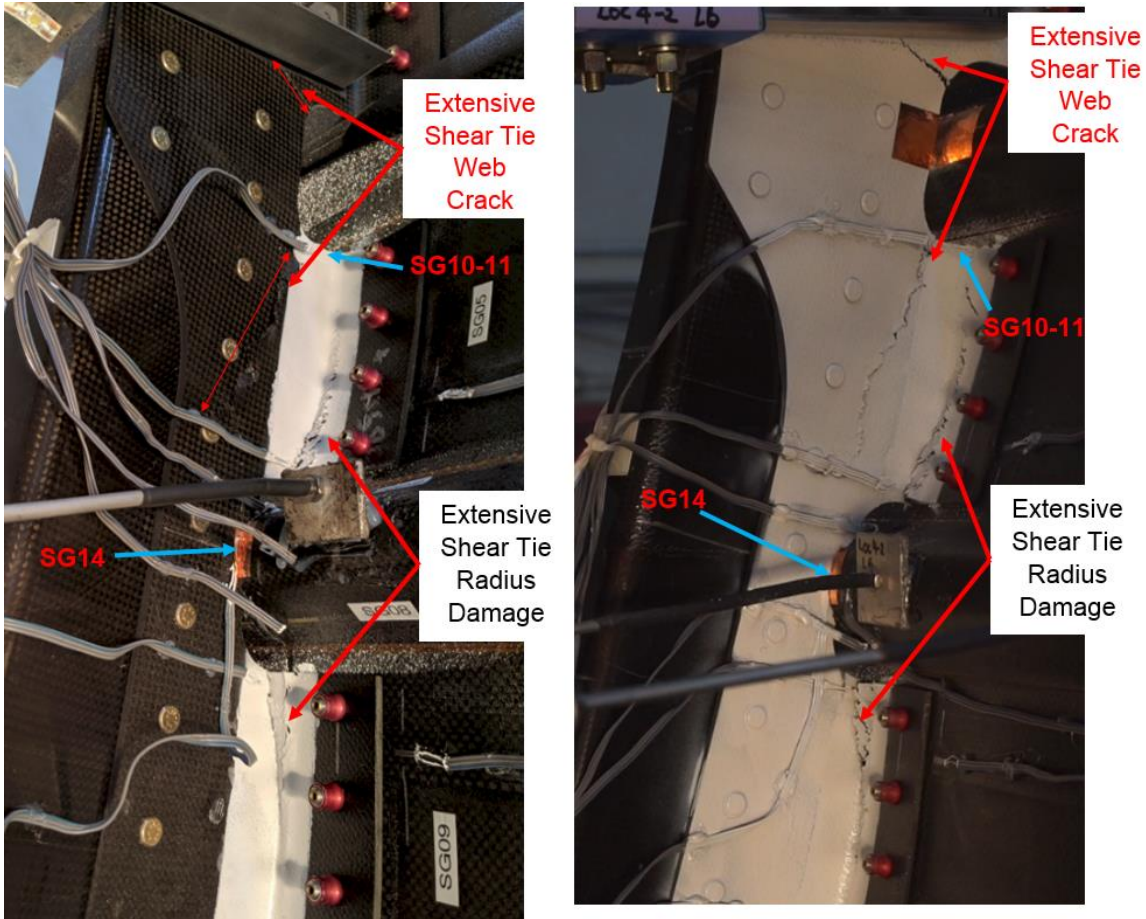
### 3.10.5 CATASTROPHIC FAILURE ON SHEAR TIE AND C-FRAME

Figure 3.59 shows the extensive internal damage of the Loc4-2 specimen after L6 test. In the last stage of loading, key failure occurred in shear tie and C-frame with abrupt fracture (fiber failures and large size crack formation) as shown.



**Figure 3.59: Extensive shear tie, stringer, and C-frame damage after Loc4-2\_L6 test.**

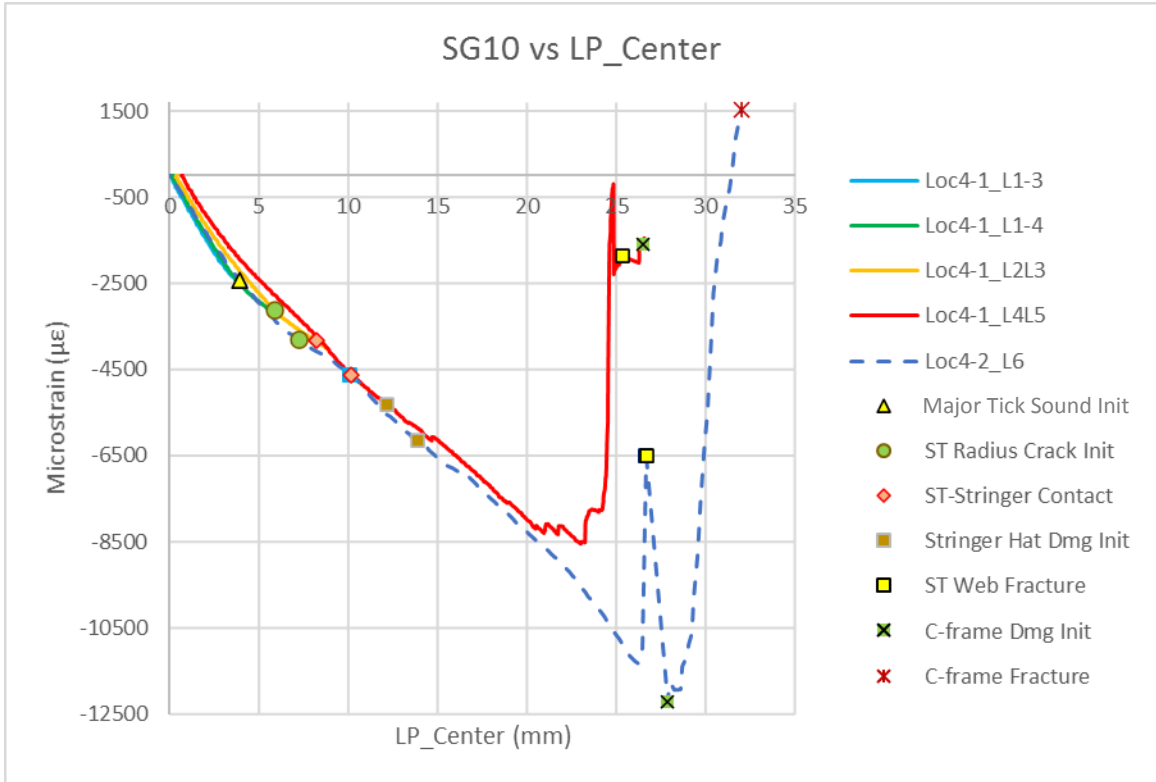
After the stringer hat damage and at the maximum load of L4L5 and L6 loading, the shear tie web fracture occurred with the extensive shear tie web cracks propagating diagonally from the two round corners of Loc2 mouse hole to Loc3 and to the floor joint respectively shown in Figure 3.60.



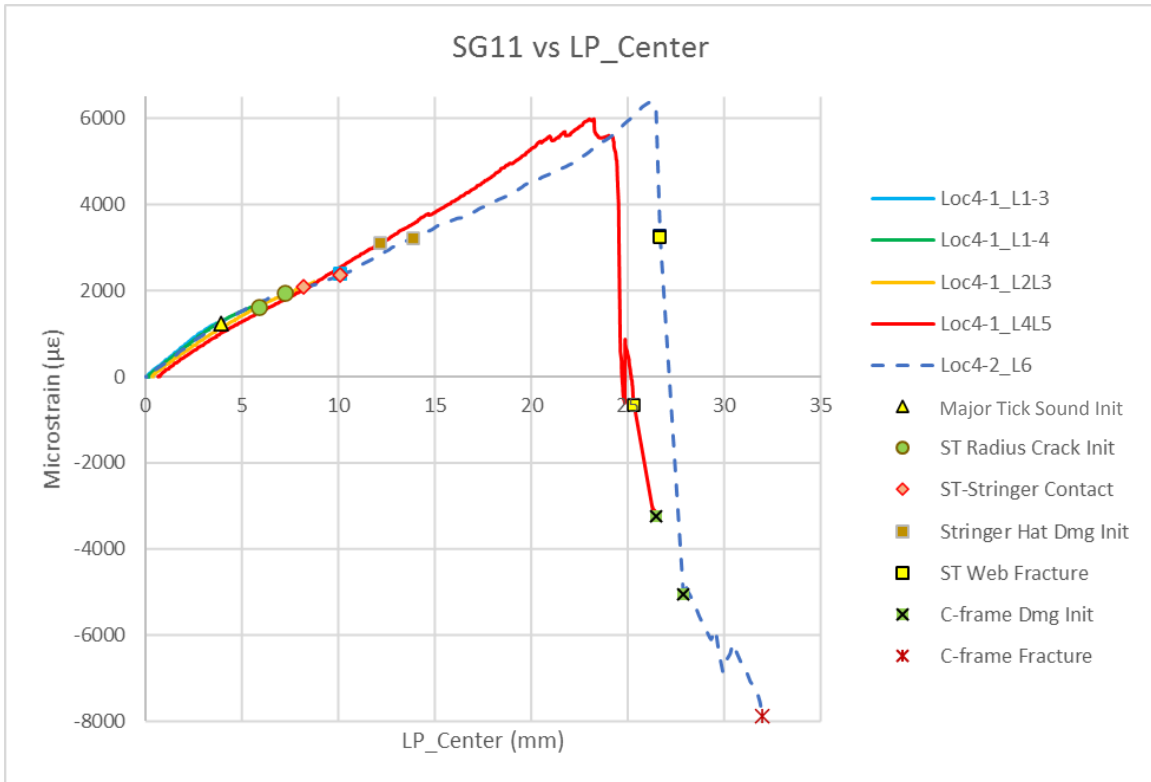
**Figure 3.60: Extensive shear tie damage at maximum load in Loc4-1\_L4L5 test (Left) and in Loc4-2L6 test (Right).**

The abrupt shear tie web fracture was also captured from the strain curves from SG10-11 and SG14. The locations of SG10-11 and SG14 are shown in Figure 3.36 and Figure 3.60. The abrupt and large strain change is indicated by a yellow square mark in Figure 3.61 to Figure 3.63. The back-to-back SG10-11 is the nearest strain gauges from the shear tie web crack. In Figure 3.61 and Figure 3.62, catastrophic shear tie web fracture accompanies with abrupt change of the bending strain reversely at the back-to-back strain gauge.



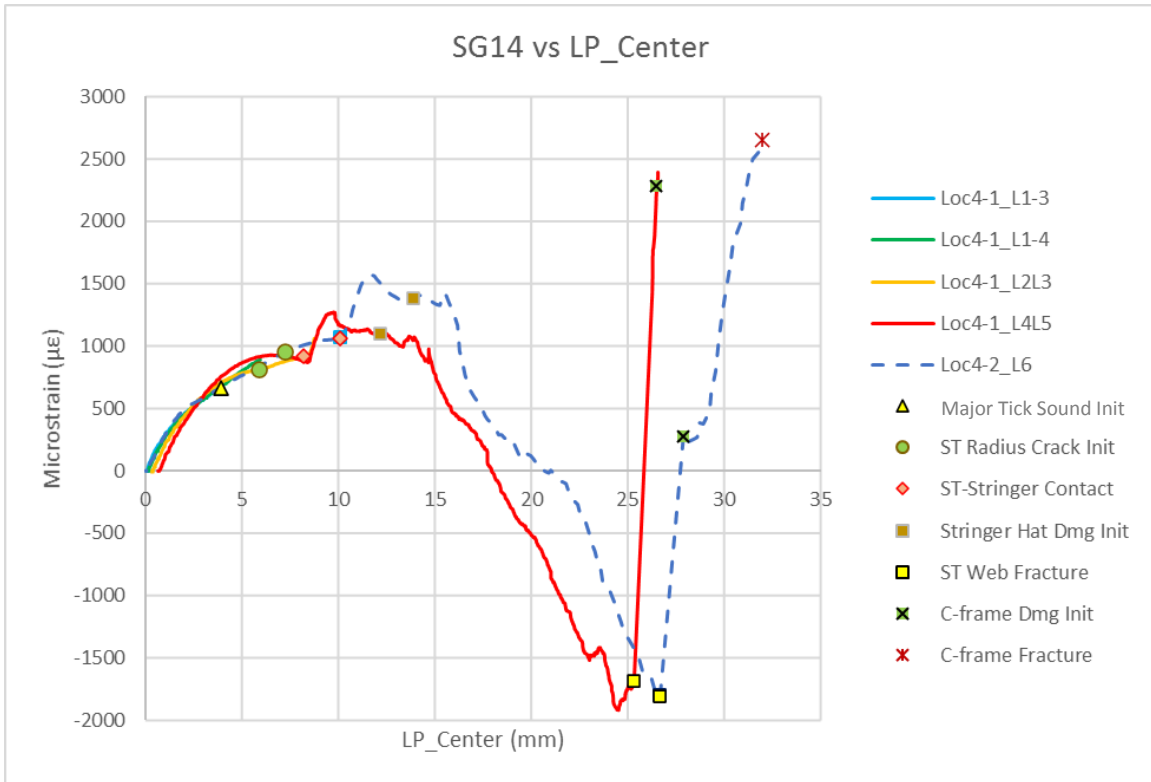


**Figure 3.61: Strain curves from SG10 near shear tie radius region at lower side of Loc2 mouse hole.**



**Figure 3.62: Strain curves from SG11 near shear tie radius region at lower side of Loc2 mouse hole.**

The SG14 is located at Loc4 shear tie mouse hole web, the nearest location from stringer contact point. In Figure 3.63, after shear tie-stringer contact, due to the interaction between shear tie web and stringer hat, the curved shape at SG14 along the shear tie primary axis is converted reversely to its original curved shape showing compressive strain in SG14. At shear tie web fracture, the compressive strain is released abruptly, and abrupt increasing tension strain is shown. It is caused by direct contact between stringer and C-frame outer flange. The stringer behavior pushing the C-frame outer flange and interaction between the components at Loc4 mouse hole will be introduced in next description about C-frame failure (pg. 115-116).



**Figure 3.63: Strain curves from SG14 installed on ST. web near mouse hole section at Loc4.**

After the shear tie web fracture, the C-frame fracture was followed with abrupt cracking starting at a Hi-Lok bolt on the web of the loading location (Loc4) and at the floor joint through the lower bolt line shown in Figure 3.64. Through the video examination, when the shear tie web was fractured, the stringer (at Loc4) started to contact and push the C-frame outer flange causing the C-frame local web twisting and buckling (initiated at Hi-Lok bolts) as shown in Figure 3.65. Then, abrupt C-frame cracking occurred starting at the Hi-Lok bolt on the C-frame web of Loc4 by stress concentration under combined shear and bolt pulling as well as through the lower bolt line of the floor joint under shear in the shear dominated boundaries as shown in Figure 3.64 and Figure 3.65.

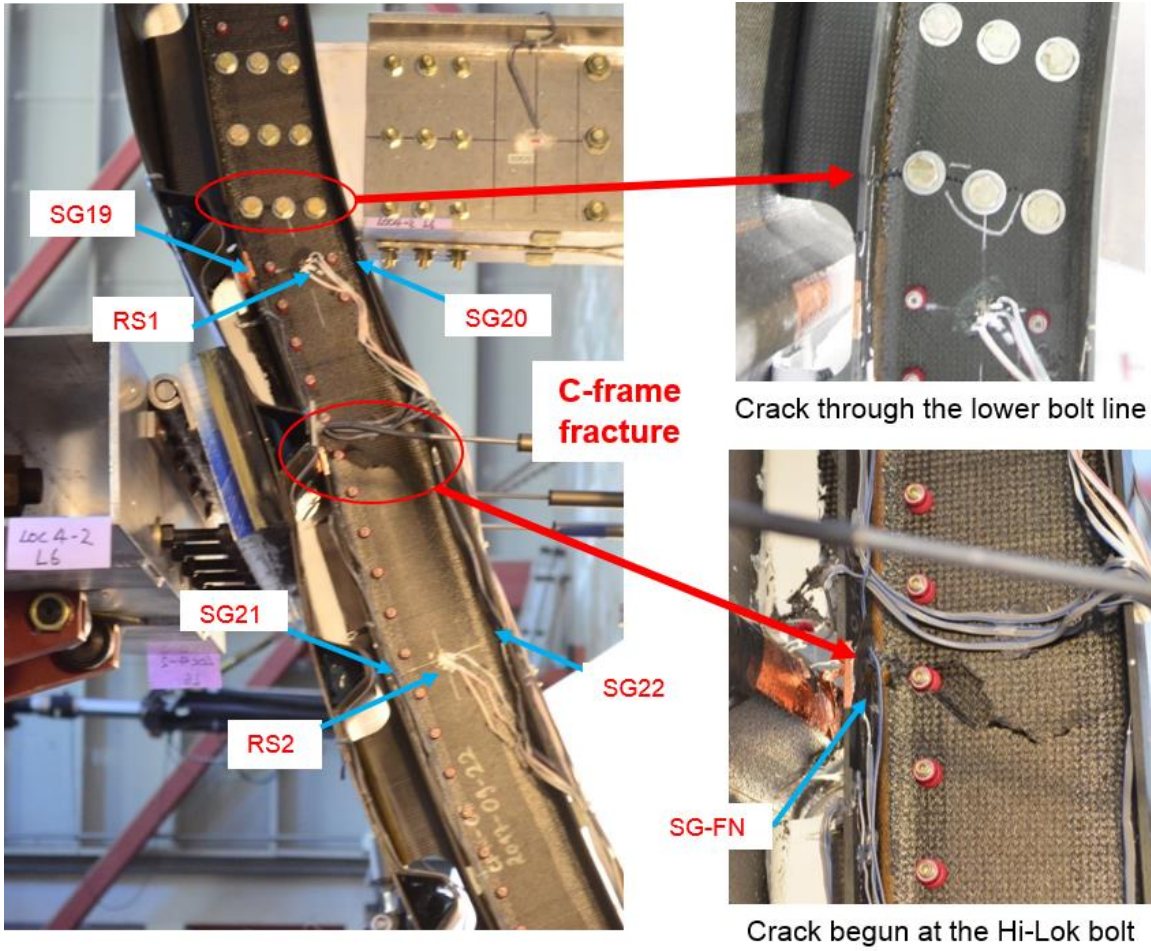
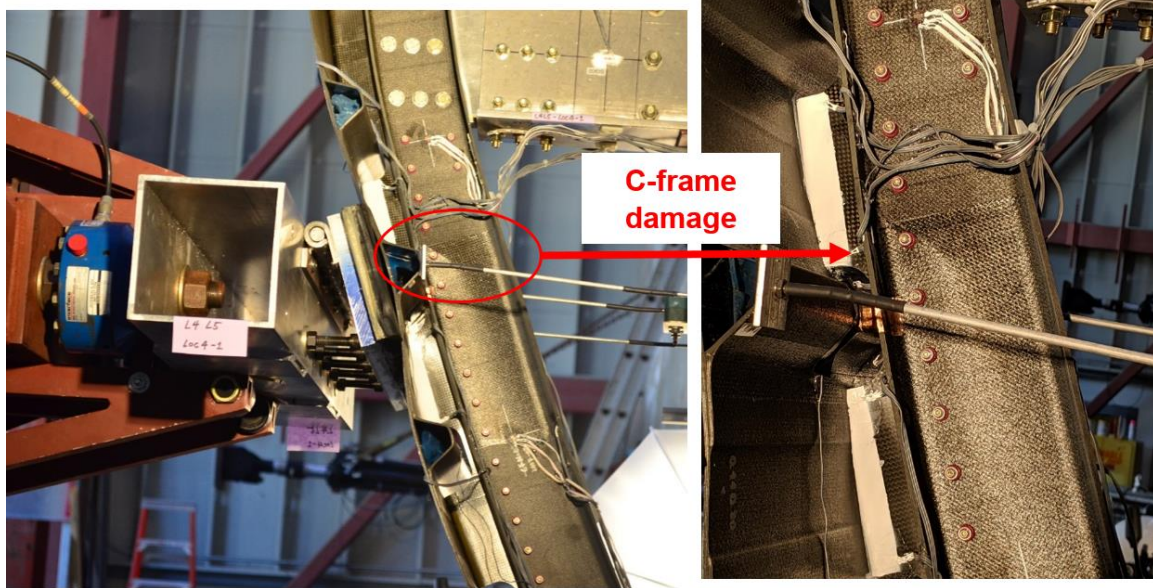


Figure 3.64: C-frame fracture at Loc4 and floor joint at maximum stroke in Loc4-2\_L6.



Loc4 stringer pushing the outer flange of C-frame

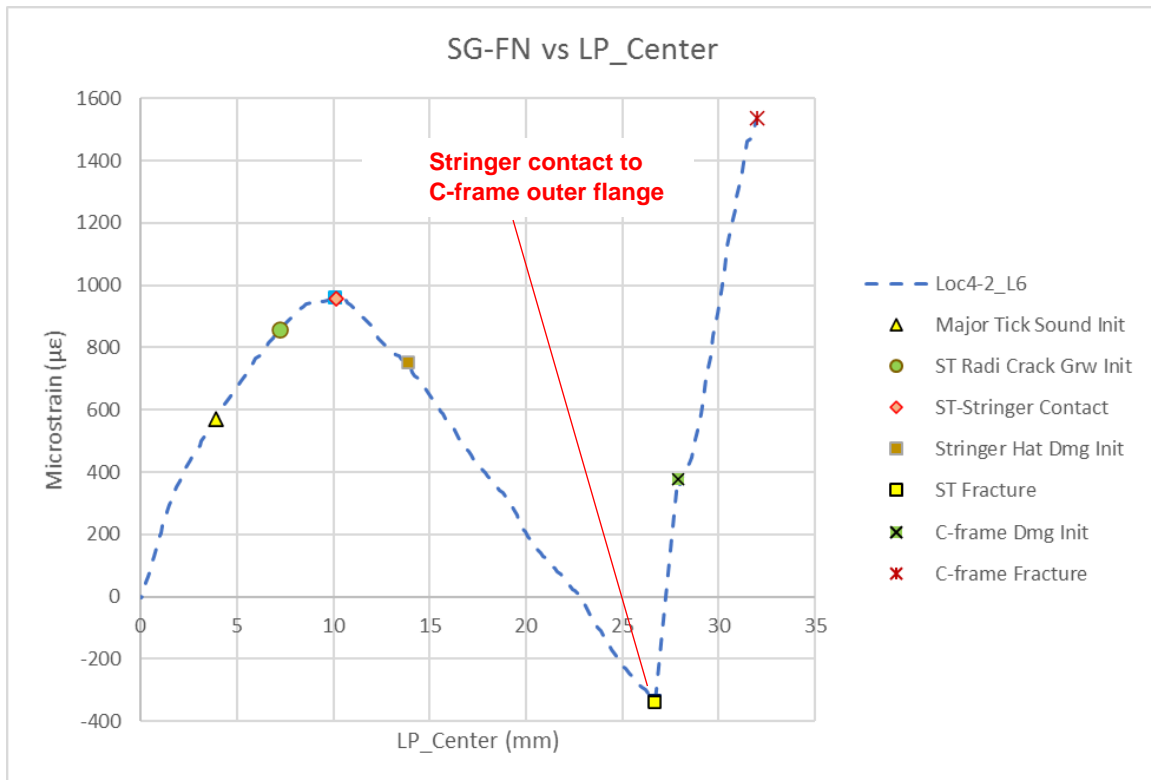
**Web local twisting and buckling**  
under combined bolt pulling and  
shear modes due to stringer push

**Figure 3.65: C-frame damage initiation at the Hi-Lok fastener on the web at Loc4 right after shear tie web fracture in Loc4-1\_L4L5.**

All C-frame strain data was examined from gauges applied on C-frame. The SG locations are shown in Figure 3.35 and Figure 3.64. All linear gauges were installed on the inner surface of flanges at Loc2 and Loc6. The additional linear gauges at Loc4, SG-FN and SG-SN, were installed in Loc4-2 test. The rosette gauges, RS1 and RS2 were installed on the web at Loc2 and Loc6, respectively.

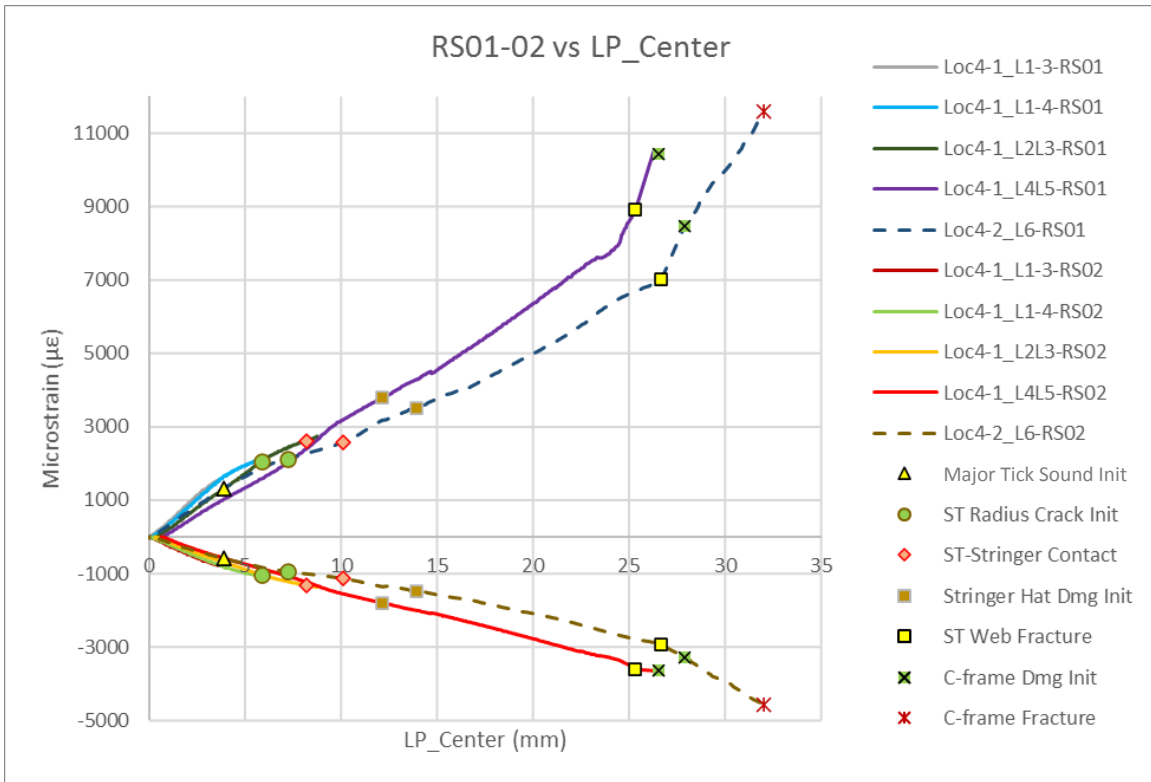
In Loc4-2\_L6 test, the stringer contact and push phenomenon at the loading location (Loc4), was captured in the strain curve from SG-FN as shown in Figure 3.66. In early stage, the curvature of C-frame outer flange at Loc4 becomes flattened and reversal to its original curved shape. After shear tie-stringer contact, due to the interaction between shear tie web and stringer hat, which is shear tie web penetration to stringer hat,

the curvature at SG-FN is recovered to its original curve shape. Right after shear tie web fracture (highlighted with yellow square), the curvature of C-frame outer flange started to be flattened and going to reversal again to its original curved shape because the stringer kept pushing the outer flange at Loc4 until C-frame fracture.



**Figure 3.66: Bending strain curves from SG-FN on inner surface of outer flange at Loc4.**

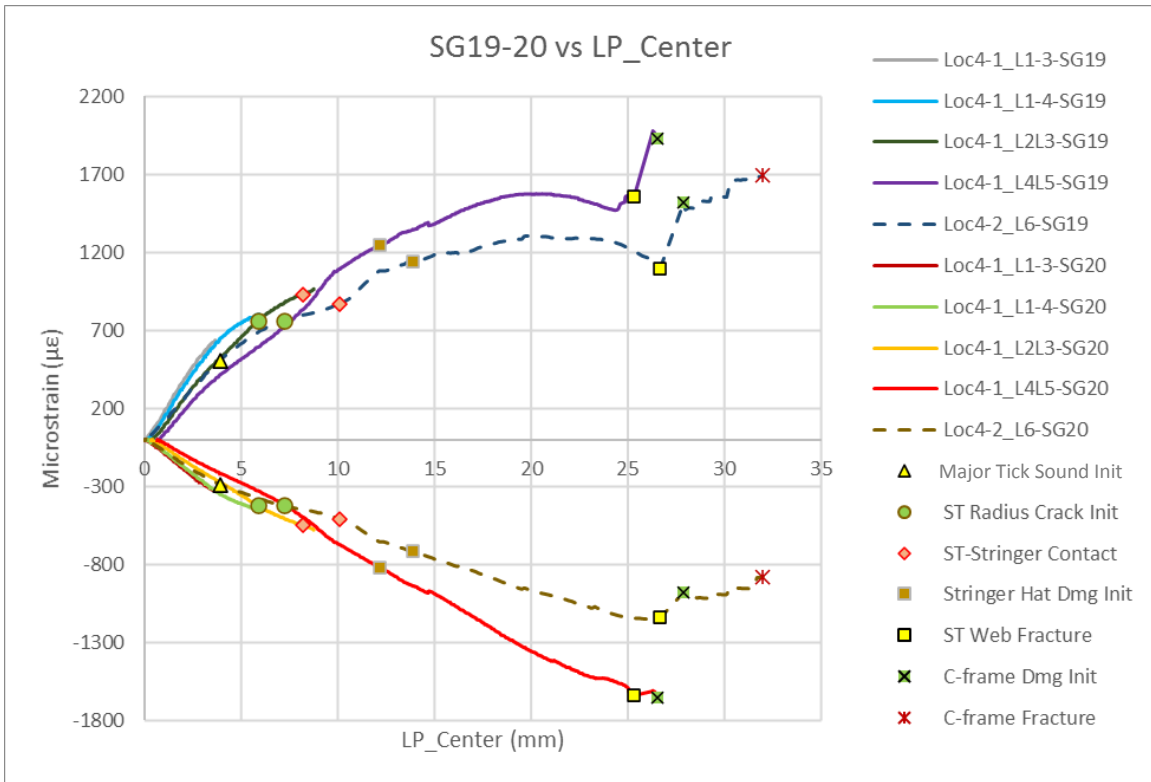
The highest strain is the in-plane shear strain from RS-01 at Loc2 (4 to 7.5 times higher than the strain from the other gauges), and the second highest strain is the in-plane shear strain from RS-02 at Loc6. The shear strain curves are shown in Figure 3.67.



**Figure 3.67: Shear strain curves from RS01 and RS02 at Loc2 and Loc6 respectively.**

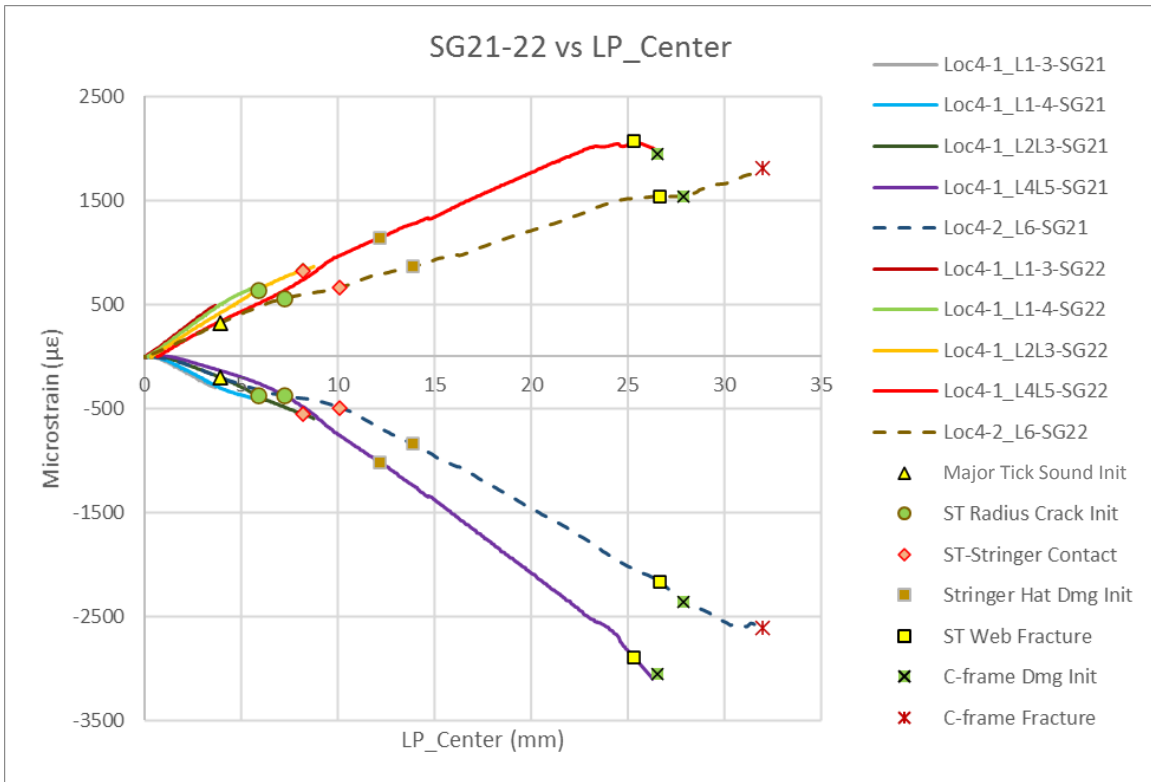
Also, as shown in Figure 3.68 and Figure 3.69, the bending strain level is lower at Loc2 than at Loc6 overall. It means the region between Loc2 and Loc4 is more shear dominated than the region between Loc4 and Loc6, as more shear load flowed above the loading location (Loc4) to the floor joint as this is the stiffer load path.

From the strain plots in Figure 3.68 and Figure 3.69, the curvature of C-frame flanges, at Loc2, was decreasing overall until C-frame fracture, and, the curvature of C-frame flanges, at Loc6, was increasing overall until C-frame fracture.



**Figure 3.68: Bending strain curves from SG19 and SG20 at Loc2.**



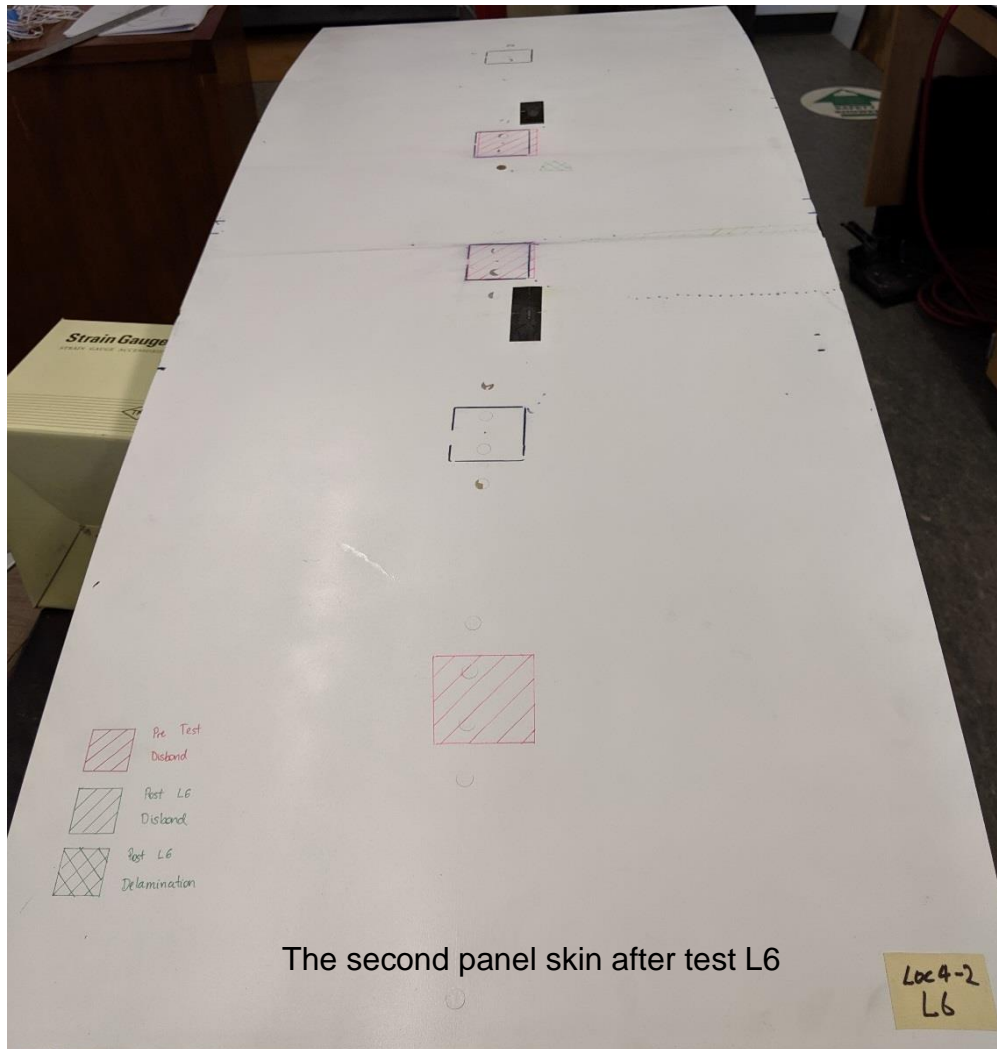


**Figure 3.69: Bending strain curves from SG21 and SG22 at Loc6.**

Through the video and strain examination, it turned out that the C-frame was fractured by the stringer contact showing combined shear and bolt pulling (by local twisting) failure modes.

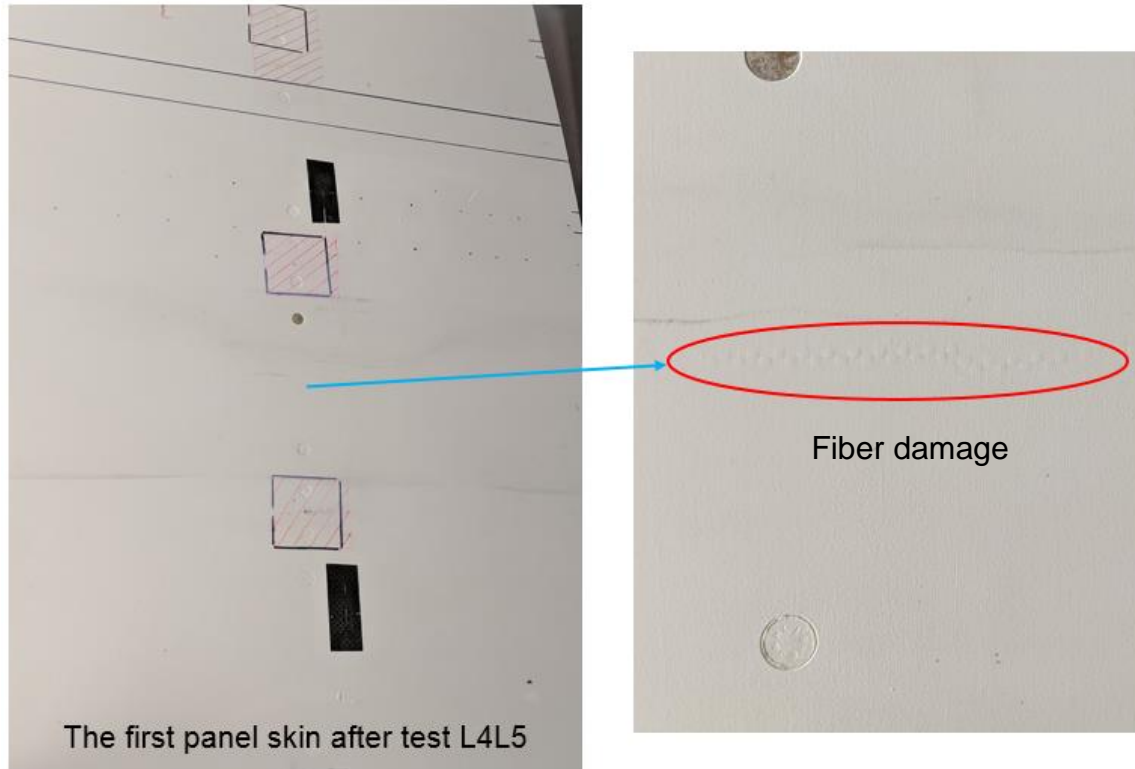
### 3.10.6 EXTERNAL DAMAGE DETECTABILITY

As shown in Figure 3.70, after Loc4-2 test, there is no obvious external damage sign on outer skin surface observable by the visual inspection except the rubber bumper mark and paint chipping on bolts at the loading location.



**Figure 3.70: No obvious external damage sign on skin (red hatched areas are pre-existing shim-to-skin disbanding from non-destructive testing).**

In Figure 3.71, after Loc4-1 tests, barely visible skin crack was observed on outer skin surface at Loc4. In Loc4-1 tests, there were successive loading and unloading causing accumulated damages in the specimen. It may cause the skin crack.

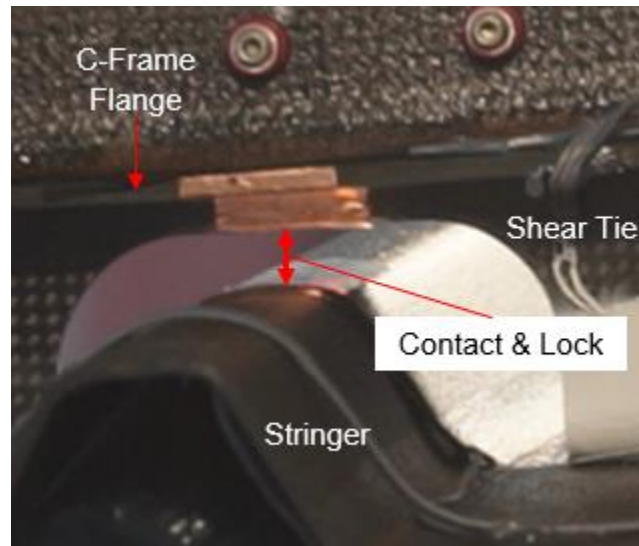


**Figure 3.71: Barely visible skin crack observed at Loc4 in the first panel.**

### 3.10.7 EXPERIMENTAL CONCLUSION – LOC4

The damage initiated at the loading location (Loc4) in the shear tie radius region showing delamination and fiber crushing mode. As load increased, the crack grew gradually along the shear tie radius from Loc4 upward and downward. Shear tie web-stringer hat contact occurred (see Figure 3.72) which led to cutting of the stringer hat due to the shear tie web penetration. The penetration of the shear tie into the stringer hat caused locking of the shear tie and connected C-frame, thereby preventing rotation and lateral movement. With further loading, the extensive shear tie web diagonal cracks occurred abruptly between the loading location and the floor joint. Lastly, the abrupt C-

frame fracture was followed due to the stringer contact at Loc4 with cracks beginning at a Hi-Lok bolt on the web as well as along the lower bolt line of the floor joint in the shear dominated zone between the loading point and the upper floor beam boundary (through stiffest load path).



**Figure 3.72: Stringer-shear tie contact, shear tie penetration, and locking C-frame.**

Energy absorption comparison is possible from the load vs displacement curves. For the combined load history for the 1<sup>st</sup> generation Frame04-1 and Frame03 experiments, the energy required to produce the final state of damage (C-frame failure) was 1811 J per frame as shown in Figure 3.73 [8]. The energy was determined by calculating the area under the load-displacement curve as shown.

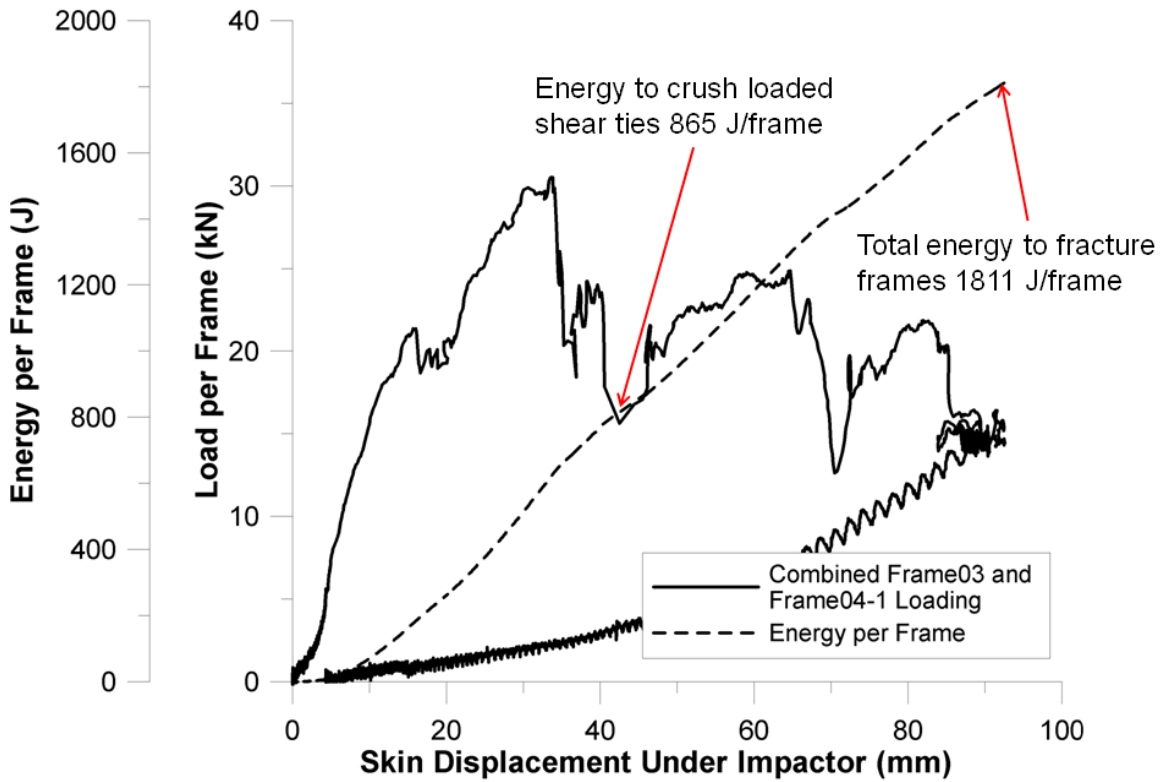
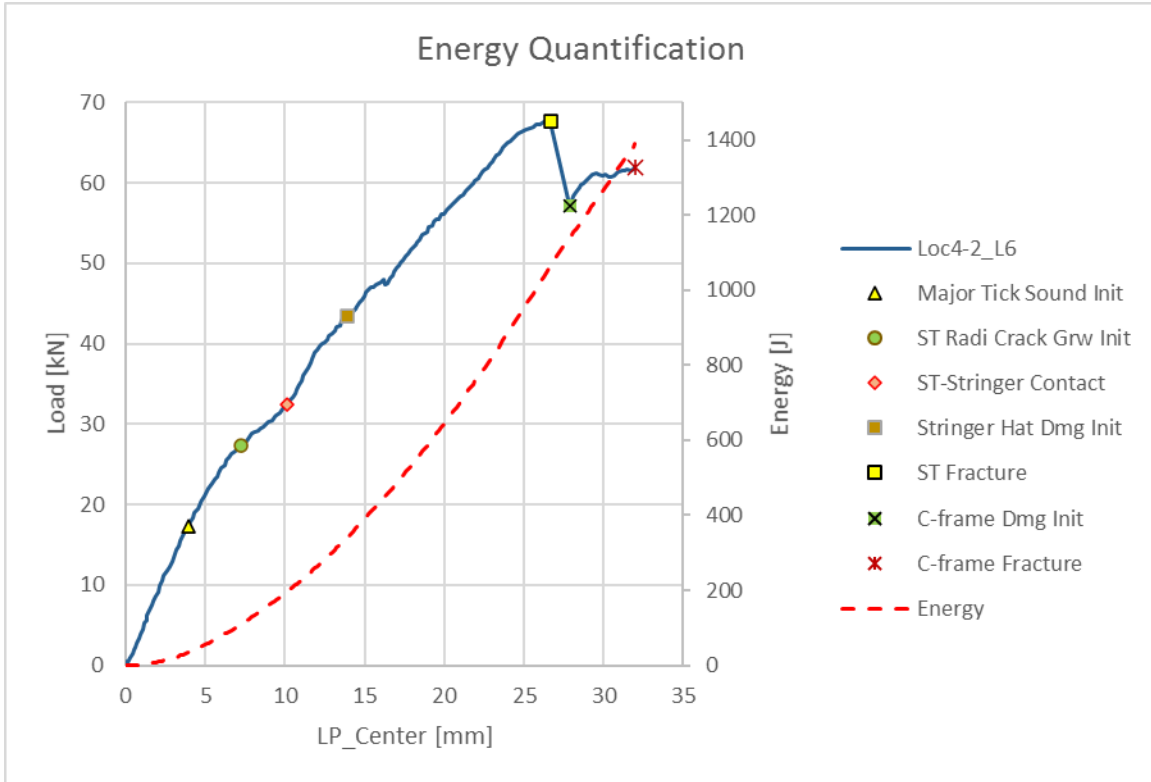


Figure 3.73: Frame03 and Frame04-1 combined loading and energy per frame [8].

As shown in Figure 3.74, the Loc4-2 loading curve and energy is plotted, and, in Table 3.10, the energy required at each key event is summarized. For the final state of damage (extensive C-frame and shear tie fracture), the required energy is 1389 J.



**Figure 3.74: Loc4-2 loading curve and energy.**

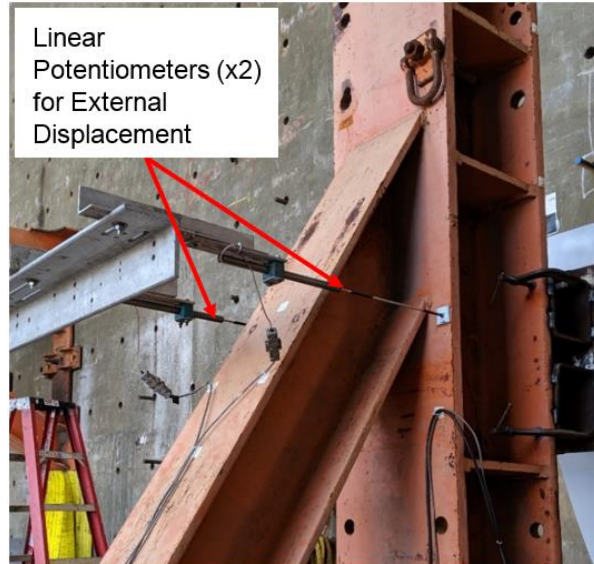
**Table 3.10: Energy required at each key event.**

Key Event	Skin disp. (mm)	Load (kN)	Energy (J)
Major Cracking Sound Init (ST Radius Delam)	3.9	17.36	34.4
ST Radius Crack Grw Initi	7.2	27.29	110
ST-Str Contact	10.1	32.47	196
Str Hat Dmg Initi	13.9	43.38	342
ST Web Fracture	26.7	67.61	1066
C-frame Dmg Initi	27.9	57.14	1141
C-frame Fracture	32.0	61.97	1389

The typical mass of GSE ranges from 3000 kg (belt loader) to over 15000 kg (cargo loader), and its velocity ranges 0.5 m/s to 1 m/s [8]. When the high mass and low velocity (specifically at 0.5 m/s) impact is applied to aircraft, the kinetic energy ranges from 375 J to over 1875 J. The reasonable energy boundaries for a GSE blunt impact were estimated in a range between 1000 J to 3000 J [14]. Therefore, the blunt impact by the accidental contact of a heavy cargo loader leads to the significant internal damage.

### 3.11 SPECIFIC SETUP FOR LOC3 TESTS

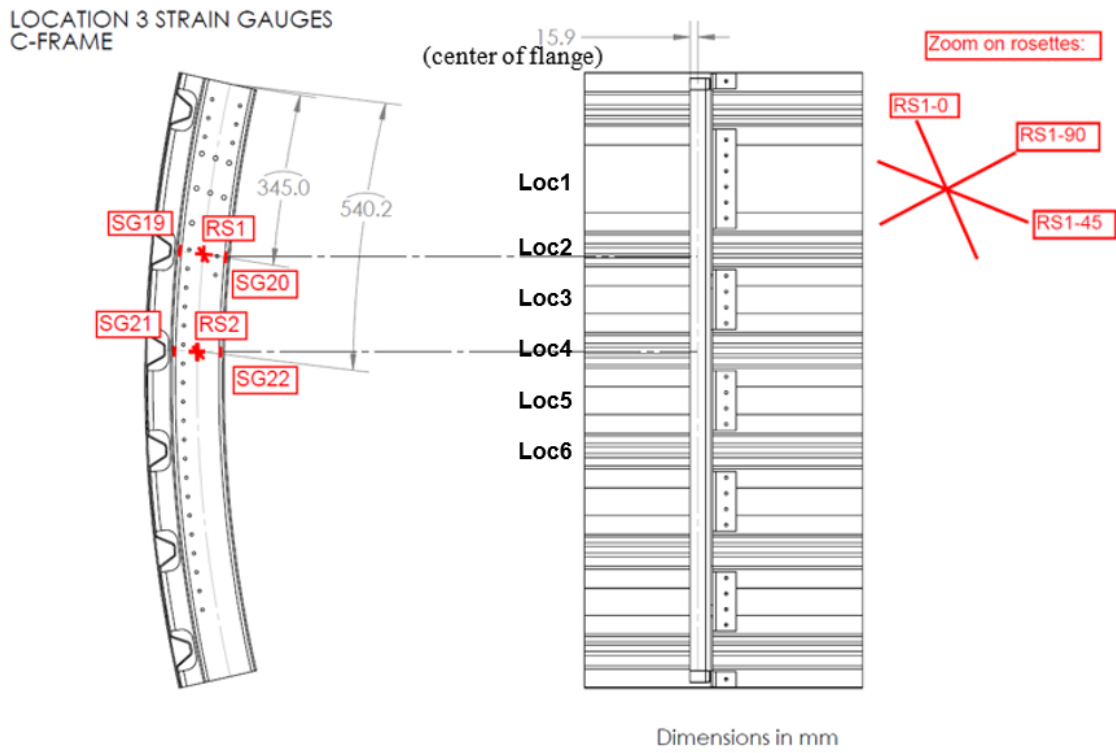
Like Loc4 test-set, to measure the values of the displacement, load level, and strains as well as to monitor the shear tie-stringer contact occurrence, linear potentiometers (LPs), load cells (LCs), strain gauges (SGs), and contact sensors (CSs) were installed. The linear potentiometer installed on the inner surface of skin at Loc3, but during the Loc3-2 test, the target parts were disbanded from the skin. Therefore, the linear potentiometers installed on the vertical loading frame at the loading position (Figure 3.75) were used to measure displacement as named external displacement. The contact sensors (CSs) were installed using thin copper tape positioned between shear tie and stringer at Loc2 and Loc4 to indicate when the stringer makes physical contact with the shear tie during loading.



**Figure 3.75: Linear potentiometers (LPs) for the external displacement.**

In Loc3 specimens, the strain was monitored by 22 linear strain gauges (SGs) and 2 rosettes ( $0^\circ$ ,  $45^\circ$  and  $90^\circ$ ). By the section force and stress analyses from the preliminary finite element models, strain gauge locations were determined based on the critical spots. All SG locations are shown in Figure 3.76 to Figure 3.79.





**Figure 3.76: C-frame strain gauges for Loc3 specimens.**

LOCATION 3 STRAIN GAUGES  
SHEAR-TIE

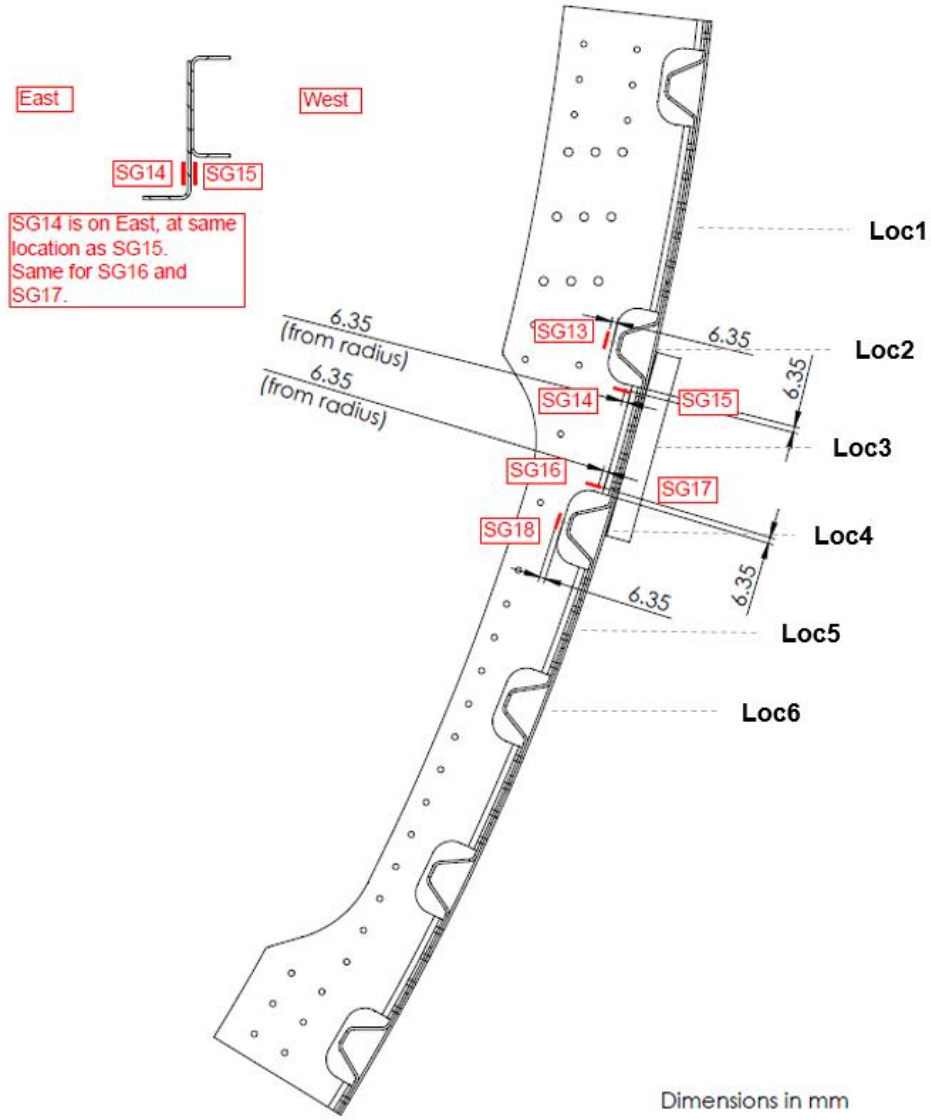


Figure 3.77: Shear tie strain gauges for Loc3 specimens.

LOCATION 3 STRAIN GAUGES  
STRINGERS

ALL FLA GAUGES

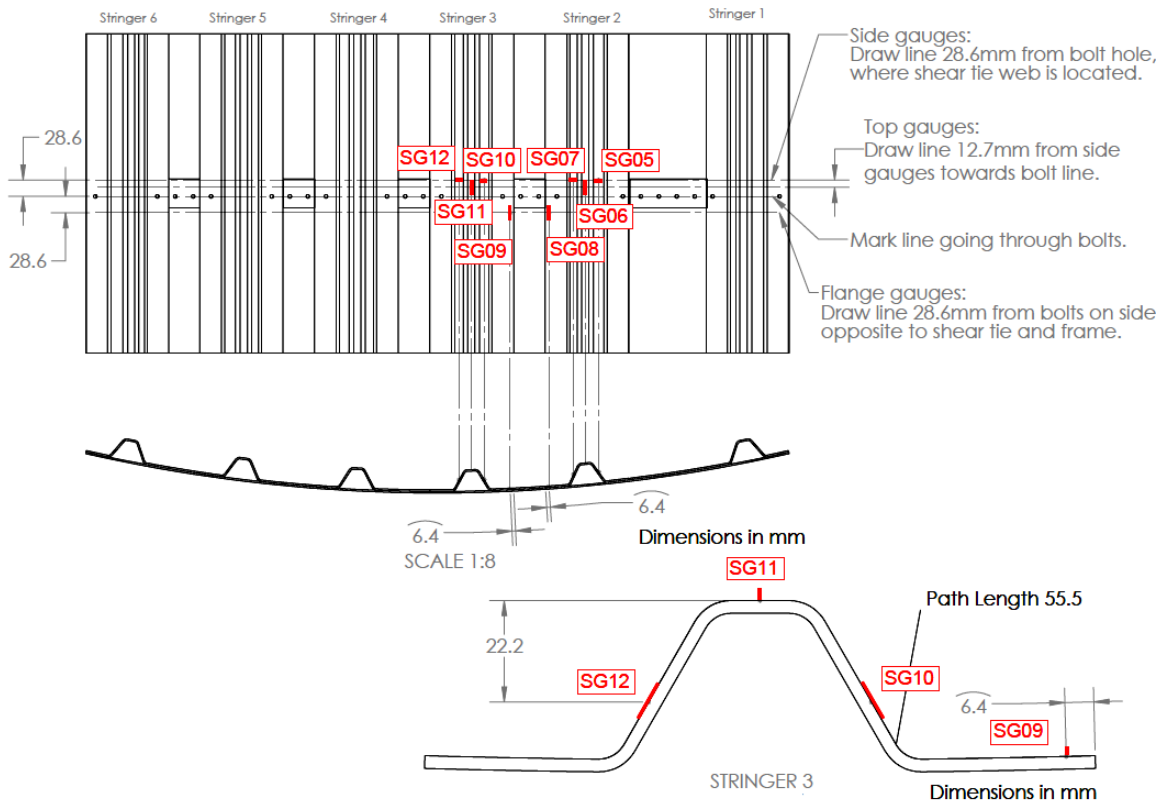
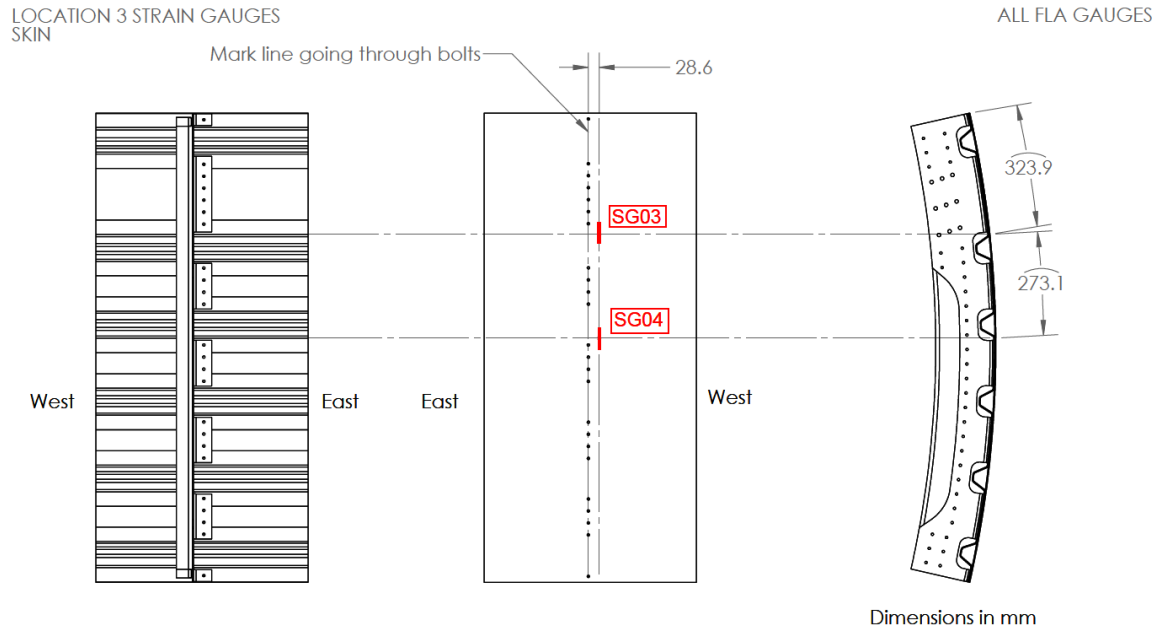


Figure 3.78: Stringer strain gauges for Loc3 specimens.

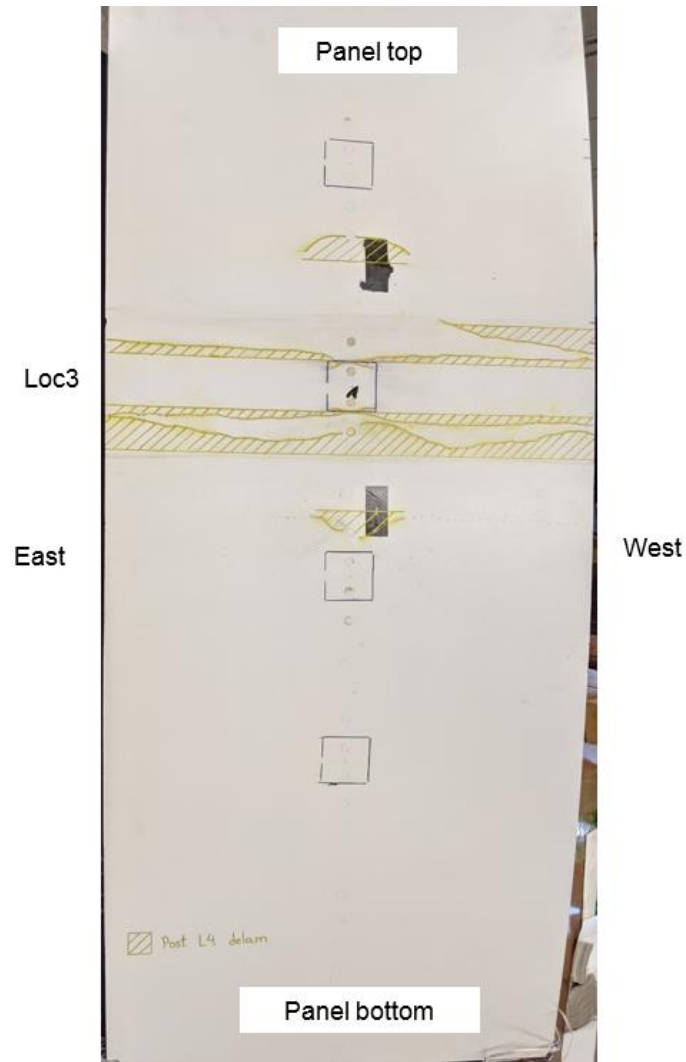


**Figure 3.79: Skin strain gauges for Loc3 specimens.**

### 3.12 EXPERIMENTAL RESULTS – LOC3

The experimental data for Loc3 were post-processed and interpreted by Wiggers for the final report to the FAA. Based on her analysis, summarized here, the key physical phenomena and damage mechanism are introduced while modifying some observation such as shear tie radius delamination occurrence which is hard to detect in extensive and abrupt radial crushing, and C-frame failure mechanism.

Most of all, from the early stage of the Loc3-2 test, complex delamination failure occurred between the stringer flange (at lower Loc2 as well as upper Loc4) and skin in the co-cured outer panel as shown in Figure 3.80 and Figure 3.81.



**Figure 3.80: A-scan results after Loc3-2 test.**



**Figure 3.81: Visible skin-stringer disbond after Loc3-2 test.**

From ultrasonic A-scan results (Figure 3.80), the skin-stringer disbond initiated both at the panel's center and at the side ends (stringer free edges), and it may likely not occur in case of a wide panel along stringer direction with multiple shear ties and C-frames. Moreover, this disbond did not occur in Loc3-1 test. It accompanied the crack at stringer heel in the very early stage of the loading influencing the structural response. Due to this, the event of shear tie-stringer contact occurred earlier with less shear tie damage in Loc3-2 test by comparison with the Loc3-1 test results.

It was difficult to precisely quantify the damage progression and extent of skin-stringer disbond and correlating with strain data. Moreover, this failure influenced other components' failure by changing the load path in the complicated structure. Nevertheless, these parts are not described further in this thesis to be more focused on other key damage on shear tie, stringer hat, and C-frame.

For Loc3 tests, the loading definition with six different loading levels is summarized in Table 3.11.

**Table 3.11: Loading protocol for Loc3 specimens.**

<b>Specimen ID</b>	<b>Load Level</b>	<b>Manual Load Stop Definition</b>
<b>Loc3-1</b>	Pre-test	1/5 load of expected shear tie corner crack
	L1	Damage at shear tie corner near Loc2 stringer (Delamination)
	L2	Entire shear tie radius damage (crack all through ST radius at Loc3)
	L3	Stringer hat damage (past contact between stringers and shear tie)
<b>Loc3-2</b>	Pre-test	1/3 load of the pre-test in Loc3-1 tests
	L4	C-frame fracture

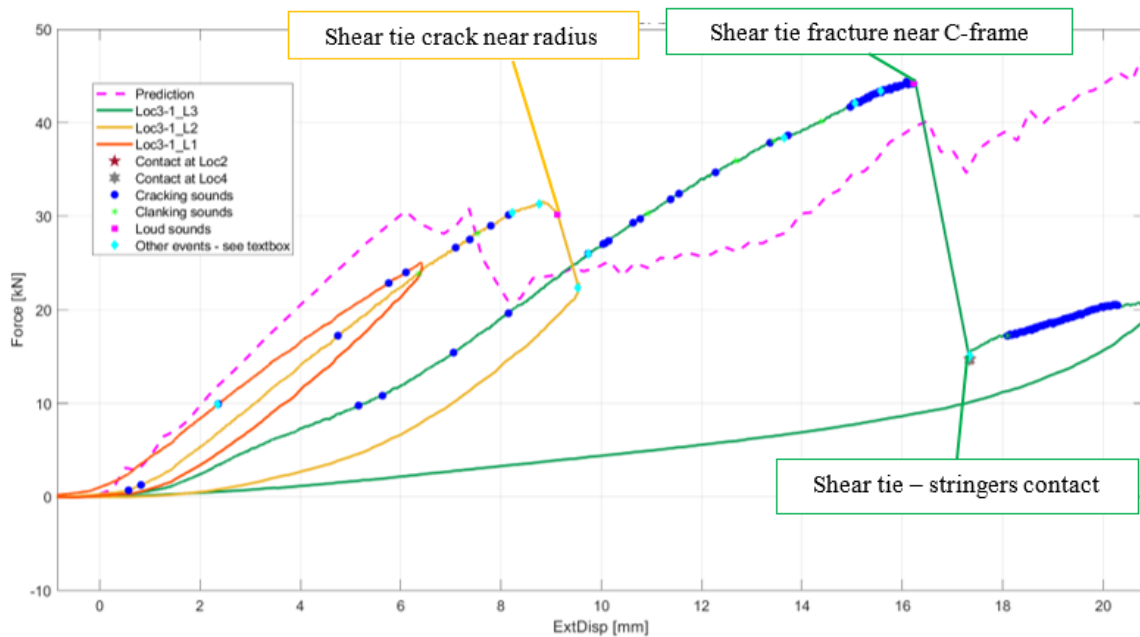
Before the main tests, the pre-test was conducted to check that all sensors were active, and data recorded correctly. For the first specimen Loc3-1, loading protocol was planned with a few load cycles, L1 to L3, correlated with the predicted key event sequence as described in Table 3.11. L1 damage event is the first major cracking sound hypothetically indicating delamination initiation by the low interlaminar tensile strength. L2 damage event is visually confirmed shear tie corner crack all through the entire shear tie radius region. L3 damage events are a second crack on the shear tie web above the radius region, and the stringer hat damage by contact stress between stringers and shear tie. Loc3-1 specimen was quasi-statically loaded to observe the sequence of key event occurrence at each load level. For the second test specimen, Loc3-2, the loading protocol was planned with one semi-dynamic load cycle, L4, to produce significant C-frame damage with fracture.

For each load cycle, the test was manually paused at the key events within the limit of pre-decided expected load-level and displacement. When the loading was paused,

thorough visual inspection was conducted. After finishing all the tests, the major physical events are carefully assessed through the load-displacement curve, strain data, and video examination.

### 3.12.1 LOC3-1 DAMAGE SEQUENCE

The load-displacement curves for Loc3-1 tests are shown in Figure 3.82 with the main event notification.



**Figure 3.82: Force vs external displacement for Loc3-1 tests.**

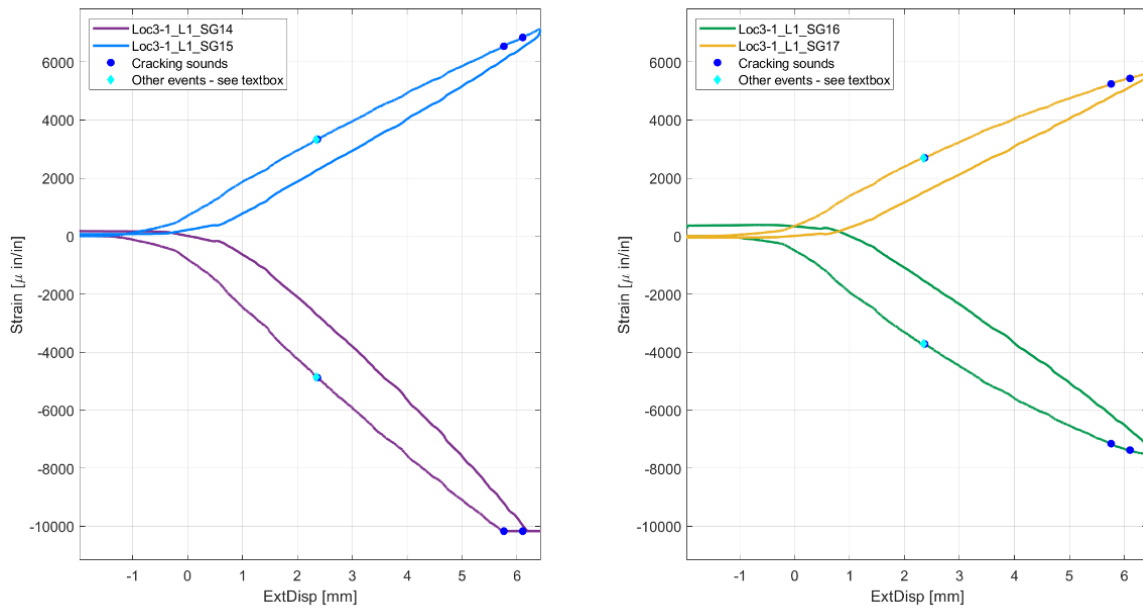
After Loc3-1\_L1, there was some paint chipping as shown in Figure 3.83, but it was hard to detect the obvious signs of shear tie delamination through visual inspection.



By monitoring the load-displacement curve and strain curves, the softening was confirmed especially the strain curves from (back-to-back) SG16-17 as shown Figure 3.84.

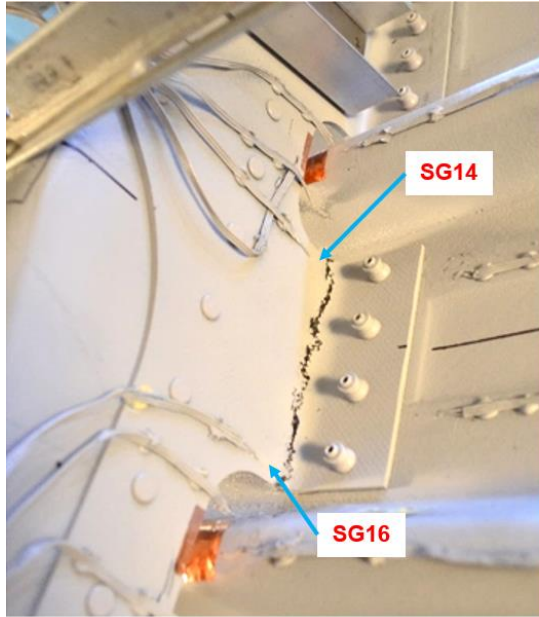


**Figure 3.83: Paint chipping observed on Loc3 shear tie radius after Loc3-1\_L1.**

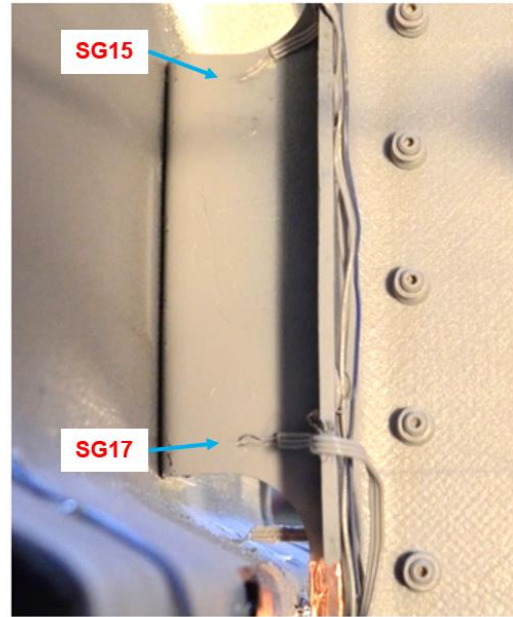


**Figure 3.84: No evidence of radius delamination in strain curves during Loc3-1\_L1.**

The first load drop occurred in Loc3-1\_L2, because of a shear tie crack on entire radius region abruptly as shown in Figure 3.85. This is due to fiber crushing by the direct compressive loading to the shear tie, and the development of radius crushing involves delamination (it is found the previous large-scale and small-scale tests [8,11]). This crack did not penetrate through the entire thickness, as shown in the west side picture of Figure 3.85.



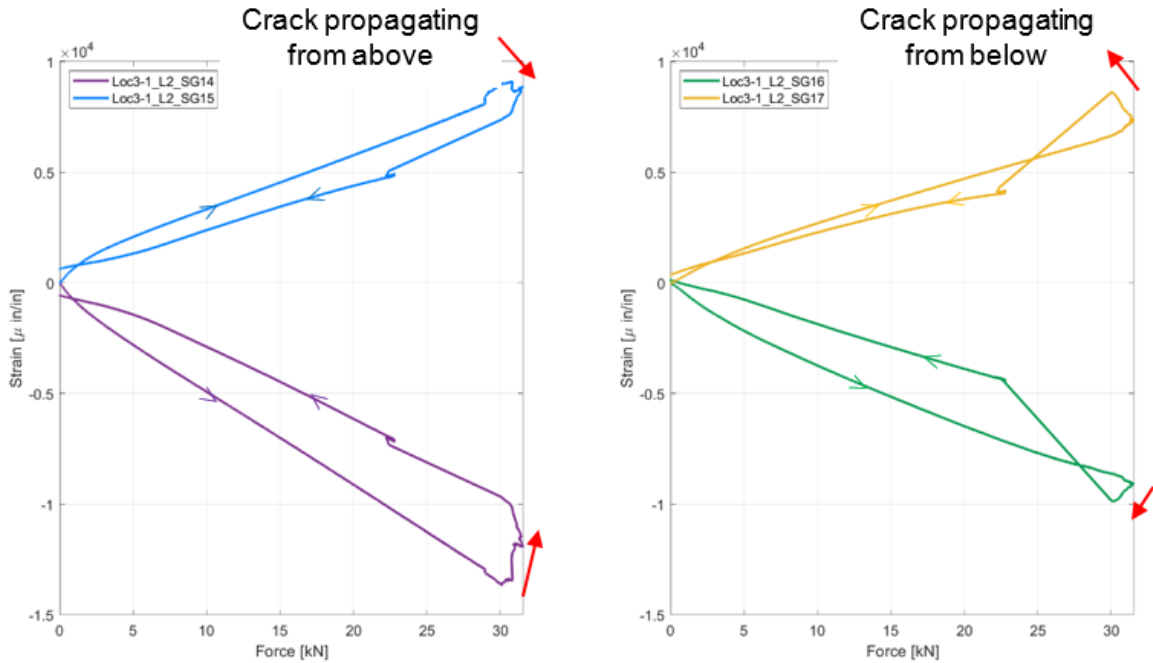
Shear tie crack as seen from East side



No crack as seen from West side

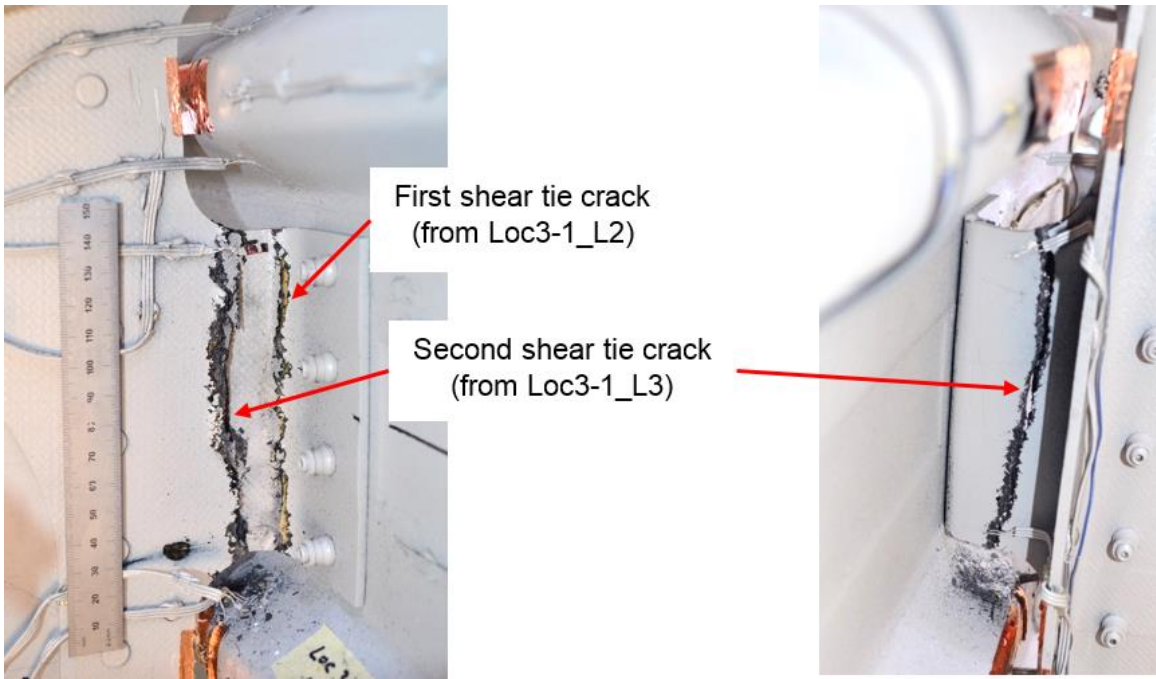
**Figure 3.85: Shear tie crack observed in Loc3-1\_L2.**

The locations of back-to-back strain gauges near shear tie radius are shown in Figure 3.85. The back-to-back strain gauges showed abrupt strain change as the crack propagates along the corner as shown in Figure 3.86.

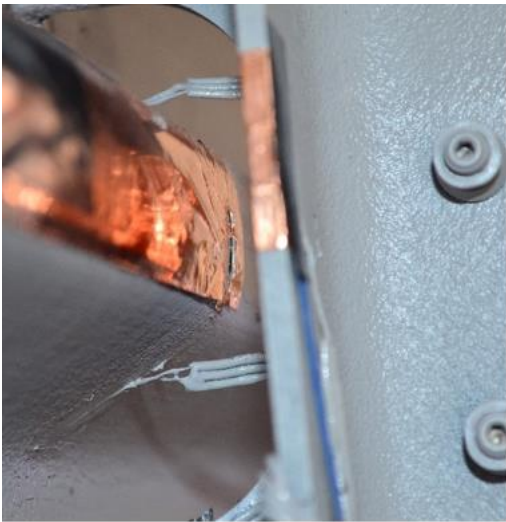


**Figure 3.86: Shear tie strain vs load for Loc3-1\_L2.**

During Loc3-1\_L3 testing, the second crack occurred on the shear tie web below the outer flange of C-frame (Figure 3.87). It was due to shear tie web buckling by the eccentric (effect of the eccentric shear center of open C section) compressive loading. By this damage, stringers 2 and 3 (at Loc2 and Loc4, respectively) contacted shear tie, as indicated by the contact sensors. As load increased further, stringer hat was cut by shear tie web penetration (Figure 3.88). As stringer hat damage progressed, the damage initiated in lower Loc1 and upper Loc5 shear tie radius (Figure 3.89).



**Figure 3.87: The second crack on shear tie web after Loc3-1\_L3.**



**Stringer 2**



**Stringer 3**

**Figure 3.88: Stringer hat damage after Loc3-1\_L3.**



Upper Loc5



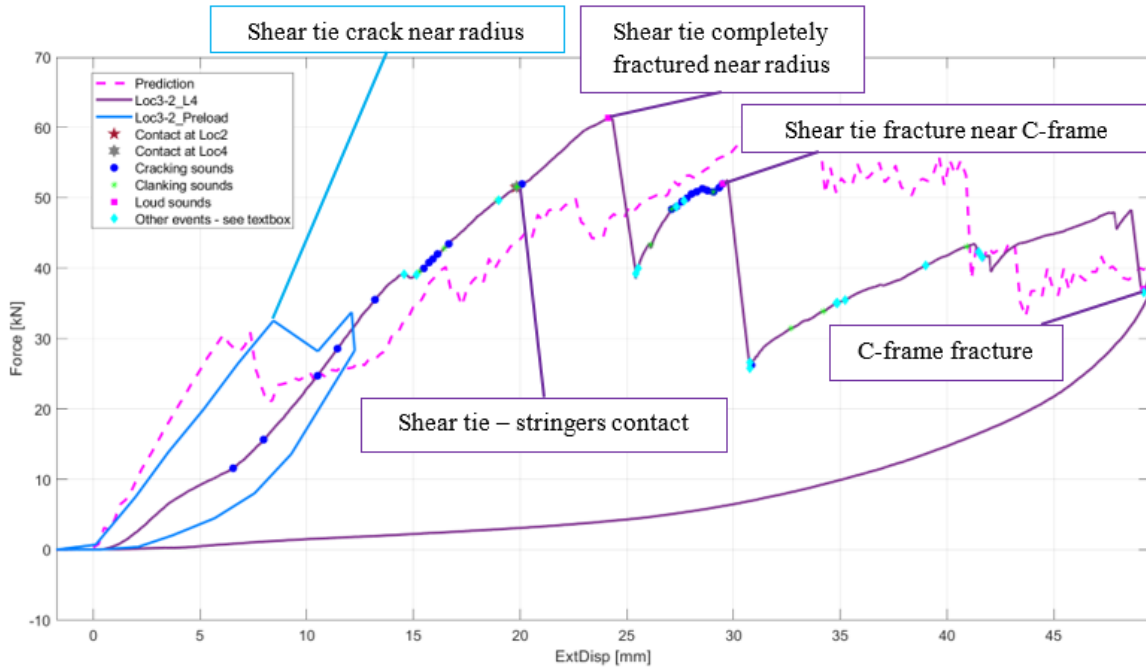
Lower Loc1

**Figure 3.89: Shear tie radius damage at lower Loc1 and upper Loc5 after Loc3-1\_L3.**

After Loc3-1 tests, there was no obvious external damage sign on outer skin surface by the visual inspection except rubber bumper mark and paint chipping on bolts.

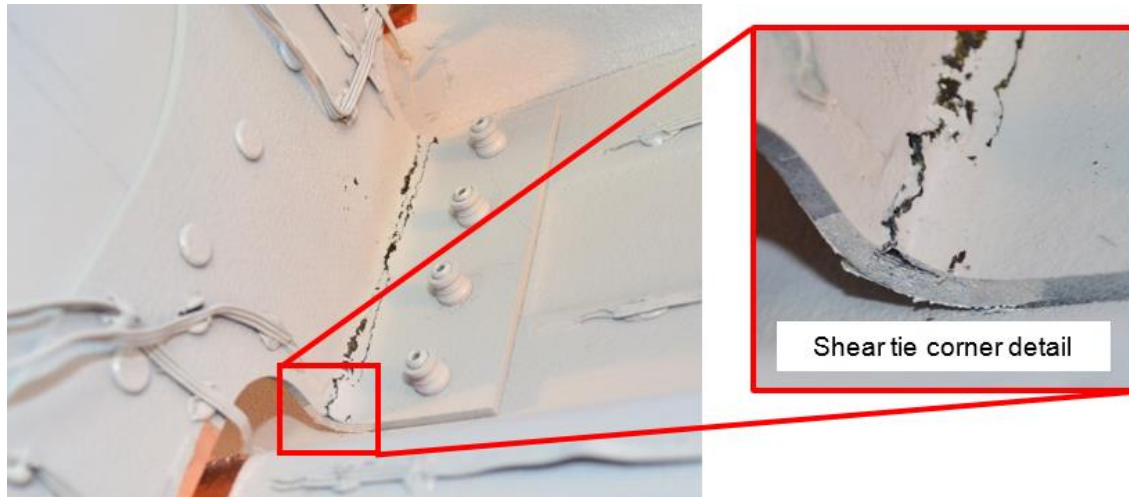
### 3.12.2 LOC3-2 DAMAGE SEQUENCE

The load-displacement curve for Loc3-2 test is shown in Figure 3.90 with the main event notification.



**Figure 3.90: Force vs external displacement for Loc3-2 test.**

During Loc3-2\_Pre-test, due to a shake table controller mishap, the load level achieved was somewhat equivalent to Loc3-1\_L2. This resulted in shear tie crack along radius region as shown in Figure 3.91. In close-up view of Figure 3.91, delamination was captured in shear tie radius region as shown.

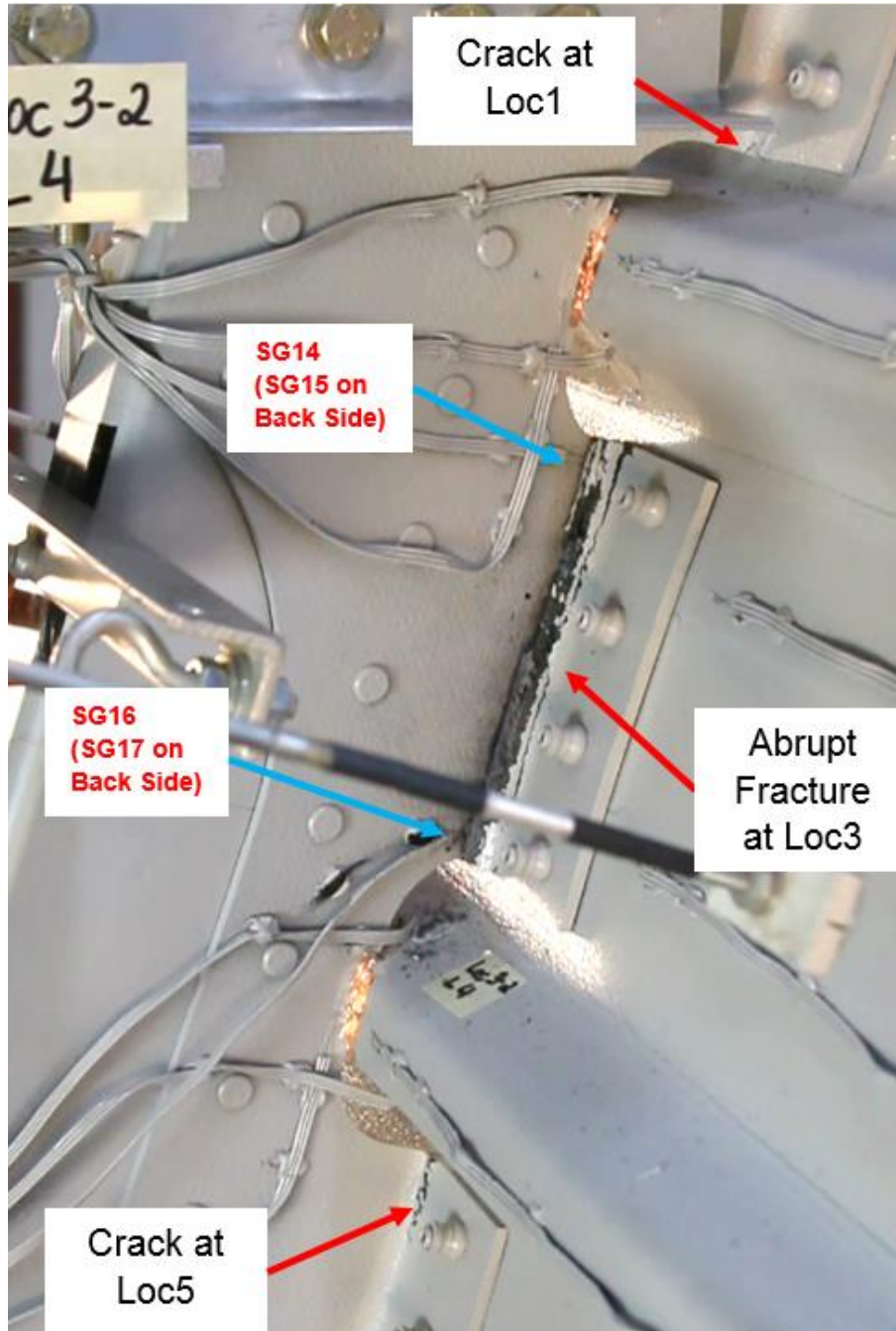


**Figure 3.91: Loc3-2\_Preload damage – radius delamination detected.**

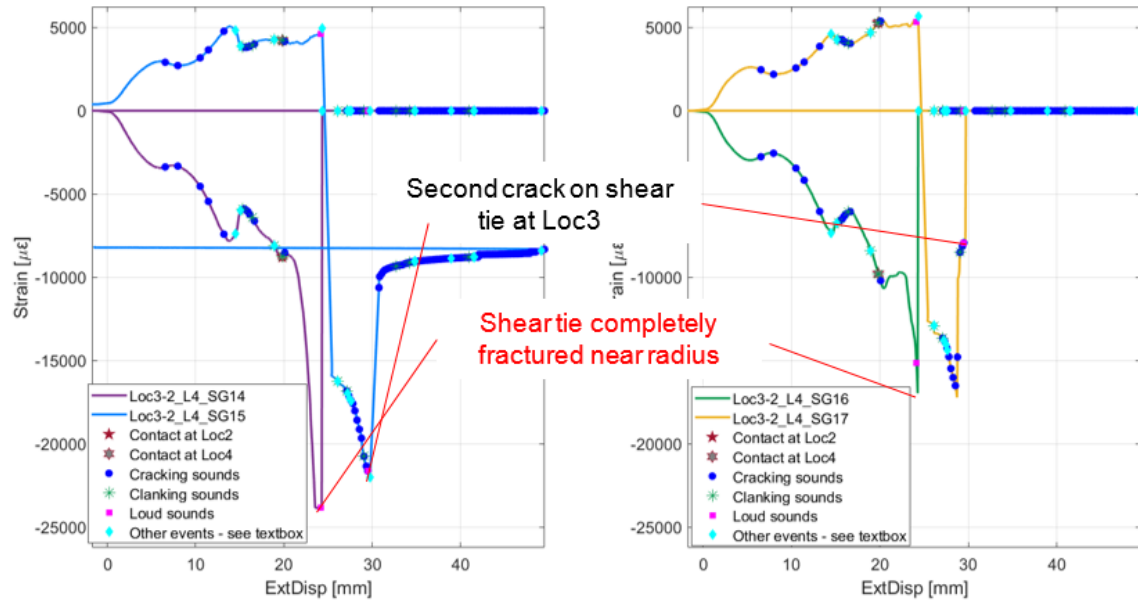
Because of the mishap resulting in scarcity of data points, the test results of Loc3-1 specimen were substituted for the preload results of Loc3-2 test. The key results are described here after the event of shear tie-stringer contact as notified in Figure 3.90.

The pre-existing crack on shear tie radius region (from Loc3-2\_Preload) continued to increase, until complete fracture along the radius region as shown in Figure 3.92. This was captured on shear tie strain curves from back-to-back SG14-15 and SG16-17 (Figure 3.92 and Figure 3.93) showing abrupt strain change. Simultaneous to this catastrophic failure, a crack initiated on shear tie lower corner at Loc1 and upper shear tie corner at Loc5, as observable on Figure 3.92.





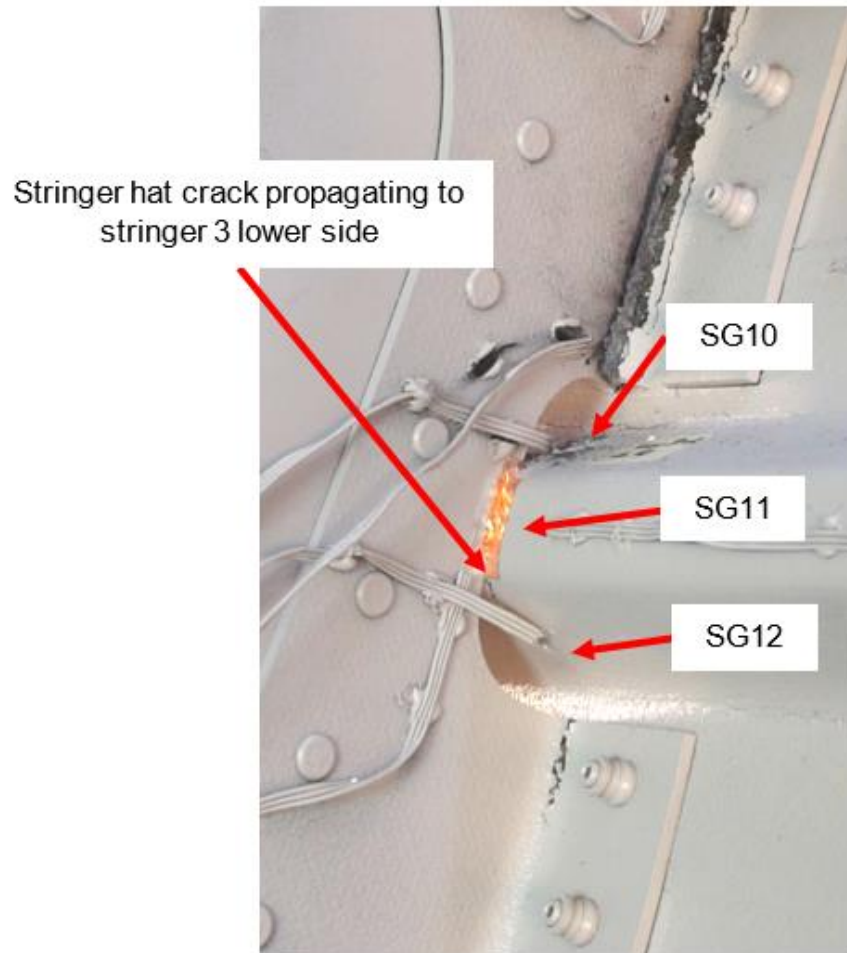
**Figure 3.92: Complete fracture along the shear tie radius during Loc3-2\_L4 test.**



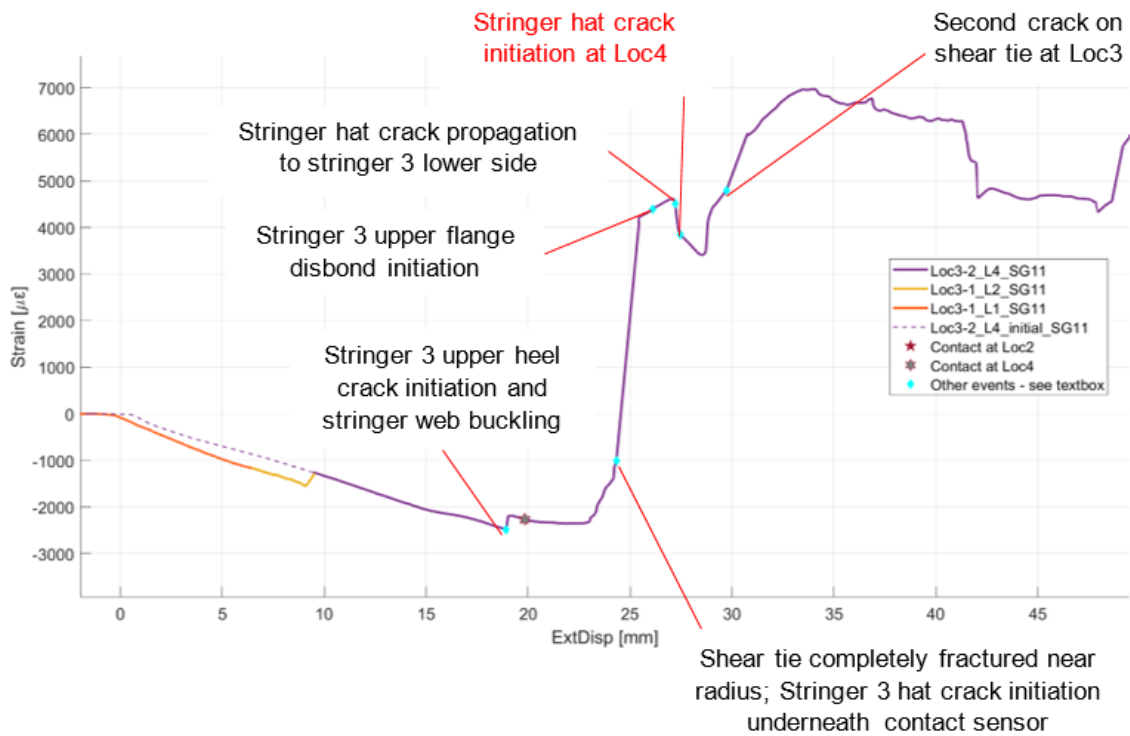
**Figure 3.93: Back-to-back SG14-15 and SG16-17.**

Due to the skin-stringer disbond from the early stage of loading, with clear evidence, the stringer hat damage occurred by the contact with shear tie, right after shear tie radius fracture. This event occurred after the second crack on shear tie web in Loc3-1 tests.

As shown in Figure 3.94, stringer hat was cut by shear tie web penetration, and it is captured in the strain curves from SG11 and SG12. Here, the strain curve from SG11 is provided in Figure 3.95. The stringer hat damage initiation shows a drop in strain.

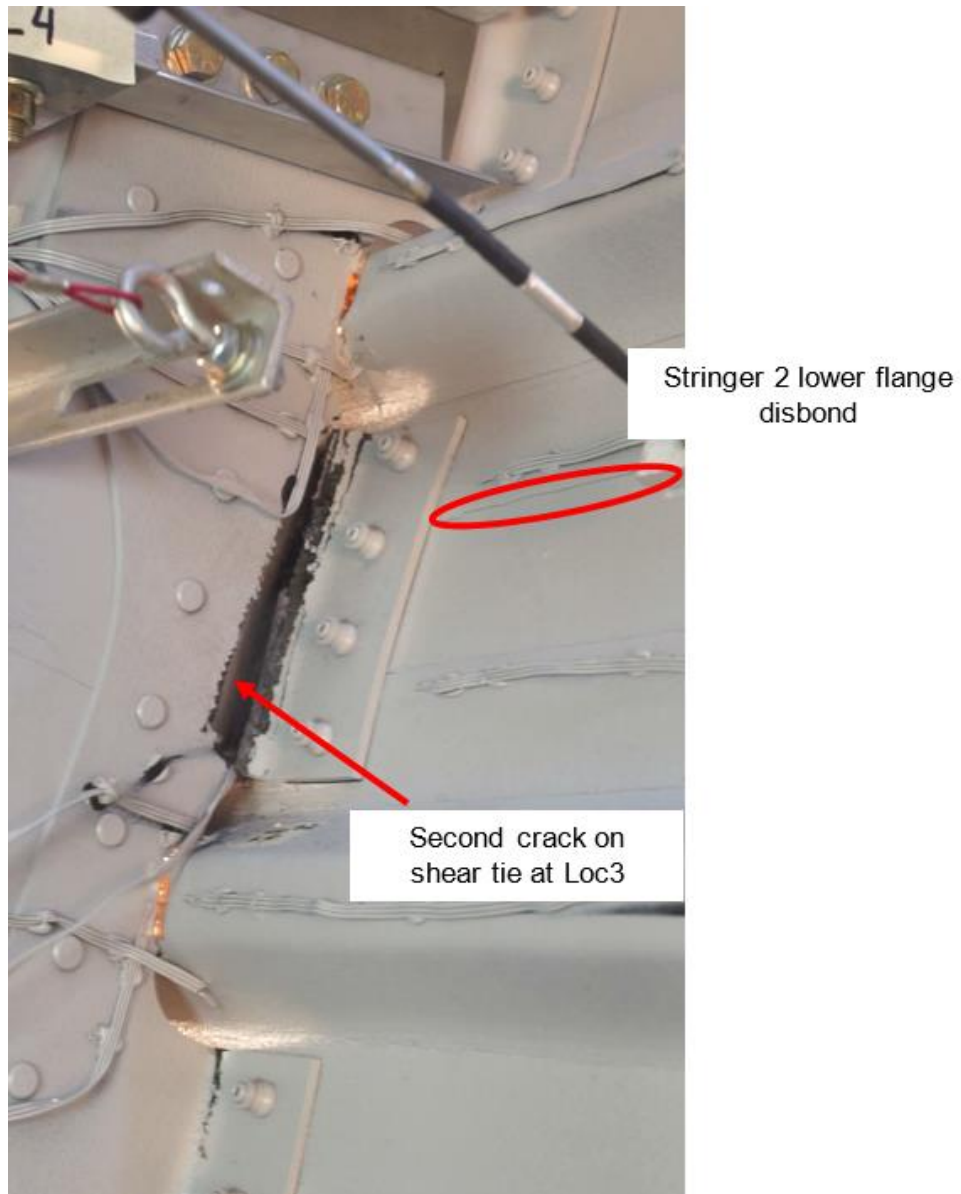


**Figure 3.94: Stringer hat cut at Loc4 by shear tie penetration.**



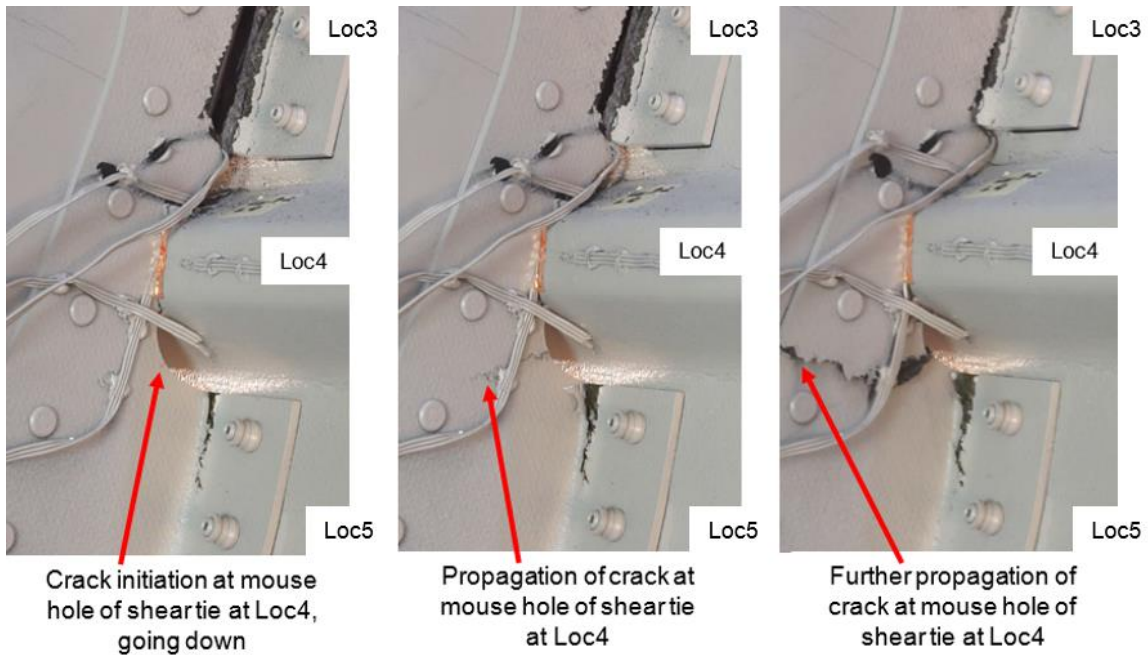
**Figure 3.95: Strain curve from SG11 installed on Str. hat at Loc4.**

As load increased, the second crack occurred on the shear tie web below the outer flange of C-frame (Figure 3.96). It was due to shear tie web buckling by the eccentric (effect of the eccentric shear center of open C section) compressive loading. This was captured on shear tie strain curves from back-to-back gauges, SG14-15 and SG16-17 (Figure 3.93) showing abrupt strain change.



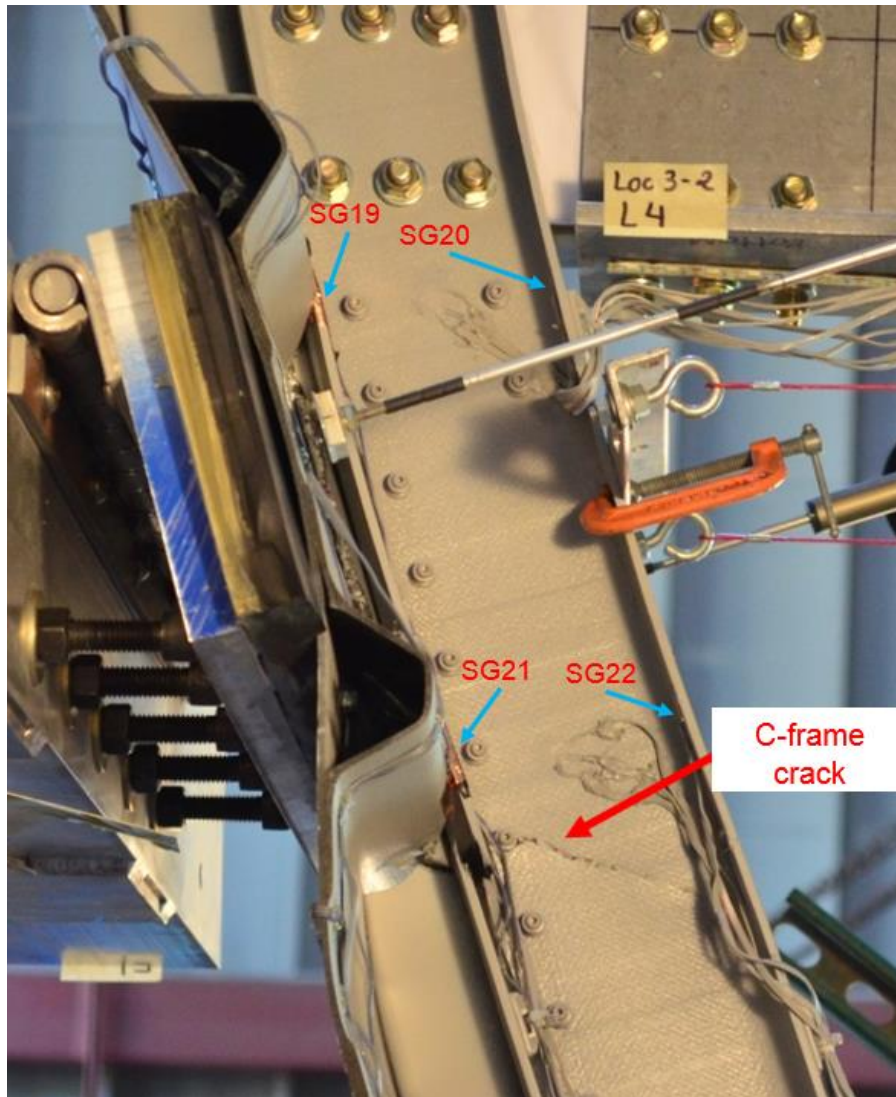
**Figure 3.96: Second fracture on shear tie web due to buckling by eccentric compressive load during Loc3-2\_L4 test.**

With the second shear tie web fracture at Loc3 and increasing load, shear tie kept penetrating stringers at Loc2 and Loc4 causing severe damages on both components until C-frame failure. Figure 3.97 shows the damage mechanism leaving severe damage on both components crushing each other.



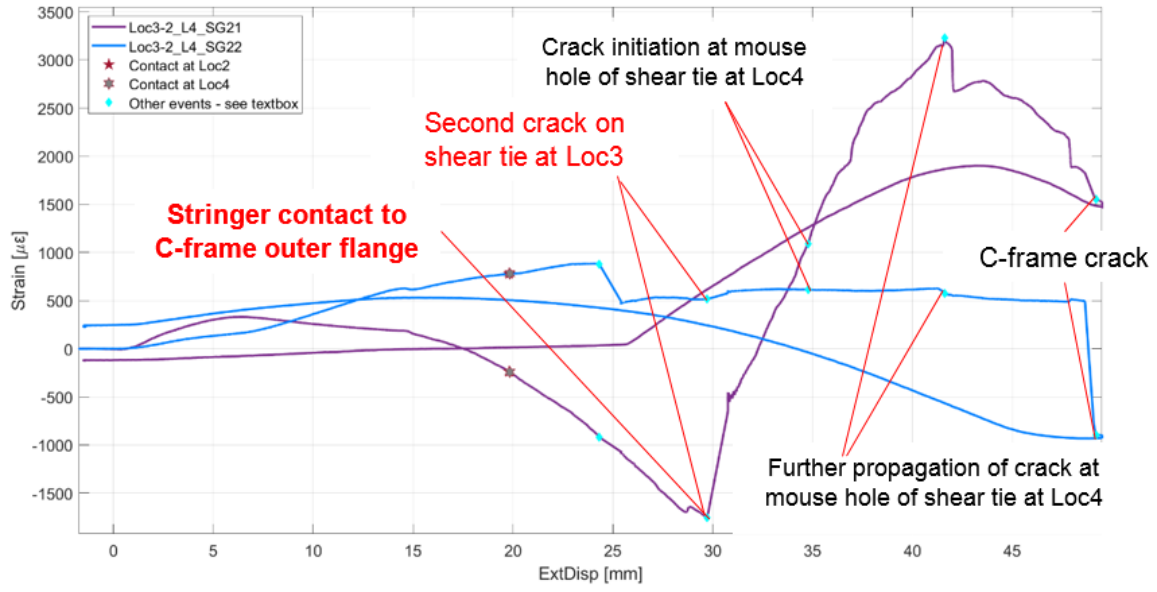
**Figure 3.97: Shear tie crack propagation and stringer cut at Loc4 mouse hole.**

When shear tie web was fractured secondly at Loc3, stringer at Loc4 contacted and started to push the C-frame outer flange causing the C-frame local web twisting and buckling initiated at a Hi-Lok bolt on the C-frame web at Loc4. Then, abrupt diagonal web cracking occurred starting at the Hi-Lok bolt by stress concentration under combined shear and bolt pulling (Figure 3.98). This mechanism was confirmed through video examination, and it showed the exact same failure mechanism observed in Loc4 tests.

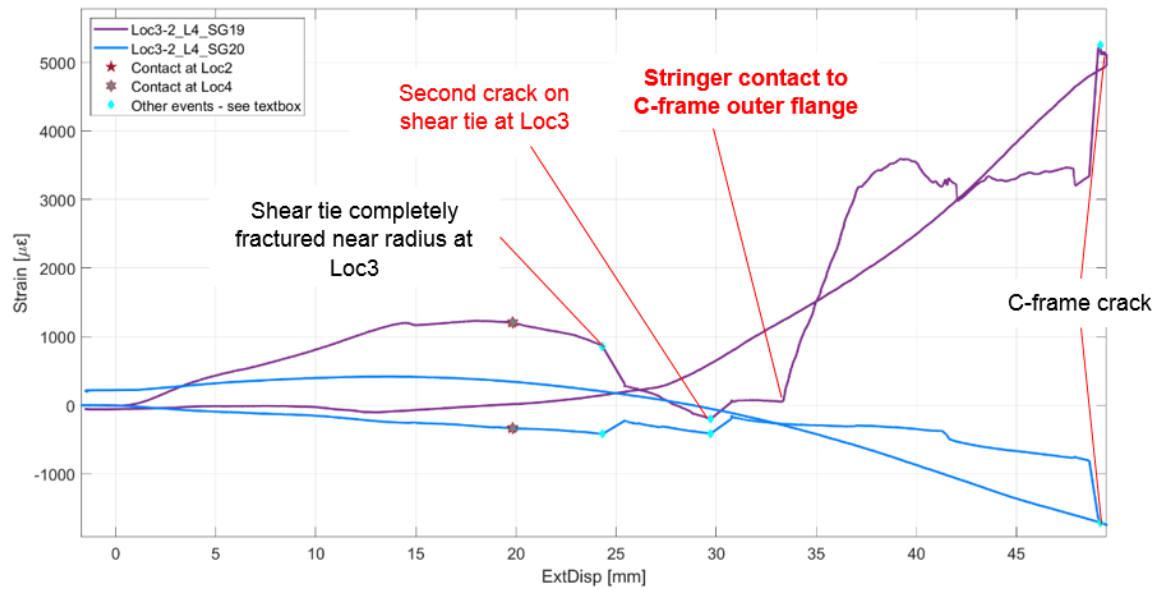


**Figure 3.98: C-frame crack at Loc4 under combined shear and bolt pulling state.**

The stringer-C-frame contact at Loc4 and Loc2 is confirmed the strain curves from SG21 and SG19, respectively (Figure 3.99 and Figure 3.100). The location of SG19 and SG21 is shown in Figure 3.76 and Figure 3.98, and all linear gauges were installed on the inner surface of flanges. After stringer contact, the curvature of C-frame outer flanges at Loc4 and Loc2 started to be decreasing because the stringer kept pushing the outer flanges.



**Figure 3.99: Bending strain curves from linear gauges at Loc4 flanges.**



**Figure 3.100: Bending strain curves from linear gauges at Loc2 flanges.**



C-frame in-plane shear stress level needs to be checked from rosette RS1 and RS2 at Loc2 and Loc4, respectively.

After Loc3-2 test, through visual inspection, barely visible skin crack was observed on outer skin surface at Loc3 skin bolt with rubber bumper mark and paint chipping on bolts as shown in Figure 3.101.



**Figure 3.101: Barely visible skin crack at skin bolt after Loc3-2 test.**

### 3.12.3 EXPERIMENTAL CONCLUSION – LOC3

Damage initiated at the loading location (Loc3) in the shear tie radius region showing fiber crushing failure mode which involves delamination. As load increased, the radius region was fractured abruptly in entire radius at Loc3, and then shear tie web

fracture was followed due to buckling by eccentric compressive loading. This damage led to cutting of the stringer hat as well as additional shear tie cracking at mouse hole due to the contact and penetration between the components at Loc2 and Loc4. With further loading, the increasing damage level at contact locations led to direct stringer contact with the outer flanges of the C-frame. Lastly, the abrupt C-frame fracture was contact induced failure due to direct stringer push to C-frame flange at Loc4 showing diagonal cracking starting at the Hi-Lok bolt on the C-frame web.

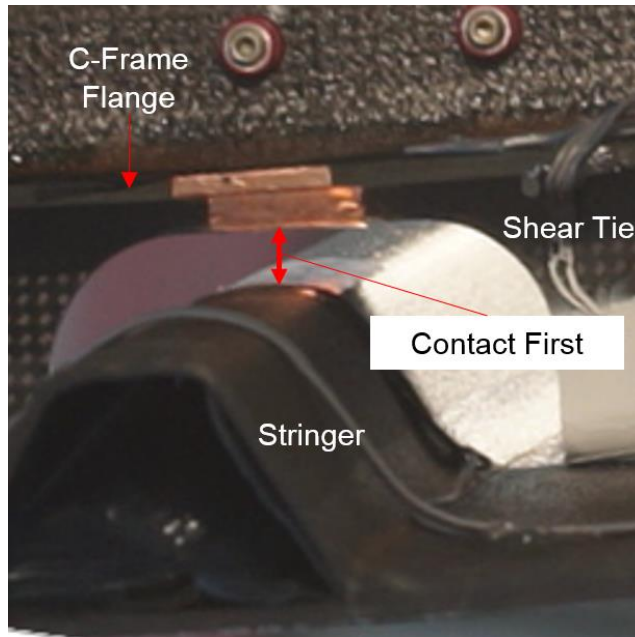
### 3.13 EXPERIMENTAL CONCLUSIONS

To understand the damage formation and mechanism to more realistic composite fuselage structures during HEWABI events near the floor joint, a series of large-scale specimens were built, and blunt loading tests was conducted. The damage phenomena were assessed including damage initiation, location, modes, sequence, extent, and external damage detectability through the examination of video record, visual inspection, A-scan, and strain data.

Damage initiated at the shear tie radius closest to the loading location, showing combined delamination and fiber crushing failure modes. With further loading, shear tie-stringer contact occurred. This contact leads to cutting of the stringer hat due to the shear tie contact and penetration into the stringer hats, which subsequently prevents the C-frame and shear tie assembly from deforming laterally. With further loading, extensive shear tie and stringer hat damage occurred, leading to stringer-C-frame contact. Lastly,

the C-frame was fractured by the stringer contact showing combined shear and bolt pulling (by local twisting) failure modes.

The loading locations explored were quite stiff due to the floor structure interaction. Shear dominated failure with significant internal damage in the shear tie, stringer, and C-frame developed. However, the damage extent is more localized in comparison with the 1<sup>st</sup> generation Frame03 (dynamic) test's broad damage extent in which large rotation of the C-frame resulted in damage near the far-away boundary conditions fixtures [8, 11]. In the 2<sup>nd</sup> generation test panels, the C-frame was stiffened with continuous and thicker shear ties (2.5 mm thickness in the 1<sup>st</sup> generation vs. 3.5 mm thickness in the 2<sup>nd</sup> generation). Thus, the C-frame's lateral movement and rotation was minimized. In comparison with the 1<sup>st</sup> generation Frame01 and Frame02 (quasi-static) tests, the same C-frame failure mechanism was observed without large rotation of C-frame in these 2<sup>nd</sup> generation tests. That is because severe damage to the shear tie led to contact between the stringer and C-frame and ultimately resulting in C-frame failure. However, as shown in Figure 3.102, in the 2<sup>nd</sup> generation specimen, the geometry of component assembly at the mouse hole led to delay of stringer-C-frame contact as shear tie contacted the stringer first and failure progressed for a while by the geometry interaction.



**Figure 3.102: Geometry interaction at mouse hole.**

As studied through the large-scale experiments, the shear tie is the key component governing damage extent influencing other components' failure mode and the overall structural behavior. Understanding the role of the shear tie, how design choices affect subsequent damage modes under HEWABI events, allows for improved damage-resistant designs, informed definition of damage extent for use in damage tolerance studies, and knowledge about where inspection and repair focus must be applied.

For future work, the loading rate effect should be examined conducting true dynamic tests for the 2<sup>nd</sup> generation large-scale experiments. For skin-stringer disbond observed in Loc3-2 test, multiple circumferential components with wider skin may be considered.

Chapter 3, in part is currently being prepared for submission for publication of the material. Nam, Moonhee; Wiggers de Souza, Chaiane and Kim, Hyonny. Nam, Moonhee was the primary investigator and author of this material.

## 4 EXPERIMENT AND FE MODELING OF C-FRAME FAILURE

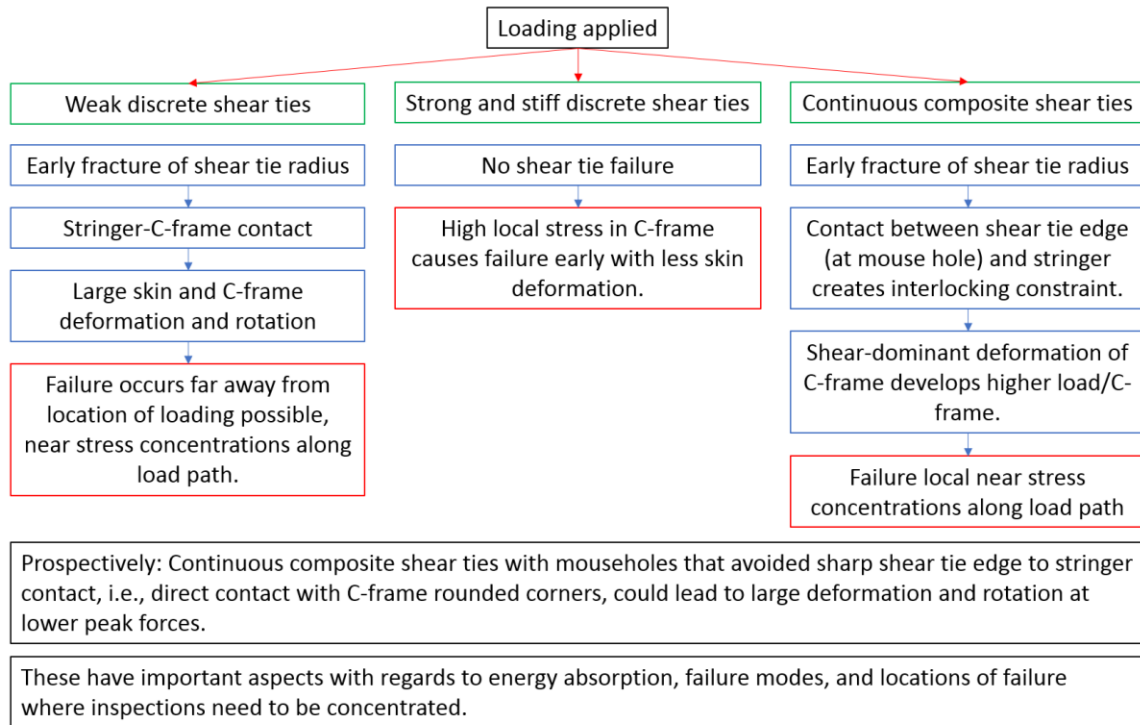
---

In the fuselage structure, the C-frame is a main load-bearing component maintaining the cross-section geometry during operational loading and reacts against the transverse load from HEWABI events. It resists the transverse load by reinforcing the skin outer panel. If it is severely damaged, overall structural system is compromised leading to possible failure during flight operation. Therefore, the investigation of C-frame failure is of high importance, and it was not deeply studied (particularly, the analysis of) as part of the 1<sup>st</sup> generation HEWABI research [8, 11].

From the results of large-scale experiments, several key failure modes were observed in the C-frames shown in Figure 2.4, Figure 2.5, Figure 2.6, Figure 3.64, Figure 3.65, and Figure 3.98. In the 1<sup>st</sup> generation Phase 1 panel tests and in the 2<sup>nd</sup> generation panel tests, after shear tie fracture, the C-frame failed by stringer contact, causing both local cracking at these locations of high contact stress. In the 1<sup>st</sup> generation Phase 2 Frame03 test, after shear tie fracture, the C-frame failed by large rotation losing stability. The faraway failure occurred near the boundaries along the load paths. In the 1<sup>st</sup> generation Phase 2 Frame04-2 test, the C-frame failed by direct shear from the strong shear ties [8, 11].

Through the observations across all large-scale tests conducted, the C-frame failure can be classified with the presence of large rotation of the C-frame by the influence of shear tie (the shear tie transfers the transverse load to C-frame as well as stabilizes C-frame laterally) and interaction with stringer. In the 2<sup>nd</sup> generation large-size

test specimens, the large deformation (particularly rotation) of the C-frame did not occur because of the usage of continuous and thicker shear tie reflecting the realistic design found in some composite aircraft fuselage structures in current service. These stiffer shear ties in the 2nd generation specimen also interacted with the C-frame in an interlocking manner, due to shear tie edge to stringer hat penetration (see Figure 3.72), such that global rotation of the C-frame was constrained. Shear tie stiffness can also result in dramatically different failure modes, for example, in the 1<sup>st</sup> generation Frame04-2 test, the strong discrete 7075 aluminum shear ties did not allow C-frame's large deformation. Those C-frames showed local failure initiated quite early in the test, at or near a local bolt. On the other hand, in the 1<sup>st</sup> generation Frame03 test which had softer and relatively weaker composite shear ties, losing discrete shear ties during the early stage of the test loading allowed the large rotation of C-frames, and consequently C-frames failed near the boundary fixtures. In Figure 4.1, the flow chart is described about how C-frame failure could develop and how it is affected by shear ties.



**Figure 4.1: C-frames failure development by the influence of three types of shear ties.**

Here, research focused on C-frame failure will be described. Topics include (i) combined bending-twisting failure observed in the 1st generation Phase 2 Frame03 test [8, 11] (ii) direct shear failure of the C-frame observed in Phase 2 Frame04-2 test [8, 11]. For shear and bolt pulling loading states (by stringer contact and eccentric compression) observed in the 2<sup>nd</sup> generation Loc3 and Loc4 tests will be discussed at the end of Section 4.2 with the future work plan.



## 4.1 BENDING AND TWISTING FAILURE OBSERVED IN FRAME03 TEST

As shown in Figure 4.2, C-frames were fractured near boundary fixtures showing large rotation in combined bending and twisting state by open C-section shear center offset effect, after losing shear ties in the Fram03 test [8, 11]. This section is for completing Frame03 FE simulation by updating frame element FE modeling definition validated through element-level tests. Previous FE simulations included detailed study of the shear tie progressive failure and how it affected global response of these HEWABI test specimens [11], but did not include the final failure mode: frame failure.

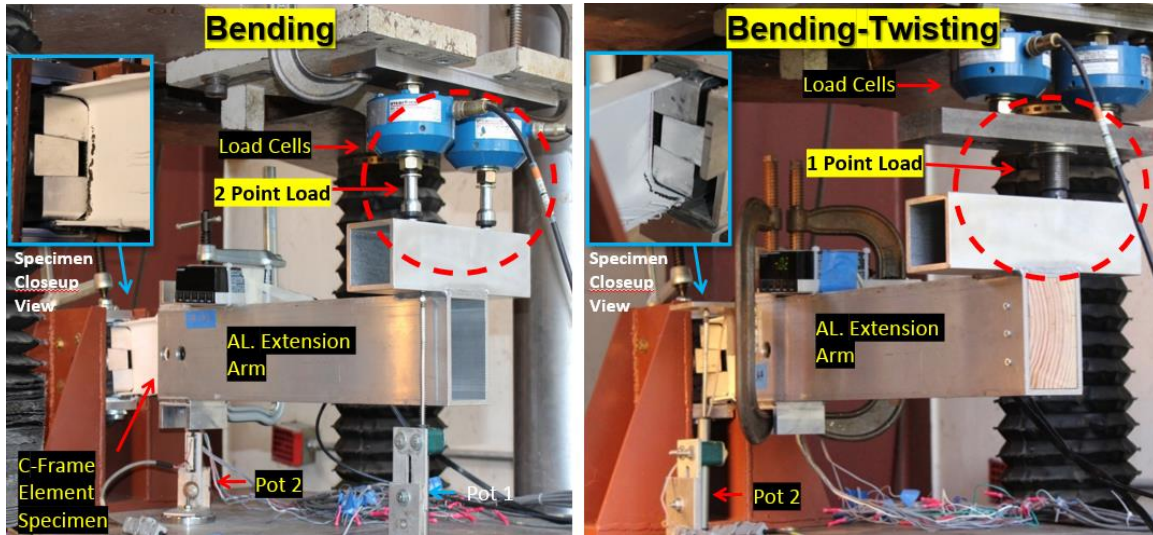


**Figure 4.2: Combined bending-twisting failure in C-frames [8,11].**

### 4.1.1 C-FRAME ELEMENT-LEVEL TESTS

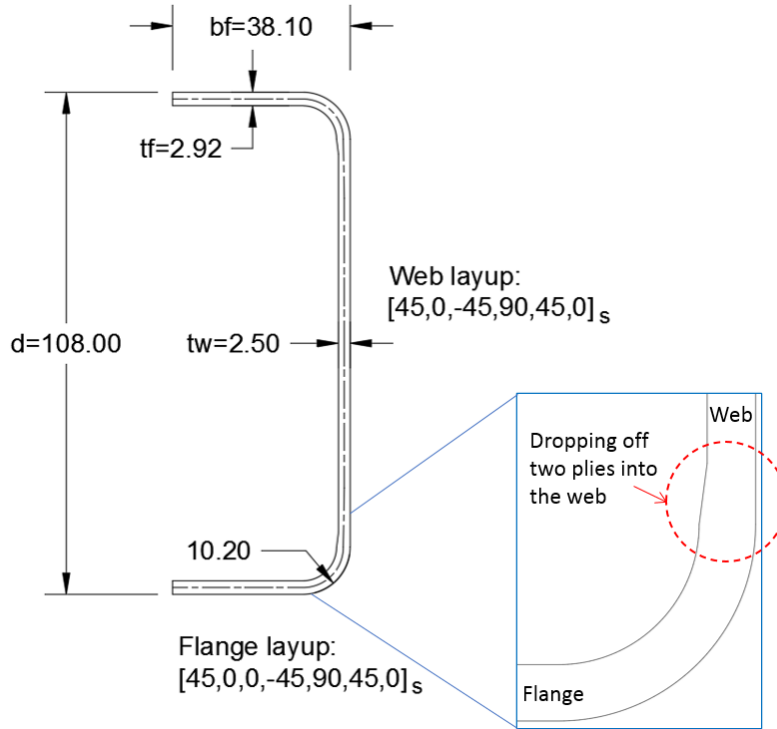
C-frame element testing is directly focused on inducing bending and combined bending-twisting failure mode under simple geometry and loading conditions. Since the C-frame members are difficult and costly to produce, a short section of C-frame beam was inserted into an extension arm (aluminum box beam) and tested as a combined fixed-end cantilever beam. The test setup is shown in Figure 4.3. For bending test, 2 point load

was applied preventing twist. On the other hand, for combined bending-twisting test, one point load was applied through a position away from the shear center, thereby inducing twist.



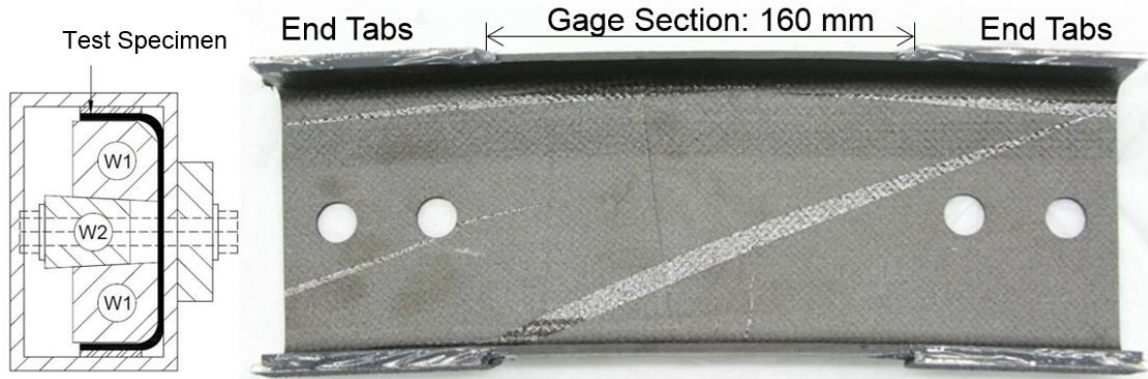
**Figure 4.3: C-frame bending and combined bending-twisting tests.**

Cytec X840/Z60 6k woven carbon/epoxy prepreg was used, and the C-frame's section geometry and layup stacking information is shown in Figure 4.4.



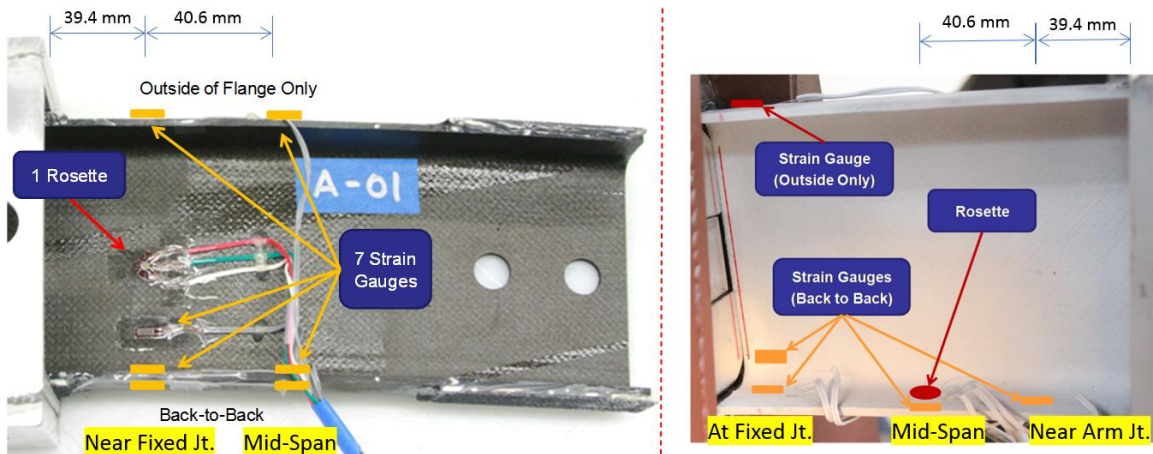
**Figure 4.4: C-frame section information (Dimensions in mm).**

The specimen was cut to length and aluminum tabs were bonded to the outside of the flanges (visible in Figure 4.5) with structural epoxy. These served to fill the gap between the specimen and fixture, as well as provide a padded-up flange to avoid failure due to the wedge-clamping stresses.



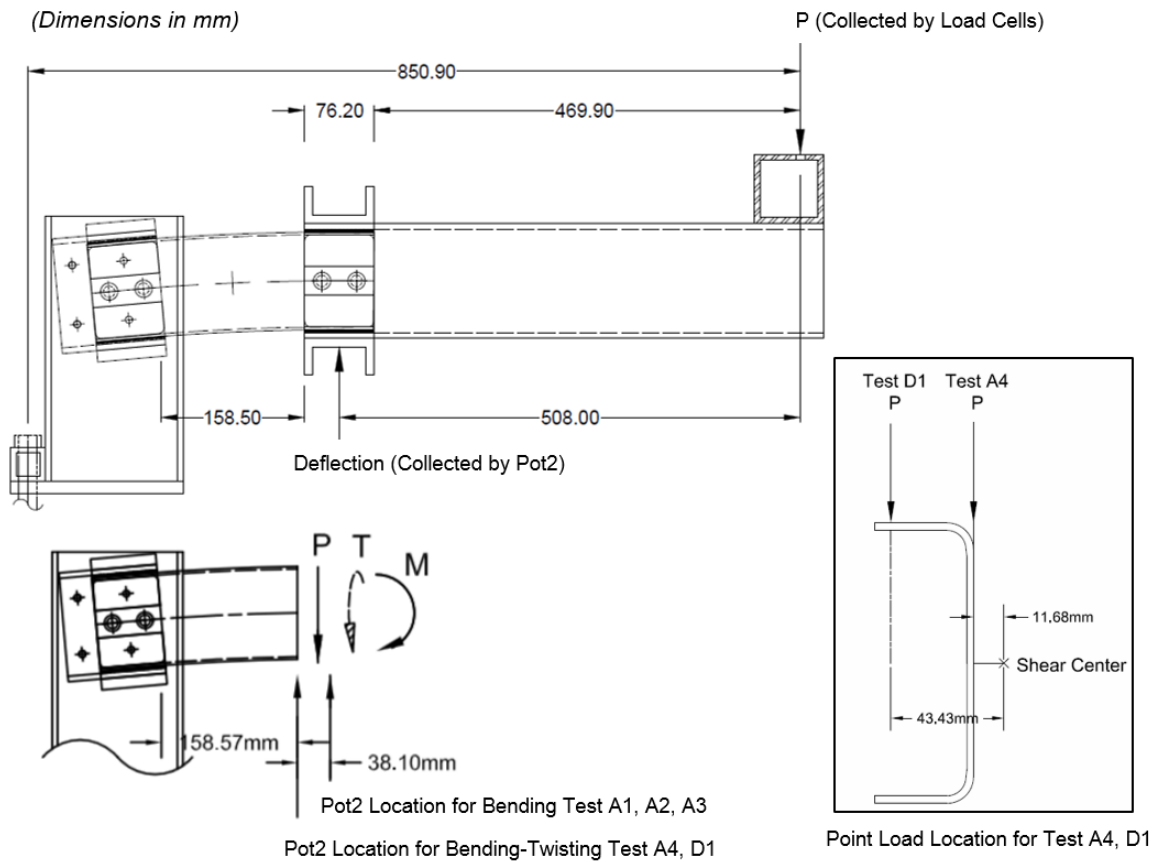
**Figure 4.5: Specimen preparation; wedge grip detail (Left) and specimen with end tabs bonded to outer flange (Right).**

Figure 4.6 shows the location of applied strain gauges. Seven linear strain gauges and one rosette were applied on bending test specimen. Nine linear strain gauges and one rosette were applied on combined bending-twisting test specimen. Back-to-back strain gauge pair was applied to detect the bottom flange buckling mode.



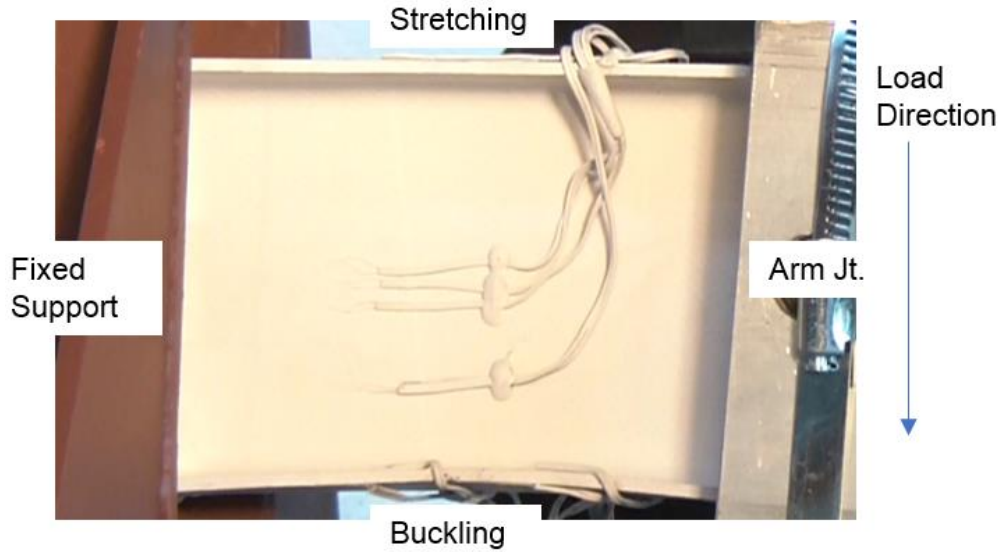
**Figure 4.6: Strain gauge location for bending test (Left) and for combined bending-twisting test (Right).**

The overall specimen configuration and layout are shown in Figure 4.7. Load and displacement data were collected from the load-cell and string pot (labeled as pot2) as shown. In combined bending-twisting tests, the load point location is different between A4 and D1. More torsion was applied in D1 test.



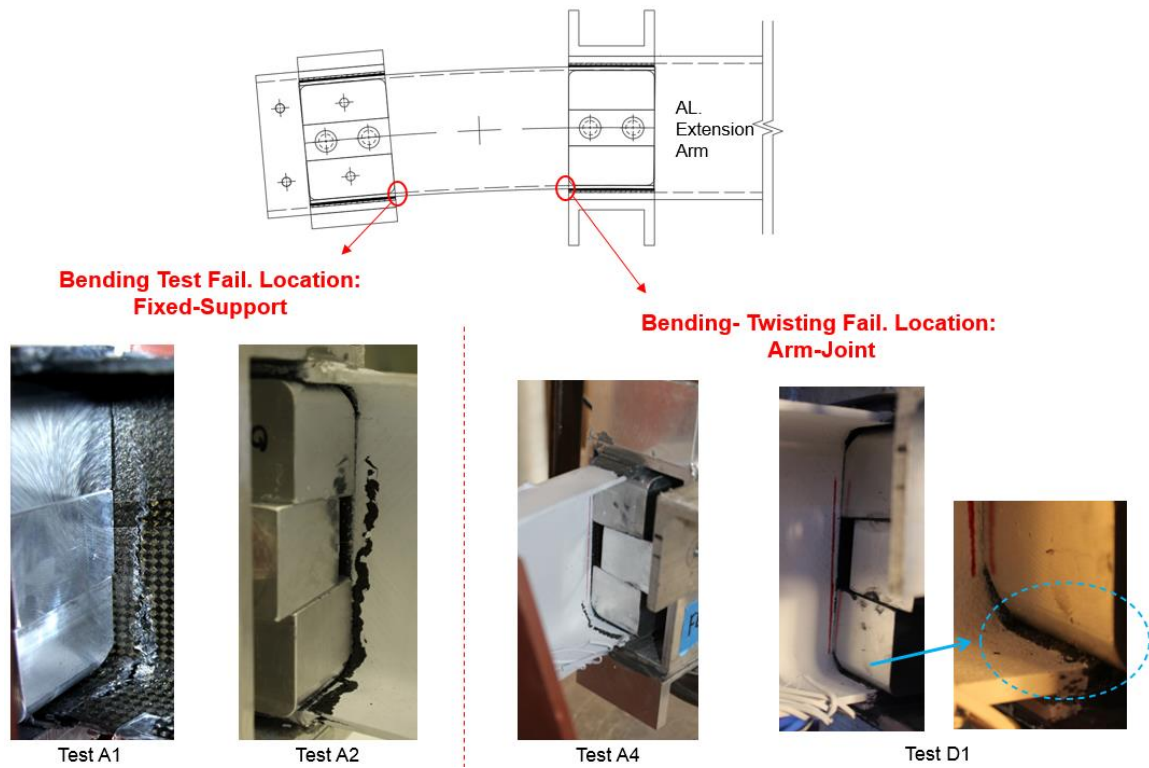
**Figure 4.7: Overall configuration and location of point load and string pot.**

C-frame tests were conducted with quasi-static loading. As load increased, buckling of the compression flange, and stretching of the tension flange were observed as shown in Figure 4.8.



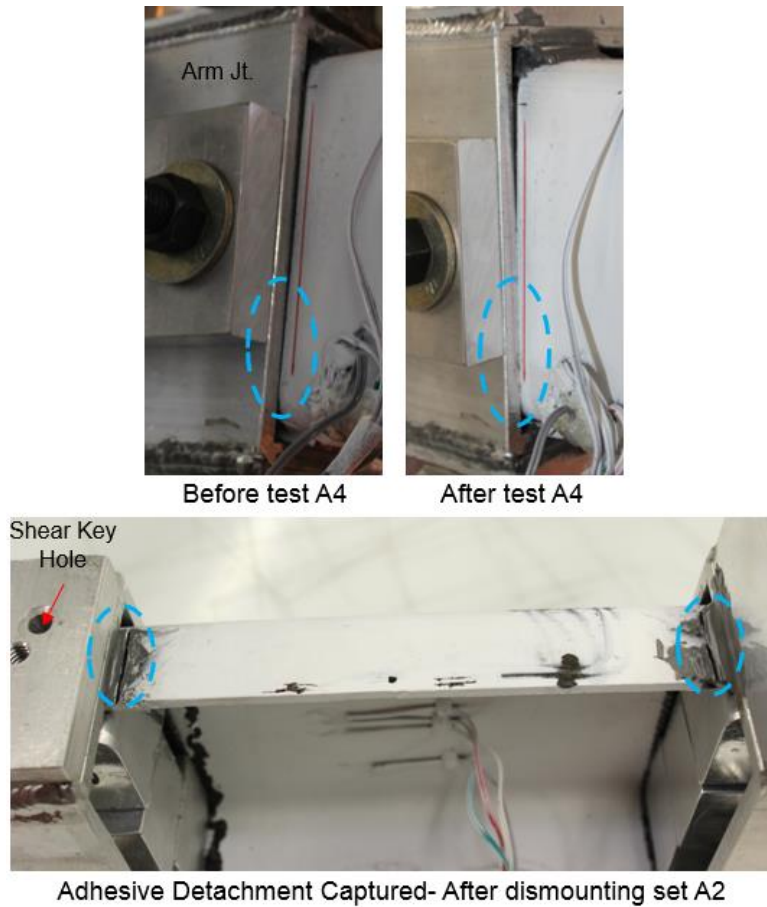
**Figure 4.8: Loaded specimen view; bottom flange buckling prior to failure.**

As shown in Figure 4.9, at the end of tests, the abrupt compression flange fracture with fiber failure occurred adjacent to the fixed-support end and the arm joint for bending and combined bending-twisting test, respectively.



**Figure 4.9: Compression flange fracture with fiber failure.**

During tests, from the early stage to the end of each test, some amount of slip occurred at the contact surfaces between specimen and aluminum rectangular tube at both wedge grip joints (see Figure 4.10). It was the key challenge to overcome in the interpretation of test data. Although C-clamp and shear keys were applied at these joints, slip could not be completely stopped. It affected test results significantly and made hard to compare test results with FEA results.

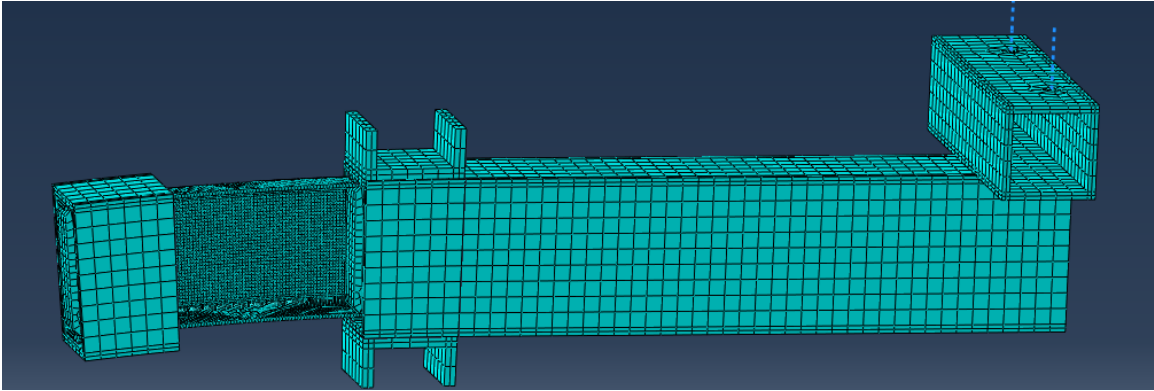


**Figure 4.10: Challenges to controlling slip and adhesive detachment at joints.**

#### 4.1.2 FE MODEL FOR C-FRAME BENDING AND TWISTING TEST

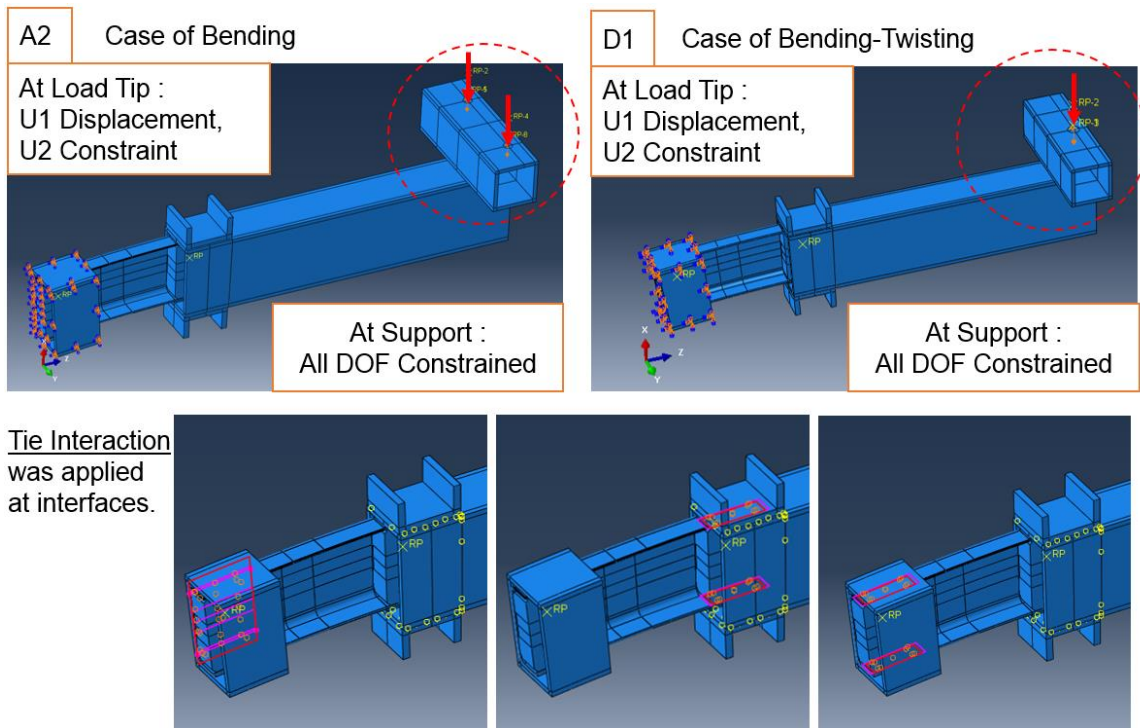
Abaqus/Explicit solver was used for the progressive failure analysis implementing the Hashin-Rotem failure criterion to analyze the C-frame composite component. As shown in Figure 4.11, 8 node reduced integration continuum shell (SC8R) elements, with hourglass control, were applied to composite C-frame with 2.54 mm (0.1 in) mesh size. 8 node reduced integration solid (C3D8R) elements were applied to the metal parts with enhanced hourglass and distortion control, which is to prevent spurious deformation modes and excessive element distortion.





**Figure 4.11: Meshed FE model.**

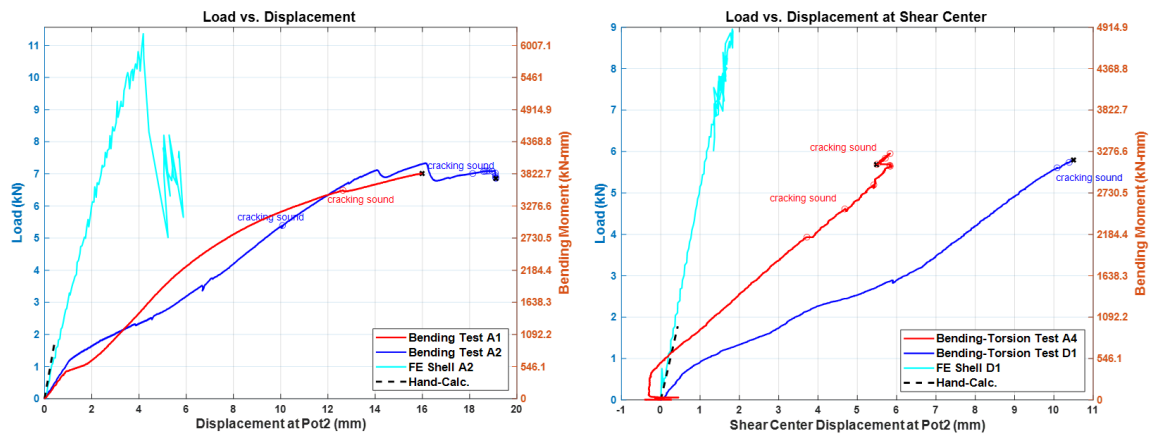
In Figure 4.12, applied boundary conditions are shown with tie-interaction at interfaces.



**Figure 4.12: Applied BCs and tie-interaction at interfaces.**

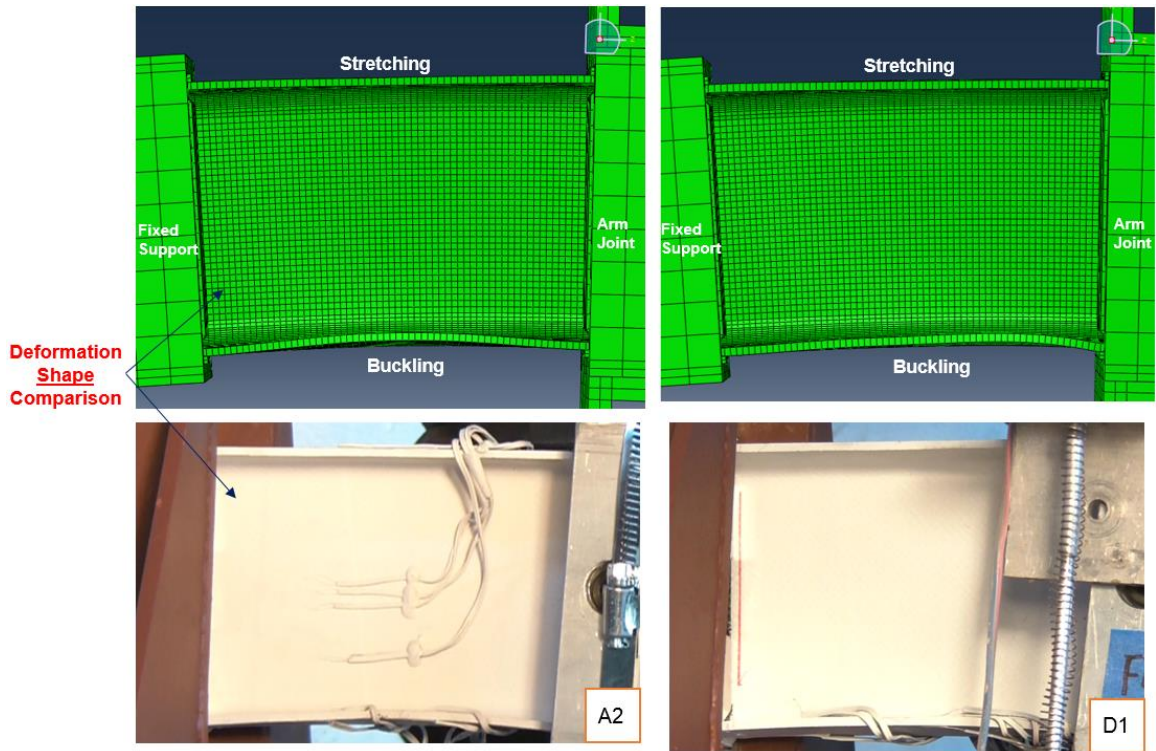
### 4.1.3 RESULT COMPARISON (TEST VERSUS FEA) AND CONCLUSION

The load-displacement curve comparison is shown in Figure 4.13 for bending and combined bending-twisting case. The curves show the significant discrepancy in the stiffness and ultimate strength between test and FEA results. It is mainly caused by the unknown boundary condition related to the friction and slip at the connection joints as mentioned previous section. In the plot, the hand-calculation prediction is from simple elastic load-deflection formula for bending using the effective modulus,  $E1$ , under assumption of homogeneous and isotropic material, and simplified C-section geometry. It shows good agreement with FEA in the initial stiffness as shown.



**Figure 4.13: Load-displacement curves for bending and combined bending-twisting case.**

As shown in Figure 4.14, the FE-predicted deformed shape plot shows the buckling and stretching mode in compression and tension flange, respectively, which matches the experimentally-observed deformation shape prior to failure.



**Figure 4.14: Buckling and stretching deformation shape in bending (Left) and combined bending-twisting (Right).**

From strain curves, the buckling mode as well as stretching mode were confirmed in compression and tension flange, respectively, prior to failure. The strain gauge locations are shown in Figure 4.6. In the left plot of Figure 4.15 and Figure 4.16, the buckling mode in bottom flange was confirmed in both measured and computational (back-to-back) strain curves showing diverging behavior. In the right plot of Figure 4.15 and Figure 4.16, the stretching mode in top flange was confirmed in both measured and computational strain curves. The FE-predicted strain curves qualitatively agree with measured strain curves in both buckling and stretching modes.

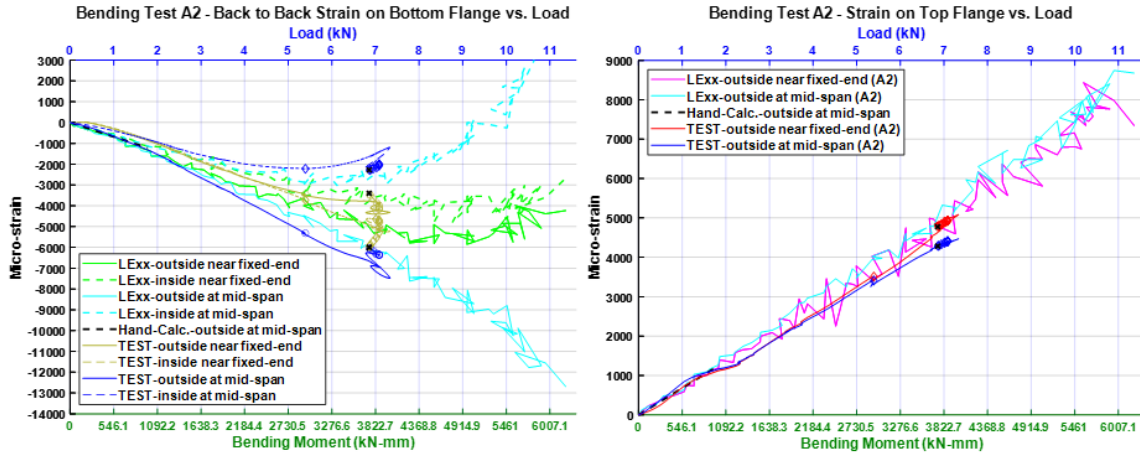


Figure 4.15: Buckling in compression flange and stretching in tension flange of specimen A2.

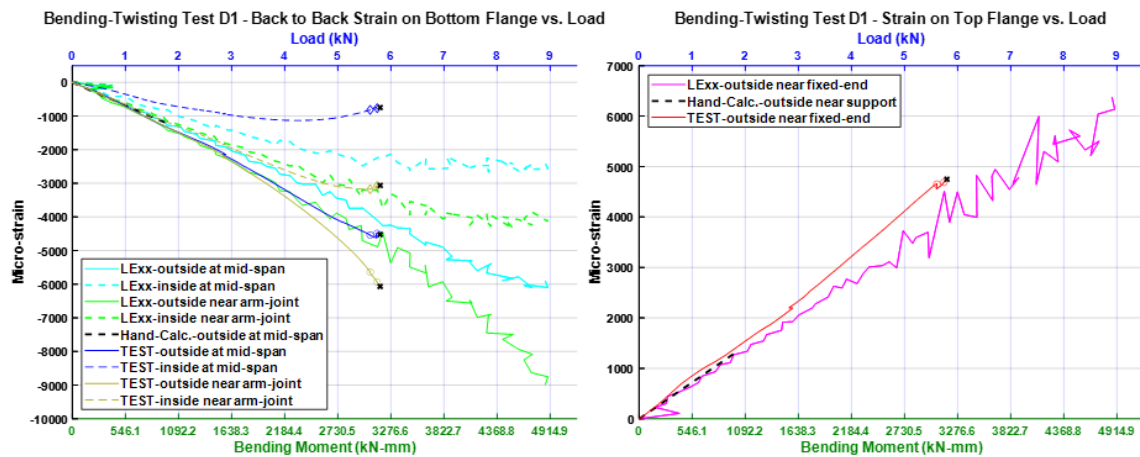


Figure 4.16: Buckling in compression flange and stretching in tension flange of specimen D1.

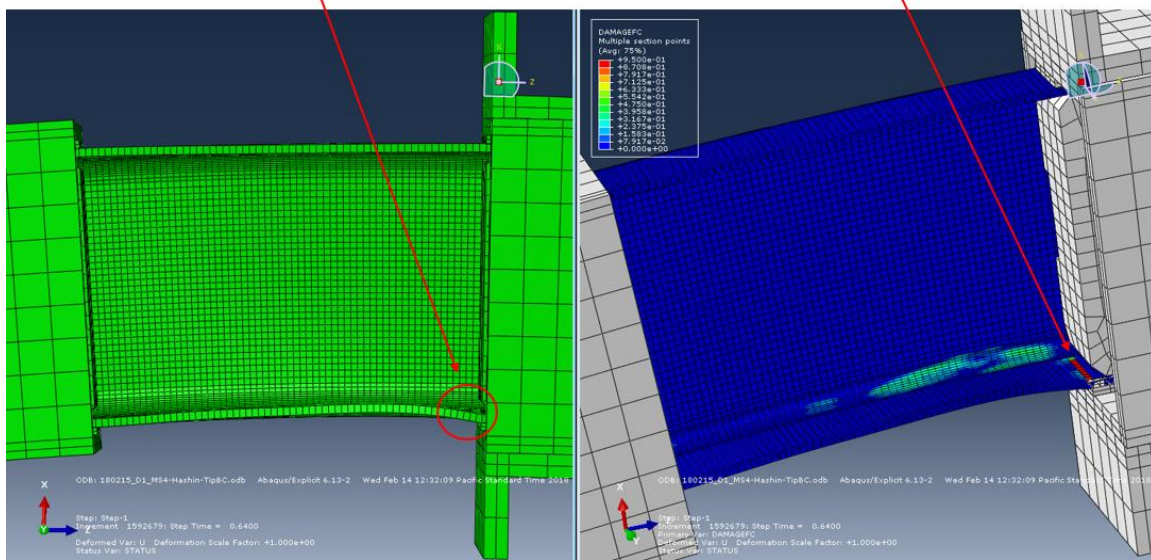
The FE model predicted the fiber failure and corresponding failure locations right after the maximum reaction force in FE simulation. In the bending case, as shown in Figure 4.17, the FE model predicted the fiber tension failure in the tension flange at the fixed support which is different from the results in bending tests. On the other hand, in the combined bending-twisting case, as shown in Figure 4.18, the FE model predicted the



Failure mode right after maximum reaction force:

- Almost all plies (10 layers out of 14) are fully damaged in the compression flange at arm joint.
- No element deletion but sudden bulge at the location

Fiber compression damage in 1 and 2 direction (Damage index: 0.95); No element deletion because not all plies are fully damaged. The model predicts the failure location in the test.

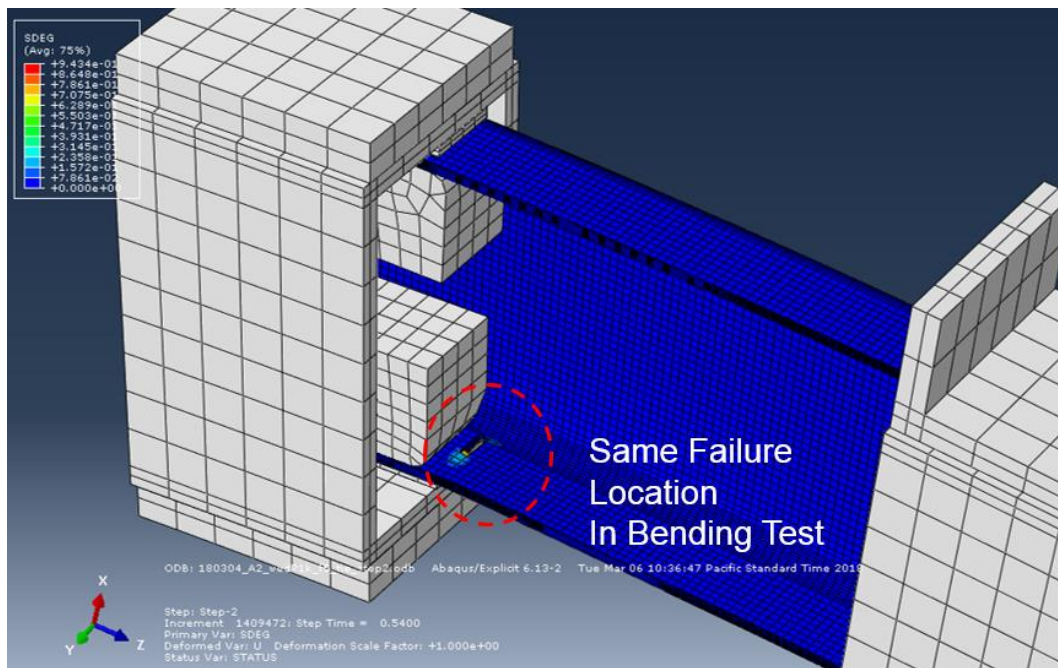


**Figure 4.18: Failure prediction in combined bending-twisting case.**

In conclusion, although the FE model refinement was processed with implementation of Hashin-Rotem failure criterion, the FE model results show significant discrepancy between tests and FE results in the stiffness and ultimate strength. However, buckling and stretching modes in the compression and tension flanges were captured in FE simulation from the computational strain results (the computational strain curve qualitatively agrees with the test results). The FE model predicts the failure location and compression fiber failure mode for combined bending-twisting test but cannot predict the correct failure location for bending test.

It is important to eliminate or minimize uncertainty at boundary fixtures. To eliminate uncertainty in connections, Heimbs [21] modeled cured epoxy adhesive applied at the interface between a specimen and fixture to cover its compliance under load, and a

contact formulation with friction coefficient of 0.5 was applied at the interface between the adhesive and the metal surface in the fixtures. To prove effect of the boundary condition by including slip phenomenon observed in tests, hypothetical wedge pressure and friction coefficient were applied at connection joints in bending failure FE simulation. As shown in Figure 4.19, the FE model predicted the correct failure location.

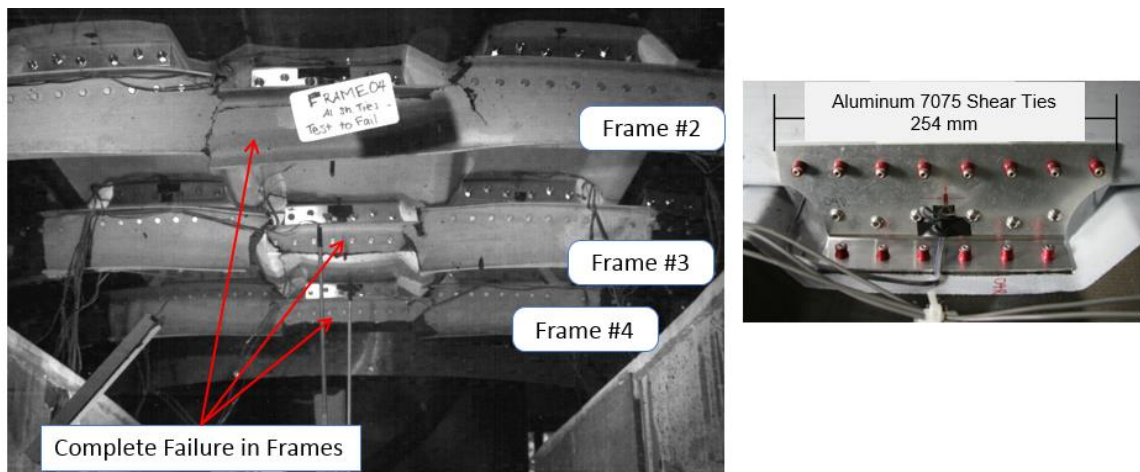


**Figure 4.19: Effect of boundary condition including slip phenomenon.**

## 4.2 DIRECT SHEAR FAILURE OBSERVED IN FRAME04-2 TEST

### 4.2.1 C-FRAME FAILURE MECHANISM OBSERVED IN FRAME04-2 TEST

As shown in Figure 4.20, abrupt fracture in C-frame by the direct shear from the strong shear tie was observed in the previously conducted 1st generation Fram04-2 test [8, 11].

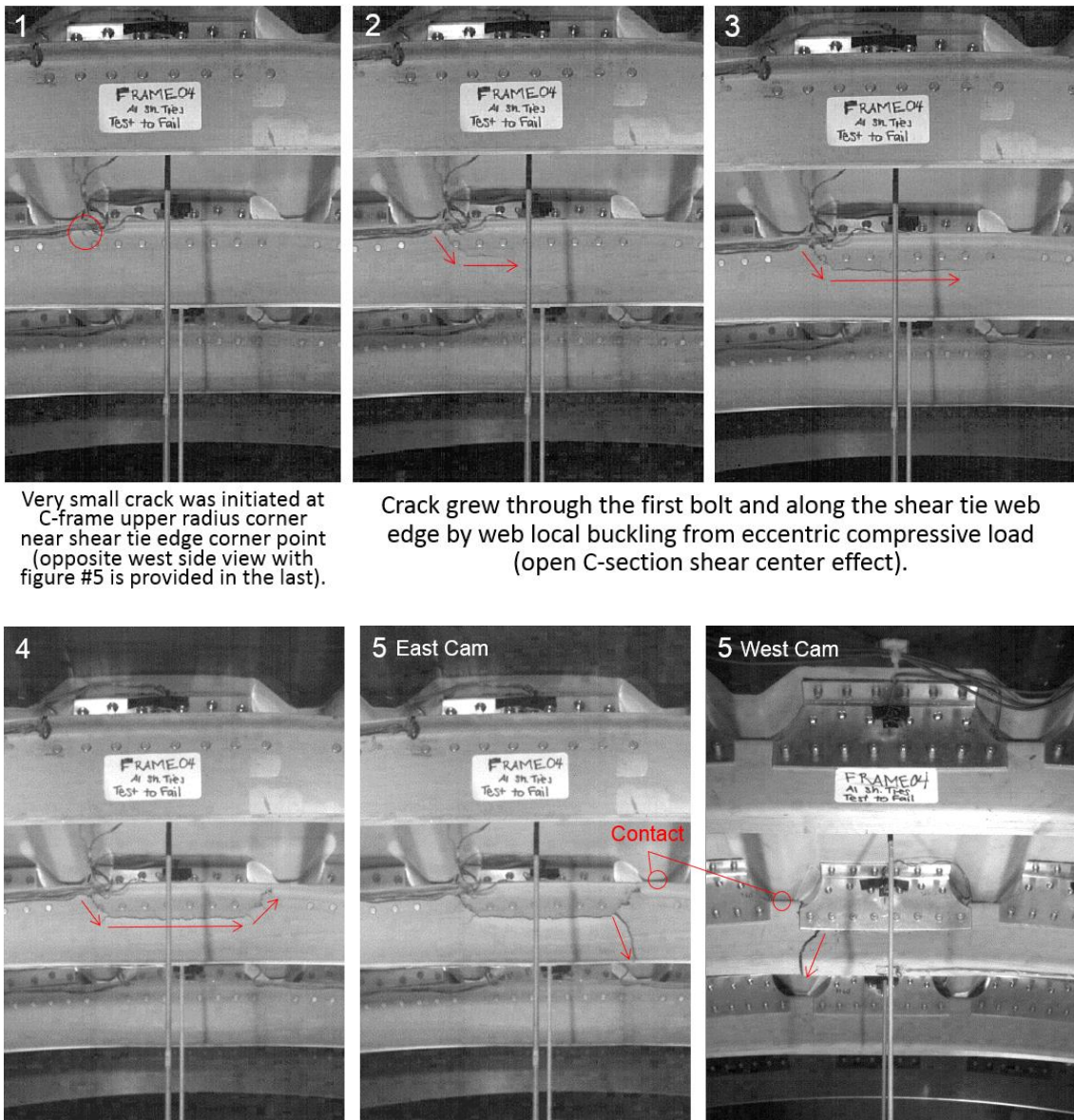


**Figure 4.20: Direct shear failure in C-frames [8,11].**

The C-frame damage mechanism was summarized from the frame by frame examination of the high speed video record as shown in Figure 4.21. As observed in frame number 1, a very small crack was initiated at the C-frame upper radius corner near the shear tie edge corner point. Then, in frame numbers 2 and 3, the crack can be observed to grow through the first bolt and along the shear tie web edge (along the bolt line) by web local buckling from the eccentric compressive load. The reason the crack



initiated one side and propagated to the other side is likely due to different BC at C-frame ends. In frame number 4, the crack propagated through the last bolt to the C-frame upper radius corner. In frame number 5, contact between the C-frame and stringer led to vertical web cracking visible in the image.



Very small crack was initiated at C-frame upper radius corner near shear tie edge corner point (opposite west side view with figure #5 is provided in the last).

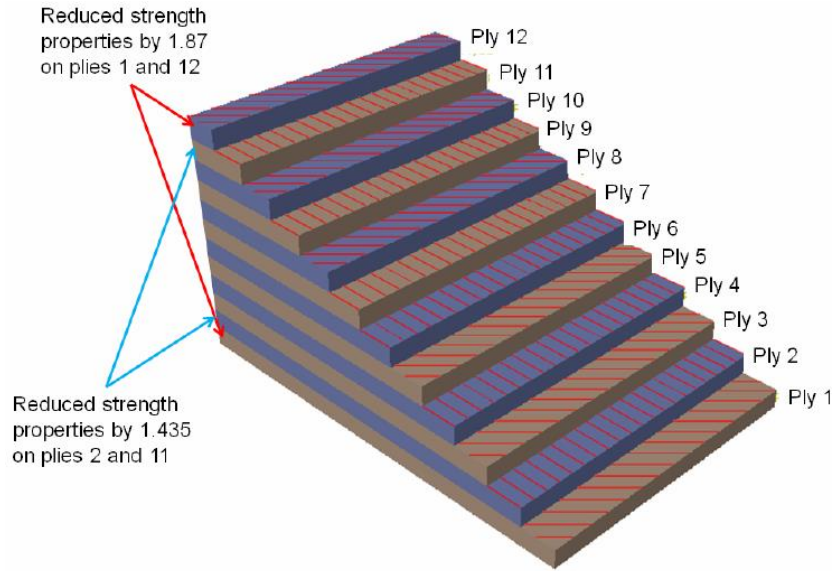
Crack grew through the first bolt and along the shear tie web edge by web local buckling from eccentric compressive load (open C-section shear center effect).

Figure 4.21: C-frame failure mechanism in the 1<sup>st</sup> generation Frame04-2 [8, 11].

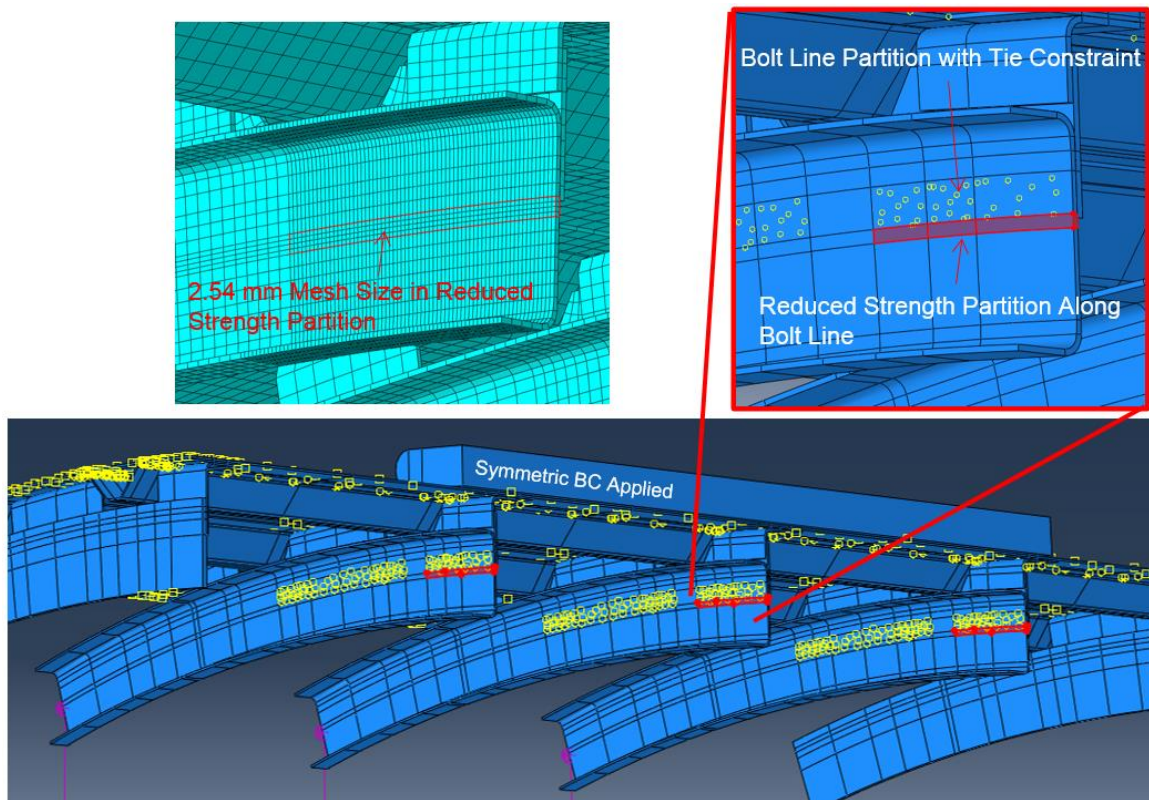
#### 4.2.2 FE MODEL FOR C-FRAME FAILURE IN FRAME04-2 TEST

As it is difficult to conduct element-level tests with equivalent boundary conditions as the C-frame of the fuselage structure, structural-level finite element analysis (FEA) was conducted and compared to the structural-level test data.

Starting with the baseline model made by DeFrancisci [8], the composite shear ties were switched to strong 7075 aluminum shear ties. Abaqus/Explicit solver was used for the progressive failure analysis implementing the Hashin-Rotem failure criterion to C-frame composite components. For all composite components, 8 node reduced integration continuum shell (SC8R) elements, with hourglass control, were applied. The global mesh size was 19 mm based on the mesh sensitivity study in previous research [8]. Importantly, as shown in Figure 4.22 and Figure 4.23, the fasteners were modeled following the effective fastener modeling scheme established by DeFrancisci [8] as strips with tie constraints to contacting surfaces between C-frames and shear ties. This was done as a low-cost alternative to modeling each individual fastener in all the connections between the C-frames and shear ties. The 17.8 mm (0.7 in) width of each fastener strip partition was applied, and a reduced strength partition was applied below the fastener strip partition with 2.54 mm (0.1 in) mesh size as shown.



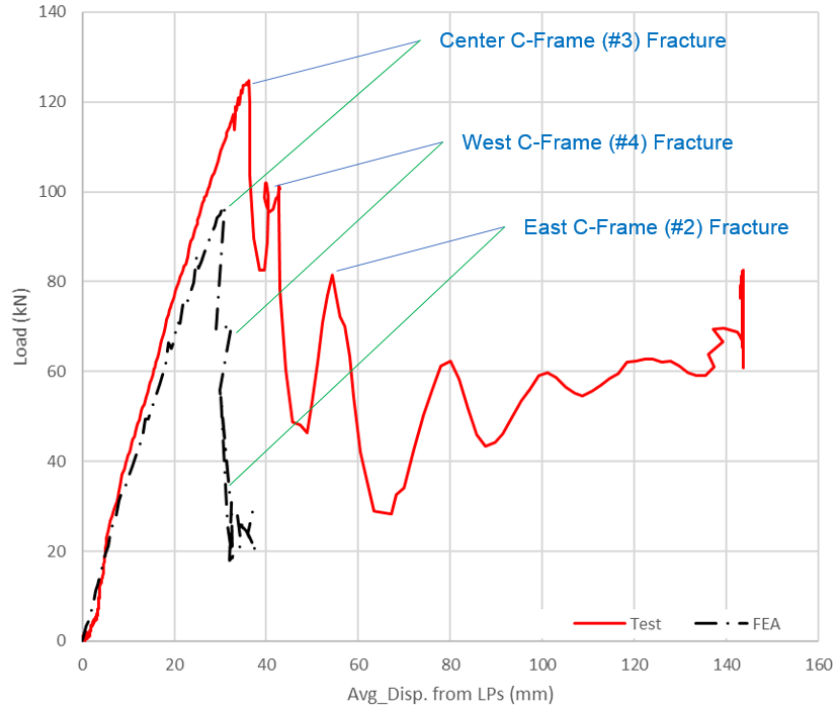
**Figure 4.22: Effective fastener model reduced strength at outer plies [8].**



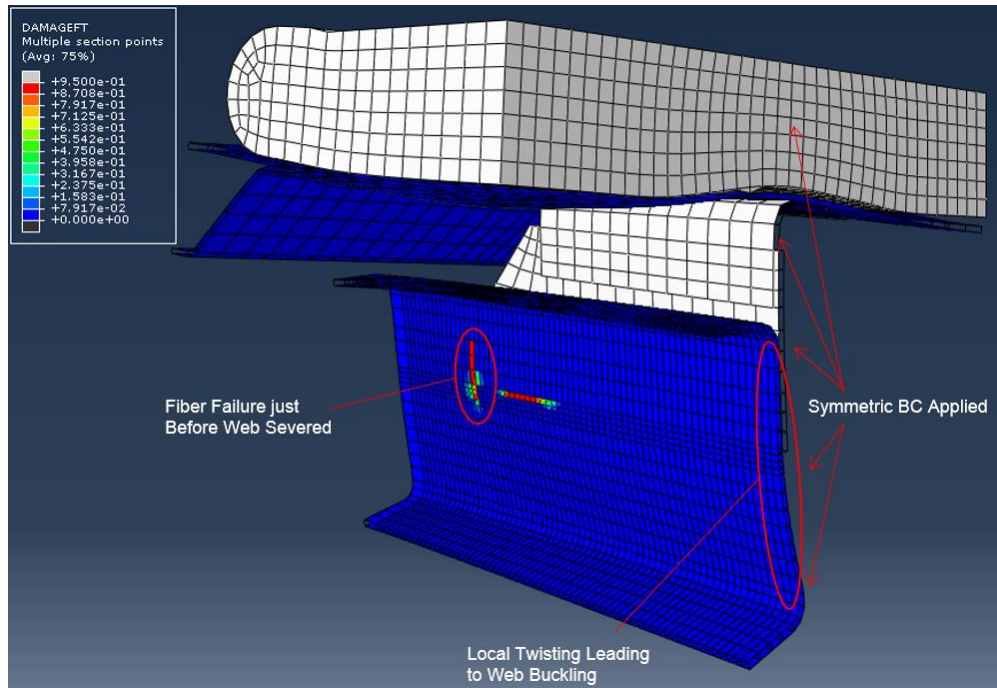
**Figure 4.23: C-frame effective fastener modeling.**

### 4.2.3 FEA RESULTS COMPARISON TO TESTS AND DISCUSSION

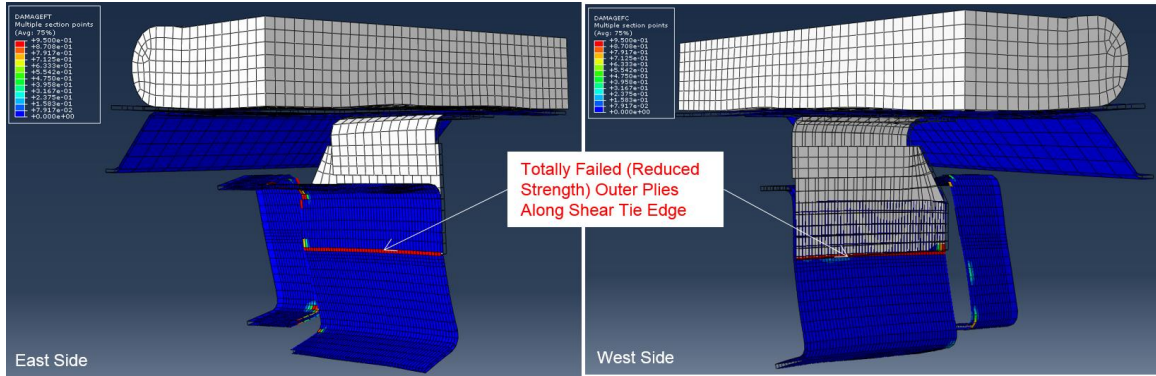
The load-displacement curve comparison between the experimental data and FEA result is shown in Figure 4.24. The two curves show good agreement in the initial elastic behavior, but the FEA result shows the earlier abrupt C-frame fracture with web severing along the shear tie vertical edge as shown in Figure 4.25 and Figure 4.26. Although the failure mode was different, key phenomena were captured in FEA related to the development of failure at the bolted connections observed in the test. More specifically, in Figure 4.26, the reduced strength outer plies for the effective fastener modeling are totally damaged along the horizontal shear tie edge (bolted connection line). In Figure 4.25 and Figure 4.26, the C-frame shows web local twisting (leading to buckling) along the shear tie horizontal bolted connection line by eccentric compressive load (open C-section shear center effect) from shear tie.



**Figure 4.24: Load-displacement curves of Frame04-2.**



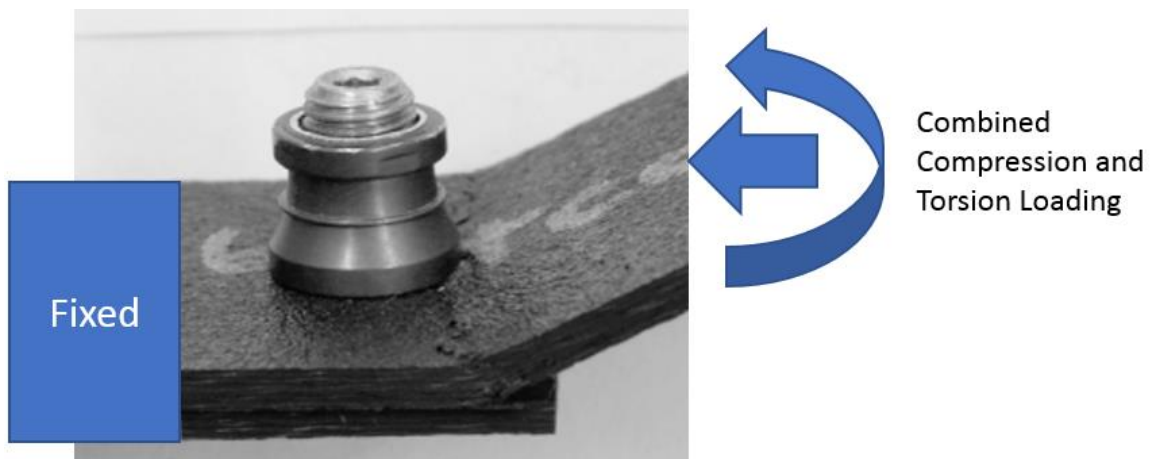
**Figure 4.25: Center C-frame behavior and fiber failure just before fracture.**



**Figure 4.26: Severed center C-frame and totally failed reduced strength plies.**

In conclusion, the FE model is able to catch the initial crack location close to the location observed in the test. However, in FEA, the C-frame fails 22% earlier showing lower strength than the test. It is suspected that inadequate material properties were applied in FE model. Especially in-plane shear strength response is difficult, as well as the in-plane fracture energy parameters were estimated using other existing similar materials. Also, in FEA, the C-frame shows different failure mode from the test. The symmetric FE model represents the identical C-frame boundary condition at both ends, but in actuality, a slightly different boundary condition was applied at each end of C-frame in the test (mainly, one side was free to allow frame elongation, whereas the other side was fully pinned, like classical simply-supported beam). It is suspected that this aspect is influencing the variance between the FE model and test data, and would require further investigation with a full model (no symmetry). C-frame failure progression in the Frame04-2 test is: that (i) a crack was initiated at upper radius corner of C-frame near the shear tie vertical edge corner, and (ii) the crack grew through the first bolt and along the horizontal bolt line with local web twisting by the eccentric compressive load from the

way the shear tie connects directly to the web offset from the shear center. These phenomena influence the development of failure at the bolted connections. To better understand and be able to simulate this phenomenon, a detailed experimental and numerical investigation at smaller scale is required, exploring combined compression and local twisting (bending) load transfer through bolted connections. This idea is conceptually shown in Figure 4.27.



**Figure 4.27: Bolt failure test example under combined compression and local bending.**

Similarly, this approach can be applicable for combined local buckling and shear crack failure (by stringer contact causing eccentric compression) initiated at the Hi-Lok bolts on the C-frame web at the loading location in the 2<sup>nd</sup> generation Loc3 and Loc4.

### 4.3 CONCLUSION OF FRAME FAILURE STUDIES

From the key failure modes observed in large-scale experiments, C-frame failure was classified with respect to the presence (or lack) of large rotation of the C-frame due to the influence of shear tie. In the 1<sup>st</sup> generation Frame03 test, losing discrete composite shear ties allowed the large rotation of C-frames, and consequently C-frames failed near the boundary fixtures at locations relatively far from the location of load application. On the other hand, in the 1<sup>st</sup> generation Frame04-2 test, the strong shear ties did not allow the C-frame to undergo large deformation. Those C-frames showed local failure initiating at or near bolted connections.

For the C-frame element test, with the short section of C-frame subjected to combined loading (bending and combined bending-twisting loading), the aim was to induce the same C-frame failure phenomena as was observed in the 1<sup>st</sup> generation Frame03 specimen. During the tests, buckling and stretching modes on the compression and tension flanges respectively was observed from the video record and measured strain in the flanges. Unfortunately, significant slip of the C-frame from the boundary fixtures kept occurring beyond initial settlement. This slippage results in added compliance which is very difficult to account for in analysis. All tests had this slippage, despite several trials at fixing it.

After C-frame element tests, the FE model refinement was processed with implementation of Hashin-Rotem failure criterion. The FE model results show significant discrepancy between tests and FE results in stiffness and ultimate strength. However, buckling of the compression flange was captured in the simulation and from the



computational strain results were found to agree qualitatively with the test results. The FE model predicts the failure location and compression fiber failure mode only for the combined bending-twisting loading case.

For C-frame bending and bending-twisting tests, the specimen's span-to-depth ratio was very low for bending failure. Re-design is required by increasing frame specimen length with the shorter aluminum arm. The discrepancy between the FEA and test result could be caused by the unknown boundary condition related to the friction and slip which occur at the connection joints. The boundary condition effect was proved by including slip phenomenon at connection joints as the updated FE simulation predicted the correct failure location in bending test. In experiments, while rigid connections are desired in order to eliminate uncertainty and achieve test results that better match FE models, such truly rigid connections are often impossible to achieve in practice. Thus, an aspect of this research focused on how to account for uncertainty more accurately from test boundary conditions provides some more broadly applicable guidance in the conduct of these types of studies and analysis correlation.

For the C-frame direct shear failure, it was difficult to conduct the element-level test with the equivalent boundary condition on the C-frame of the fuselage structure due to the complex geometry of the large-panel and the interaction between components. For Frame04-2 test, the strong shear tie played the key role in the C-frame failure by directly transferring the shear force to the C-frame. Thus, numerical investigation was conducted with full-scale FE modeling incorporating progressive damage softening via the Hashin-Rotem failure criterion. The C-frame modeling capability was not completely adequate. Although the FE model shows the good agreement for the overall elastic response and

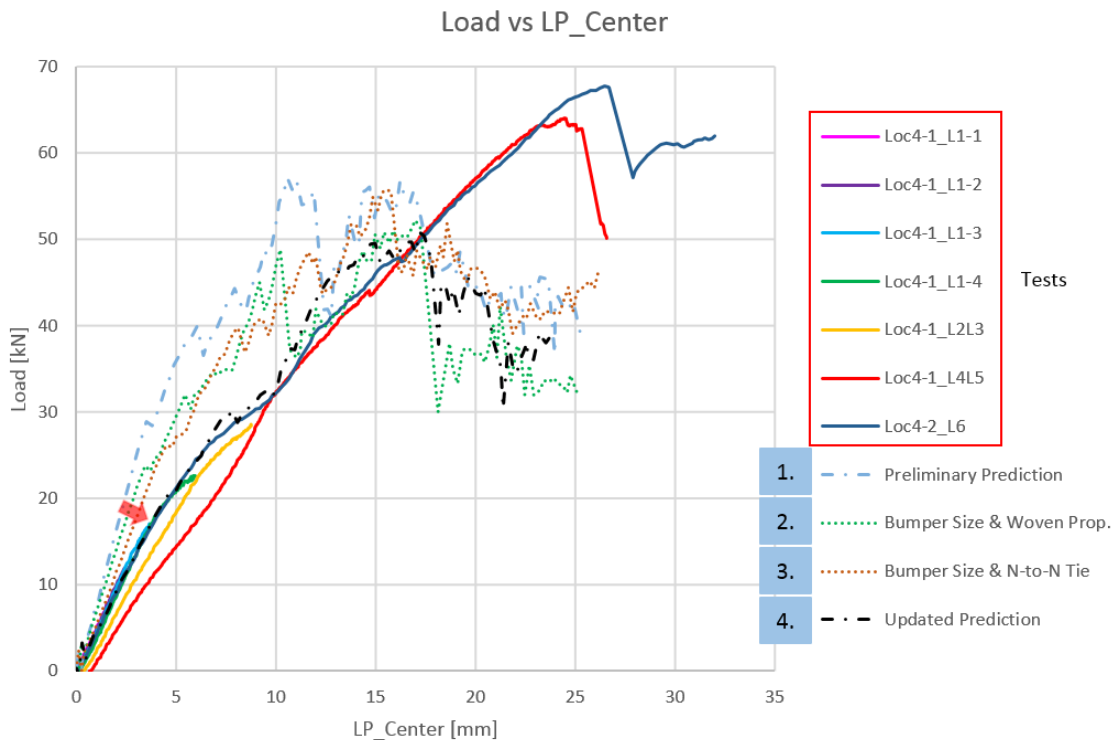
predicts failure initiation of the C-frame at the correct location, the FE model of the C-frame failed earlier showing lower strength than the test and showed different failure mode from the test.

In the Frame04-2 test, C-frame crack was initiated at the connection with shear tie and grew through the first bolt and along the horizontal bolt line with local web bending by the eccentric compressive load. To better understand and be able to simulate this phenomena, a detailed experimental and numerical investigation at smaller scale is required, exploring combined compression and local twisting (bending) load transfer through bolted connections.

## 5 LARGE SCALE FE MODEL FOR FAILURE PREDICTION AND CORRELATION WITH LARGE SCALE TESTS

---

After completion of the 2<sup>nd</sup> generation HEWABI Loc4 tests, FE modeling definitions as an improvement to the preliminary predictions were updated. As shown in Figure 5.1, three main updates were: (i) change of bumper size to reflect actual test geometry, (ii) more accurate values for the T800/3900-2 prepreg properties, and (iii) application of node-to-node constraints between the shear tie and C-frame instead of using surface tie constraint with 17.78 mm (0.7 in) width fastener strip partition. Other modeling definitions are identical to the preliminary FE model described in Section 3.6.



**Figure 5.1: FE modeling definition update after Loc4 tests.**

With the main changes labeled with “2. Bumper Size & Woven Prop.” and “3. Bumper Size & Node-to-Node Tie” in the Figure 5.1, the initial stiffness of updated FEA, labeled with “4. Updated Prediction”, shows good agreement with the test results. However, more modeling definition needs to be updated especially to accurately represent failure of the shear tie as well as the stringer, and fastener modeling in C-frame at loading location.

In this chapter, updated modeling information will be provided in detail, and the current FE model capability will be evaluated based on Loc4 test results.

## 5.1 FE MODEL UPDATE – BUMPER SIZE, COMPOSITE MATERIAL PROPERTY, NODE-TO-NODE TIE CONSTRAINT

As mentioned in Section 3.8.2, during test setup, the flat rubber bumper size changed from 254 mm x 558.8 mm x 50.8 mm (10 in x 22 in x 2 in) to 152.4 mm x 609.6 mm x 25.4 mm (6 in x 24 in x 1 in). The changed bumper size was updated in the revised FE model. In the low-velocity impact test, the boundary condition strongly affects the structural behavior. Thus, impactor size change is influential to the structural behavior.

Before and after conducting the 2<sup>nd</sup> generation HEWABI Loc4-1 experiment, material properties of the FE models kept being updated as improved values were determined. Table 5.1 shows up to date T800/3900-2 carbon/epoxy composite material properties. These properties were obtained from a combination of sources including Toray (the material manufacturer) data sheet [26], existing literature by Khaled [28] and

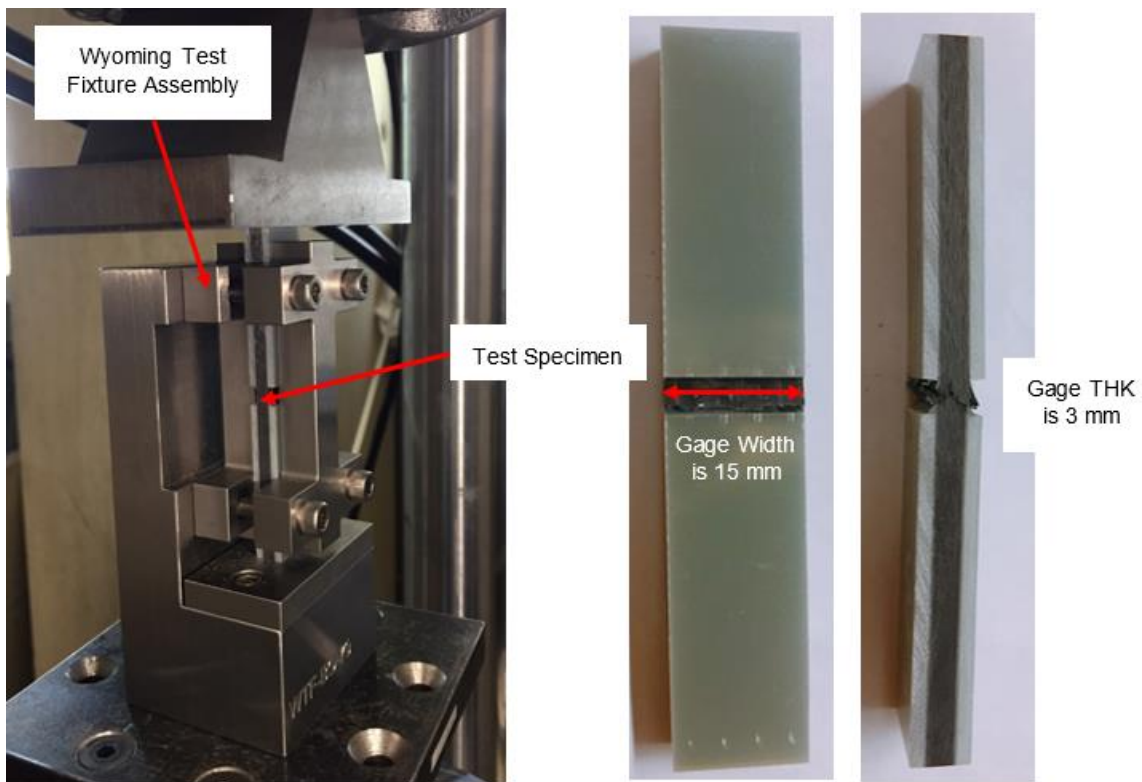
Zou [18], property data of similar prepreg (Cyttec X840/Z60) [11], and the longitudinal compressive strength of PW T800H-6K/3900-2 measured by compression coupon tests.

**Table 5.1: Updated T800/3900-2 properties.**

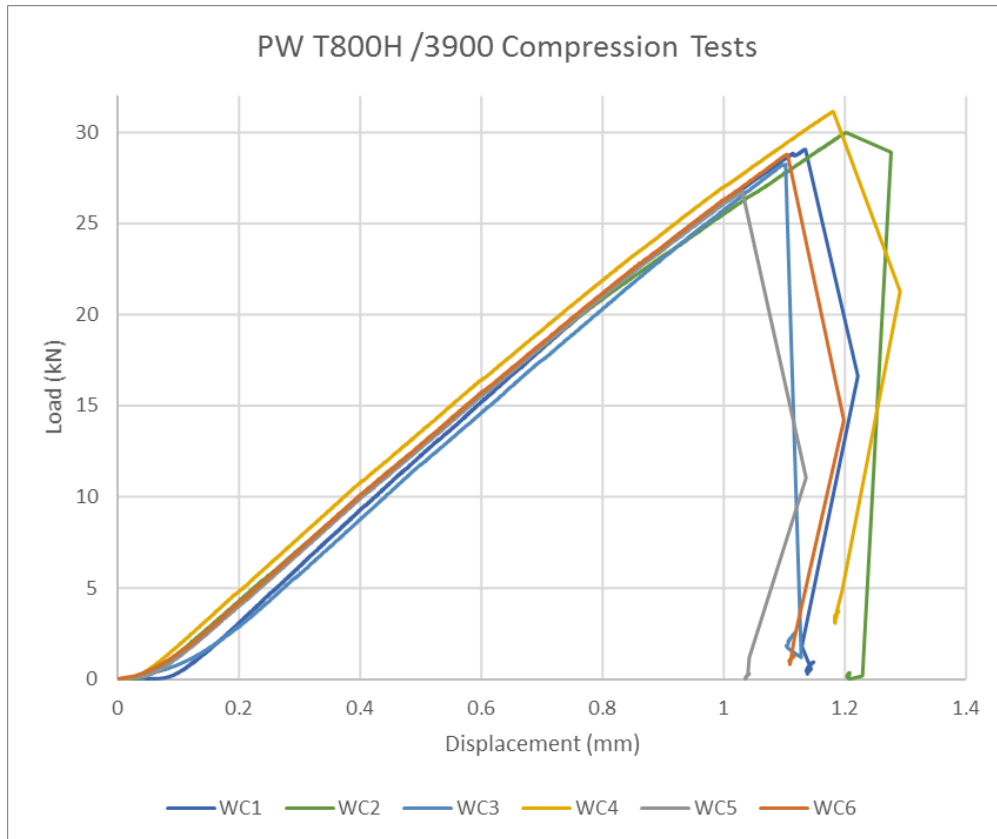
<b>Updated Properties</b>	<b>Unidirectional</b>	<b>6K Plain Weave</b>
<b>Lamina Thickness and Density</b>		
Ply Thickness (mm)	0.195	0.220
Density, $\rho$ (g/cm <sup>3</sup> )	1.60	1.50
<b>Lamina Elastic Properties</b>		
Longitudinal Young's Modulus, $E_1$ (GPa)	161.74	68.26
Transverse Young's Modulus, $E_2$ (GPa)	7.35	66.19
In-Plane Poisson's Ration, $\nu_{12}$	0.32	0.06
In-Plane Shear Modulus, $G_{12}$ (GPa)	4.00	4.00
Transverse Shear Modulus, $G_{13}$ (GPa)	2.40	2.90
Transverse Shear Modulus, $G_{23}$ (GPa)	2.31	2.76
<b>Lamina In-Plane Strength</b>		
Longitudinal Tension Strength, $F_{1t}$ (MPa)	2519	883
Longitudinal Compression Strength, $F_{1c}$ (MPa)	727	648
Transverse Tension Strength, $F_{2t}$ (MPa)	44.83	883
Transverse Compression Strength, $F_{2c}$ (MPa)	175.91	600
In-Plane Shear Strength, $F_{12}$ (MPa)	128.72	68.95
<b>Lamina In-Plane Fracture Energy</b>		
Longitudinal Tensile Fracture Energy, $G_{1t}$ (kJ/m <sup>2</sup> )	91.60	45.80
Longitudinal Compressive Fracture Energy, $G_{1c}$ (kJ/m <sup>2</sup> )	79.90	39.90
Transverse Tensile Fracture Energy, $G_{2t}$ (kJ/m <sup>2</sup> )	0.20	45.80
Transverse Compressive Fracture Energy, $G_{2c}$ (kJ/m <sup>2</sup> )	0.20	39.90

The main influence on structural behavior of the updated models was due to the improvement of woven ply elastic moduli and in-plane strength because the circumferential structural components, mainly resisting transverse loads, were fabricated with woven plies.

As shown in Figure 5.2, the compression tests were conducted at UCSD to get the longitudinal compressive strength of PW T800H-6K/3900-2 using SACMA compression test method. The compression test results are shown in Figure 5.3 and Table 5.2. The test average value of strength is 648 MPa.



**Figure 5.2: Compression coupon test (SACMA method) and test specimen (0° - 14 PW plies) after test.**

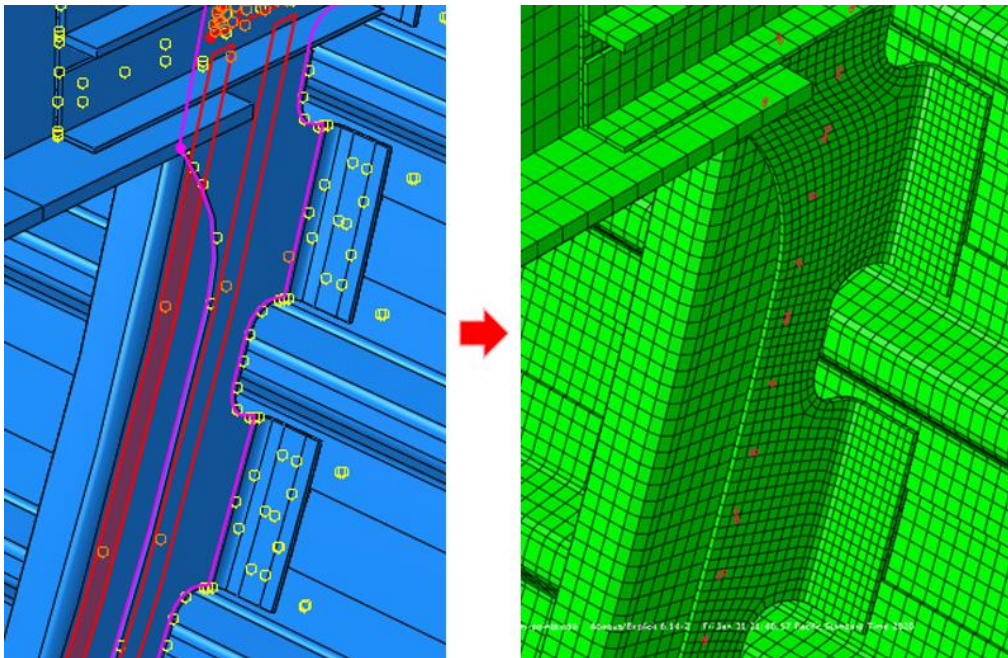


**Figure 5.3: Compression coupon test results.**

**Table 5.2: PW T800H/3900-2 compressive strength.**

0d-14p	Displ. (mm)	Max load (kN)	Compressive strength (MPa)
WC1	1.13	29.07	660.02
WC2	1.20	29.99	656.41
WC3	1.10	28.25	629.54
WC4	1.18	31.14	687.03
WC5	1.03	26.78	605.09
WC6	1.10	28.80	648.59
		<b>Avg.</b>	<b>647.78</b>

Lastly, fastener modeling method changed from 17.78 mm (0.7 in) width strip surface tie connection to point-to-point tie constraints representing individual bolt connections between the shear tie and C-frame as shown in Figure 5.4. It is more realistic fastener modeling method resulting in more compliant connection between the shear tie and C-frame versus the fastener strip surface constraint in FE model. It consequently resulted in more compliant stiffness of the structure to transverse loading.



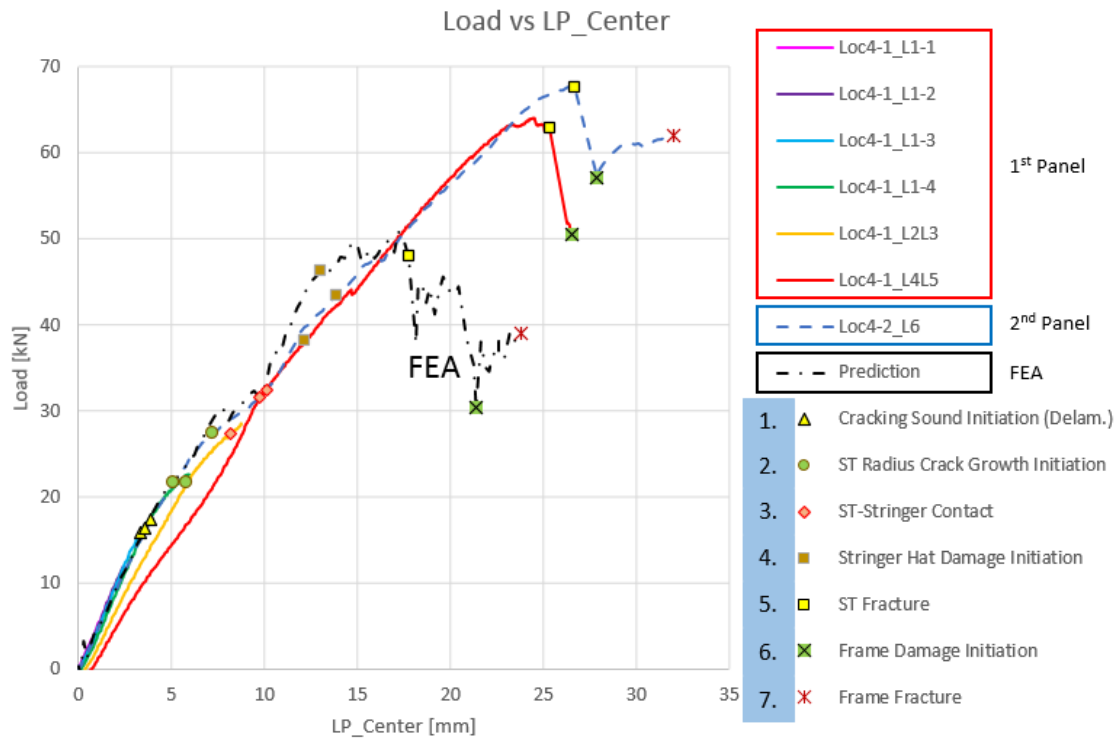
**Figure 5.4: Change of fastener modeling from strip surface tie to node-to-node tie between shear tie and C-frame.**

## 5.2 PREDICTED EVENTS AND CORRELATION WITH TEST RESULTS

With the updated modeling definition implemented, FEA results were compared with the Loc4 test results and the predicted events were examined. As shown in Figure



5.5, although the updated FE model shows good agreement relative to the test data, shear tie fracture and following C-frame fracture occur much earlier in FEA.

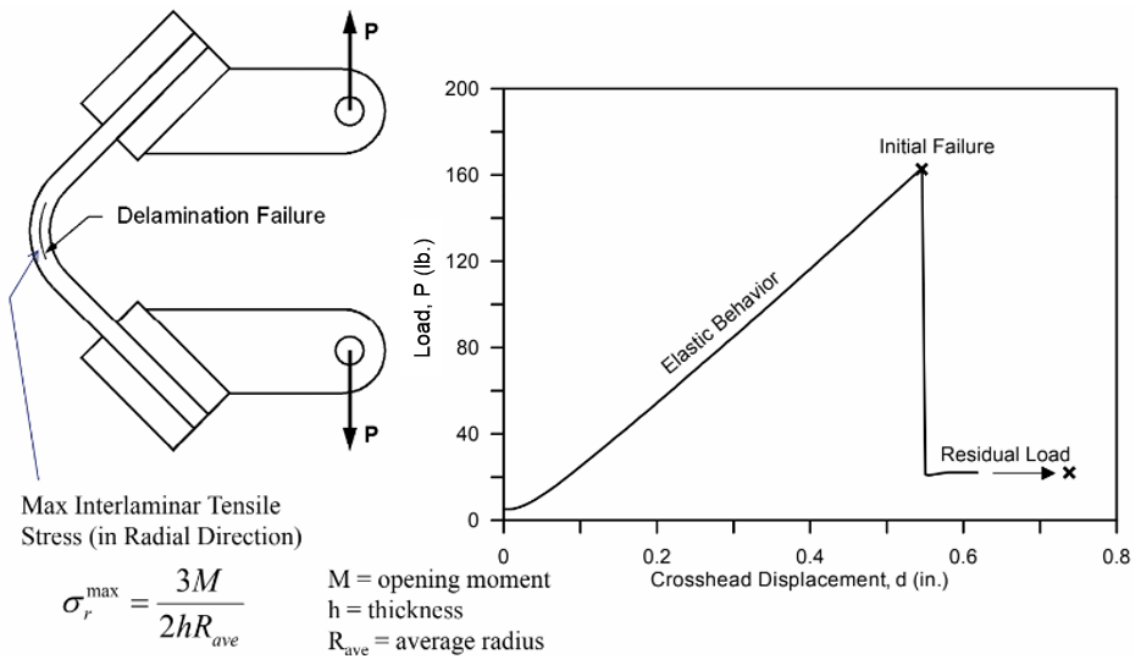


**Figure 5.5: Correlation with experimental results.**

The predicted events are numbered (1-7) in Figure 5.5. The detail description of each event is compared with test results. Event numbers 1 to 7 are shown in subsequent figures showing FEA-predicted failure events.

The current FE model does not simulate inter-laminar failure (delamination) due to the absence of interfacial surface interaction definition, i.e., cohesive surface interaction at contacting surface pairs between plies or sub-laminates. However, using the

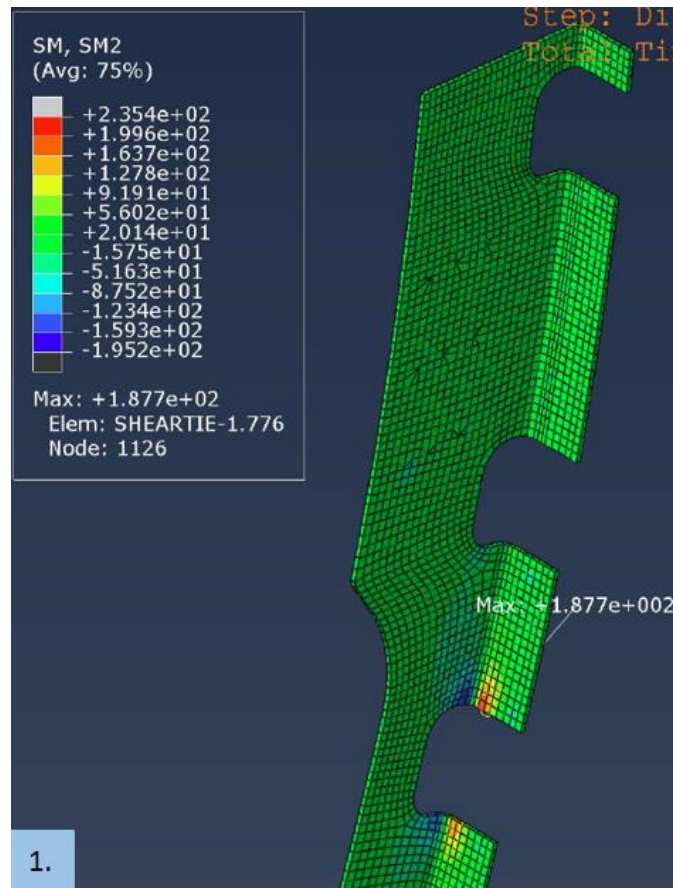
typical value of interlaminar tension strength (ILTS) for the toughened matrix material [11, 29], delamination initiation onset was estimated in the FE simulation. In Figure 5.6, interlaminar tension stress in a curved section is introduced [29]. From the equation shown in Figure 5.6, the typical value of ILTS of 6 ksi (41.37 MPa) was substituted, and the corresponding opening moment value was evaluated as 183.3 lb-in/in (0.82 kN-mm/mm).



**Figure 5.6: Interlaminar tension failure – curved beam tension specimen [29].**

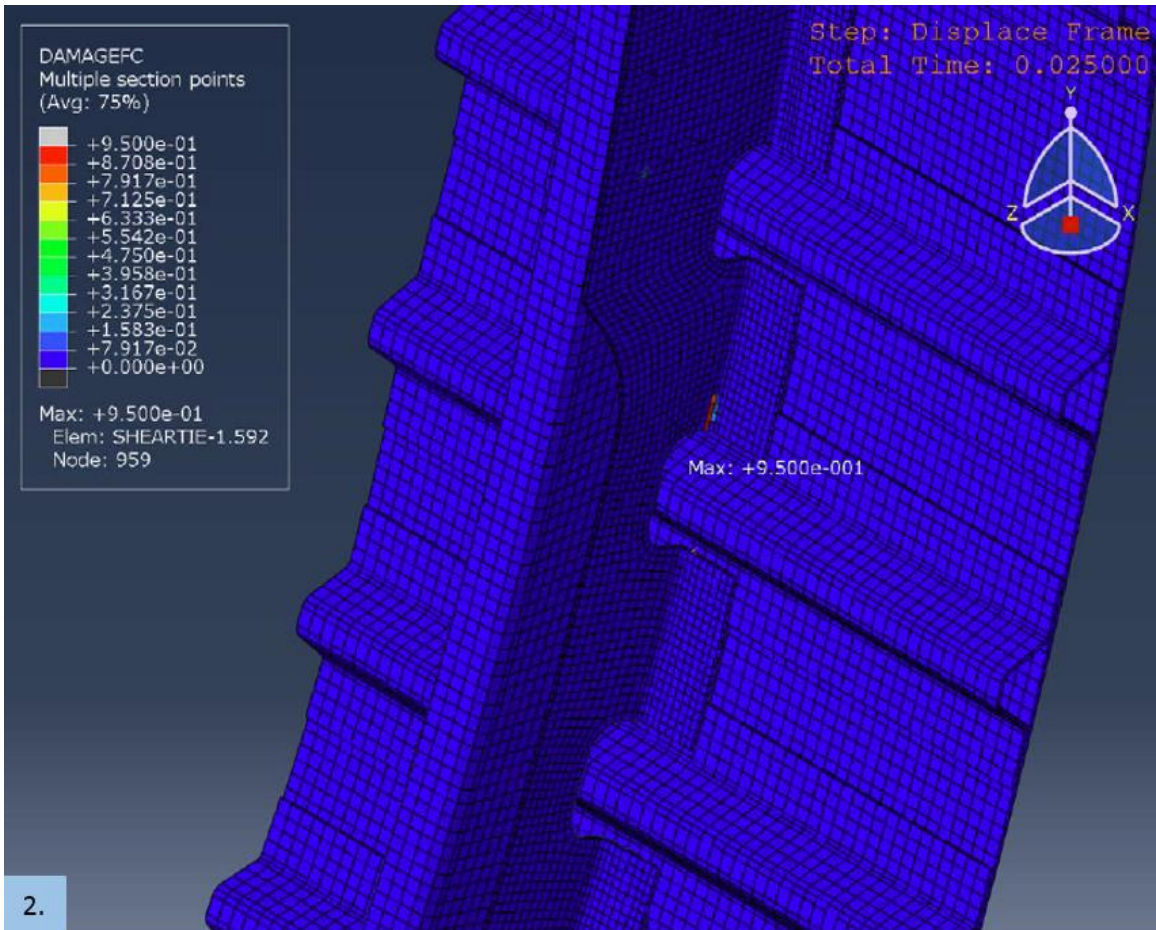
In Abaqus, the section moment SM2 is defined as bending moment force per unit width about local 1-axis [25]. As shown in Figure 5.7, SM2 relates to as the opening (or closing) moment at the shear tie radius corner. Delamination initiation was estimated

when SM2 reached the value of 183.3 lb-in/in (0.82 kN-mm/mm) opening moment. This quantity is plotted in the contour plot as shown.



**Figure 5.7: Delamination initiation estimated by critical opening moment.**

After the initiation of shear tie radius delamination (per above-described calculation), as shown in Figure 5.8, shear tie radius fiber damage initiation from the upper side of Loc4 mouse hole is predicted. Shear tie-stringer contact and stringer hat fiber damage initiation then follow (see Figure 5.9 and Figure 5.10, respectively).



**Figure 5.8: Shear tie radius damage initiation.**

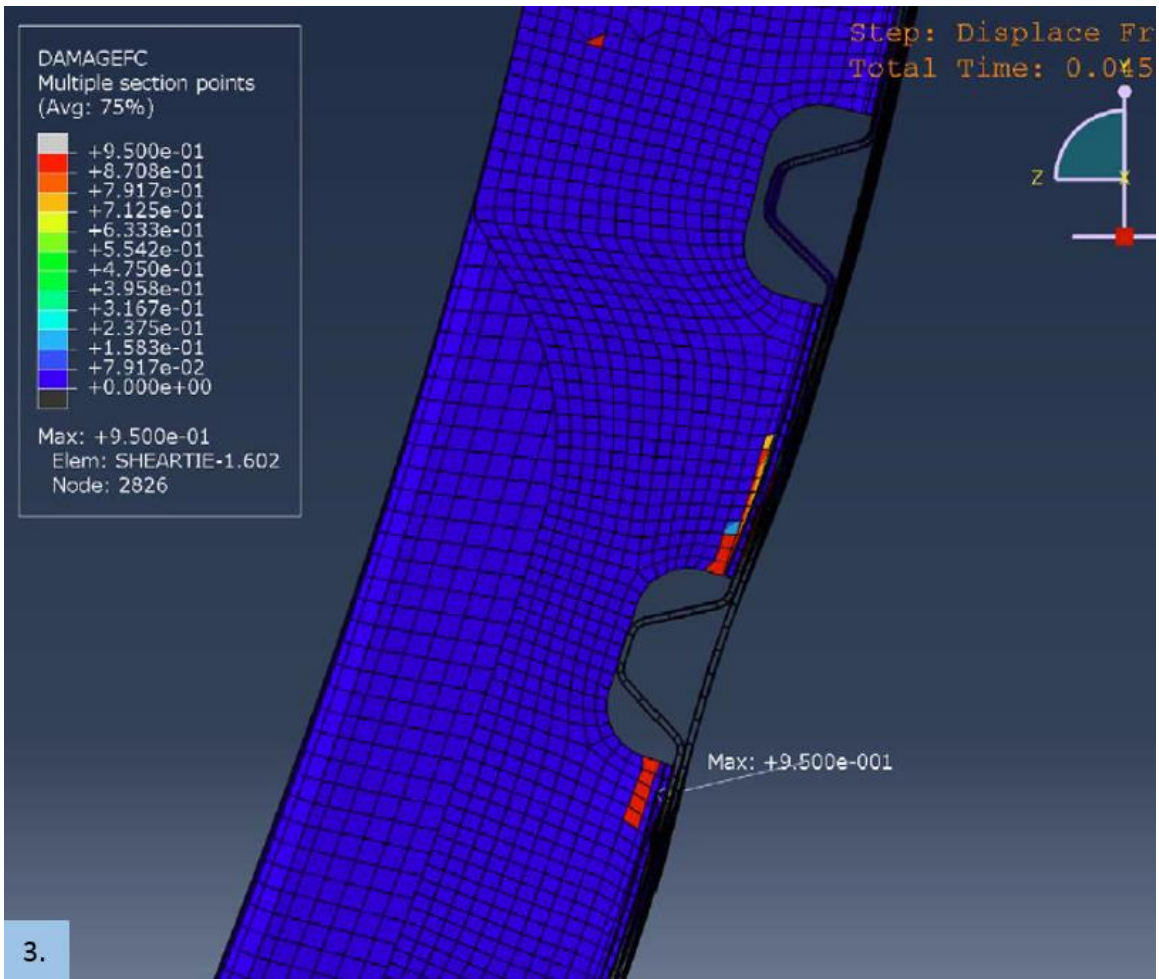
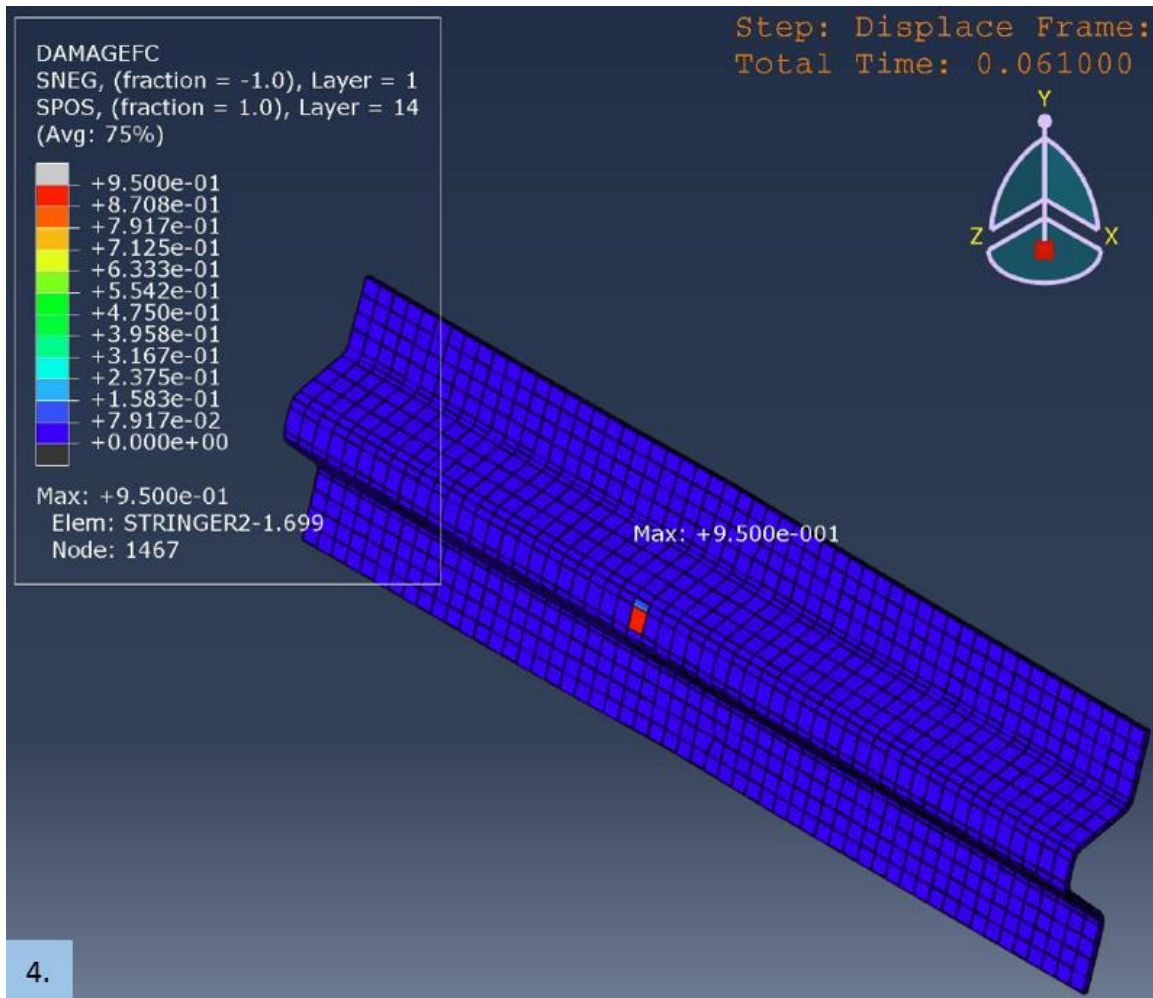


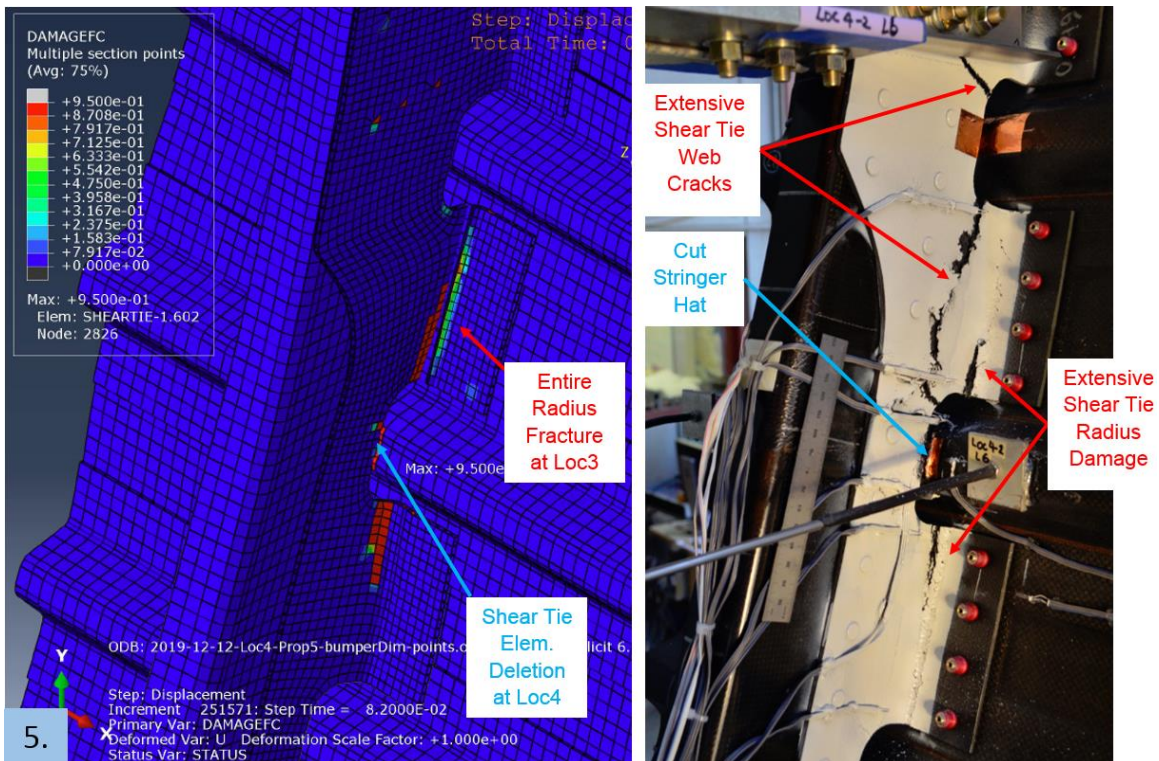
Figure 5.9: Shear tie-stringer contact.



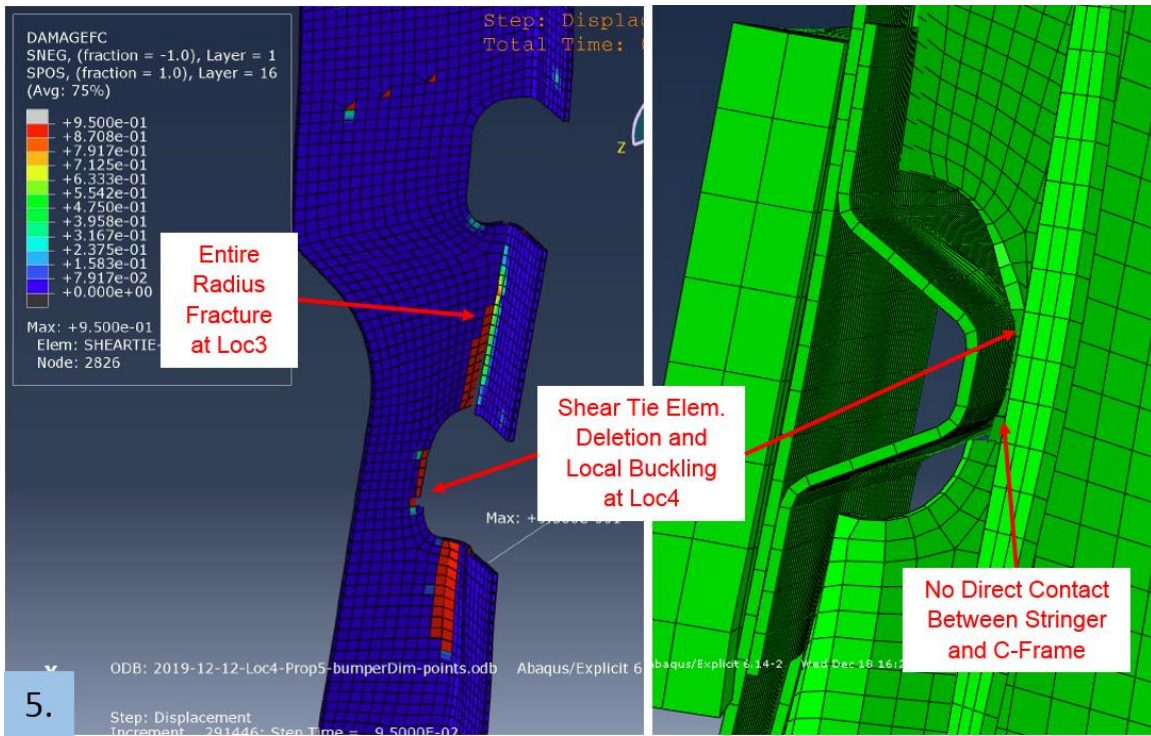
**Figure 5.10: Stringer hat damage initiation.**

The major discrepancy between FE prediction and test results is shear tie failure mode and location. As shown in Figure 5.11 and Figure 5.12, the subsequent key event in FE simulation is abrupt entire shear tie radius fracture at Loc3, which did not occur in the tests. In the tests, the radius crack grew gradually showing radius crushing and delamination mode until abrupt significant web fracture occurred with a large diagonal crack. In addition, shear tie web element deletion is predicted at Loc4. This did not occur in the tests. Furthermore, in the tests, the stringer hat was cut by the shear tie web at

Loc4. However, in FE simulation, there is not any element deletion from stringer hat contact until the end of the simulation. The shear tie web element deletion and its local deformation mode at Loc4 by crushing makes no direct contact between stringer and C-frame as shown in Figure 5.12.



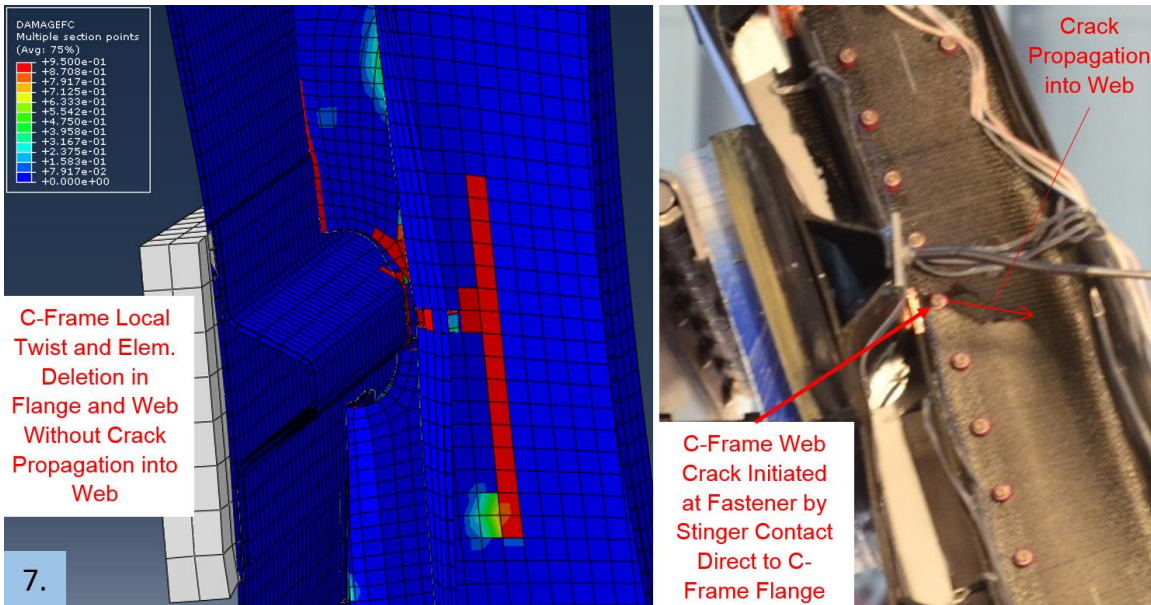
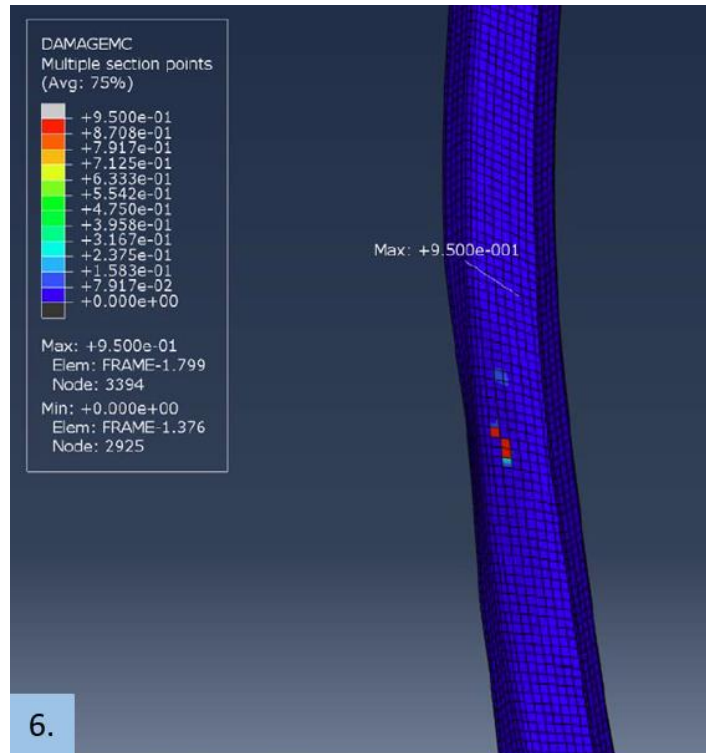
**Figure 5.11: Entire radius fractured at Loc3 in FE simulation.**



**Figure 5.12: Shear tie fracture and component interaction.**

As shown in Figure 5.13, the C-frame failure location agrees with test result, but the contact and interaction with the stringer, as well as concentrated stress at the fastener, observed in the experiment (see test photo in Figure 5.13), was not addressed and should be included in future improvements.





**Figure 5.13: C-frame damage initiation (numbered 6) and crack (numbered 7) at Loc4.**

### 5.3 CONCLUSION AND FUTURE WORK

With three major aspects of model definition improvement, the FEA prediction was shown to agree well with the initial response of the test results. However, a major discrepancy is in shear tie damage which predicted a different fracture location than the tests. FEA simulation showed much earlier shear tie fracture and subsequent C-frame fracture. More improvements to the model definition are needed, especially for better representing failure of the shear tie as well as the stringer. Fastener modeling should also be improved in the C-frame at the loading location as cracks were observed to initiate from a fastener hole.

As studied through the large-scale experiments, the shear tie is the key component governing damage extent influencing the failure modes of other components and the overall structural behavior. Chen [11] had previously modeled cohesive surface interactions to simulate the delamination which was observed in shear tie radius in the 1<sup>st</sup> generation HEWABI panel tests. As a key damage mode also observed in the current 2<sup>nd</sup> generation HEWABI panel tests, shear tie radius delamination should be included in the modeling using interfacial surface interaction definition, i.e., cohesive surface interaction at contacting surface pairs between plies or sub-laminates.

After shear tie-stringer contact, the stringer hat was observed during the tests to be cut by direct shear tie web contact and penetration. This led to geometric interlocking, constraining the lateral movement of circumferential C-frame component and eventually stringer-C-frame contact as penetration increased. In the FE prediction, stringer hat damage is predicted but there is no element deletion until the end of the analysis. In order

to accurately predict this failure mode, a 3D failure criterion such as the Hill-Tsai criterion used by Chen [11] can be considered. Accounting for this damage mode will improve the prediction of the interaction between components at the mouse hole near the loading location.

In the FE prediction, the C-frame failure location agrees with test results, but the contact and interaction with the stringer, as well as concentrated stress at the fastener needs to be more accurately accounted for. In CODAMEIN research [17, 18], shear ties to frames interactions were modeled using connector elements. For the representation of the fasteners, translational stiffness as well as axial and shear strengths were defined. This approach is recommended first. As mentioned in Chapter 4, the smaller scale study is recommended as well for the failure at fastener by concentrated stress under combined local bending and compression load state.

Accurate material properties are required for improved FEA correlation. While this sounds obvious, obtaining all the material model input properties necessary for 3D modeling of composite materials is typically not easily achieved. Many properties, especially in transverse direction, need to be assumed based on similar materials for which material property data are available. As mentioned in Chapter 3, during the manufacturing process, some T800/3900-2 coupon plates were fabricated to obtain material properties which were not provided by the material manufacturer. Updated material properties should be verified through coupon-level testing and additional review of the literature. A Styrene Butadiene Rubber (SBR) pad was used for the loading head contact face in the tests. For this material, rubber compression test is recommended to

validate chosen material parameters in the hyper-elastic bumper FE model. Lastly, rubber to skin surface friction test is recommended to achieve accurate friction coefficient.

Chapter 5 is coauthored with Wiggers de Souza, Chaiane. Nam, Moonhee was the primary author of this chapter.

## 6 CONCLUSIONS

---

For the 2<sup>nd</sup> generation HEWABI experiments, via FEA approach, smaller and simplified test panels with one circumferential component were designed successfully with appropriate BCs representing full quarter barrel fuselage response. This sub-structure definition methodology can be used in a wide range of applications when the loading area is distant enough from the representative boundary condition elements, which remains elastic.

In the 2<sup>nd</sup> generation HEWABI experiment, the significant internal damage modes to internal components (shear tie, stringer, and C-frame) were developed with very low (basically no) externally visible damage. The lack of external damage visibility hinders the damage detectability through visual inspection, but a quantitative understanding of the damage mode and extent resulting from HEWABI near floor joint is important for giving awareness of severe internal damage by HEWABI and for choosing inspection area as well as establishing damage size criteria in the evaluation of a structure's residual strength and damage tolerance capability. The importance of the visual detectability of the presence of severe internal damage is emphasized, as the current practice in aviation safety relies on visual-based first detection.

In the 2<sup>nd</sup> generation HEWABI current research, the aim is to evaluate how design parameters and loading location affect damage formation and propagation. The floor structure, continuous shear tie, and loading location lead to shear dominated failure within the zone from the loading location to floor joint fixture, causing small deformation

of the C-frame until failure develops. On the other hand, in Frame03 test of the 1<sup>st</sup> generation HEWABI research, bending dominated failure occurred in C-frame showing large deformation after losing stabilizing components, specifically the discrete shear ties. As studied through the large-scale experiments, shear ties are the key component governing damage extent influencing other components' subsequent failure mode and the overall structural behavior.

Through focused element-level C-frame bending failure study, the importance of eliminating uncertainty at boundary fixtures is identified, while acknowledging that such uncertainty of test-fixture boundary conditions is every present, especially in complex larger sized test specimens. This element-level testing activity gives a key lesson how to eliminate or minimize this uncertainty in FE modeling as well. The example of detailed FE modeling for it is shown in research by Heimbs [21]. To eliminate uncertainty in boundary condition connections, Heimbs modeled cured epoxy adhesive applied at the interface between specimen and fixture to account for its compliance under load, and a contact formulation with friction coefficient of 0.5 was applied at the interface between the adhesive and the metal surface in the fixtures. Moreover, the specimen's span-to-depth ratio was very low for the bending failure mode. Re-design is required by increasing frame specimen length with the shorter aluminum arm.

In the large scale FE simulation, simplifications were made to bolt connections to reduce computational cost. The concentrated stress at fasteners or along fastener line should be modeled for the C-frame web failure initiation and propagation. The small scale study for failure at fastener by concentrated stress is recommended. The improved

FE simulation will help predict the accurate damage location and extent after HEWABI event.

## REFERENCES

---

- [1] Maria Mrazova. Advanced Composite Materials of the Future in Aerospace Industry, INCAS BULLETIN, Vol.5, Issue 3/ 2013, pp.139-150.
- [2] Boeing 787 from the Ground Up – Composites in the Airframe and Primary Structures, Article, AERO QTR\_4.06.
- [3] Smock, Doug. Boeing 787 Dreamliner Represents Composites Revolution, Design News June 2008, Reed Business Information, 10 Jan 2010.
- [4] Jerome Greer Chandler. Fuselage Fix – Rewriting the Book with 787 Repair, AVIATIONPROS, Article, 5 Feb 2014.
- [5] Benjamin Lu, Nancy Wang. The Boeing 787 Dreamliner: Designing an Aircraft for the Future, Article, Journal of Young Investigators, 6 Aug 2010.
- [6] Xie Jian, Lu Yao. Study on Airworthiness Requirements of Composite Aircraft Structure for Transport Category Aircraft in FAA, The 2<sup>nd</sup> International Symposium on Aircraft Airworthiness (ISAA 2011), Procedia Engineering 17 (2011) 270-278.
- [7] Federal Aviation Administration. Advisory circular 25.571-1, Damage Tolerance Inspections for Repairs and Alterations.
- [8] G. K. DeFrancisci. High Energy Wide Area Blunt Impact on Composite Aircraft Structures, PhD dissertation, 2013.
- [9] Hyonny Kim, G. K. DeFrancisci, Z. M. Chen. Ground Vehicle Blunt Impact Damage Formation to Composite Aircraft Structures, Advanced Composite Materials. 23(1), 53-71, 2014.
- [10] International Air Transportation Association. Ground Damage Prevention Programme Targets 10% Cost Reduction, Industry Times, Sept (7):3, 2005.
- [11] Z. M. Chen. Experimental and Numerical Investigation of Wide Area Blunt Impact Damage to Composite Aircraft Structures, PhD dissertation, 2015.
- [12] Sutherland LS, Guedes Soares C. The Use of Quasi-Static Testing to Obtain the Low-Velocity Impact Damage Resistance of Marine GRP Laminates, Composite: Part B, 2012;43:1459-1467.
- [13] A. Wagih, P. Maiami, N. Blanco, J. Costa. A Quasi-Static Indentation Test to Elucidate the Sequence of Damage Events in Low Velocity Impacts on Composite Laminates, Composite: Part A, 2016;82:180-189.



- [14] Zoltan Mikulik, Peter Haase. CODAMEIN – Composite Damage Metrics and Inspection (high energy blunt impact threat), EASA. 2010.C13, Final Report, 31 Jan 2012.
- [15] Bishop, W.P. CODAMEIN II (Composite Damage Metrics and Inspection), EASA-funded research project, Aerospace Structural Impact Dynamics International Conference, Wichita, 6-9 Nov 2012.
- [16] Peter Haase. CODAMEIN II – Composite Damage Metrics and Inspection (high energy blunt impact threat) – 2<sup>nd</sup> Phase, EASA.2011.NP.24, Report, 14 Feb 2013.
- [17] D. Zou, P. Bishop, C. Haack, R. Thomson, A. Bezabeh. CODAMEIN III – Composite Damage Metrics and Inspection (high energy blunt impact threat) – 3<sup>rd</sup> Phase, EASA.2013. OP.12, Final Report, 02 Feb 2014.
- [18] D. Zou, C. Haack, P. Bishop, and A. Bezabeh. Damage Criticality and Inspection Concerns of Composite - Metallic Aircraft Structures under Blunt Impact, Structural Health Monitoring and Inspection of Advanced Materials, Aerospace, and Civil Infrastructure 2015, Proceedings of SPIE Vol. 9437, 94370C.
- [19] Edgar Turner. The Birth of the 787 Dreamliner, Book, 9 Nov 2010.
- [20] Derek I. Gransden, and Rene Alderliesten. Development of A Finite Element Model for Comparing Metal and Composite Fuselage Section Drop Testing, International Journal of Crashworthiness, 22:401-414 ,2017.
- [21] S. Heimbs, M. Hoffmann, M. Waimer, S. Schmeer, and J. Blaurock. Dynamic Testing and Modelling of Composite Fuselage Frames and Fasteners for Aircraft Crash Simulations, International Journal of Crashworthiness, 18(4):406-422, 2013.
- [22] R. Sturm, and F. Heieck. Energy Absorption Capacity of Braided Frames under Bending Loads, Composite Structures, 134:957-965, 2015.
- [23] Z. Hashin, A. Rotem. A Fatigue Criterion for Fiber-Reinforced Materials, Journal of Composite Materials, 7:448-464, 1973.
- [24] Z. Hashin. Failure Criteria for Unidirectional Fiber Composites, Journal of Applied Mechanics, 47:329-334, 1980.
- [25] SIMULIA. Abaqus 6.13 Documentation: Abaqus Analysis User's Manual.
- [26] TORAY. 3900 Series Prepreg Data Sheet.

- [27] L. Tong, C. Soutis. Recent Advances in Structural Joints and Repairs for Composite Materials, Springer, pp 114.
- [28] B. Khaled, L. Shyamsunder, C. Hoffarth, S. D. Rajan, R. K. Goldberg, K. S. Carney, P. DuBois, and G. Blankenhorn. Experimental Characterization of Composites to Support an Orthotropic Plasticity Material Model, Journal of Composite Materials, 0(0) 1-26, 2017.
- [29] H. Kim, Composite Failure Mechanisms, Lecture Pack of SE253A.

## APPENDICES

---

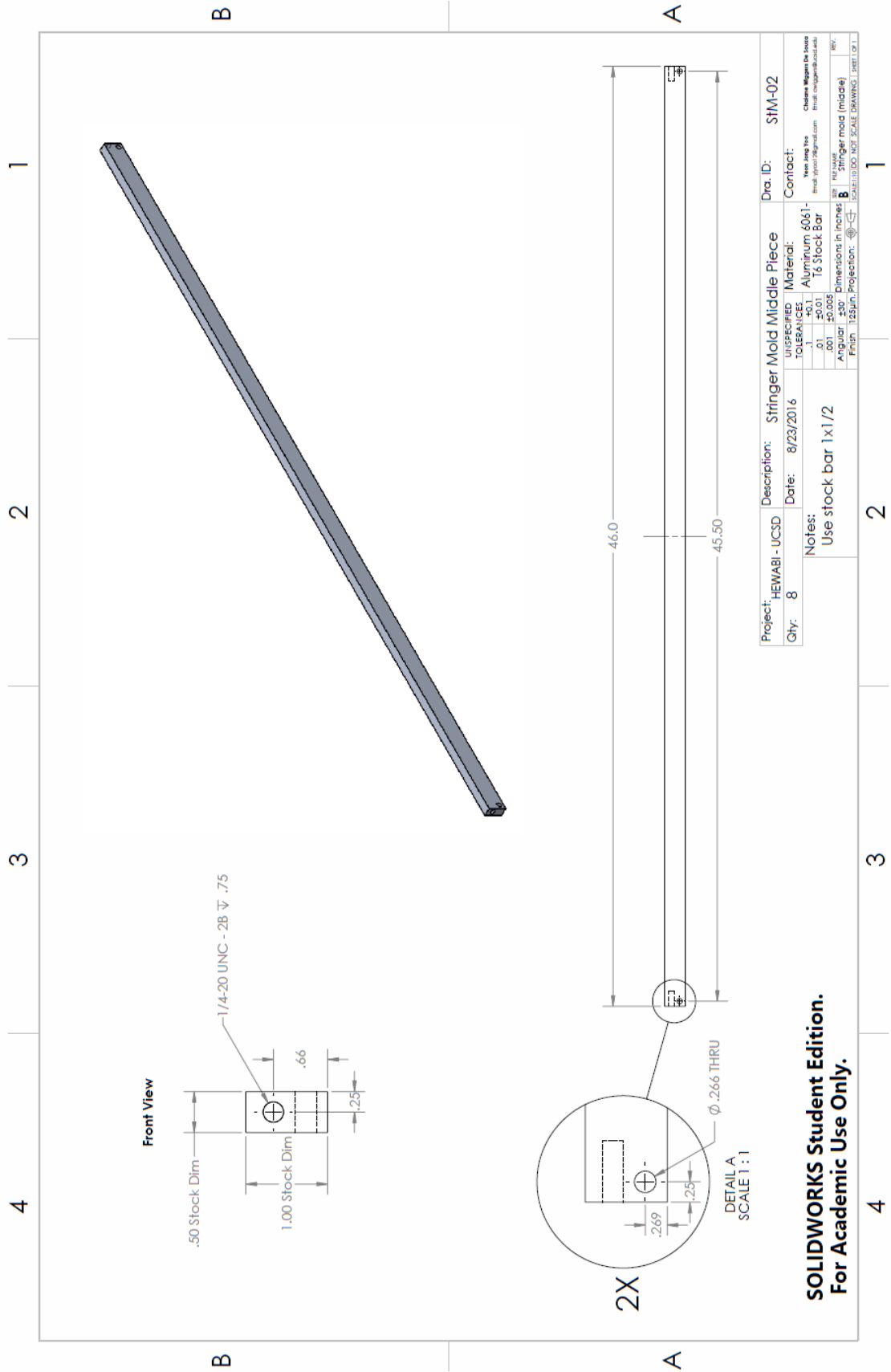
### A. MOLD DRAWINGS

This appendix includes detailed mold drawings:

- 1) Stringer inner mold
- 2) Shear tie outer mold
- 3) C-Frame outer mold







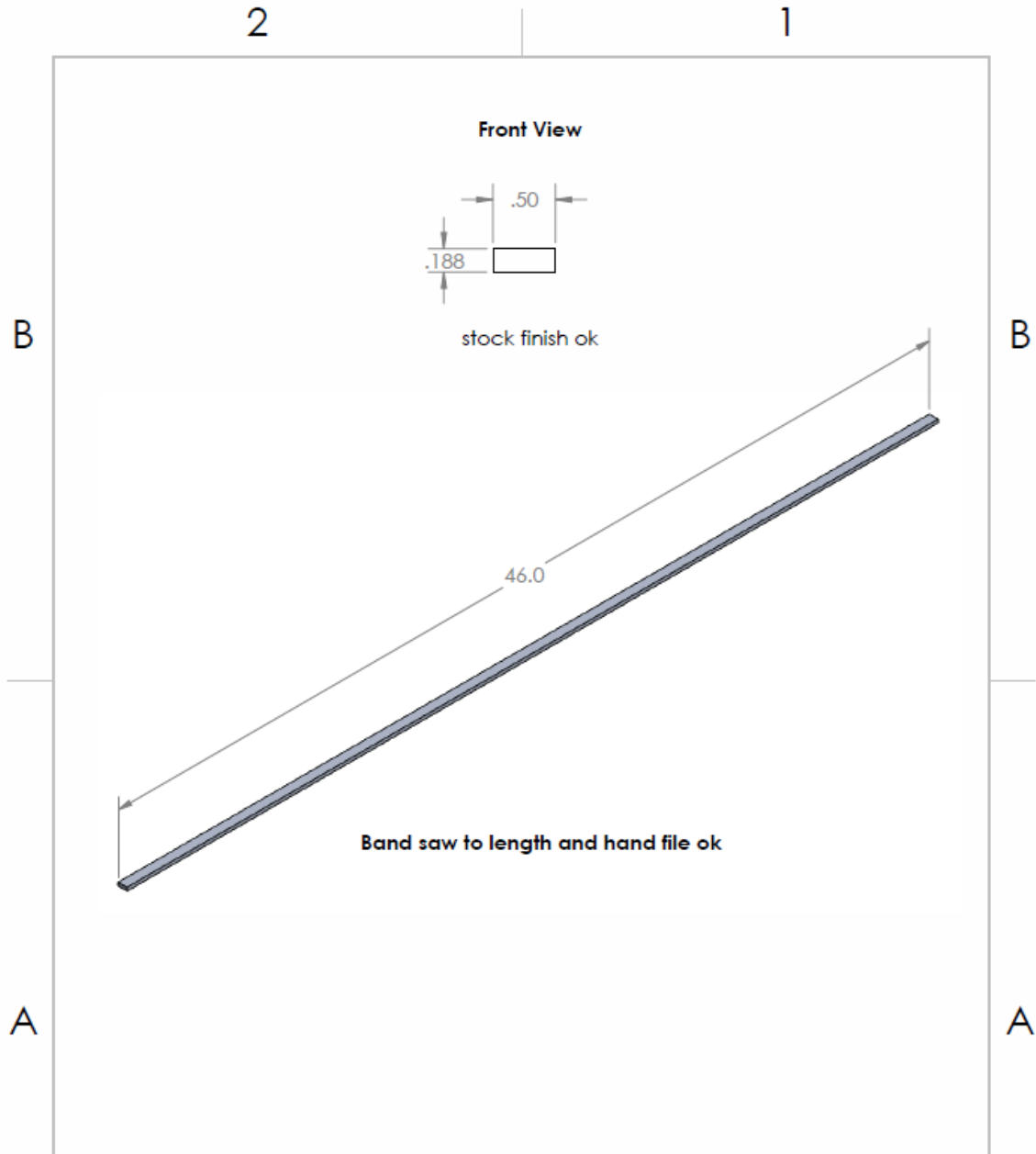
Front View

.50 Stock Dim  
 1.00 Stock Dim  
 .66  
 .25  
 1/4-20 UNC - 2B  $\nabla$  .75

2X  
 $\phi .266$  THRU  
 .269  
 .25  
 DETAIL A  
 SCALE 1 : 1

Project: HEWABI - UCSD	Description: Stringer Mold Middle Piece	Dra. ID: STM-02
Qty: 8	Date: 8/23/2016	Contact:
	UNSPECIFIED	Material: Aluminum 6061-T6 Stock Bar
	TOLERANCES	Finish: 125µm
	Angular	Dimensions in inches: 330
	Projection: 1st Angle	Scale: DO NOT SCALE DRAWING
	Notes: Use stock bar 1x1/2	Sheet: 1 of 1

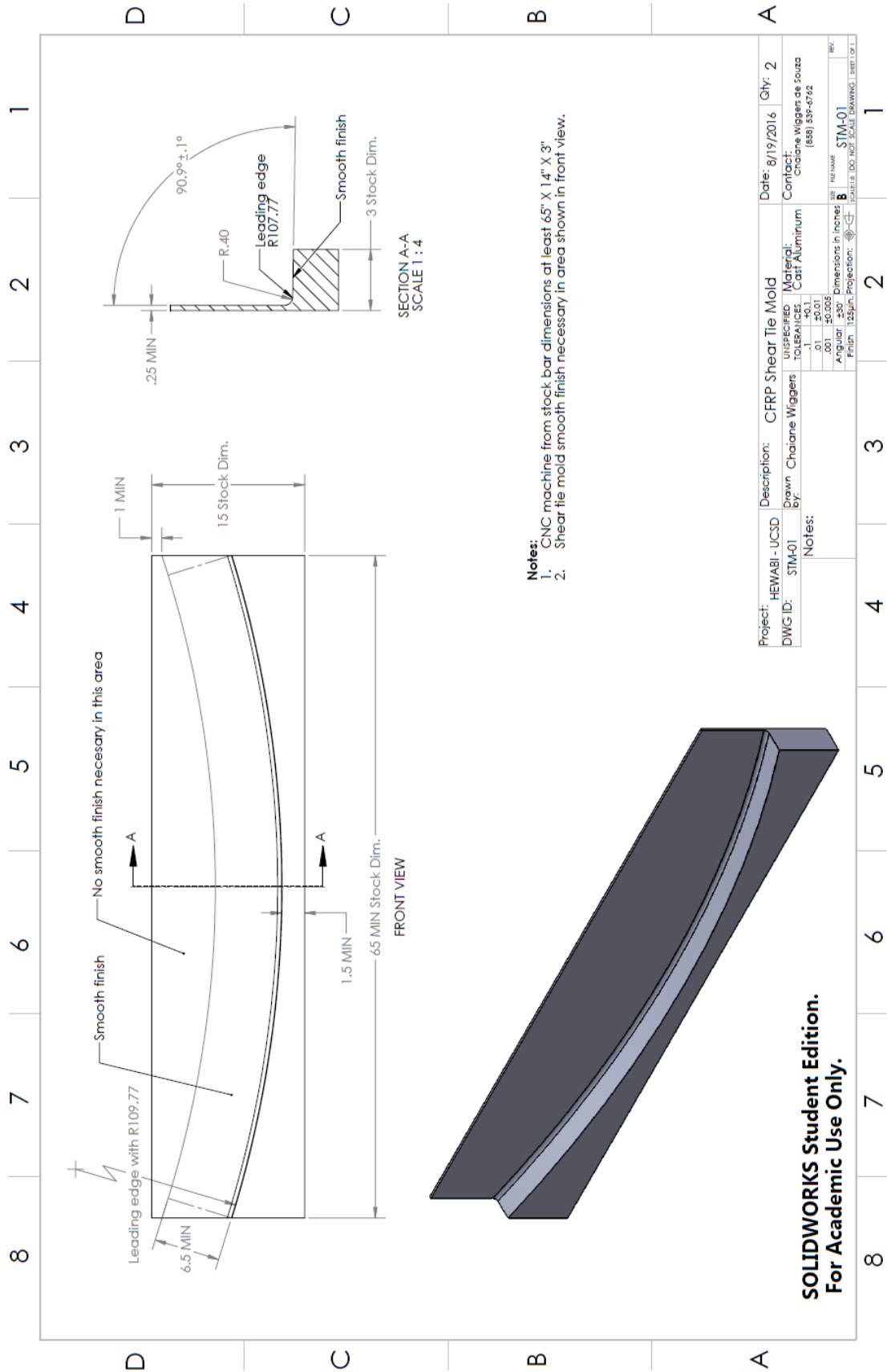
**SOLIDWORKS Student Edition.**  
**For Academic Use Only.**



Project: HEWABI - UCSD	Description: Stringer Mold Top & Bottom Pieces	Dra. ID: StM-03
Qty: 16	Date: 8/23/2016	Contact: Yeon Jong Yoo (Email: yyoo12@gmail.com) Chelene Wiggers De Souza (Email: cwiggers@ucsd.edu)
<b>SOLIDWORKS Student Edition. For Academic Use Only.</b>	UNSPECIFIED TOLERANCES	Material: Aluminum 6061-T6 Stock bar
	.1 ±0.1	Dimensions in inches
	.01 ±0.01	Projection:
	.001 ±0.005	Angular ±30°
Finish 125µin.		SCALE: 1:10 (DO NOT SCALE DRAWING) SHEET 1 OF 1

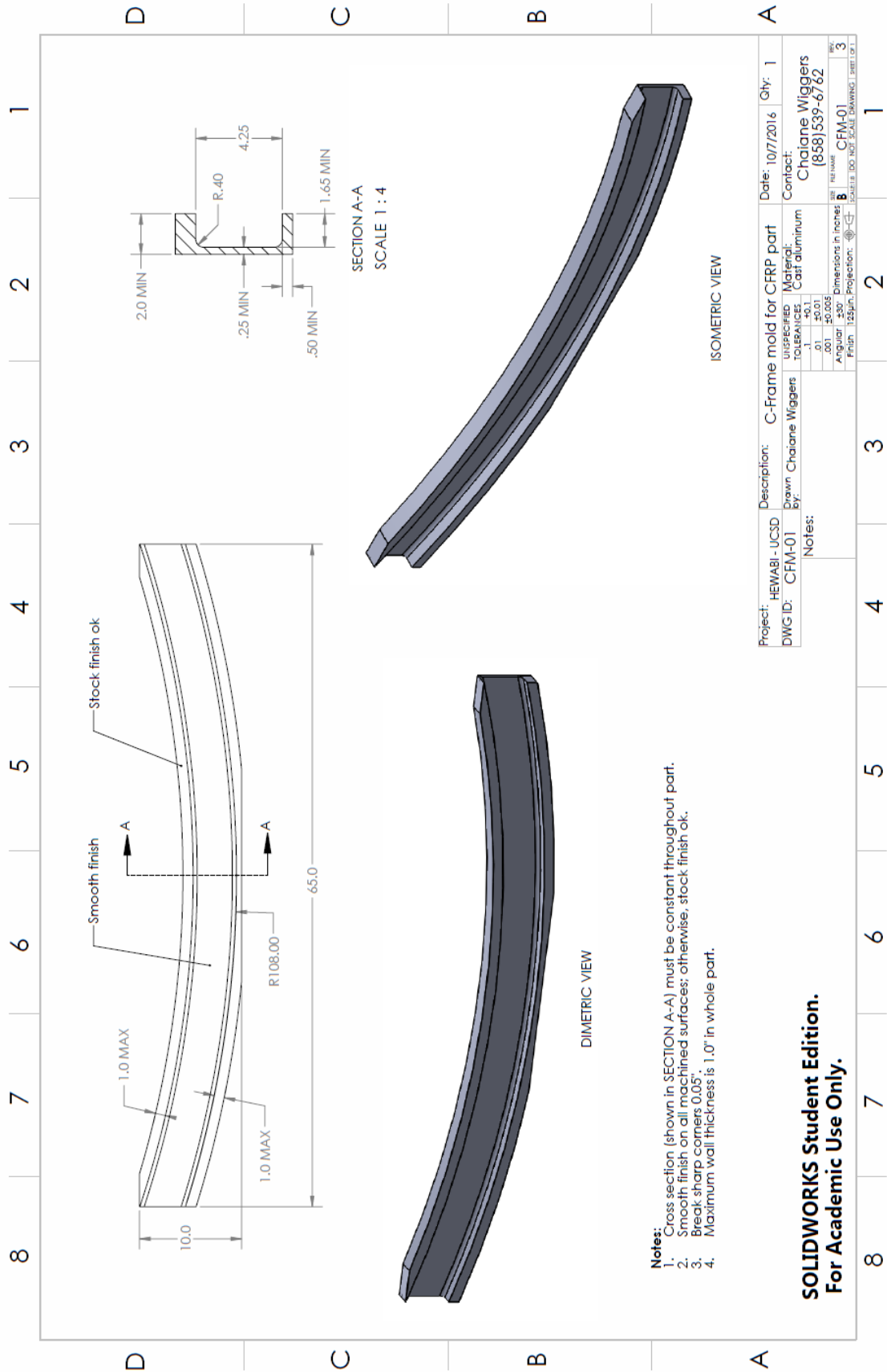
2

1



**SOLIDWORKS Student Edition.**  
**For Academic Use Only.**





SECTION A-A  
SCALE 1 : 4

ISOMETRIC VIEW

DIMETRIC VIEW

- Notes:**
1. Cross section (shown in SECTION A-A) must be constant throughout part.
  2. Smooth finish on all machined surfaces; otherwise, stock finish ok.
  3. Break sharp corners 0.05".
  4. Maximum wall thickness is 1.0" in whole part.

Project:	HEWABI - UCSD	Description:	C-Frame mold for CFRP part	Date:	10/7/2016	Qty:	1
DWG ID:	CFM-01	Drawn By:	Chaiane Wiggers	Contact:	Chaiane Wiggers (858)539-6762		
UNSPECIFIED TOLERANCES:		Material:	Cast aluminum				
.01 ±0.01							
.001 ±0.005							
Angular: ±30'		Dimensions in:	Inches				
Finish: 125µin		Projection:	ASME				
		Scale:	DO NOT SCALE DRAWING				
		Part Name:	CFM-01				
		Sheet:	3				
		Sheet:	3				

**SOLIDWORKS Student Edition.  
For Academic Use Only.**

## B. LAYUP INSTRUCTION

This appendix includes prepreg cutting plan and layup instruction with check list:

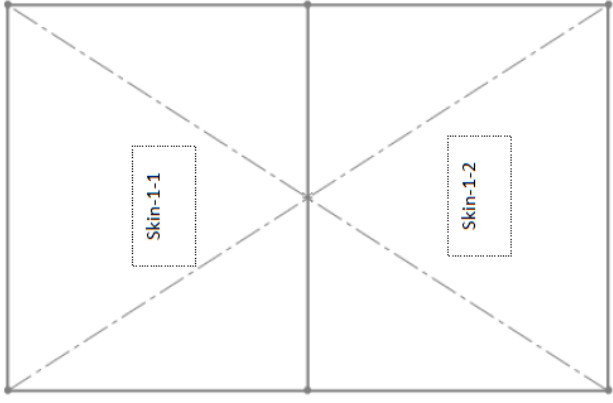
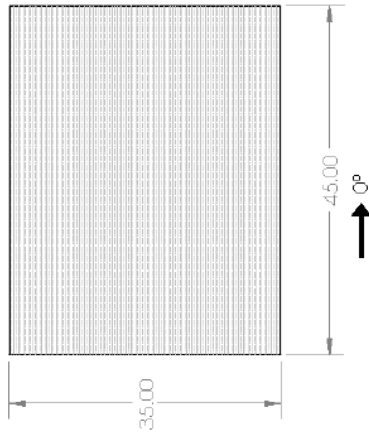
- 1) Skin layup
- 2) Stringer layup
- 3) Shear tie layup
- 4) C-Frame layup

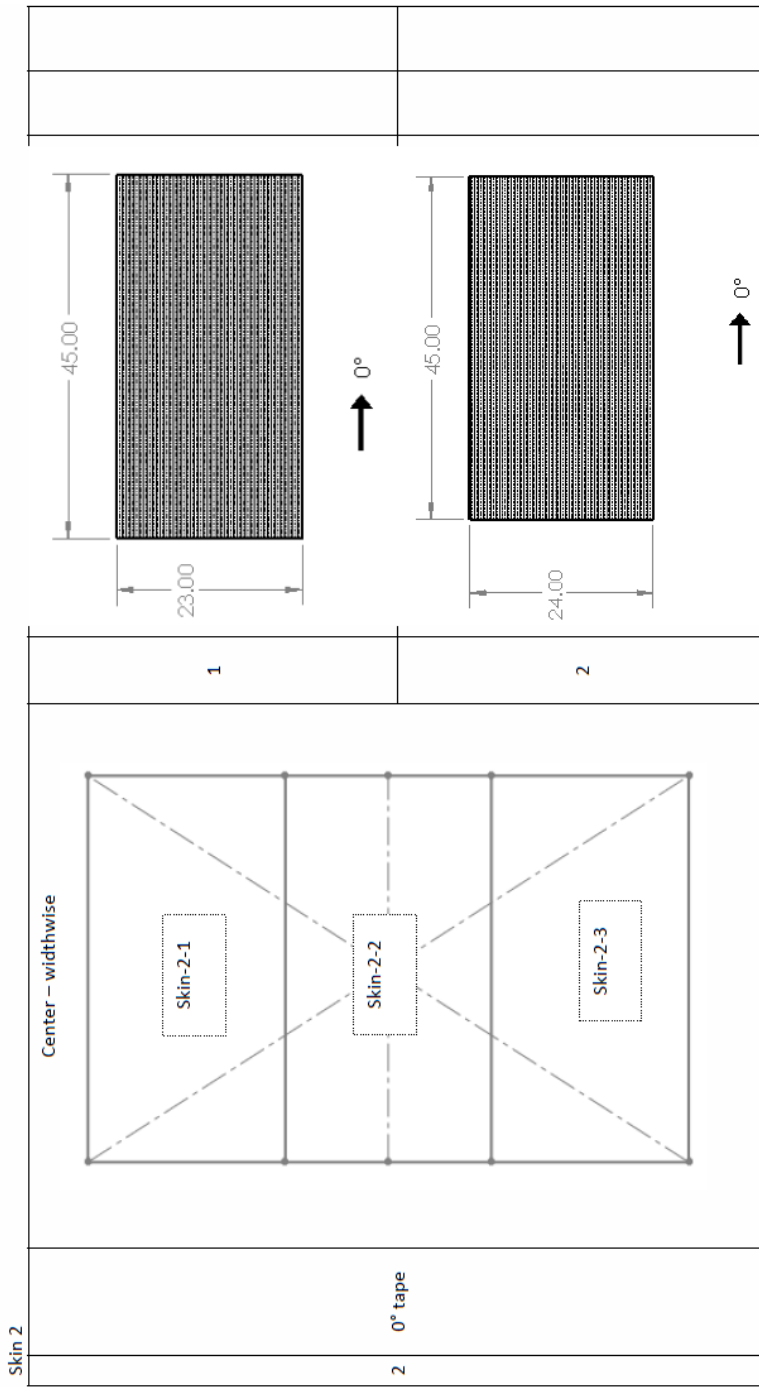
Skin 1

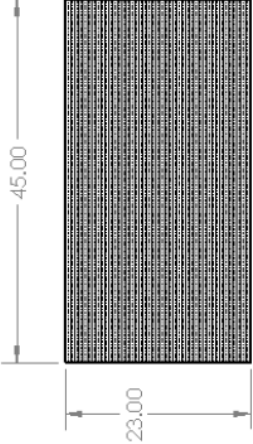
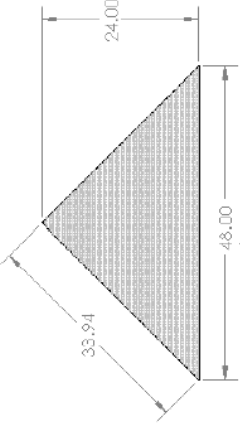
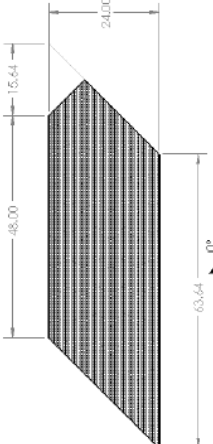
**Component: Skin - 45 x 70in**

Layout: [0w/0/45/90/-45/0/90]<sub>s</sub>

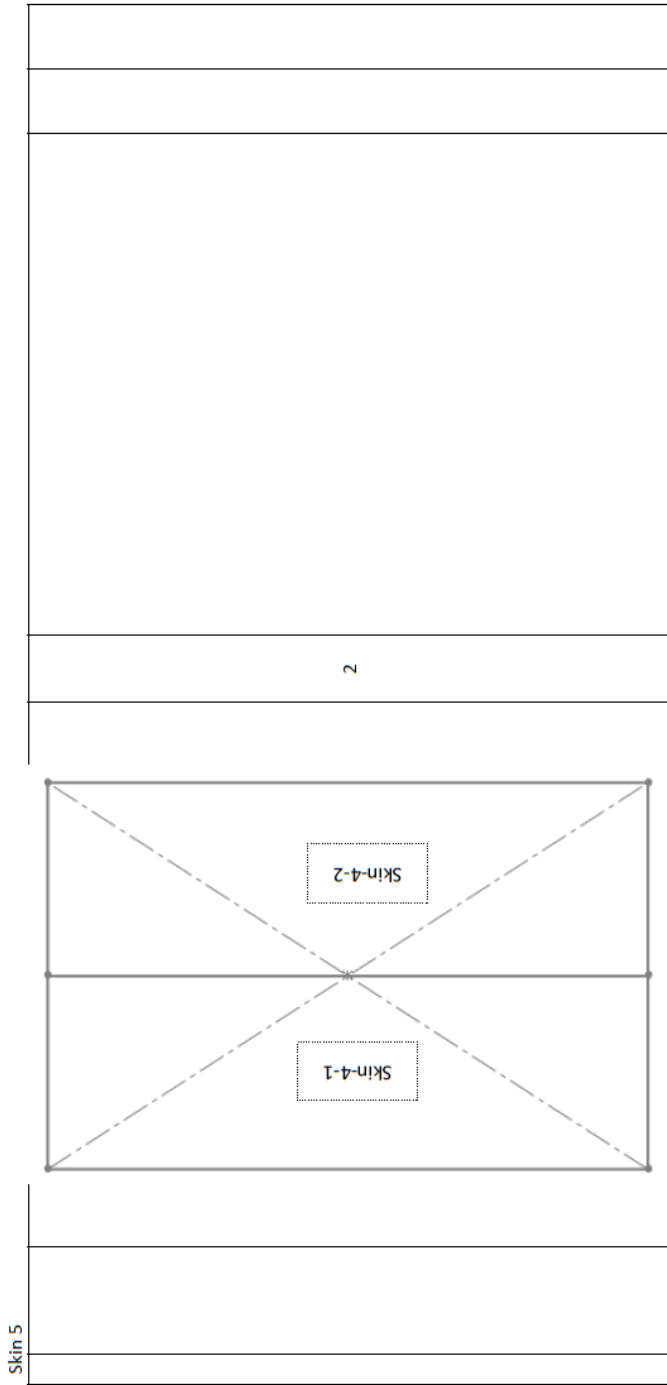
Material: T800 tape and woven

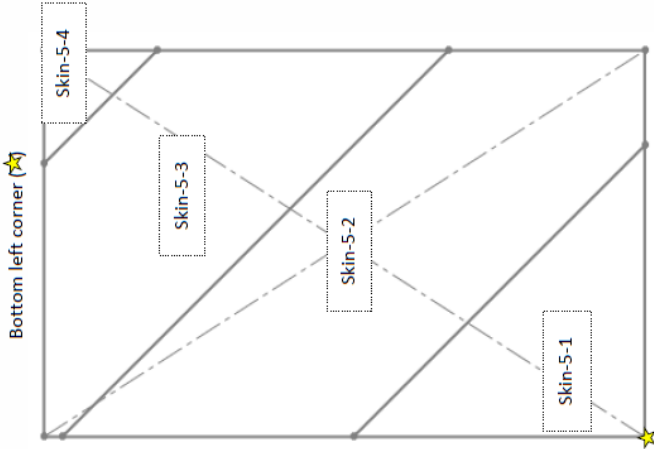
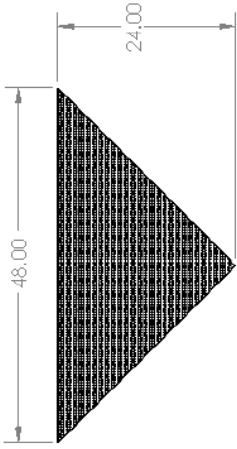
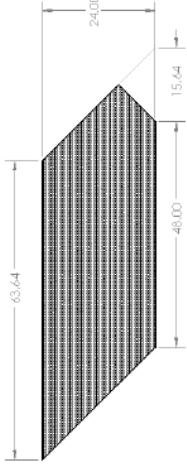
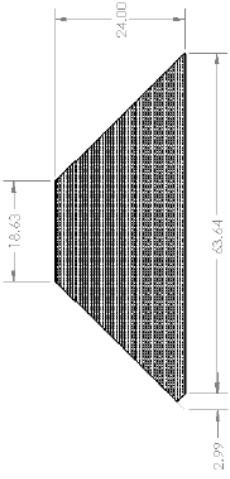
Layer	Alignment	Cut#	Ply cut	Initials
<p>1 0° woven</p>	<p>Centerline – widthwise</p> 	<p>1</p>		
		<p>2</p>		



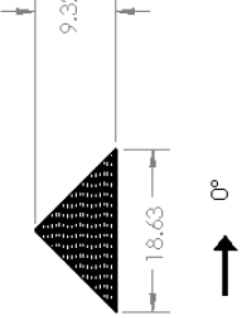
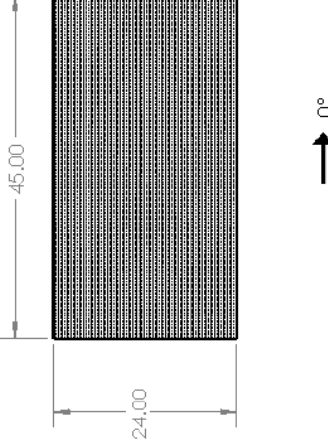
Skin 3					
3	45° tape	Right bottom corner (★)			

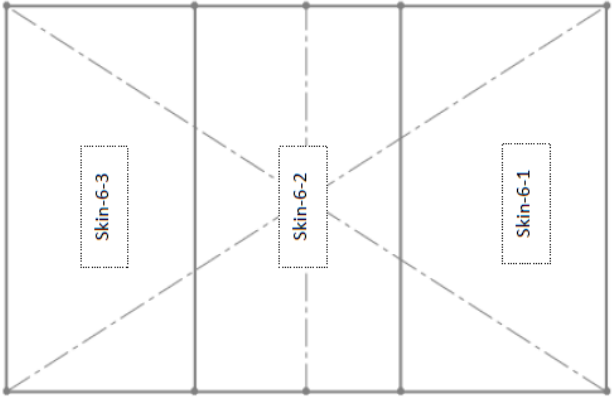
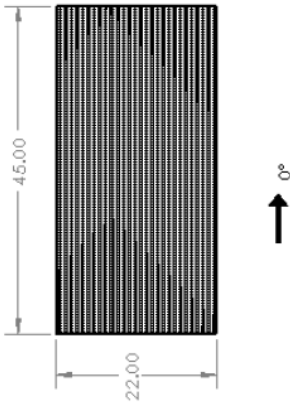
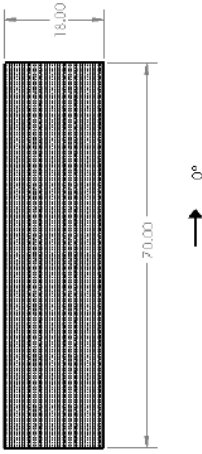
Skin 4		3		4		4 90° tape	1	
--------	--	---	--	---	--	------------	---	--

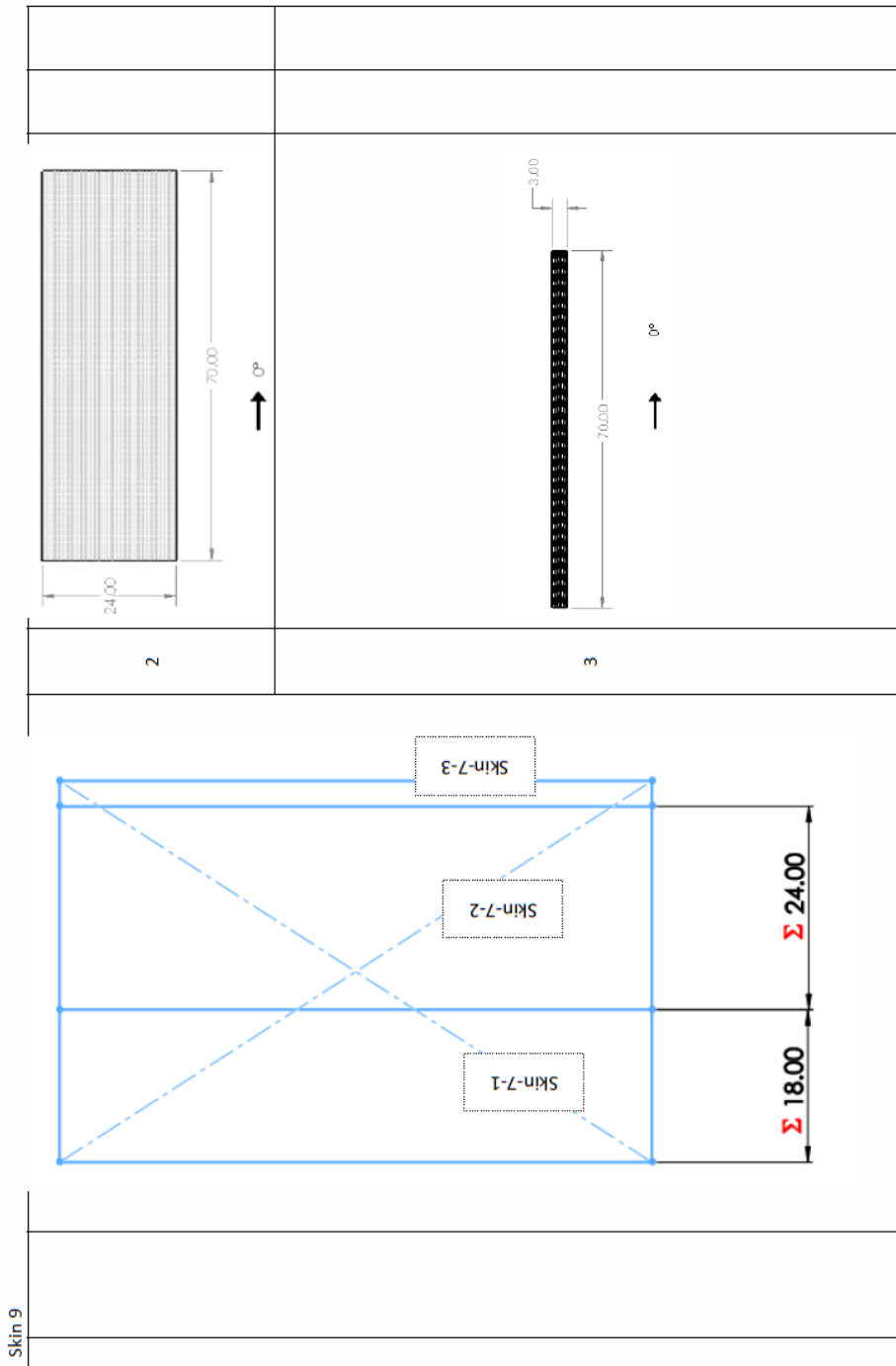


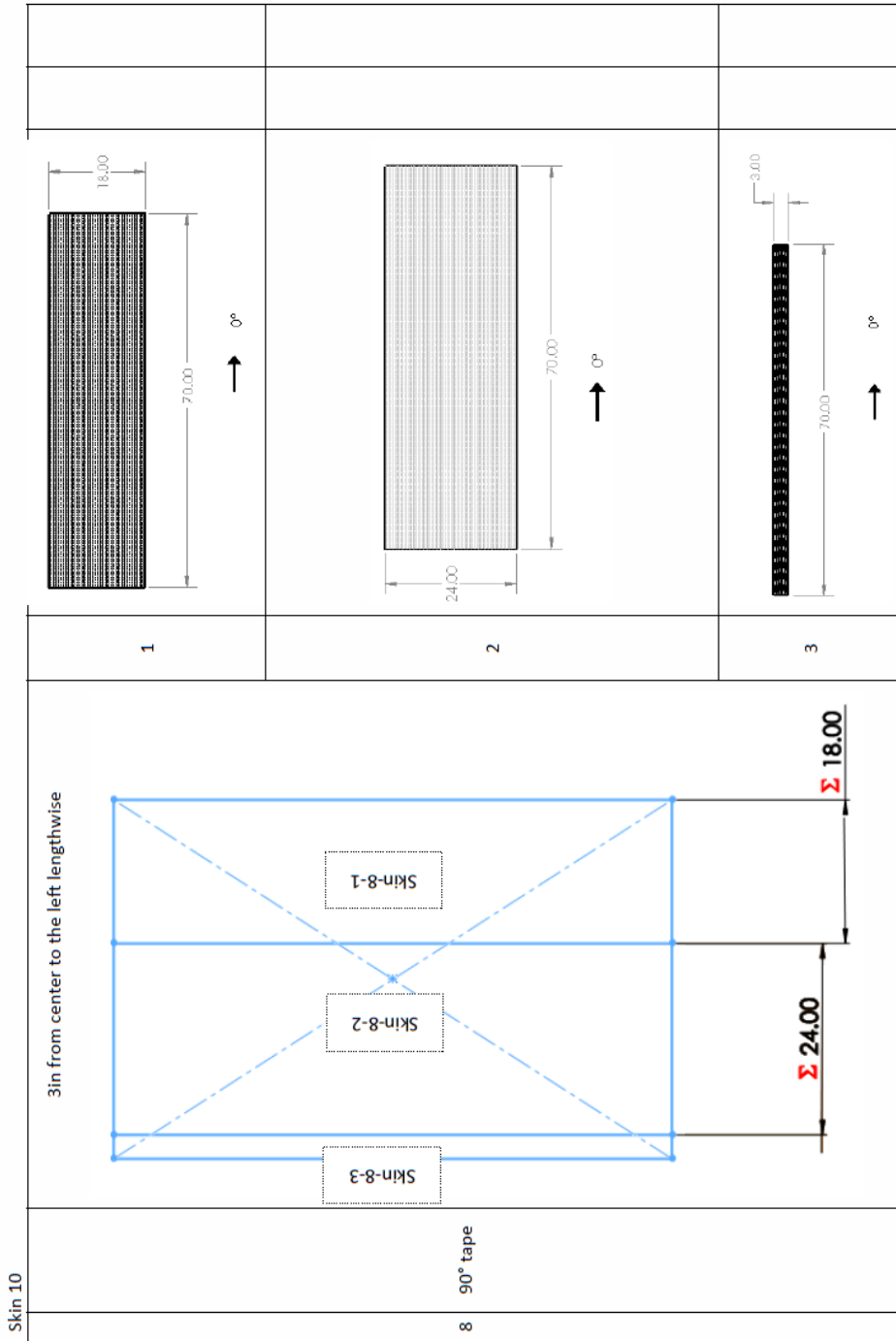
Skin 6			
5 -45° tape			
	1		
	2		
	3		

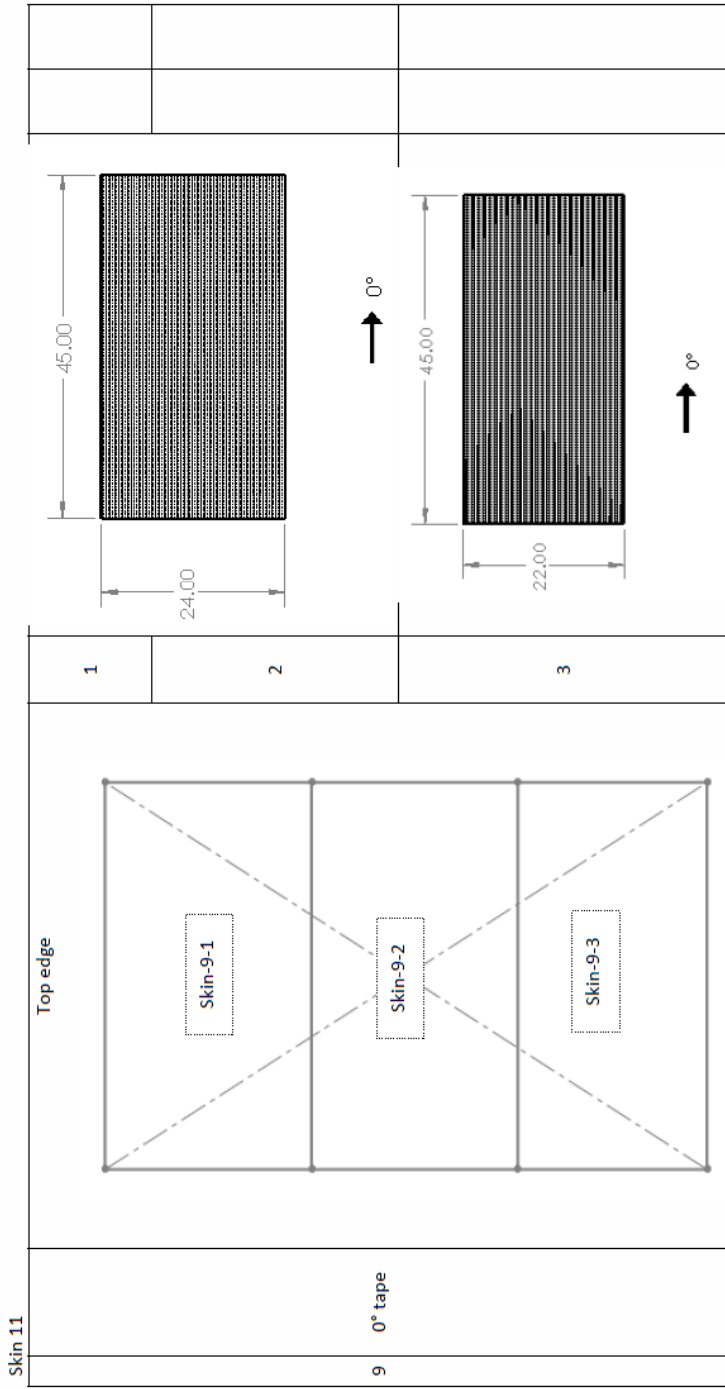


Skin 7			
	4		
6	0° tape	<p>1</p> <p>2</p> <p>Bottom edge - widthwise</p>	

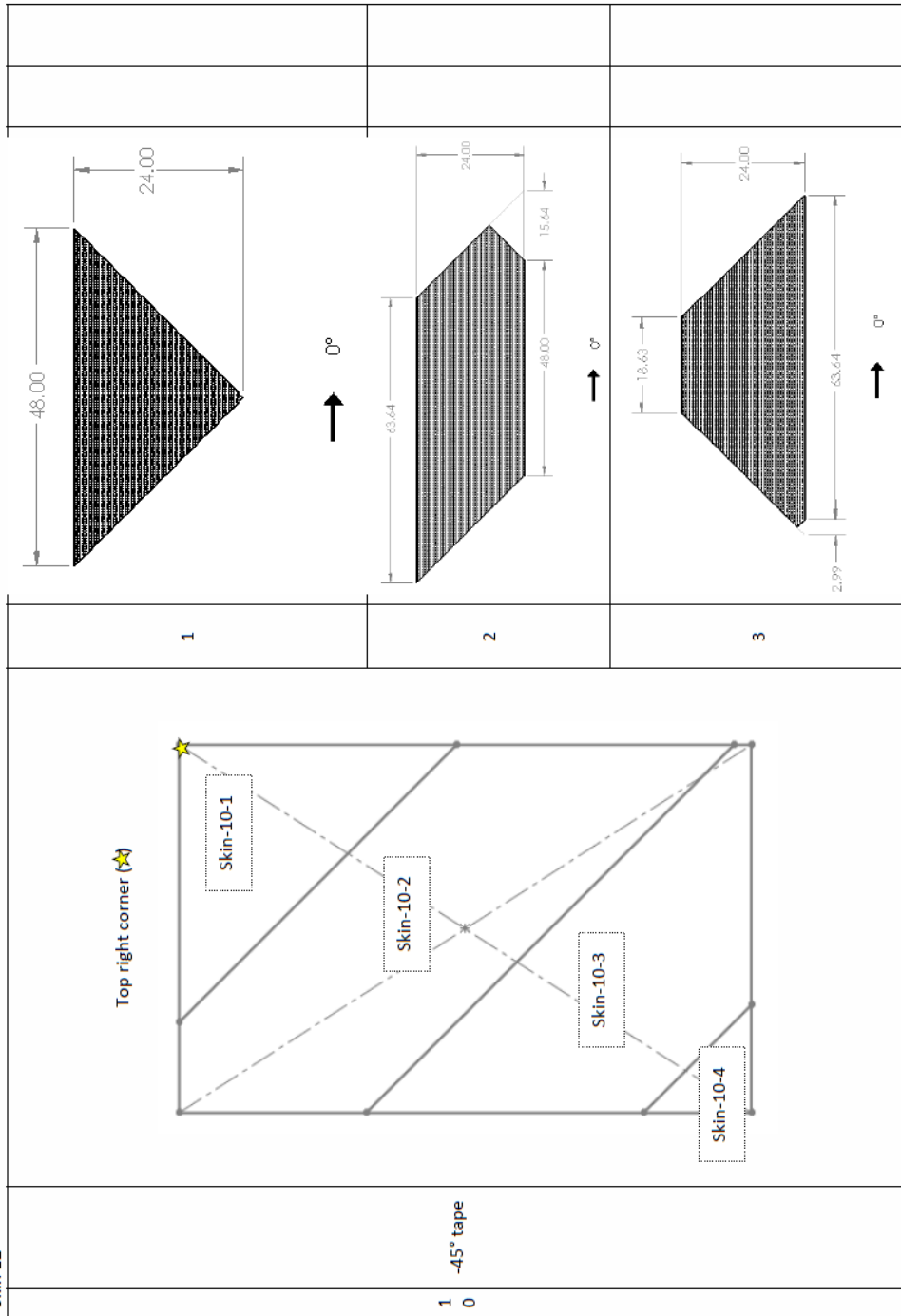
Skin 8		3		7 90° tape
	3in from center to the right lengthwise (left edge)	1		

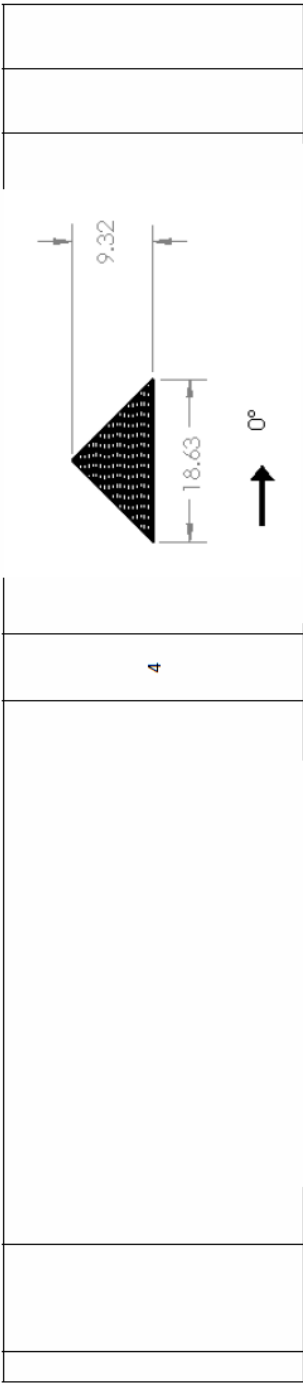
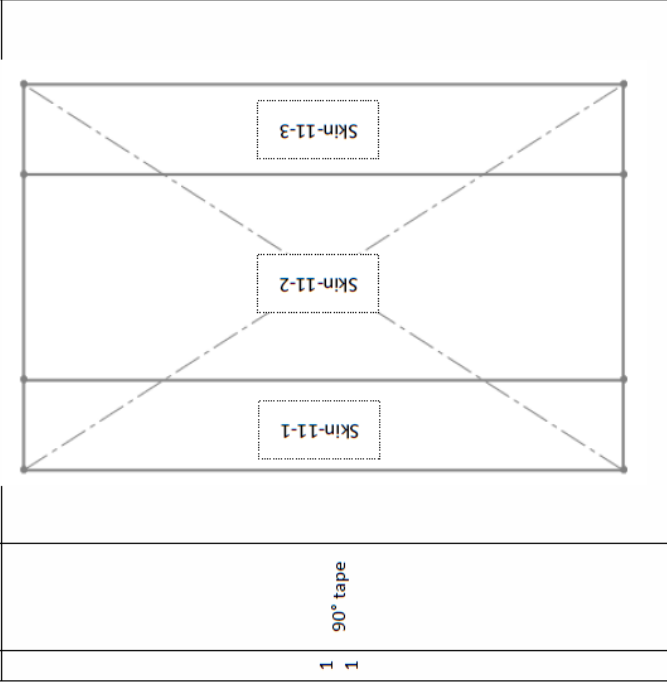


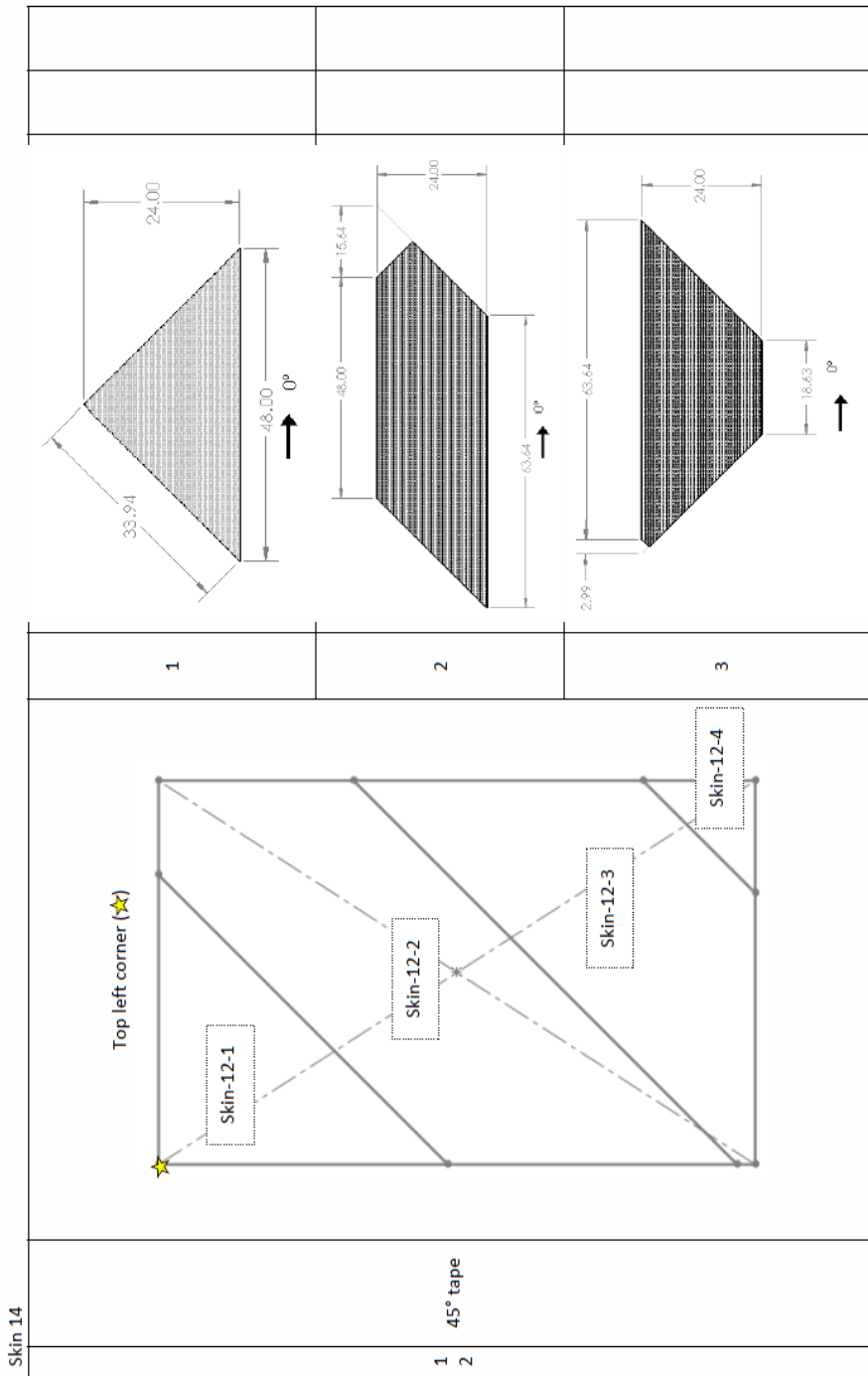




Skin 12

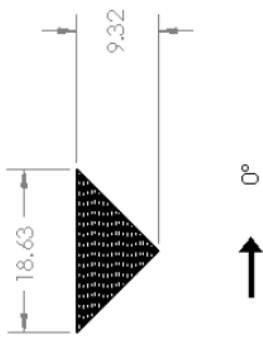
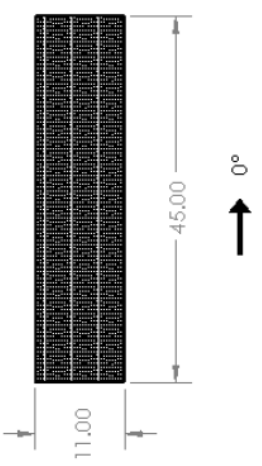
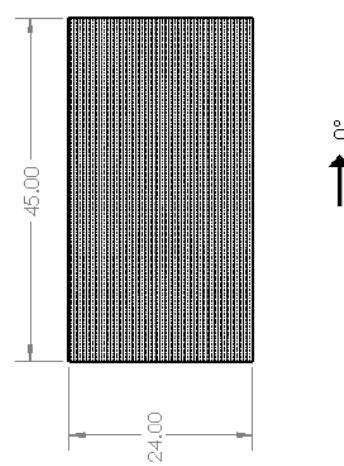


Skin 13		1	2	3
				
		<p>1 90° tape</p> <p>1</p>		

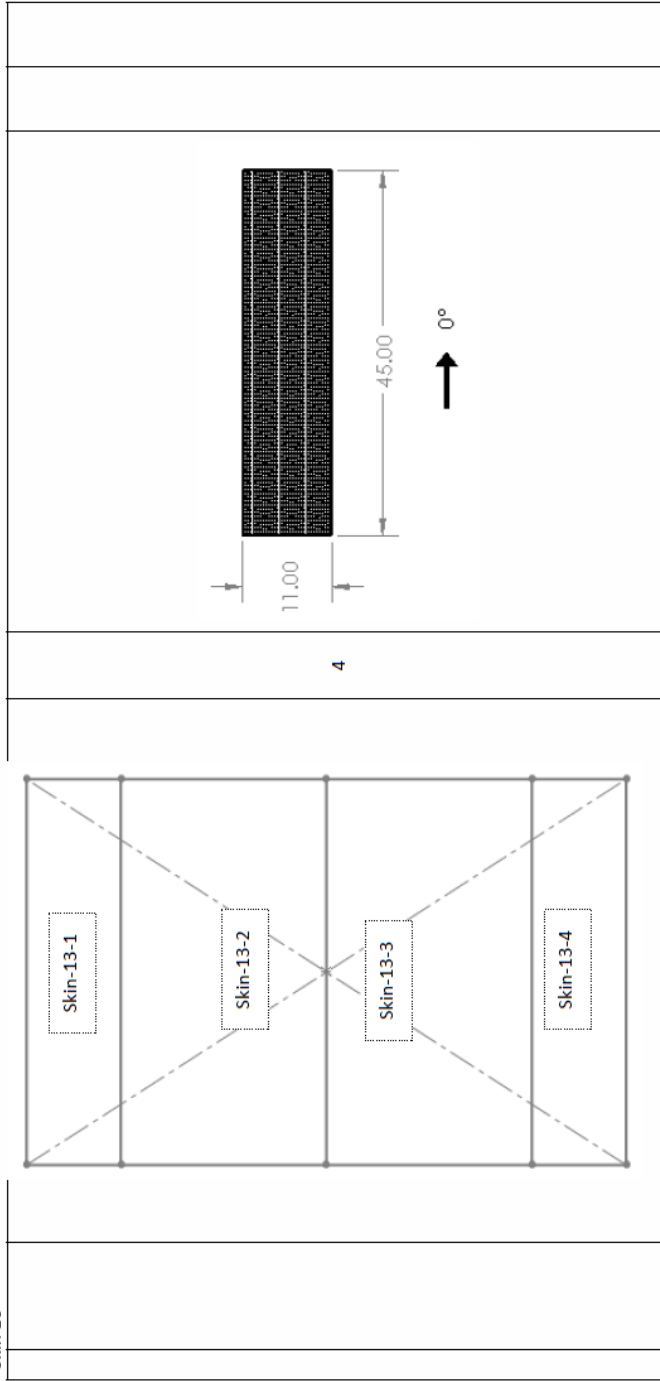


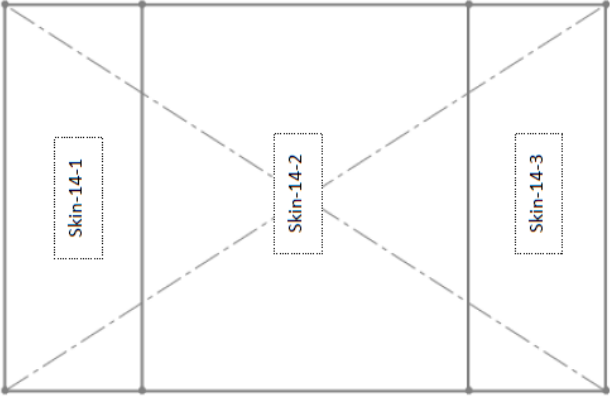
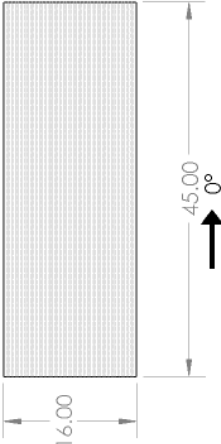
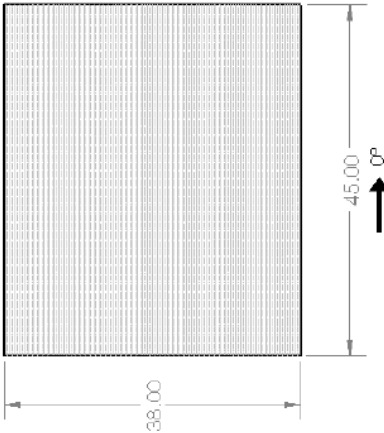


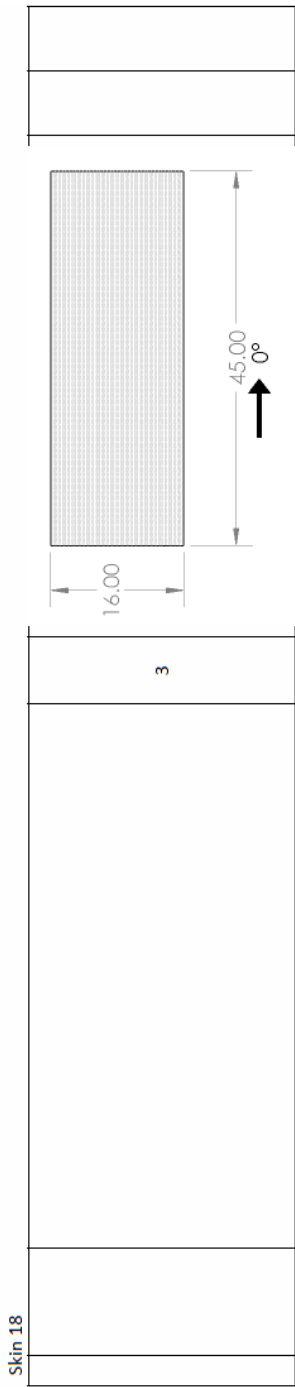
Skin 15

		4							
				1 0° tape	Center - widthwise		1 3		

Skin 16



Skin 17	<p data-bbox="422 1129 446 1291">Center - widthwise</p> 	 <p data-bbox="560 892 576 913">1</p>	 <p data-bbox="1015 892 1031 913">2</p>
	1 4 0° woven		

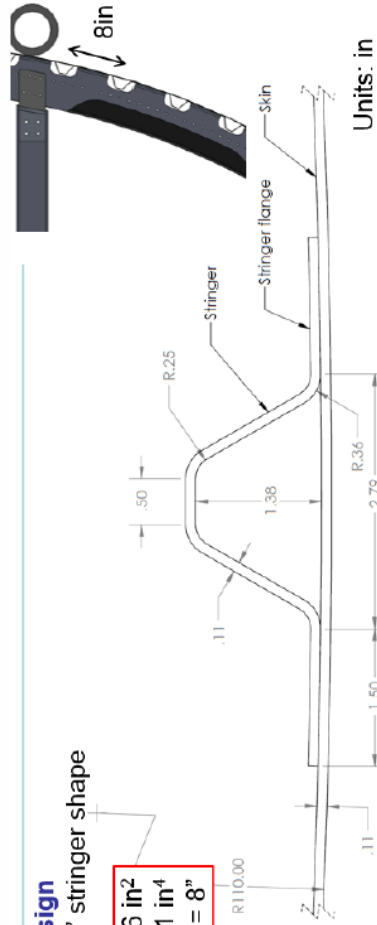


# Component: Stringer

Layout: [0w/0/45/90/-45/0/90]<sub>s</sub>  
 Material: T800 tape and woven

## New Design "Thinner" stringer shape

$A = 0.796 \text{ in}^2$   
 $I_x = 0.221 \text{ in}^4$   
 Spacing = 8"



Contents	
Disclosure.....	2
Materials needed.....	3
Cutting plan.....	4
TAPE .....	4
WOVEN.....	4
Mold Preparation.....	5
Instructions on layup and debulking.....	9
Layup.....	9
Debulking .....	10
Mold removal.....	13

Stringer 2  
Conversion of Decimal to fraction ..... 27

**Disclosure**

“Ply cut” drawings in the Layup section are with respect to the cutting point of view, i.e., when laying up the patches are flipped. For this reason, +45° plies seem like -45° and vice-versa.

Stringer 3

**Materials needed**

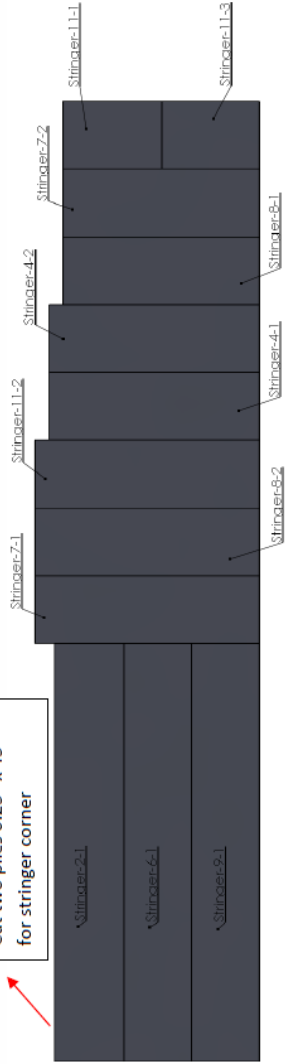
- Acetone;
- Alcohol;
- Paper towels;
- Kim wipes;
- Nitrile gloves;
- Cutting gloves;
- Utility knives and blades;
- Scissors;
- Rulers;
- Measuring tapes;
- Black Sharpies;
- Prepreg storage bags;
- Squeegees;
- Rulers;
- Cutting templates (45° and long)
- HDPE cutting boards;
- 8 HDPE stringer boards;
- 8 sets of stringer molds;
- Cutting plan;
- Layup plan;
- Prepreg material time-out sheet;
- Prepreg.

Stringer 4

Cutting plan

TAPE

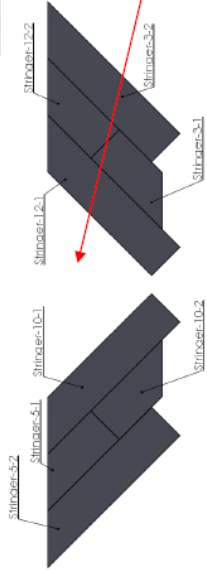
Cut two plies 0.25" x 45" for stringer corner



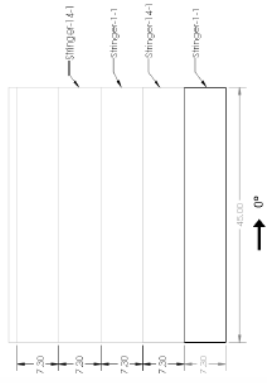
Makes 3 stringers



Cut all 8 stringers' +45°, then all -45°.


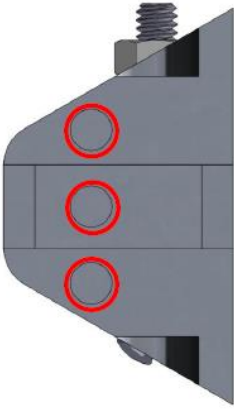


WOVEN


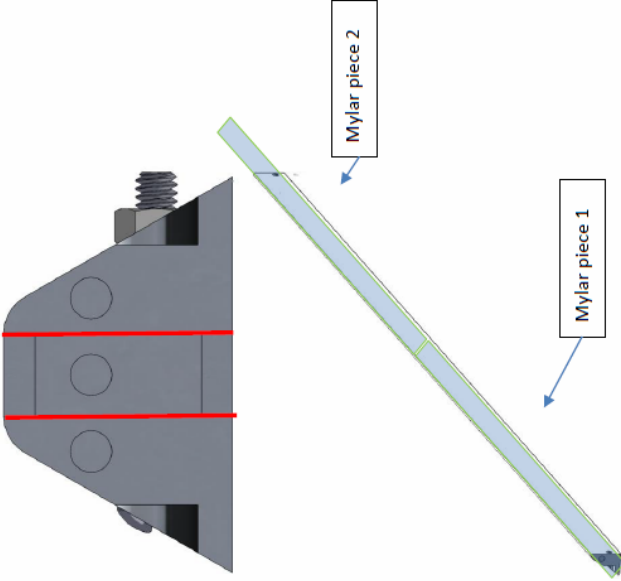




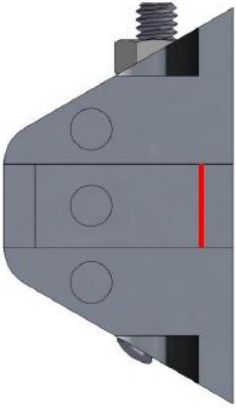
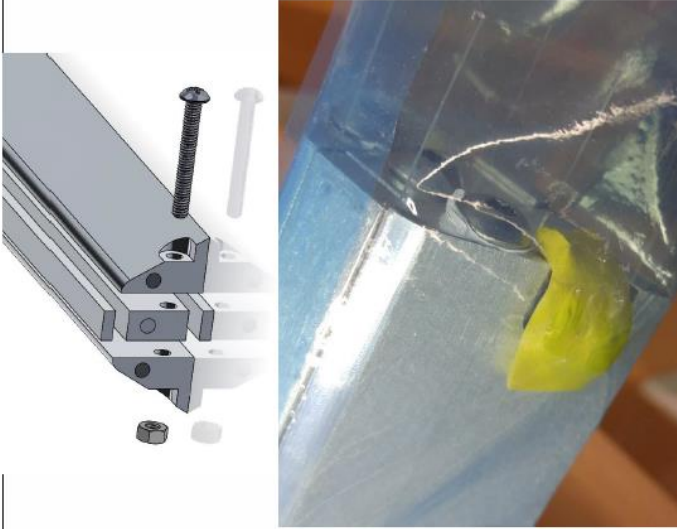
Stringer 5  
**Mold Preparation**

Step	Description	Figure
1	Check all molds for damage, and remove extra material with a utility knife if necessary.	
2	Clean all molds and HDPE boards with acetone and paper towels. Remove any excess resin from previous cures. Clean again with alcohol and paper towels until all residue is removed. If necessary, use blades. Perform a last cleaning with Kim wipes.	
3	Plug the inner threaded regions (3 on the front and 3 on the back) with 1/4", 0.75" max length bolts. Use some Teflon tape (piper's tape, PTFE tape) around the screws. This is to prevent any resin from filling the threads. Torque the bolts as tight as you can.	


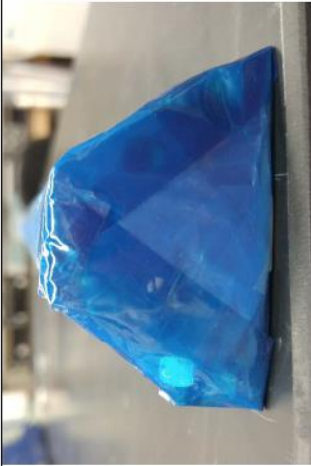
Stringer 6

			
4	<p>Cut 4 strips of 0.01" thick Mylar for each mold set with the utility knife. The dimensions are 1.25" x 27". Insert between the mold pieces as shown in picture. Let ~3in hang from each side of the mold.</p>		

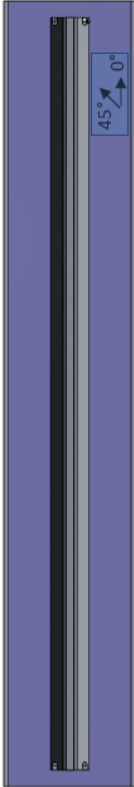
Stringer 7

5	<p>Cut 2 strips of 0.001" thick Mylar for each mold set with the utility knife. The dimensions are 0.5" x 27". Insert between the mold pieces as shown in picture.</p>	
6	<p>Set aside the mold kits. For all molds, assemble parts as shown in the drawing. Insert 2 bolts (1/4", ~2" long) with corresponding nuts, one at each end of the stringer mold. Hand tighten. Cover the protruding nut with a very small piece of tacky tape.</p>	

Stringer 8

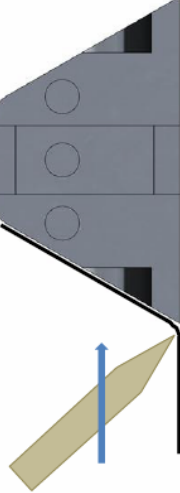
7	<p>Cut one piece (per mold set) of release film 48" x 7" with utility knife to have straight edges. Wrap the release film around the assembled mold tightly, without any wrinkles on a flat surface. Use flash tape to seal the wrap on all seams.</p> <p>Make sure the first side is tight enough on the mold before sealing the other side.</p>	
8	<p>Trim the excess Mylar pieces from the ends.</p>	
9	<p>Seal the ends of the mold carefully and place flash tape on all openings.</p>	

Stringer 9

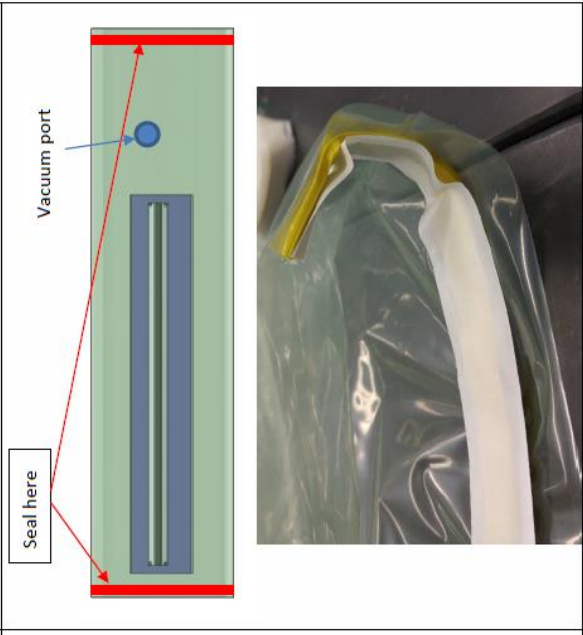
10	<p>Lay a piece of release film 7" x 48" release film on top of the 8" x 48" HDPE board. Place the stringer mold on the center of one of the boards. Draw your coordinate system for layup with a Sharpie.</p> <p>Place flash tape on top of your CSYS to avoid contamination through Sharpie.</p>	
----	---	--

### Instructions on layup and debulking

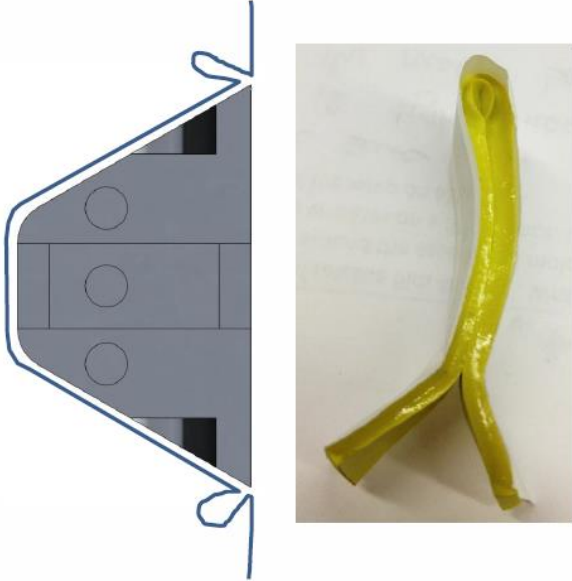
Layup

Step	Description	Figure
0	<p><b>IMPORTANT! Before cutting/layup, ensure that prepreg material has been thawed for about 2h (or until room temperature) inside its sealed bag, with desiccant inside the bag. Do not open bag until material is thawed, to avoid condensation.</b></p>	
1	<p>Start laying up from one of the sides, preferably your non-dominant side. Lay the longest side of the ply first (i.e. the longitudinal side), while lifting the free-standing side of the ply. You may need to get an extra hand to help you out.</p>	
2	<p>Use a squeegee to eliminate air bubbles while you are laying up. Carefully press the thinner edge of the squeegee towards the first corner of the stringer to avoid bridging.</p>	
3	<p>Repeat the process, paying special attention to the corners.</p>	


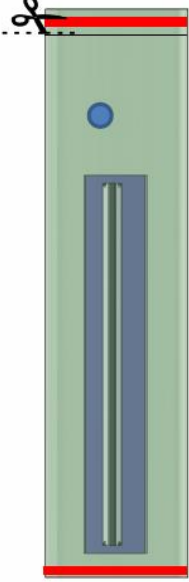
Stringer 10  
Debulking

Step	Description	Figure
0	<p>Cut the breather to size 8" x 60". Cut the peel ply to size 8" x 48".</p>	
1	<p>Cut the 18" wide vacuum tube to a length of ~72in (6ft). On a flat surface, seal one of the ends of the 18" wide vacuum tube.</p> <p>Overlap ~1in of tacky tape on the folds. Remove the tacky tape cover in sections as you work your way through the width.</p>	
2	<p>Insert the stringer board with the stringer mold prepared for debulk (with peel ply, breather, etc) inside the tube. Leave about 2ft extra on one of the sides.</p>	

Stringer 11

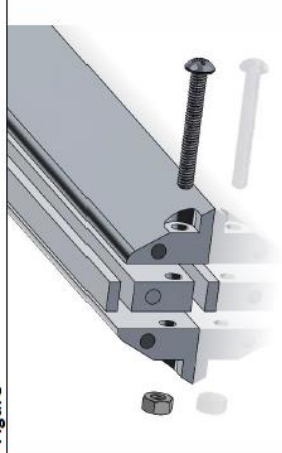
3	<p>Accommodate the bag onto the surface of the stringer. Make pleats as shown.</p> <p>If using envelope bag (recommended), no need to make pleats over the edge of the tacky tape.</p> <p>If using vacuum bag, prepare four pieces of 4.25" long tacky tape and fold as shown.</p>	 <p>The diagram shows a grey envelope bag with three circular ports and a central rectangular section. Blue lines indicate the bag is being folded onto a surface, creating pleats. The photograph shows a yellow vacuum bag with a central port and two side ports, with the top edge folded over to create pleats.</p>
4	<p>Insert the vacuum port about 1ft from the bag border. Seal the other end of the envelope, close to the border of the bag (<b>Tip:</b> it is easier to seal it over a flat surface). Pull partial vacuum.</p>	
5	<p>While pulling partial vacuum, make sure bag is well accommodated and pleats are in the right places. When done, pull full vacuum.</p>	

Stringer 12

6	<p><b>Pressure drop test.</b> Attach the pressure valve after full vacuum (usually around -30 in Hg) was achieved. Time 1min. If the pressure has dropped less than 1 in Hg, the bag seal is good. Otherwise, try to find the leak.</p>	
7	<p>When done with debulk, cut the bag on the farther (i.e. near where vacuum is applied) end of the bag very close to the tacky tape. Save the bag for next debulk.</p>	

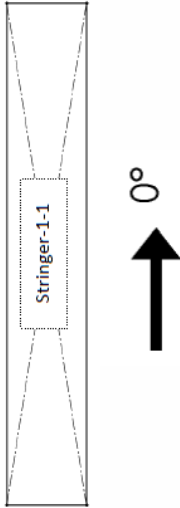
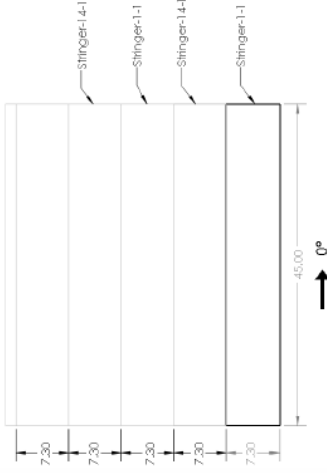
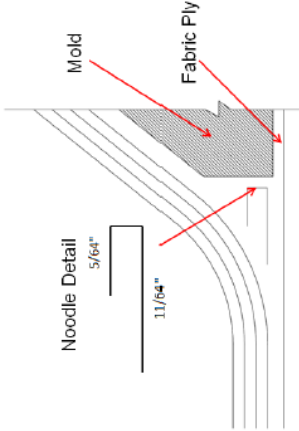


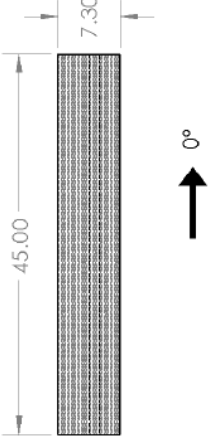
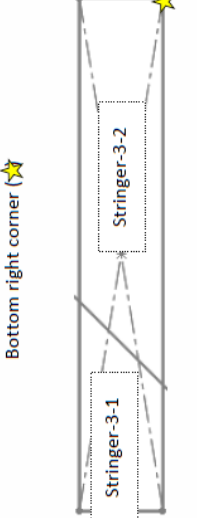
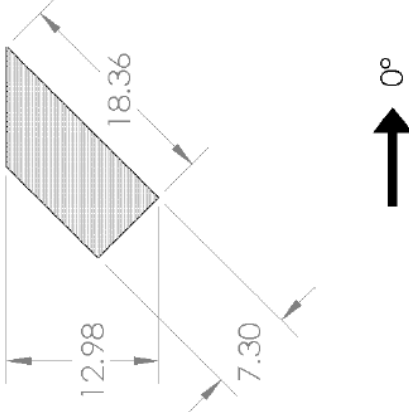
### Mold removal

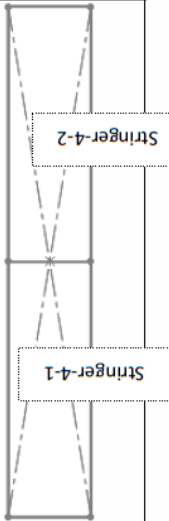
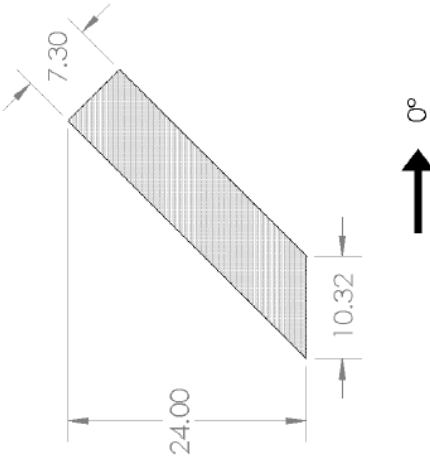
Step	Description	Figure
1	Unscrew both bolts with a Phillips wrench, one on each side of the mold.	
2	Remove the plugs from the from threaded holes. Screw a 1/4" U-bolt onto the center piece from one of the sides. Pull it out to remove the center piece.	
3	Remove top and bottom pieces.	
4	Remove both side pieces. If necessary, use a U-bolt.	
5	Remove excess release film stuck to the inner surface of the stringer.	

If there is resin built up, try wetting a piece of breather cloth with acetone. Wrap it around the stringer mold ends and protect with a plastic bag. Secure with rubber bands. Leave it on for at least 5min.

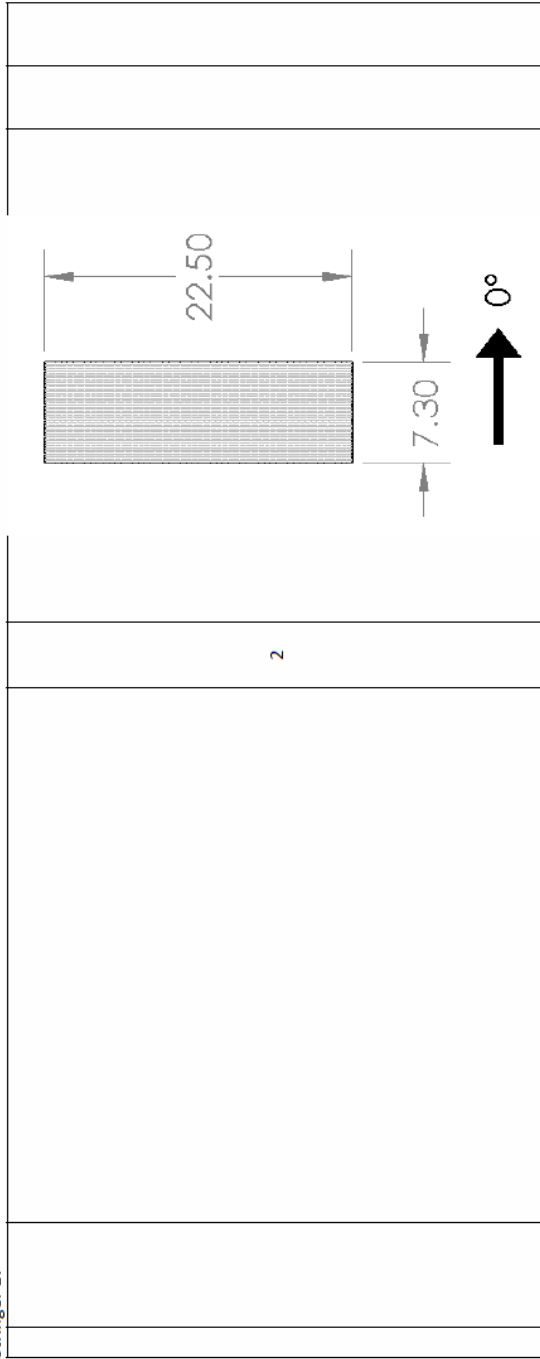
Stringer 14

Layer	Alignment	Cut#	Ply cut	Initials
<p>1 0° woven</p>	<p>Any</p> 	<p>1</p>		
	<p>Apply "Noodle" on bottom corners of stringer.</p> 			

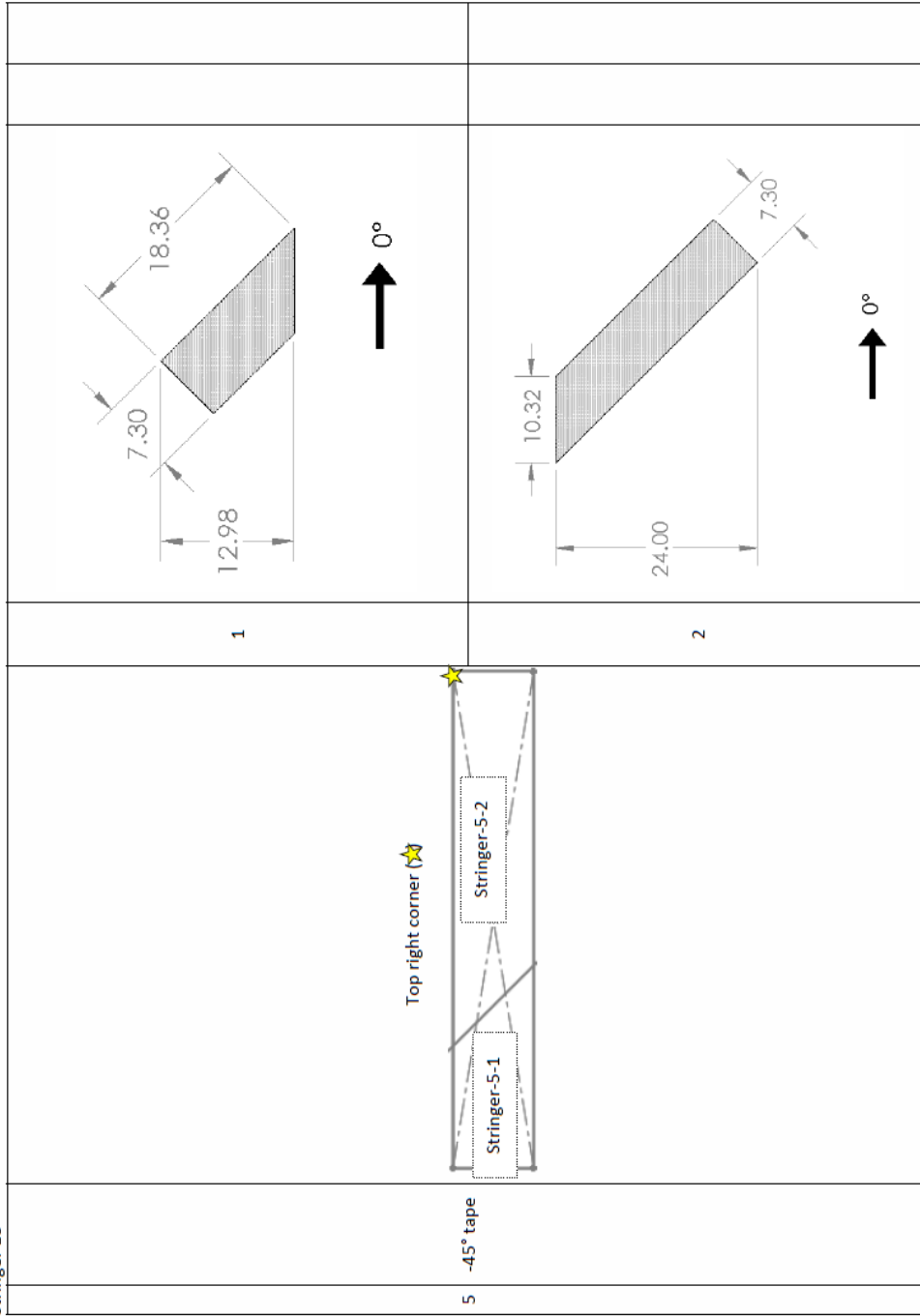
Stringer 15	2	0° tape	Any	1	
DEBULK FOR 20MIN					
	3	45° tape		1	


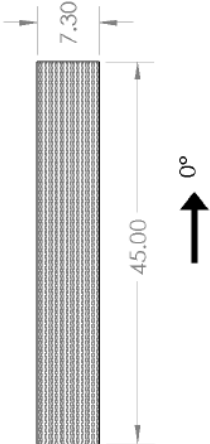
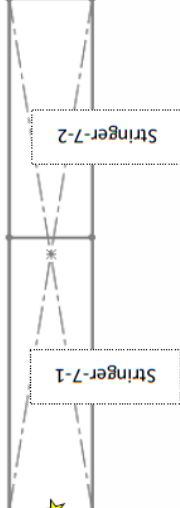
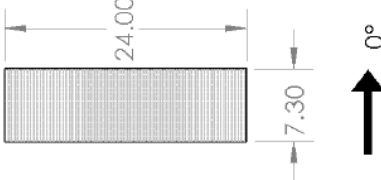
Stringer 16				
4	90° tape		2	

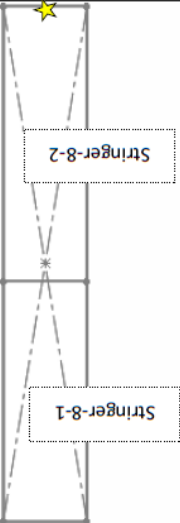
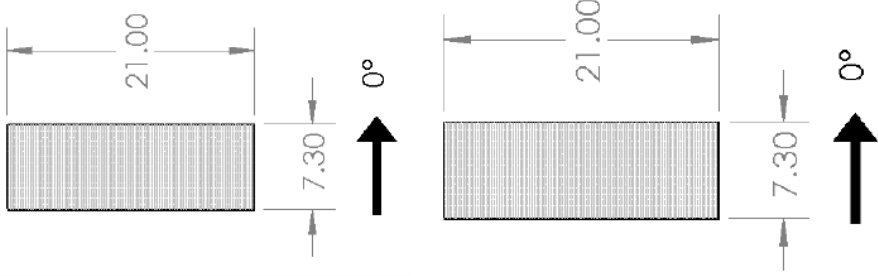
Stringer 17



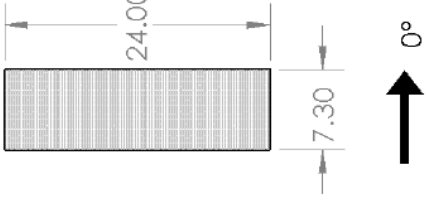

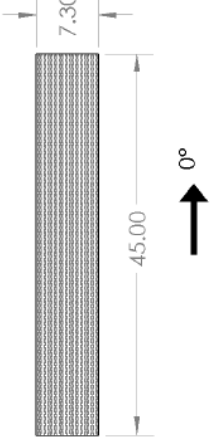
Stringer 18



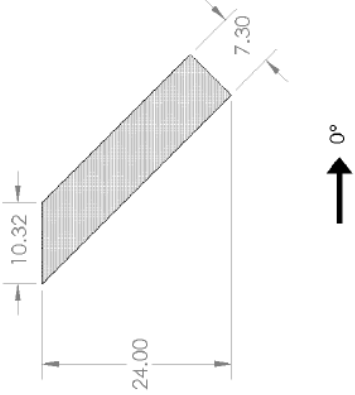
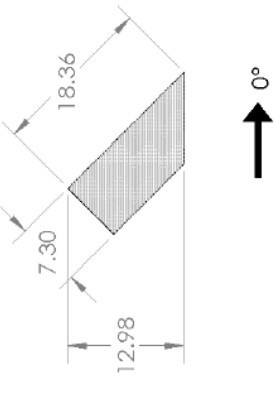

Stringer 19	DEBULK			
6	0° tape	<p>Any</p> 	<p>1</p> 	
7	90° tape	<p>Left edge (★)</p> 	<p>1</p> 	

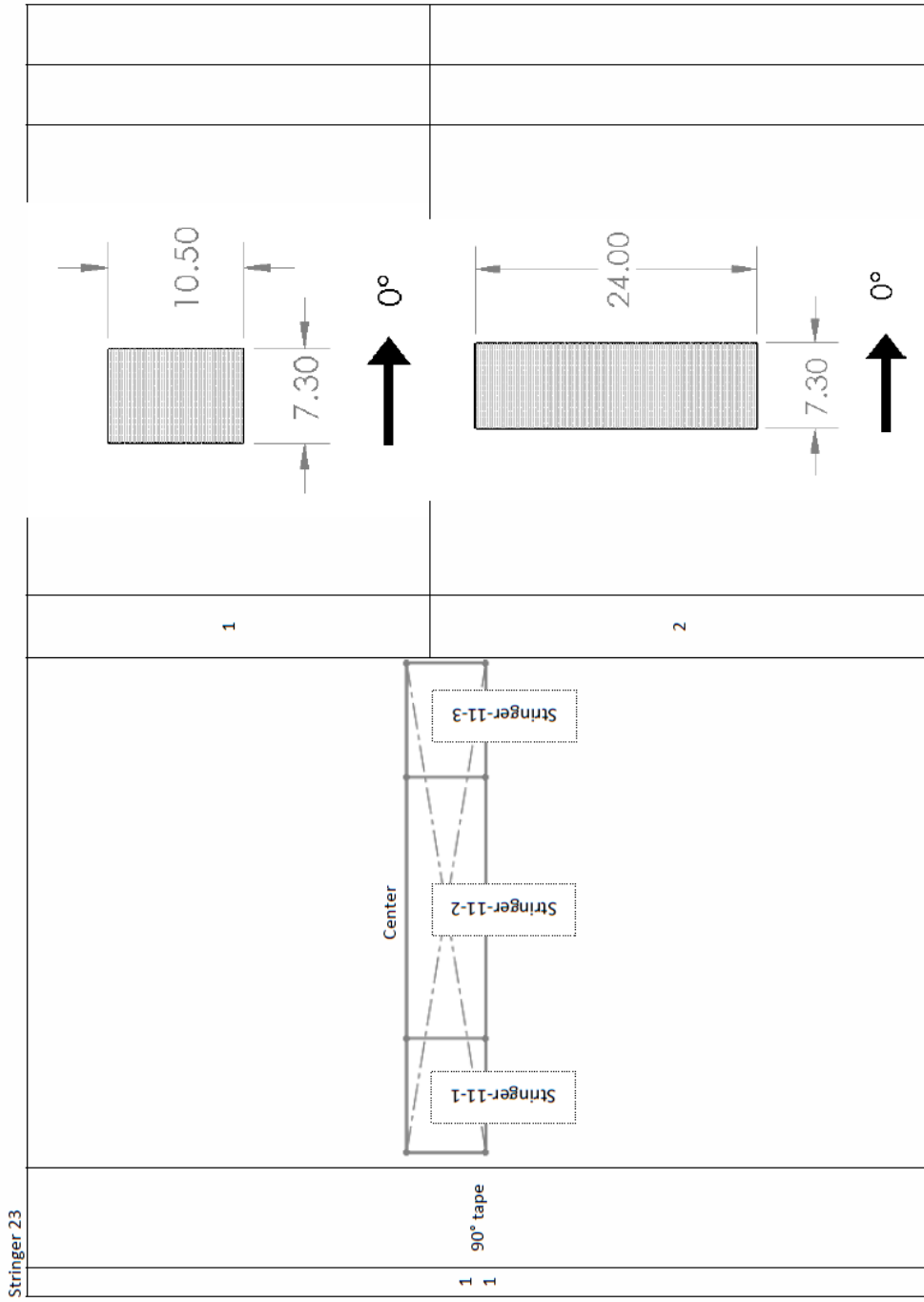
Stringer 20		
	2	
		
		8 90° tape

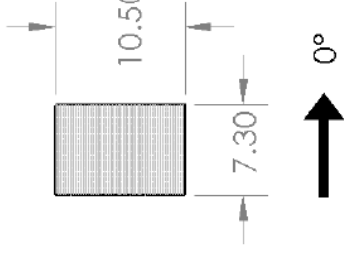

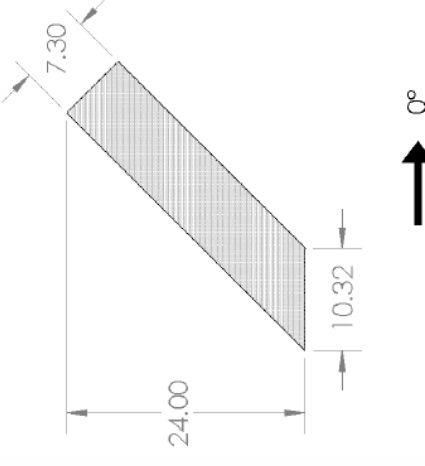


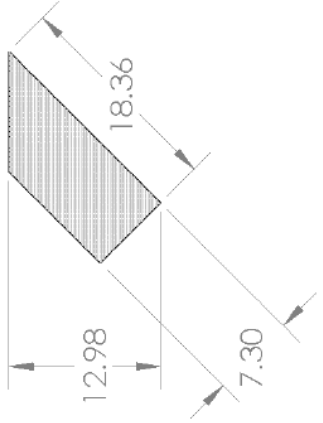
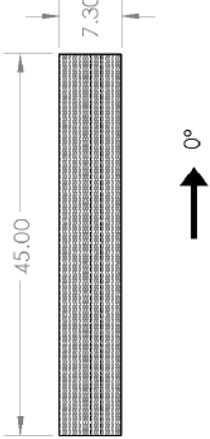
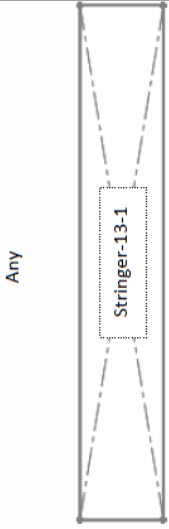
Stringer 21				2			
9	0° tape		1				

Stringer 22

DEBULK FOR 20 MINUTES			
1			
2			
1			
0	-45° tape		



Stringer 24				
1 45° tape 2				

Stringer 25			
	2		
			DEBULK FOR 20 MINUTES
		<p>1 0° tape</p> <p>3</p>	

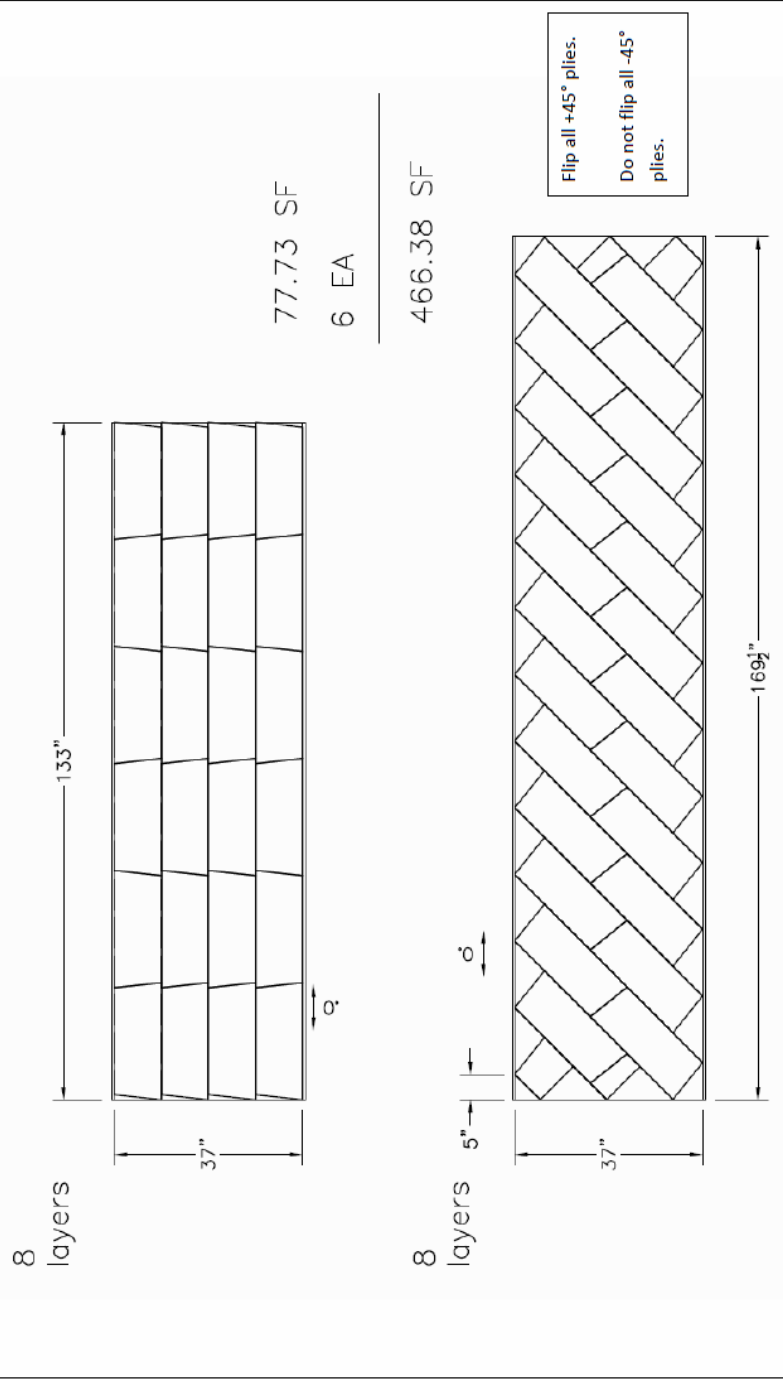
Stringer 26	1 4	0° woven	Any	1			
-------------	--------	----------	-----	---	--	--	--

Shear Tie - Normal THK 1

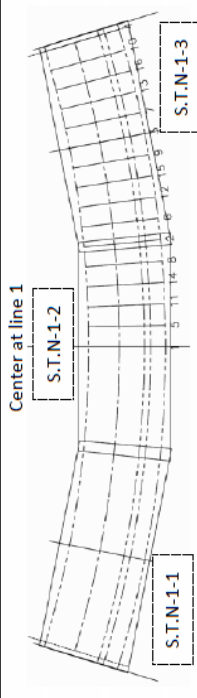
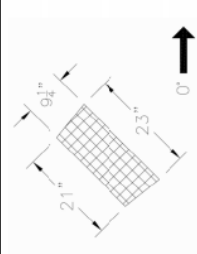
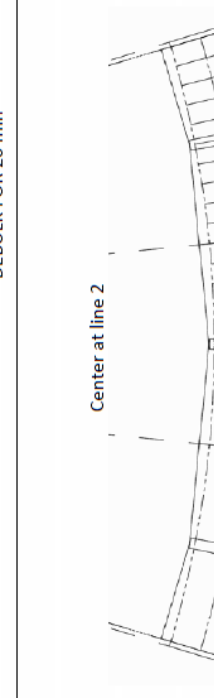
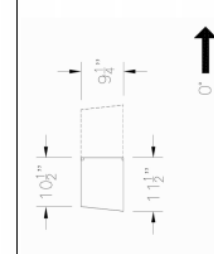
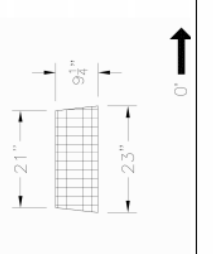
**Component: Shear-Tie Normal THK**

Layup: [45/0/-45/0/45/0/-45/0],

Material: T800/3900-2 woven



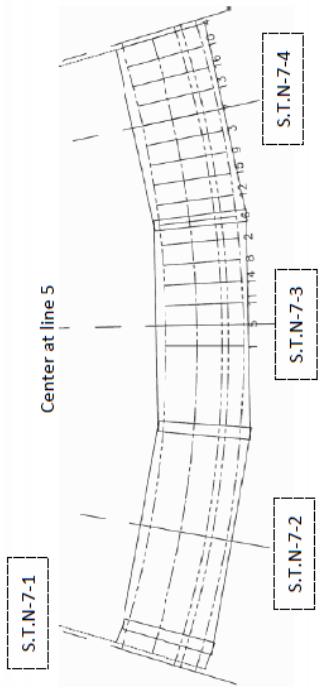
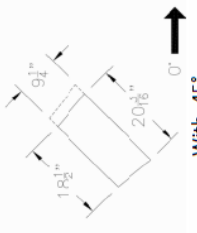
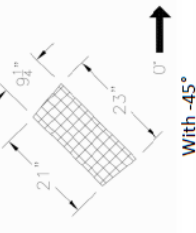
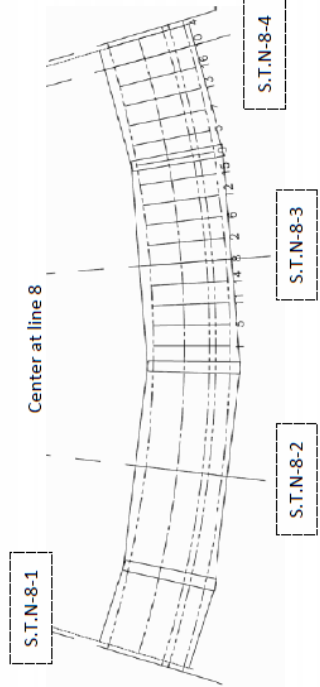
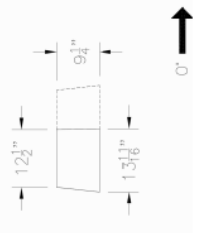
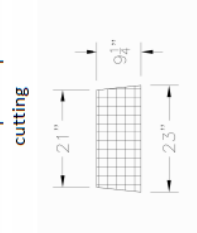
Shear Tie - Normal THK 2

Layer	Alignment	Cut#	Ply cut	Initials
1 45° woven	 <p>Center at line 1 S.T.N-1-2 S.T.N-1-1 S.T.N-1-3</p>	1		
		2		
		3		
DEBULK FOR 20 min				
2 0° woven	 <p>Center at line 2 S.T.N-2-1 S.T.N-2-2 S.T.N-2-3 S.T.N-2-4</p>	1		
		4		
		2		
3				
3 -45° woven	<p>Center at line 1 : Same as the 1st layer configuration with -45° (Flip patches)</p>	1	Same as the 1st layer with -45°	
		2		
		3		
4 0° woven	<p>Center at line 2 : Same as the 2nd layer configuration</p>	1	Same as the 2nd layer	
		4		
		2		Same as the 2nd layer
3				



Shear Tie - Normal THK 3		DEBULK FOR 20 min					
5	45° woven		4		<p>Patch #1 is the left part of patch #4 after cutting</p>	1	
			2			3	
6	0° woven		1		<p>Patch #4 is the left part of patch #1 after cutting</p>	4	
			2			3	

Shear Tie - Normal THK 4

7	<p>-45° woven</p>  <p>Center at line 5</p> <p>S.T.N-7-1</p> <p>S.T.N-7-2</p> <p>S.T.N-7-3</p> <p>S.T.N-7-4</p> <p>Same as the 5th layer configuration with -45° (Flip patches)</p>	 <p>4</p> <p>With -45°</p> <p>Patch #1 is the left part of patch #4 after cutting</p>  <p>1</p> <p>With -45°</p>
8	<p>0° woven</p>  <p>Center at line 8</p> <p>S.T.N-8-1</p> <p>S.T.N-8-2</p> <p>S.T.N-8-3</p> <p>S.T.N-8-4</p>	 <p>4</p> <p>With 0°</p> <p>Patch #1 is the left part of patch #4 after cutting</p>  <p>1</p> <p>With 0°</p>
<p>DEBULK FOR 20 min</p>		

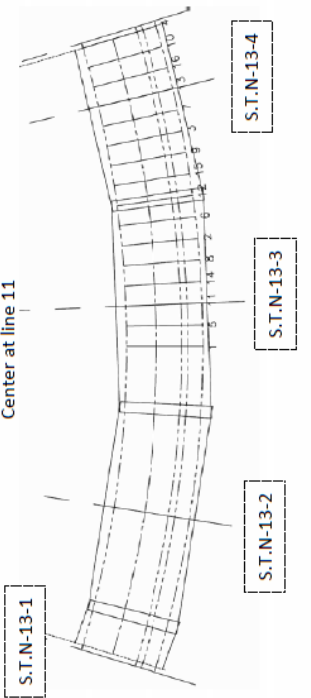
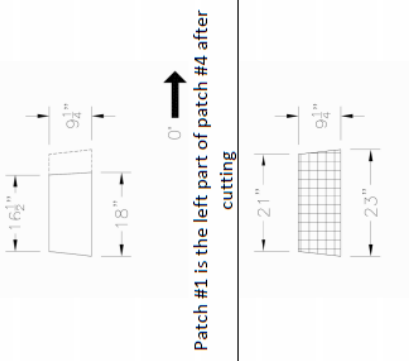
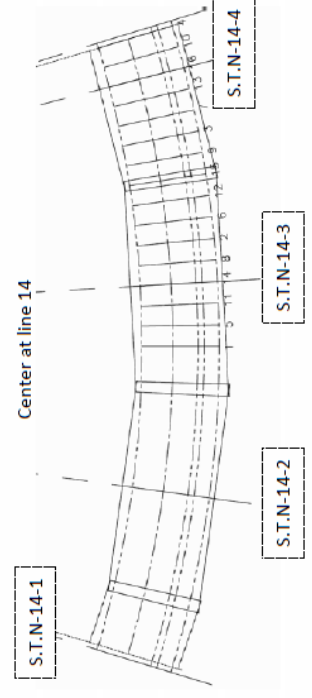
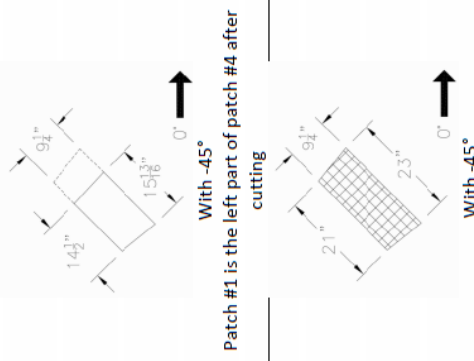
Shear Tie - Normal THK 5

9	0° woven		<p>Patch #4 is the left part of patch #1 after cutting</p>
10	-45° woven		<p>Patch #1 is the left part of patch #4 after cutting</p>

Shear Tie - Normal THK 6

11	0° woven		<p>4</p>		
1			<p>1</p>	<p>Patch #1 is the left part of patch #4 after cutting</p>	
2			<p>2</p>		
3			<p>3</p>		
DEBULK FOR 20 min					
12	45° woven		<p>1</p>		
4			<p>4</p>	<p>Patch #4 is the left part of patch #1 after cutting</p>	
2			<p>2</p>		
3			<p>3</p>		

Shear Tie - Normal THK 7

13	0° woven	 <p>Center at line 11</p> <p>Same as the 11th layer configuration</p>	<p>4</p> <p>1</p> <p>2</p> <p>3</p>	 <p>Patch #1 is the left part of patch #4 after cutting</p> <p>Patch #1 is the left part of patch #4 after cutting</p>	
14	-45° woven	 <p>Center at line 14</p>	<p>4</p> <p>1</p> <p>2</p> <p>3</p>	 <p>With -45°</p> <p>Patch #1 is the left part of patch #4 after cutting</p> <p>With -45°</p>	
				DEBULK FOR 20 min	

Shear Tie - Normal THK 8

<p>15</p> <p>0° woven</p>		<p>1</p> <p>4</p> <p>2</p> <p>3</p>	<p>(Cut then flip above patch) Patch #4 is the left part of patch #1 after cutting</p>
<p>16</p> <p>45° woven</p>		<p>4</p> <p>1</p> <p>2</p> <p>3</p>	<p>Patch #1 is the left part of patch #4 after cutting</p>
<p>DEBULK FOR 20 min</p>			

Frame 1

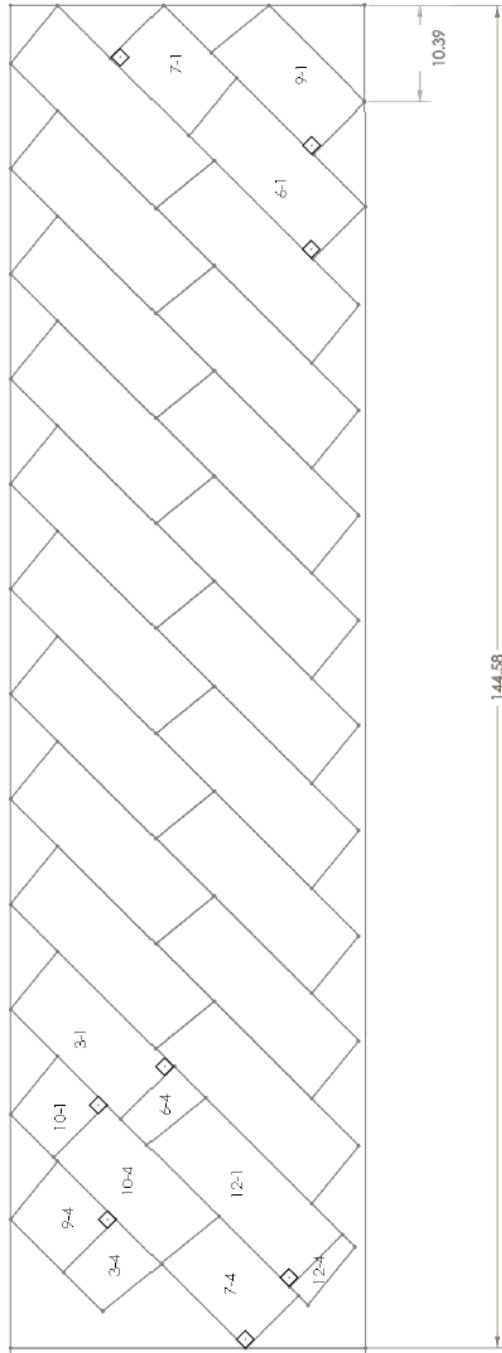
**Component: Frame**

Layout: [45/0/-45/45/0/-45]<sub>s</sub> (Web),

[45/0/0/-45/45/0/0/-45]<sub>s</sub> (Flange)

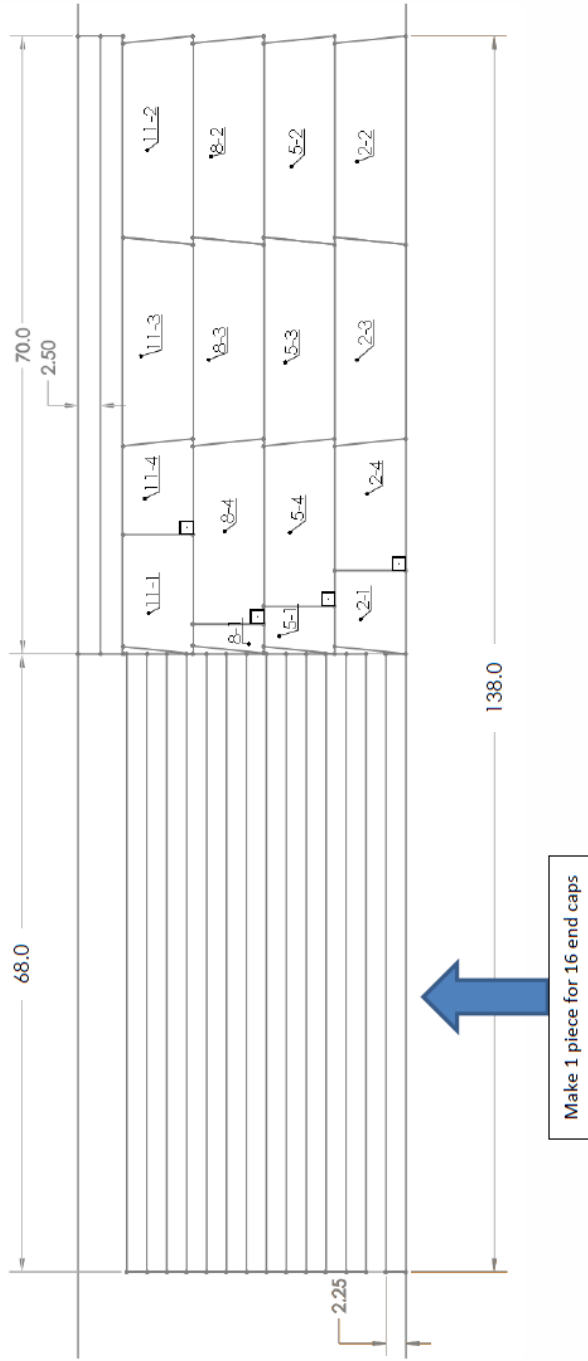
Material: T800 woven

Cutting plan:



**Flip all +45° plies**  
**Do not flip all -45° plies**

Frame 2

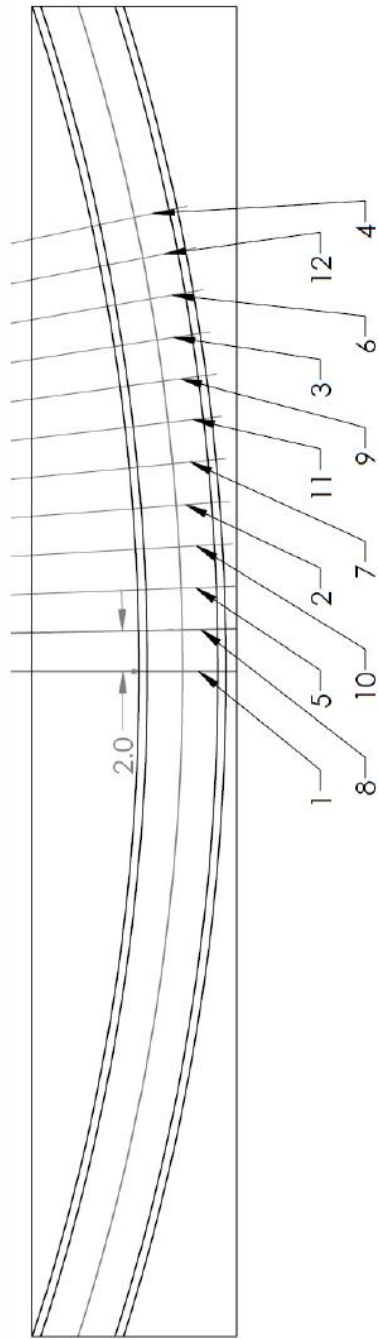


Each frame needs 8 end caps.


Use the 2.5" end caps for the bottommost plies. Use the 2.25" end caps for the topmost plies.



Frame 3  
Location of splices



Frame 4  
**Mold Preparation**

Step	Description	Figure
1	Check all molds for damage, and remove extra material with a utility knife if necessary.	
2	Clean all molds with acetone and paper towels. Remove any excess resin from previous cures. Clean again with alcohol and paper towels until all residue is removed. If necessary, use blades. Perform a last cleaning with Kim wipes.	
3	Check if splices' positions are correctly marked on the mold. If not, mark them.  It may be useful to use a marked plastic (with Sharpie and templates) to help you mark and position your splices.	 <p>The diagram shows a curved mold with 12 numbered positions (1-12) marked along its length. A scale bar indicates a distance of 2.0 units between positions 1 and 2. The positions are distributed across the curve, with positions 1-6 on the left side and positions 7-12 on the right side.</p>


Frame 5

4	<p>Cut 8 strips of release film to lay on the mold. Pieces can be cut 10" x 10". Use flash tape to unite the different pieces. Start at the web, from the center outwards. Then, tape all release film at all inner flanges, from the center outwards. Overlap a little bit of flash tape. Tape all release film at all outer flanges.</p>	
5	<p>Mark the coordinate system on the mold. Place flash tape on top of your CSYS to avoid contamination through Sharpie.</p>	

Frame 6

## Instructions for layup and debulking

### Layup

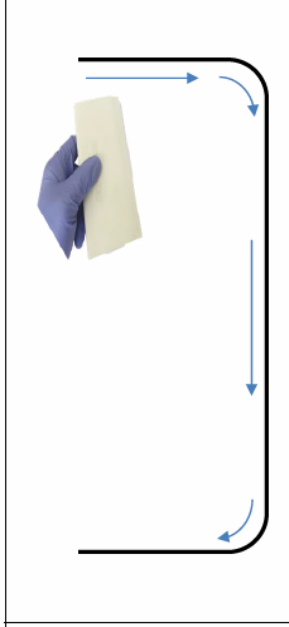
Step	Description	Figure
0	<p><b>IMPORTANT!</b> Before cutting/layup, ensure that prepreg material has been thawed for about 2h (or until room temperature) inside its sealed bag, with desiccant inside the bag. Do not open bag until material is thawed, to avoid condensation.</p> <p><b>Attention!</b> The margins for the C-frame are very narrow, therefore it is necessary to take extra caution when laying up to avoid sticking the prepreg at the wrong position.</p>	
1	<p>Mark the center of the first ply cut with a Sharpie on the film. Find the location of the splice for the layer you are laying up.</p> <p>Then, align the center of the ply with the location of the splice. Place the corners of the ply on the edge of the mold.</p> <p>Lay up subsequent plies, overlapping 1in (overlapping is constant throughout the ply; when in doubt, measure on the inner side of the curve) between subsequent plies.</p>	 <div style="display: flex; flex-direction: column; align-items: flex-start;"> <div style="border: 1px solid black; padding: 5px; margin-bottom: 5px;"> <p>1-Align the center of the ply to the center of the splice location marked on mold.</p> </div> <div style="border: 1px solid black; padding: 5px; margin-bottom: 5px;"> <p>2-Place the corners of the ply on the edges of the mold.</p> </div> <div style="border: 1px solid black; padding: 5px;"> <p>3-Press down the ply from one side to another.</p> </div> </div>

Frame 7

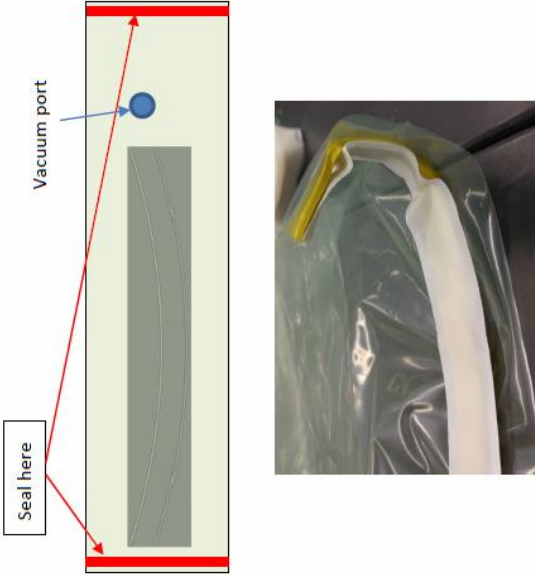
2

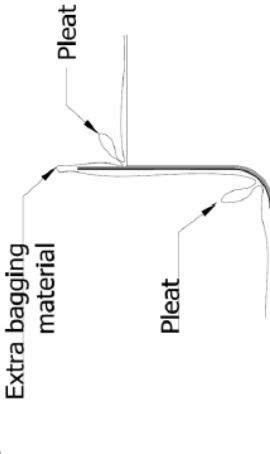
Work your way with squeegees and your hands from the border towards the other side. Press the prepreg against the fillet carefully, while holding the ply end on your other hand.

Make sure the prepreg is well adhered to one corner before moving to the next.

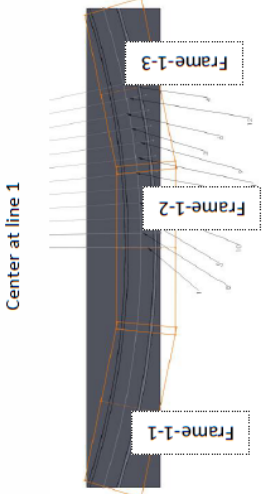
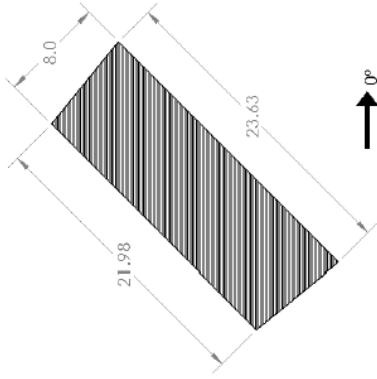


Frame 8  
Debulk

	Description	Figure
0	<p>Cut the breather to size 12" x 70".            Cut the peel ply to size 12" x 70".            Cut the 27" wide vacuum tube to a length of ~85in.</p>	
1	<p>On a flat surface, seal one of the ends of the 27" wide vacuum tube with white tacky tape.             Overlap ~1in of tacky tape on the folds. Remove the tacky tape cover in sections as you work your way through the width.</p>	
2	<p>Place the peel ply over the C-frame. With your hands, press it against the composite almost as if it was another ply. Remove any wrinkles before putting the breather on.             Place the breather on top of the peel ply.             Insert the C-frame mold prepared for debulk (with peel ply, breather, etc) inside the tube. The molds are heavy; hence, use caution and teamwork to lift it up. Leave about 2ft extra on one of the sides.</p>	

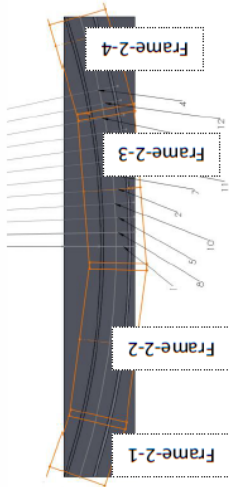
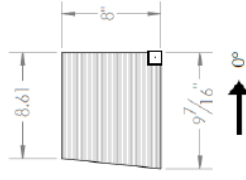
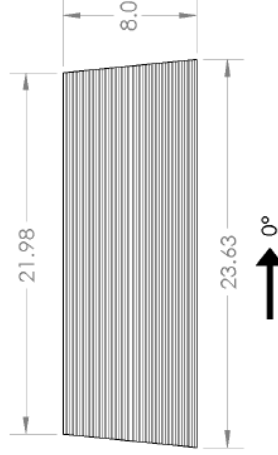
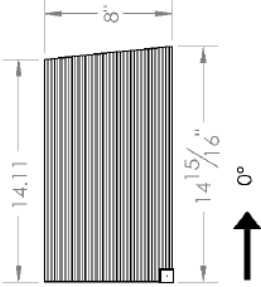
<p>Frame 9</p> <p>3</p>	<p>Accommodate the bag onto the surface of the C-frame. Make pleats as shown.</p>	
<p>4</p>	<p>Insert the vacuum port about 1ft from the bag border, with the vacuum port base inside the envelope bag. Seal the other end of the envelope with yellow tacky tape, close to the border of the bag (<b>Tip:</b> it is easier to seal it over a flat surface). Pull partial vacuum.</p>	
<p>5</p>	<p>While pulling partial vacuum, make sure bag is well accommodated and pleats are in the right places. Also make sure the corners are not bridging. When done, pull full vacuum.</p>	
<p>6</p>	<p>When done with debulk, cut the bag on the farther (i.e. near where vacuum is applied) end of the bag very close to the tacky tape. Save the bag for next debulk.</p>	

Frame 10

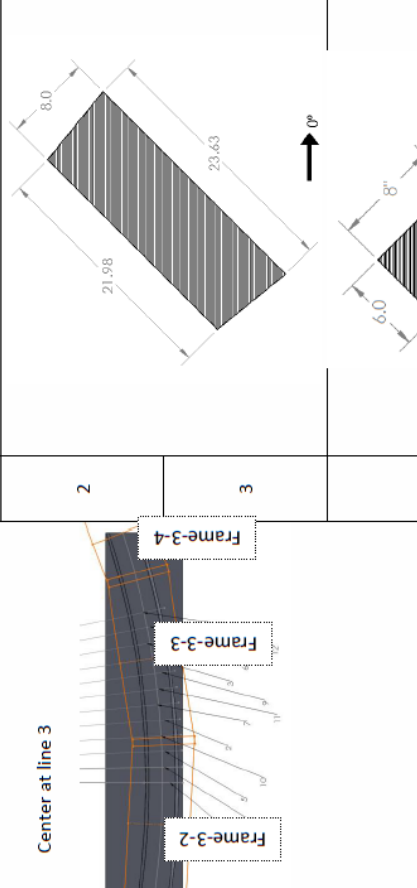
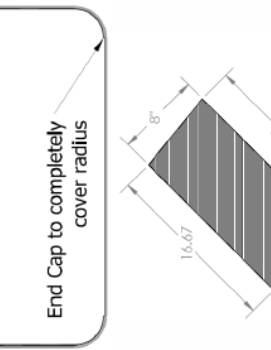
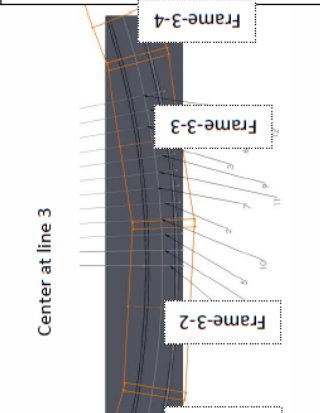



Layer	Alignment	Cut#	Ply cut	Initials
<p>1</p> <p>45° woven</p>		<p>1</p> <p>2</p> <p>3</p>		
<p>DEBULK FOR 20 min</p>				



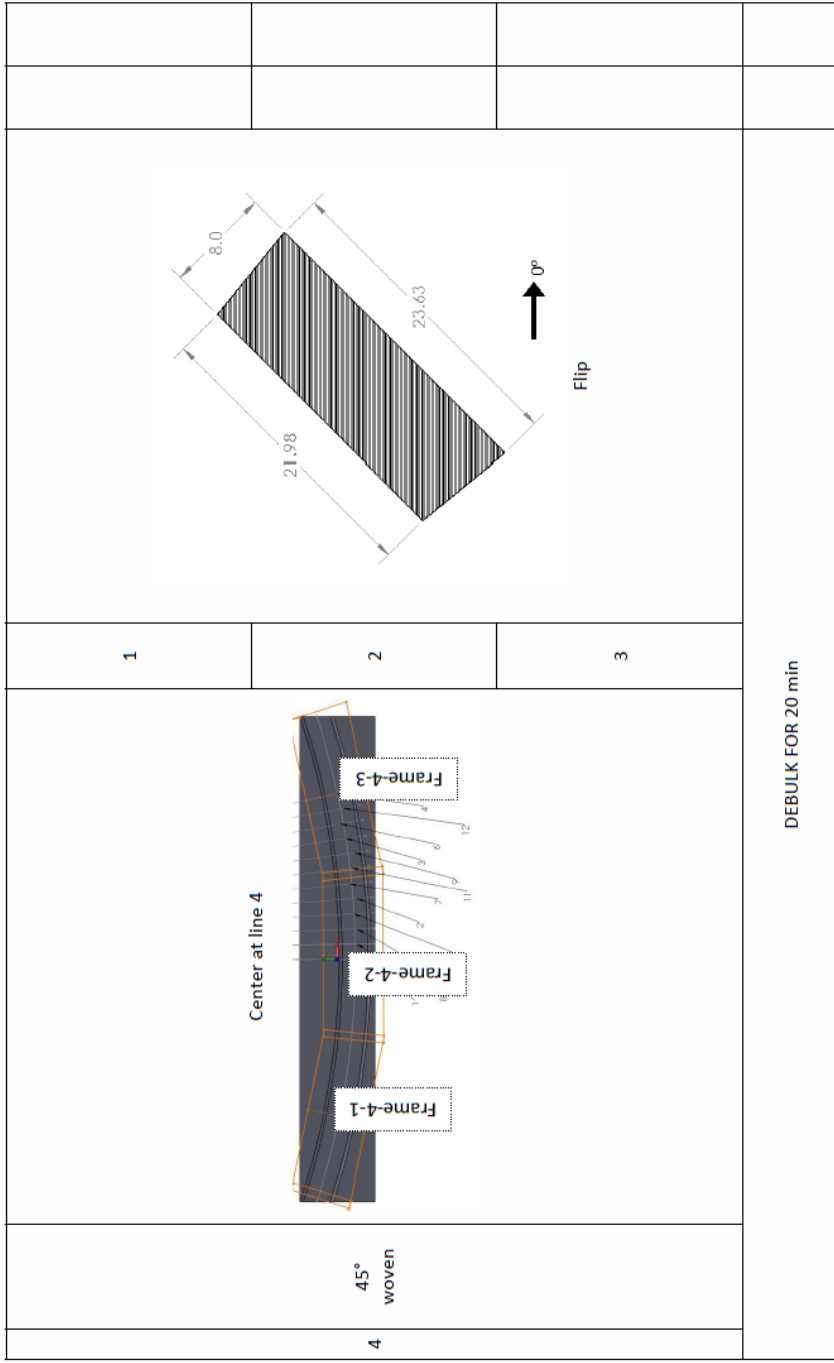
Frame 11

	 <p>Center at line 2</p> <p>Frame-2-1</p> <p>Frame-2-2</p> <p>Frame-2-3</p> <p>Frame-2-4</p>	1		
2 0° woven		2		
		3		
		4		

Frame 12

<p>2 0° woven for flange 5</p>		<p>1</p>		
<p>3 -45° woven</p>		<p>2</p>		
		<p>3</p>		
		<p>4</p>		

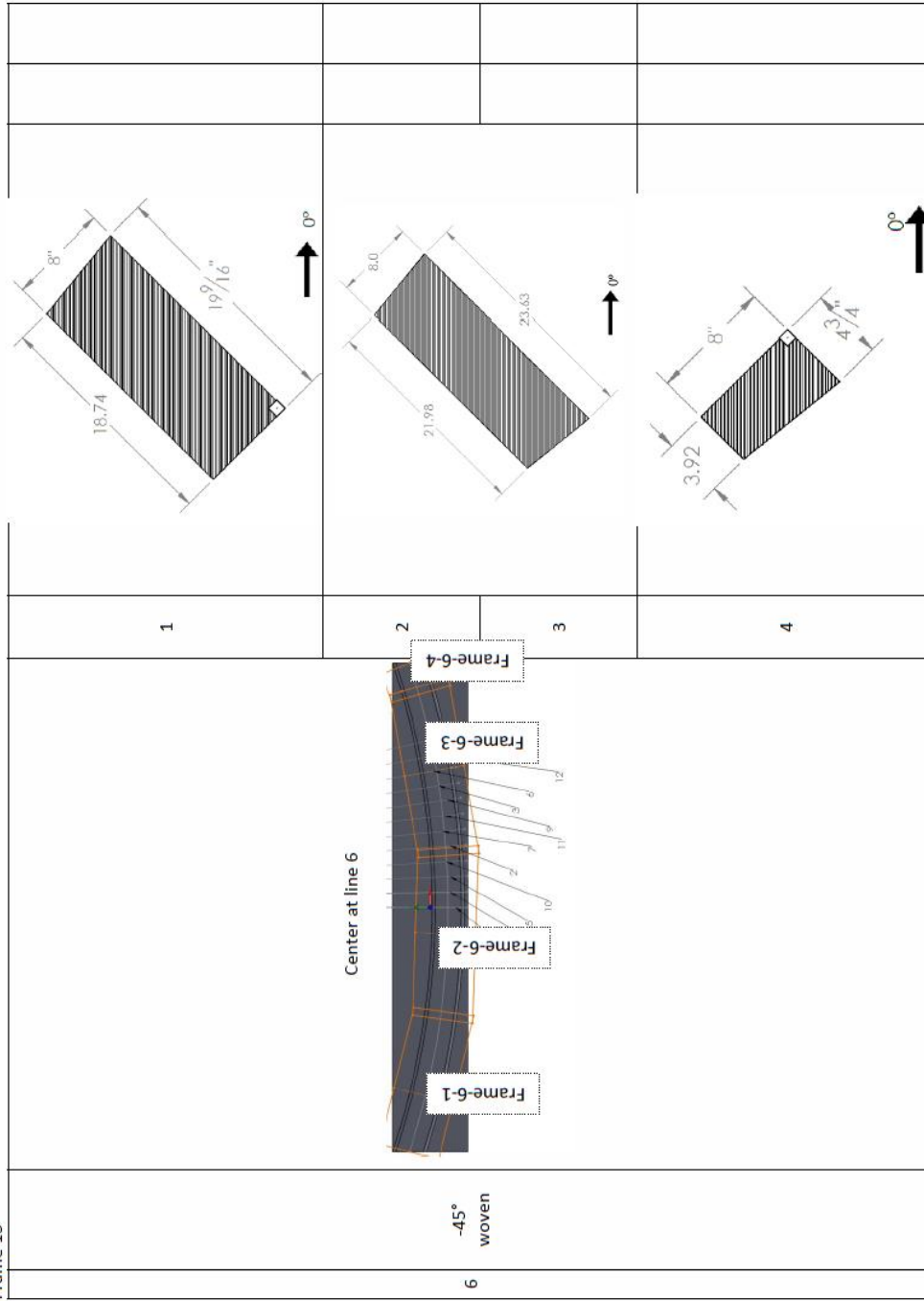
Frame 13



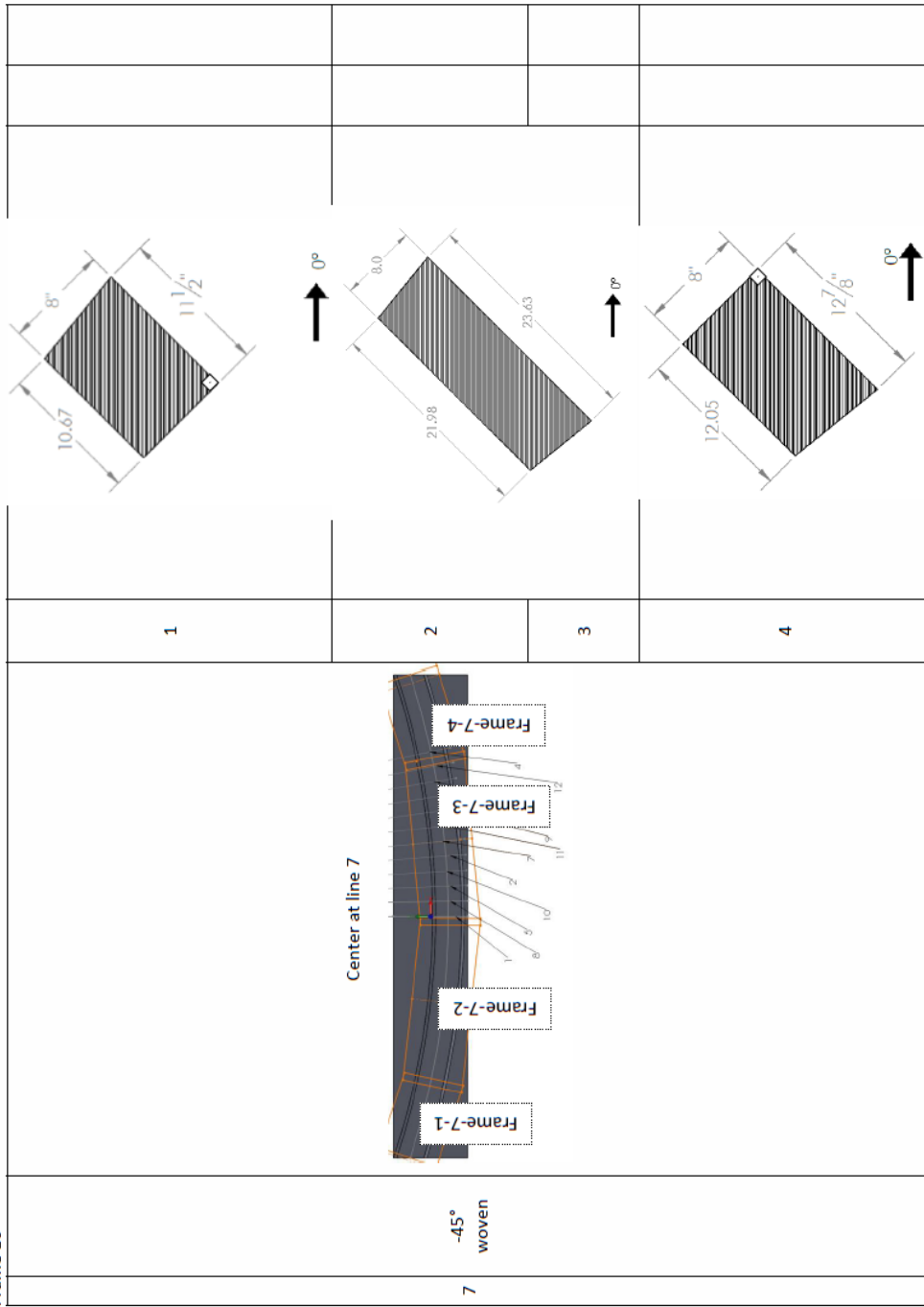
Frame 14

<p>5 0° woven</p>		<p>1</p>		<p>2</p>		<p>3</p>		<p>4</p>		<p>End Cap to completely cover radius</p>
<p>5 0° woven for flange</p>										

Frame 15



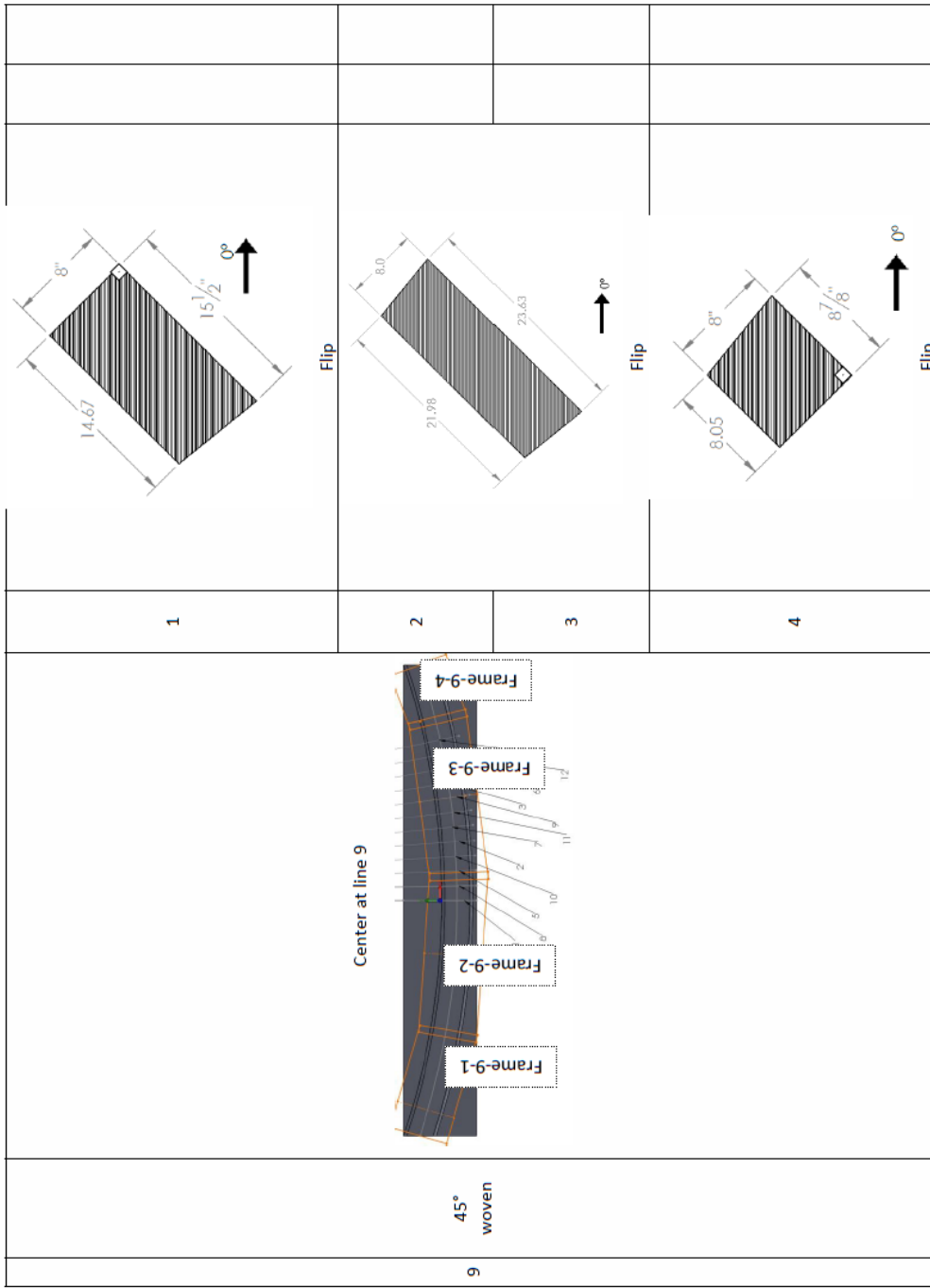
Frame 16



Frame 17

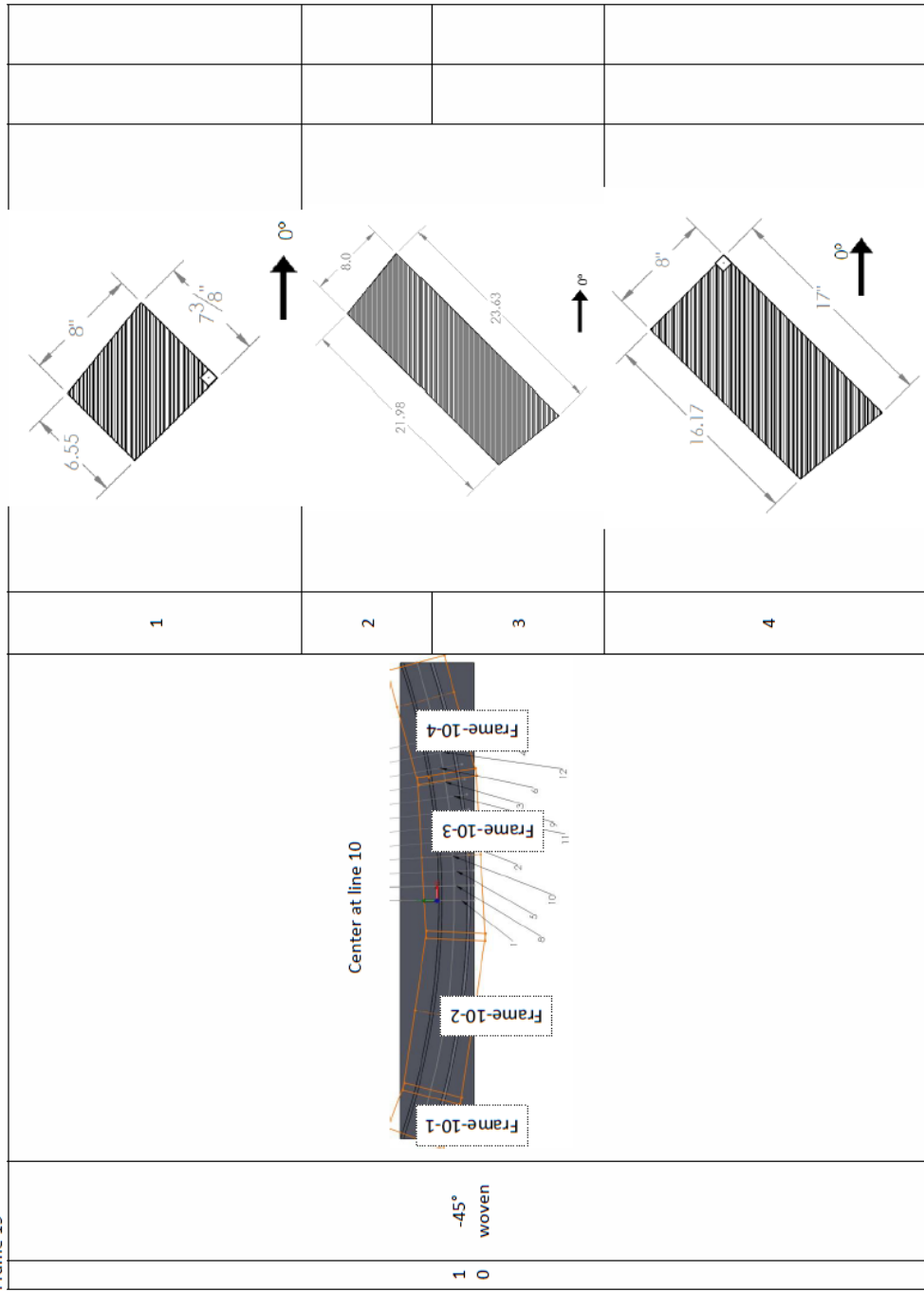
		DEBULK FOR 20 min				
7	0° woven for flange					
5				1		
				2		
				3		
				4		

Frame 18

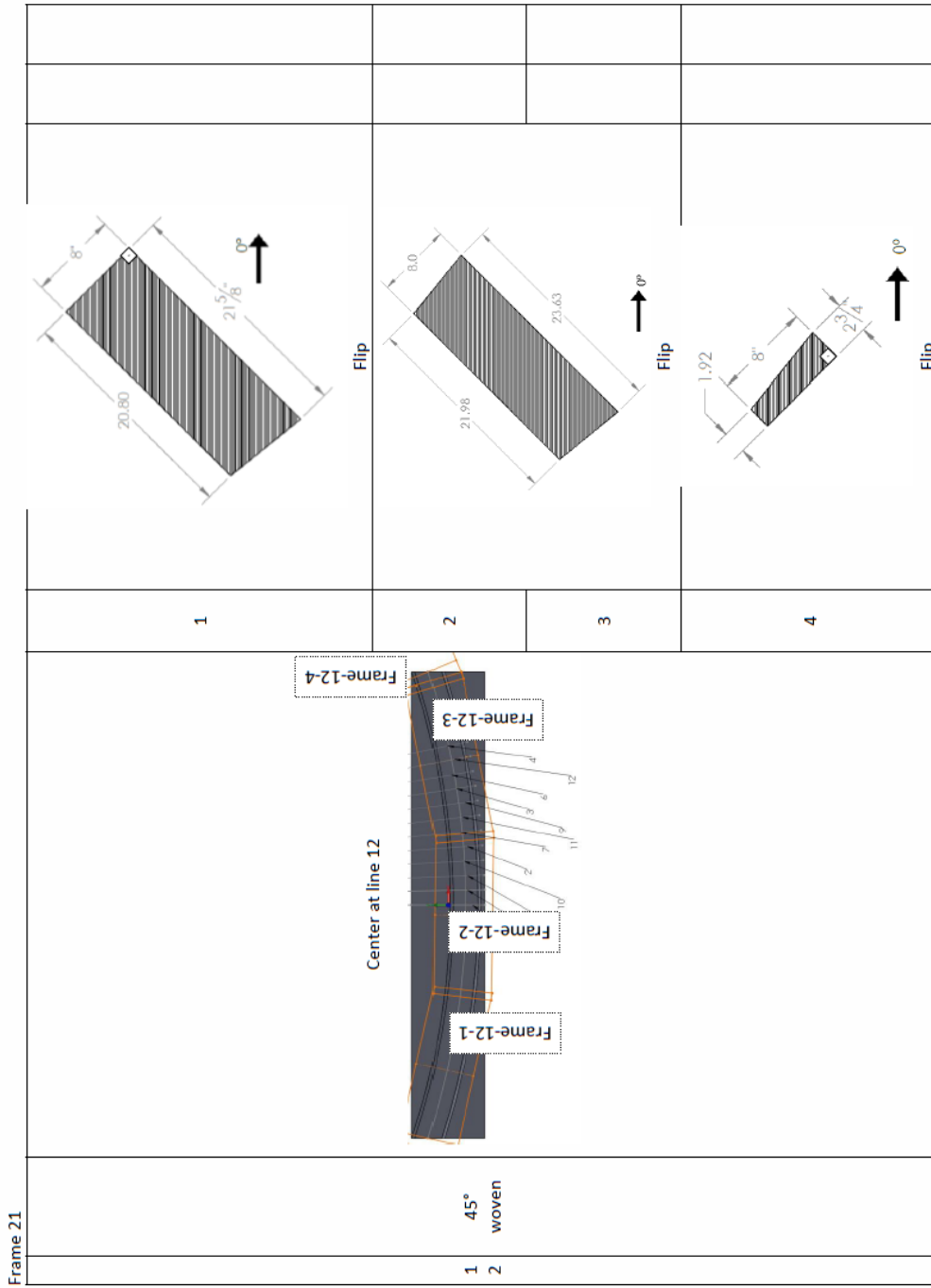




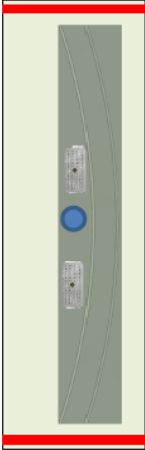

Frame 19







Frame 22

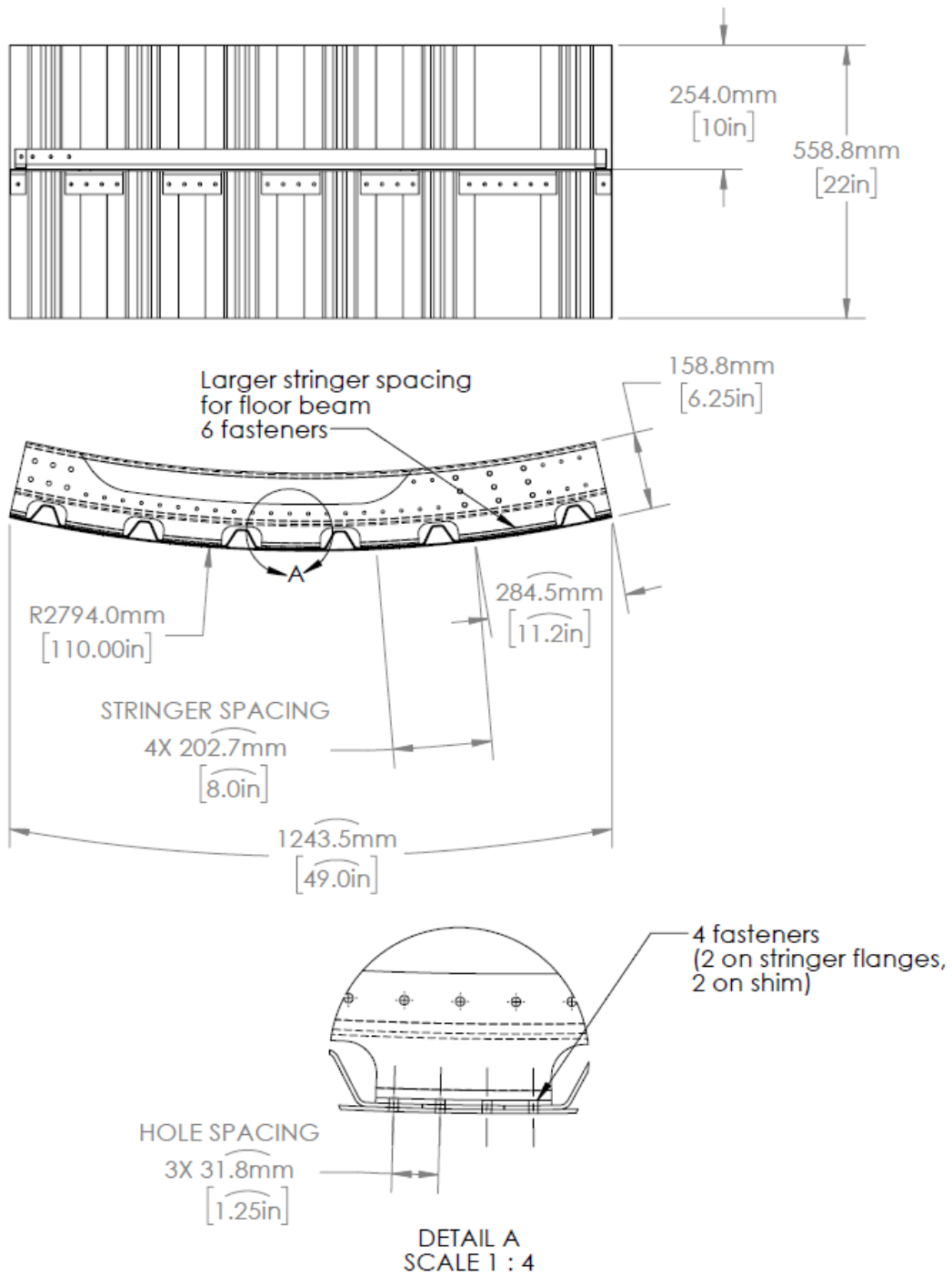
	<p><b>Final debulk.</b> Insert one desiccant or more in the bag, wrapped in breather. Place the base of the vacuum port at the center of the mold. Insert the mold prepared for debulk (peel ply, breather, etc) in the envelope bag. Cut the excess of bag at the end.</p> <p>Follow debulking instructions.</p>			
	<p><b>Pressure drop test.</b> Attach the pressure valve after full vacuum (usually around -30 in Hg) was achieved. Time 1min. If the pressure has dropped less than 1 in Hg, the bag seal is good. Otherwise, try to find the leak.</p>			
	<p>Number the C-frame and keep it in the freezer. Be careful to not release any vacuum in the process by inadvertently pressing the vacuum port.</p>			

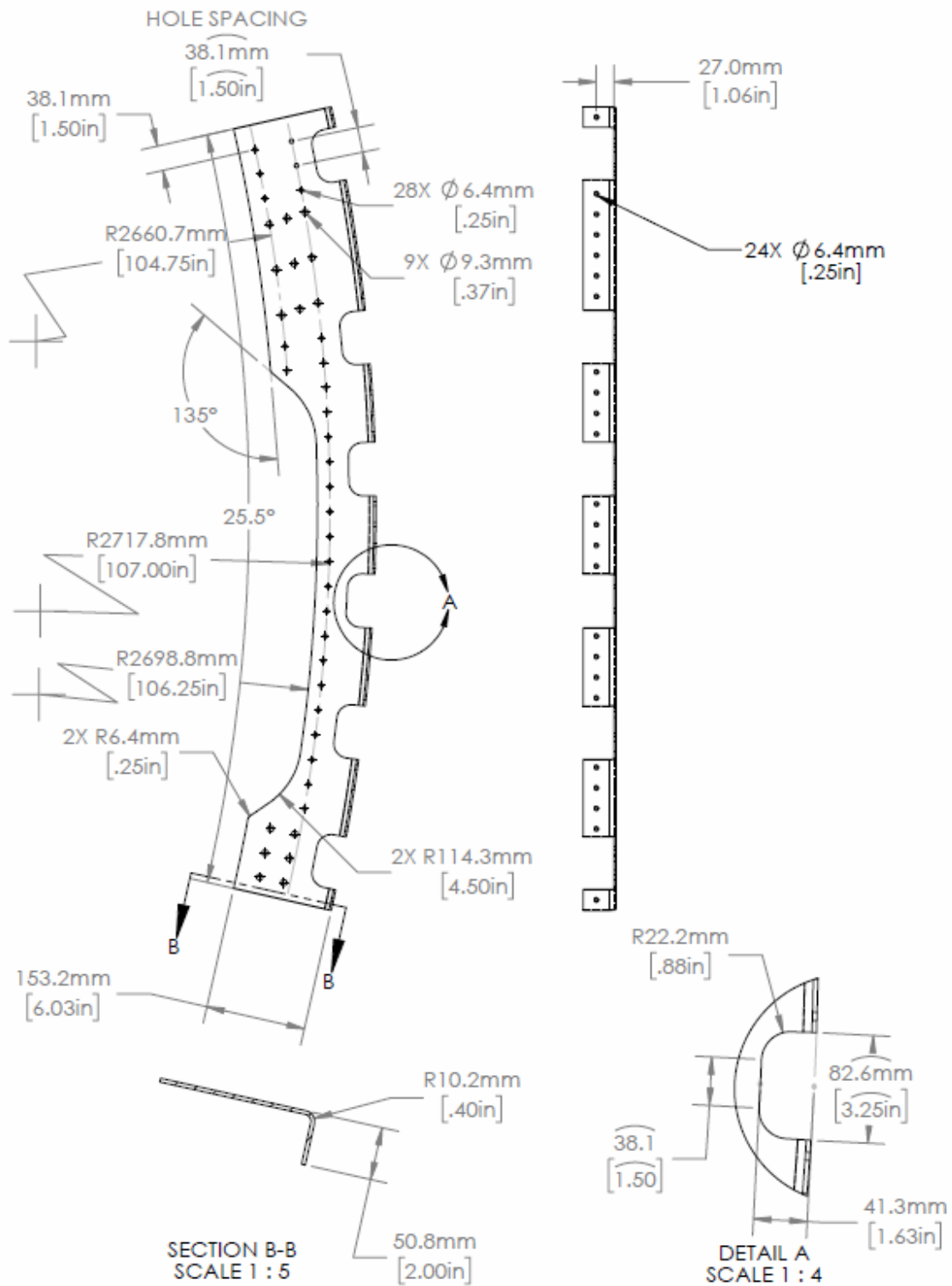
## C. SPECIMEN AND FIXTURE DRAWINGS

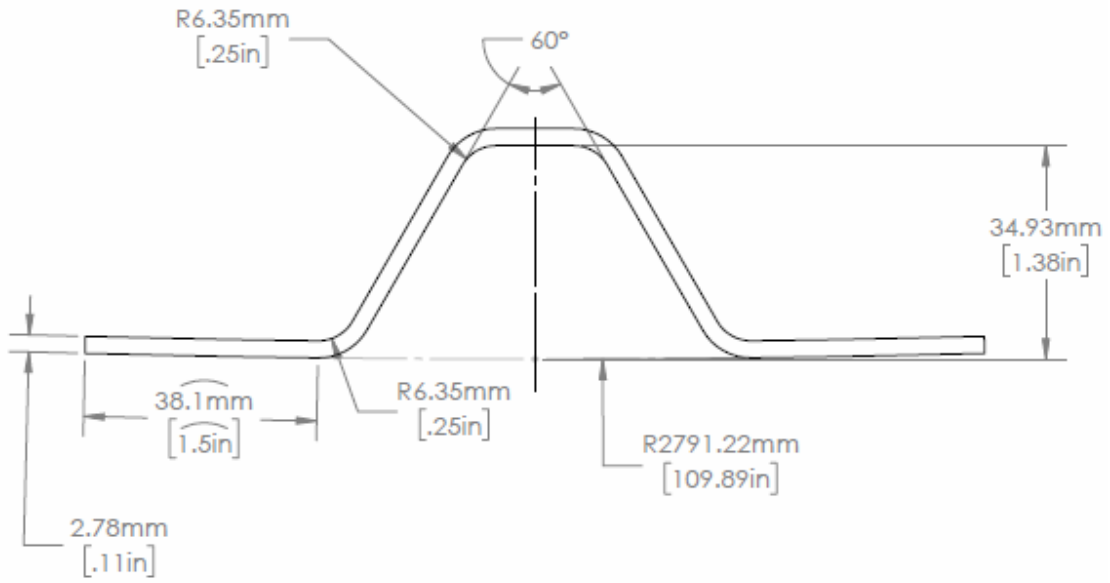
This appendix includes test specimen and fixture detail drawings:

- 1) Specimen detail
- 2) Floor joint and beam detail
- 3) Low beam and joint detail

1) Specimen detail

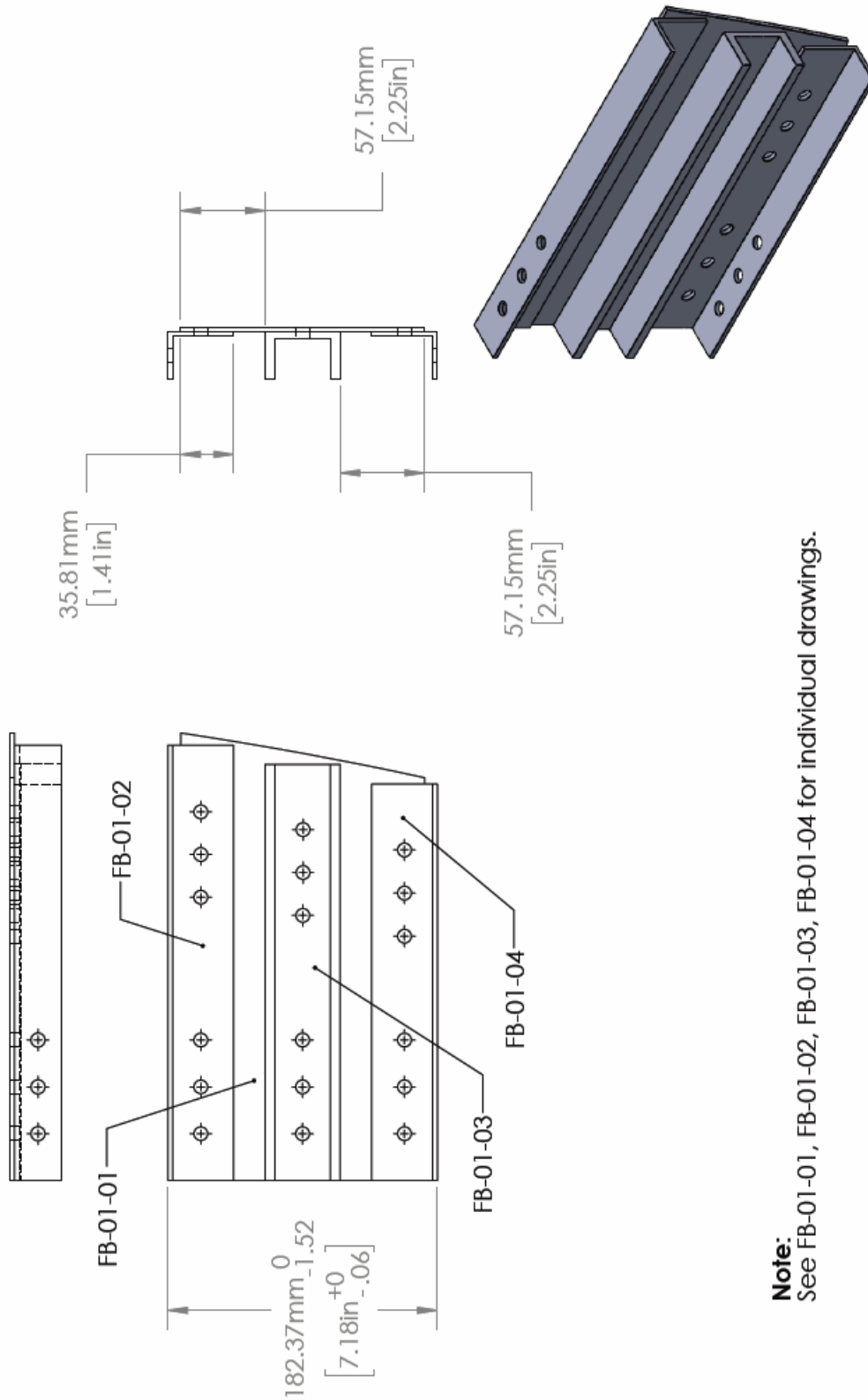




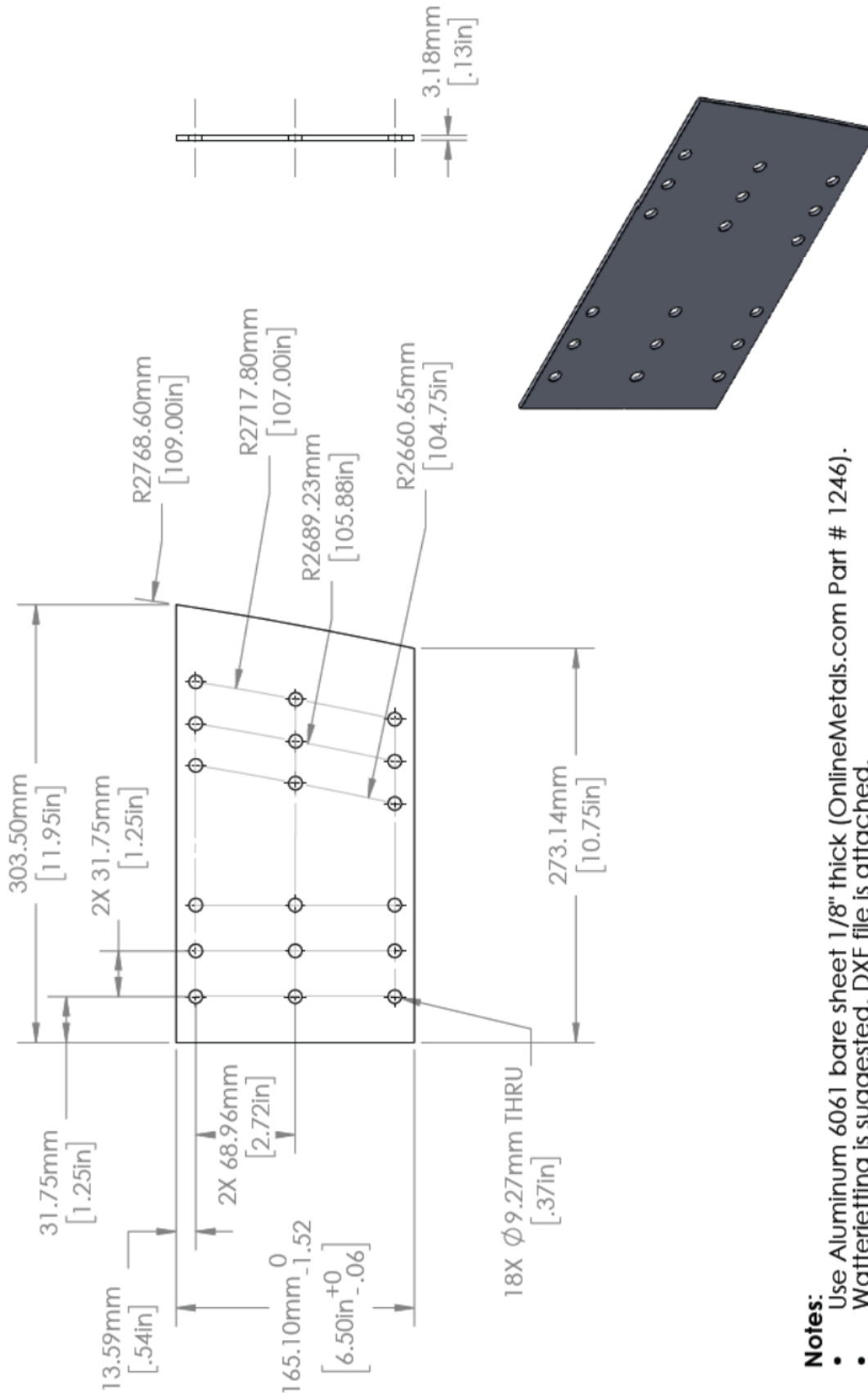


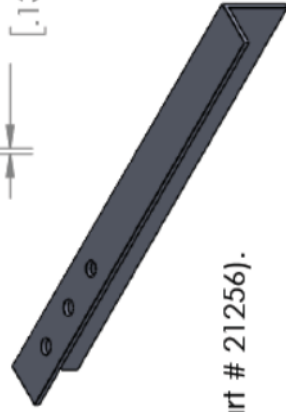
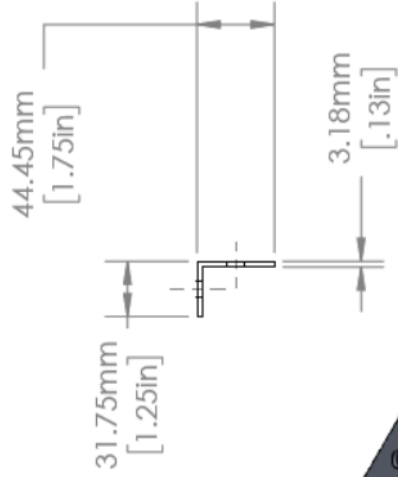
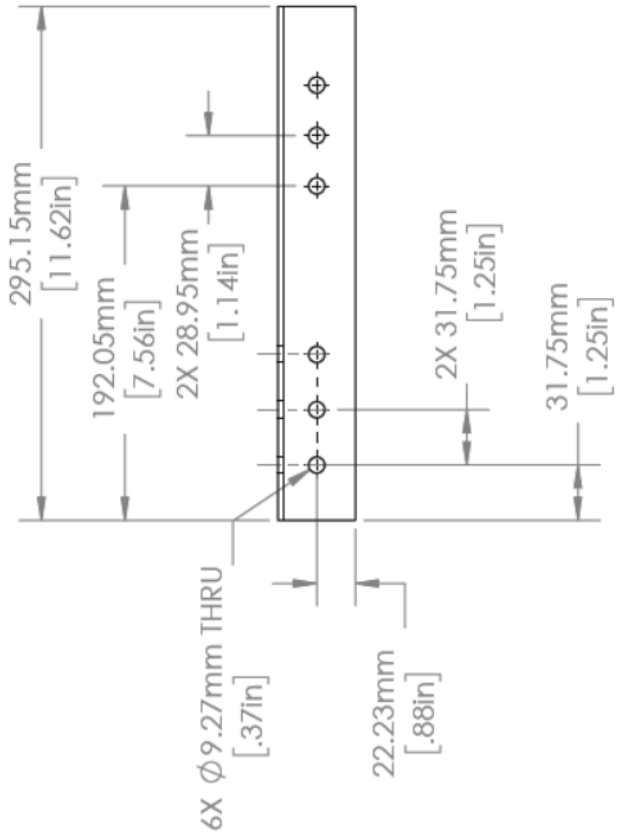
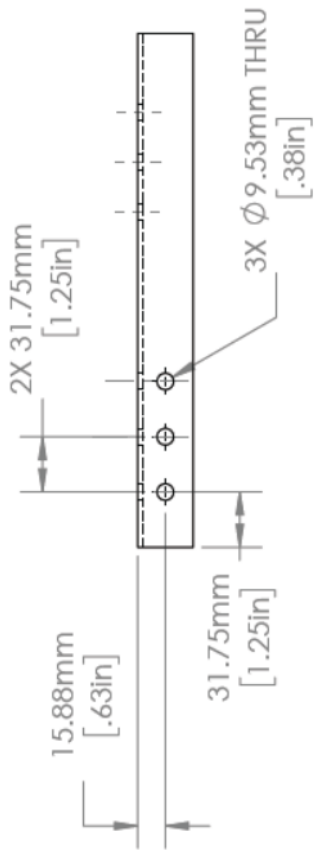


2) Floor joint and beam detail

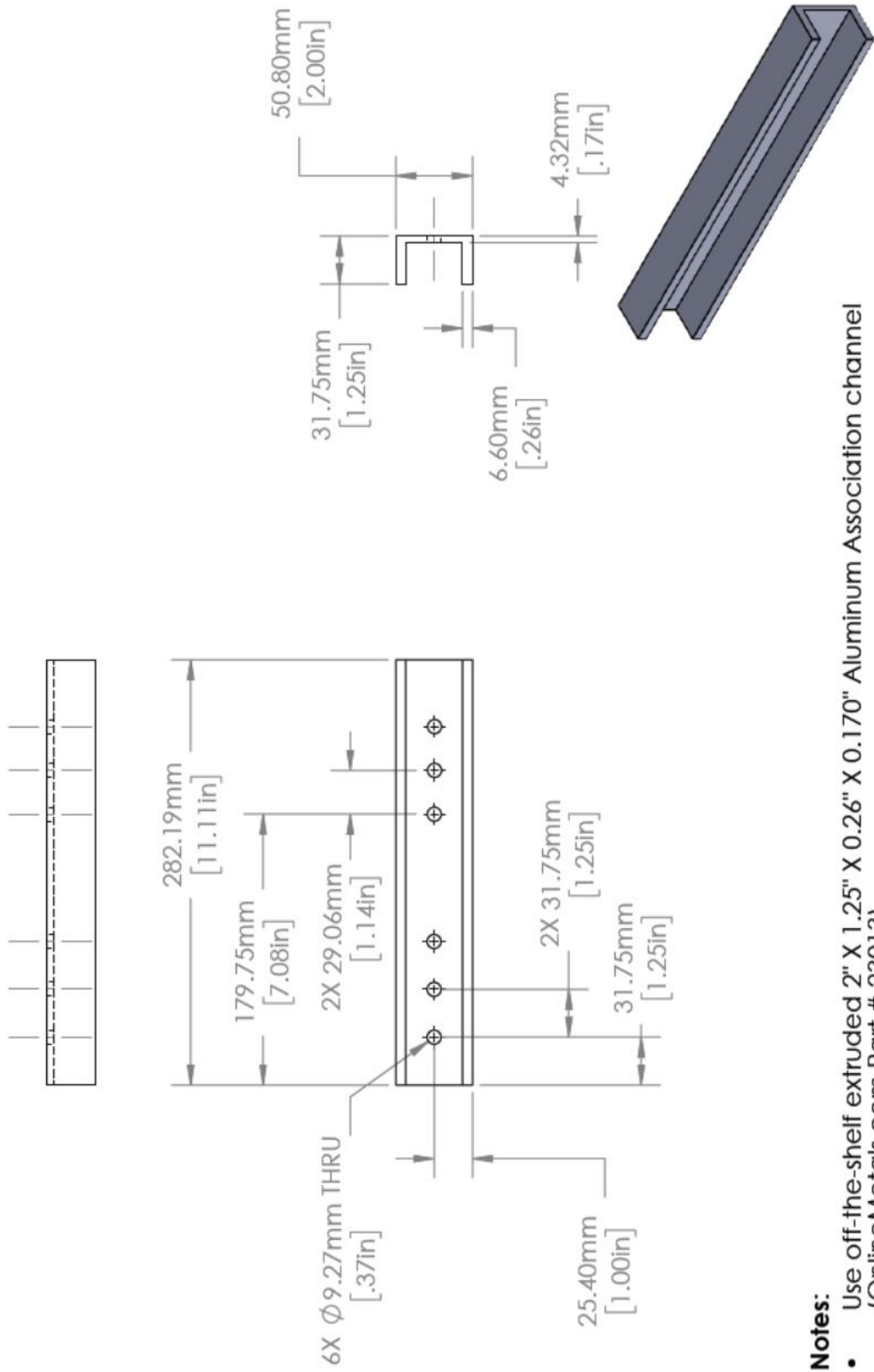


**Note:**  
See FB-01-01, FB-01-02, FB-01-03, FB-01-04 for individual drawings.

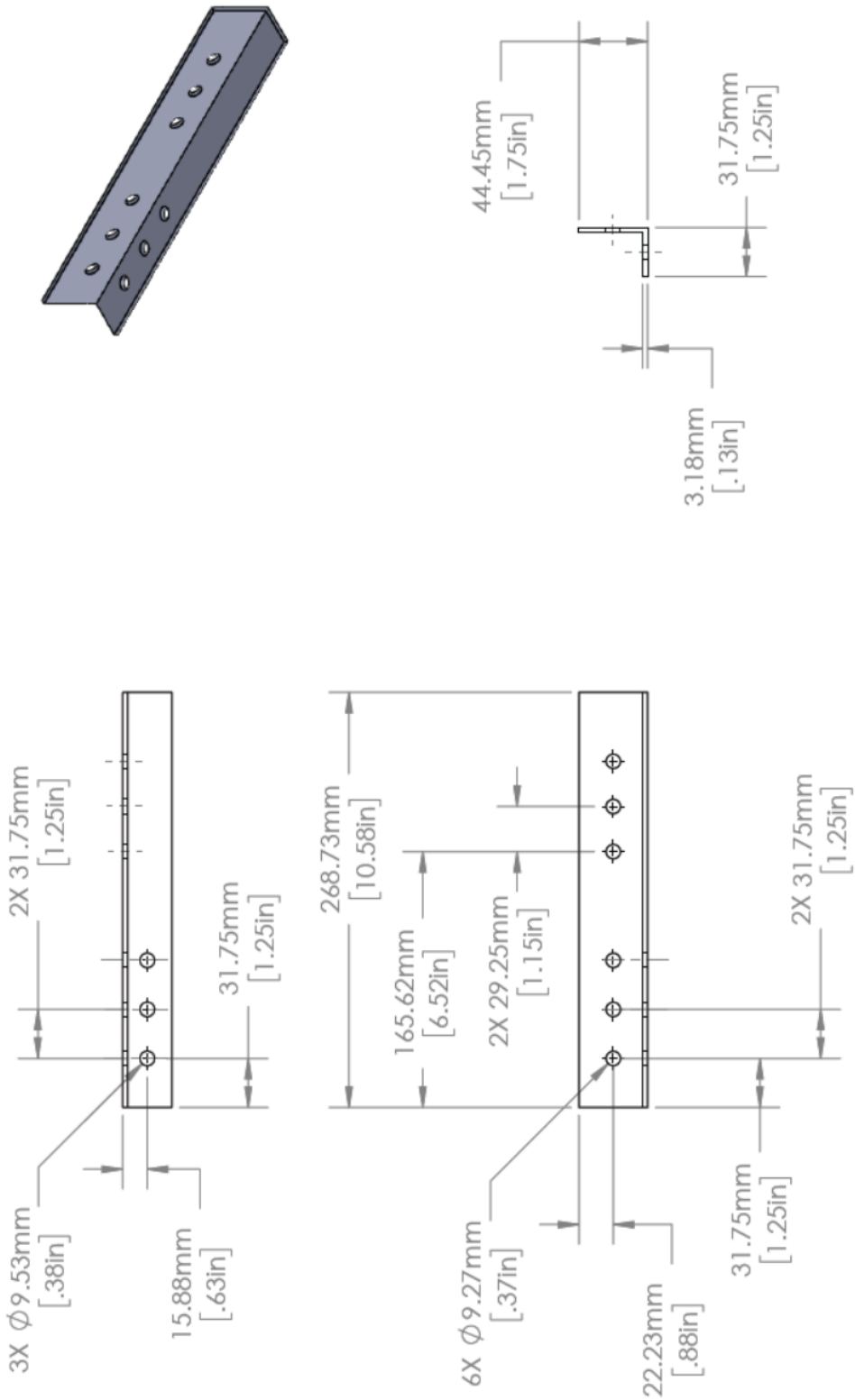




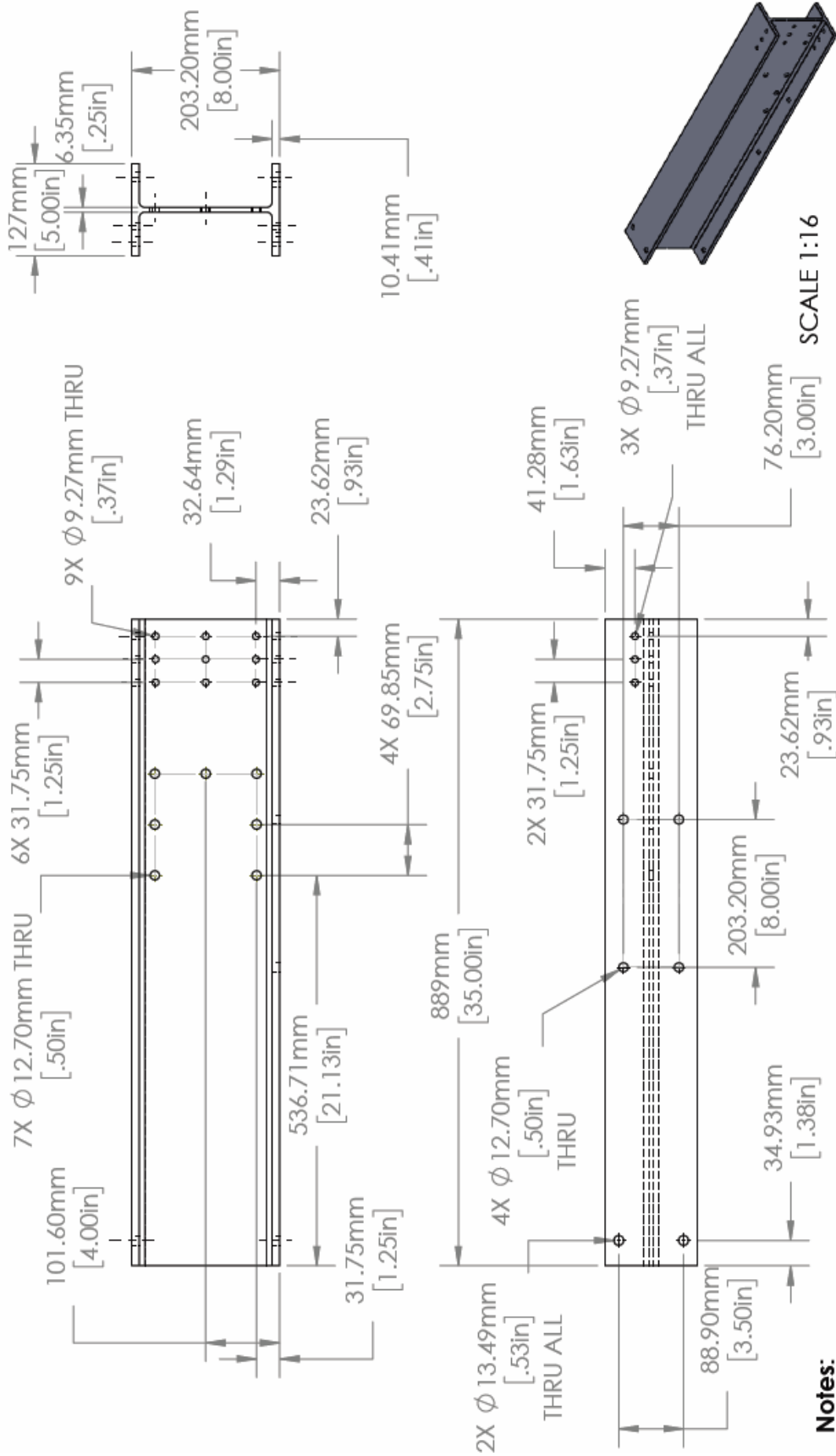
- Notes:**
- Use off-the-shelf extruded structural Aluminum angle (OnlineMetals.com Part # 21256).
  - Stock finish OK on all surfaces.



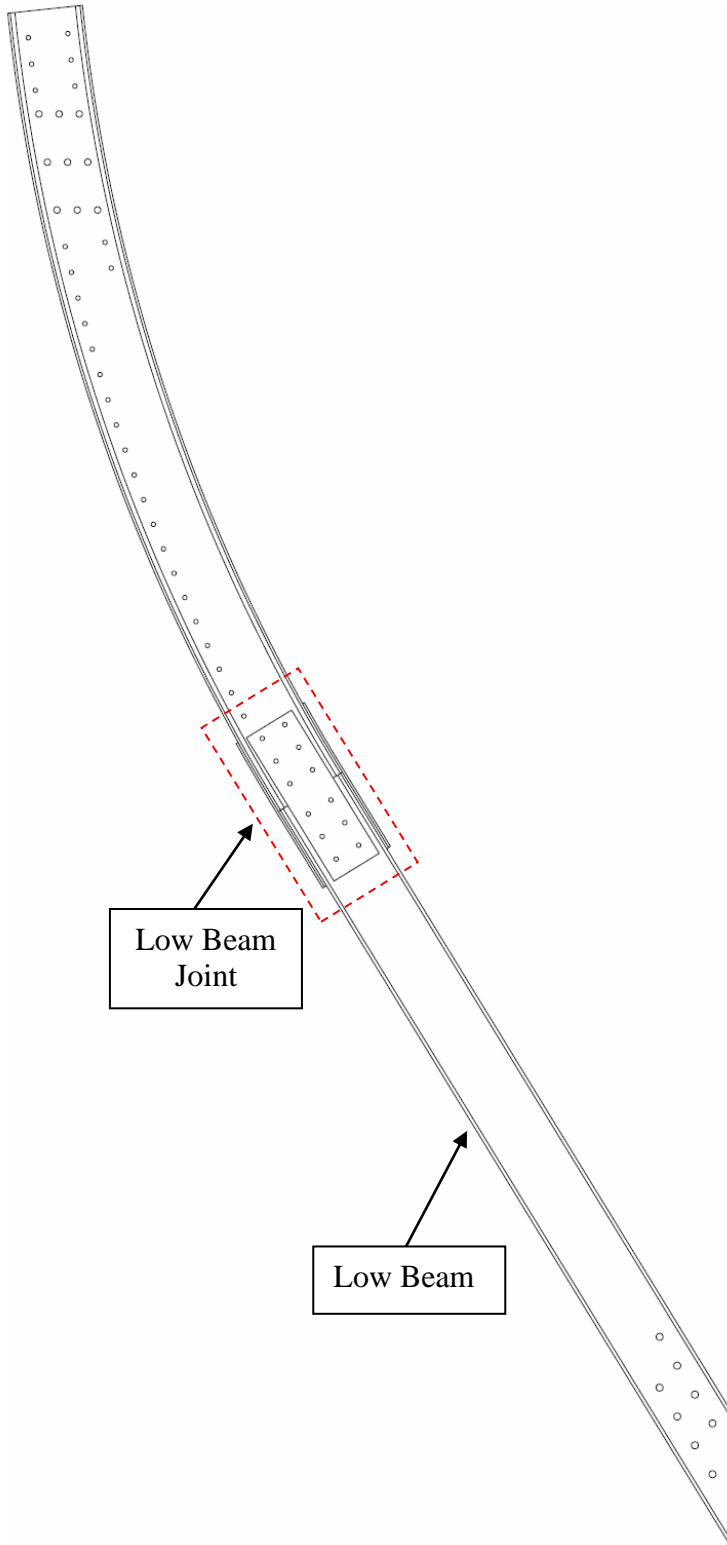
- Notes:**
- Use off-the-shelf extruded 2" X 1.25" X 0.26" X 0.170" Aluminum Association channel (OnlineMetals.com Part # 23013).
  - Stock finish OK on all surfaces.



- Notes:**
- Use off-the-shelf extruded structural Aluminum angle (OnlineMetals.com Part # 21256).
  - Stock finish OK on all surfaces.



### 3) Low beam and joint detail



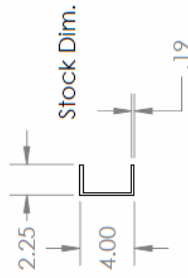
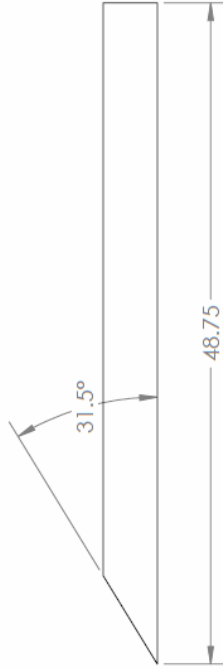
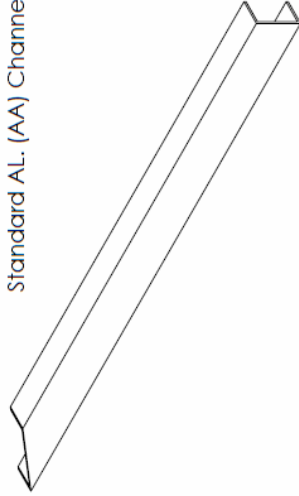
2

1

B

B

Standard AL. (AA) Channel



A

A

**PROPRIETARY AND CONFIDENTIAL**  
 THE INFORMATION CONTAINED IN THIS DRAWING IS THE SOLE PROPERTY OF <INSERT COMPANY NAME HERE>. ANY REPRODUCTION IN PART OR AS A WHOLE WITHOUT THE WRITTEN PERMISSION OF <INSERT COMPANY NAME HERE> IS PROHIBITED.

UNLESS OTHERWISE SPECIFIED:		NAME	DATE
DRAWN		MOORE	01/29/19
CHECKED			
BIG APPR.			
MFG APPR.			
G.A.			
COMMENTS:			
Qty: 4pcs			
Dimensions in inches			
DIMENSIONS ARE IN INCHES		HEWABI - UCSD	
TOLERANCES:		TITLE:	
FRACTIONAL: ±		Low Beam	
ANGULAR: MACH ±	BEID ±	AL. Channel (AA) 4X2.25X0.19	
TWO PLACE DECIMAL ±		SIZE	DWG. NO.
THREE PLACE DECIMAL ±		A	LB1
INTERFER GEOMETRIC TOLERANCING PER:		SCALE: 1:10	WEIGHT:
MATERIAL:	AL. 6061-T6	SHEET 1 OF 1	
FINISH:			
NEXT ASY:	USED ON:		
APPLICATION:			

2

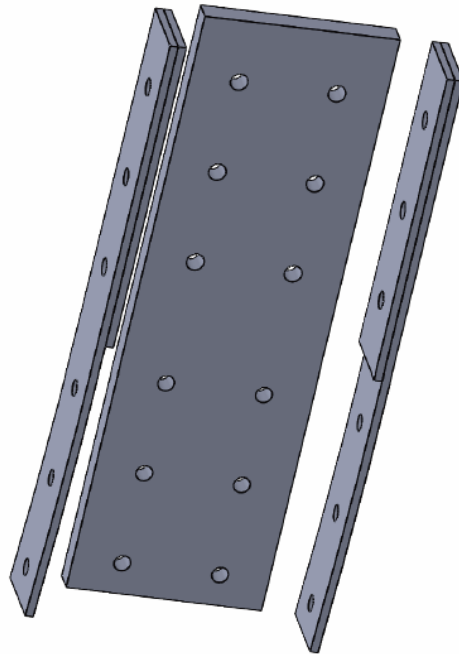
1



2

1

B



B

A

<p><b>PROPRIETARY AND CONFIDENTIAL</b>          THE INFORMATION CONTAINED IN THIS DRAWING IS THE SOLE PROPERTY OF &lt;INSERT COMPANY NAME HERE&gt;. ANY REPRODUCTION IN PART OR AS A WHOLE WITHOUT THE WRITTEN PERMISSION OF &lt;INSERT COMPANY NAME HERE&gt; IS PROHIBITED.</p>		<p>UNLESS OTHERWISE SPECIFIED:          DIMENSIONS ARE IN INCHES          TOLERANCES:          FRACTIONAL: ± BEND ±          ANGULAR: MACH ±          TWO PLACE DECIMAL ±          THREE PLACE DECIMAL ±</p>		<p>DRAWN</p>	<p>NAME          Mognitee          Nishi</p>	<p>DATE          01/28/19</p>	<p>HEWABI - UCSD</p>
		<p>INTERPRET GEOMETRIC TOLERANCING PER:          MATERIAL A36 Steel          FINISH          NEXT ASST USED ON</p>	<p>CHECKED          BIG APPR.          MFG APPR.          G.A.          COMMENTS:</p>	<p>TITLE:          Low Beam Joint</p>			<p>SIZE DWG. NO. REV          A J0</p>
<p>APPLICATION</p>		<p>DO NOT SCALE DRAWING</p>		<p>SCALE: 1:2 WEIGHT: SHEET 1 OF 1</p>			<p>1</p>

A

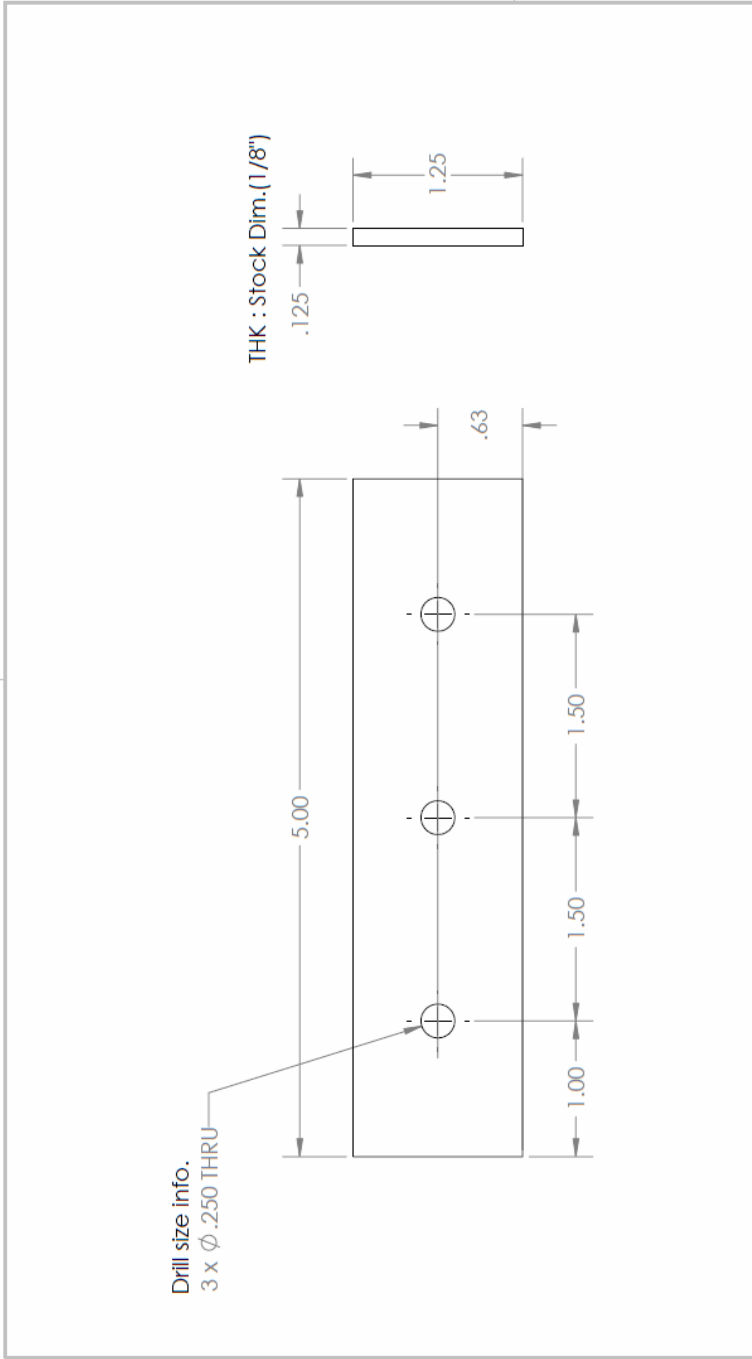
2

1



2

1



B

B

A

A

UNLESS OTHERWISE SPECIFIED:		NAME	DATE
DIMENSIONS ARE IN INCHES		Modena	01/28/19
TOLERANCES:		DRAWN	
FRACTIONAL: ±		CHECKED	
ANGULAR: MACH ±		BIG APPR.	
TWO PLACE DECIMAL ±		MFG APPR.	
THREE PLACE DECIMAL ±		G.A.	
INTERFEROMETRIC TOLERANCING REF:		COMMENTS:	
MATERIAL		Qty: 2pcs	
FINISH		Dimensions in inches	
NEXT ASY	USED ON	SCALE: 1:1	WEIGHT:
APPLICATION		SIZE	DWG. NO.
		A	J2
		REV	REV
		SCALE: 1:1	WEIGHT:
		SHEET 1 OF 1	

HEWABI - UCSD

Flange Shim on Metal Beam  
THK : 1/8"

TITLE:

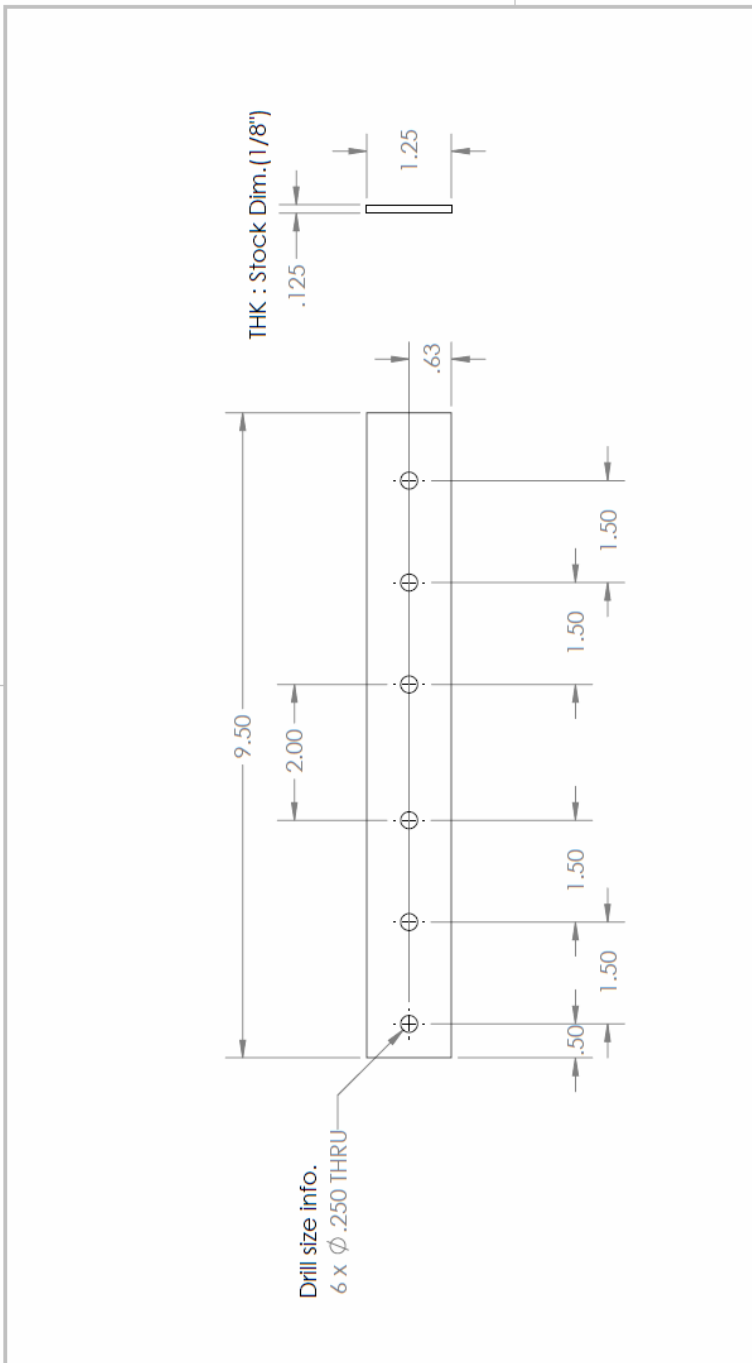
PROPRIETARY AND CONFIDENTIAL  
THE INFORMATION CONTAINED IN THIS DRAWING IS THE SOLE PROPERTY OF HEWABI. ANY REPRODUCTION IN PART OR AS A WHOLE WITHOUT THE WRITTEN PERMISSION OF HEWABI COMPANY IS PROHIBITED.

1

2

2

1



B

B

A

A

UNLESS OTHERWISE SPECIFIED: DIMENSIONS ARE IN INCHES TOLERANCES: FRACTIONAL: ± ANGULAR: MACH ± BEID ± TWO PLACE DECIMAL ± THREE PLACE DECIMAL ±		DRAWN	NAME	DATE
INTERSECT GEOMETRIC TOLERANCING PER:		CHECKED	Moqthero	01/28/19
MATERIAL A36 Steel		BIG APPR.		
FINISH		MFG APPR.		
INERT ASSY		G.A.		
USED ON		COMMENTS: Qty: 2pcs		
APPLICATION		Dimensions in inches		
DO NOT SCALE DRAWING				
HEWABI - UCSD		SIZE	DWG. NO.	REV
Flange connecting plate THK : 1/8"		A	J3	
SCALE: 1:2		WEIGHT:	SHEET 1 OF 1	

2

1